CIVIL ENGINEERING JOURNAL

číslo 3/2023

Obsah:

CIVIL ENGINEERING JOURNAL

Article no. 22

THE CIVIL ENGINEERING JOURNAL 3-2023

DEFORMATION RULE OF BORED PILE & STEEL SUPPORT FOR DEEP FOUNDATION PIT IN SANDY PEBBLE GEOLOGY

Xuansheng Cheng[1], Jiuru He[1], Xinlei Li[1], Qingchun Xia[1], Hongling Su[2], Chaobo Chen[2]

1. *Key Laboratory of Disaster Prevention and Mitigation in Civil Engineering of Gansu Province, Lanzhou University of Technology, Lanzhou 730050, China, email: cxs702@126.com*
2. *China Railway 21st Bureau Group Fourth Engineering Co., LTD., Lanzhou 730070, China)*

ABSTRACT

Regarding the whole excavation process of the support system of the Southwest Jiaotong University Station of Chengdu Metro Line 6 (the deep foundation pit bored pile & steel support and support system) as the engineering background, this paper studies the deformation rule of the deep foundation pit bored pile & steel support of the sandy pebble foundation. The deformation rule of this support system, the settlement rule of the ground surface outside the pit, and the rule of the uplift of the loose at the bottom of the pit are studied. A key analysis of the positive corner of the foundation pit is conducted, and the rationality of the optimization of the support scheme is evaluated. This paper provides effective guidance for the subsequent deep foundation pit construction and provides a reference for deep foundation pit construction.

KEY WORDS

Sand pebble geology, Deep foundation pit, Bored pile, Steel support, Deformation rule

INTRODUCTION

With the development of cities, the frequency of deep foundation pits is increasing, and the requirements on the type of foundation pit support are also increasing. A single type of foundation pit support has been unable to satisfy people's support needs for the excavation process. Many foundation pits now use combined structures for support. Many scholars have conducted detailed scientific studies on foundation pit support in various areas.

In the 1930s, researchers abroad specialized in the study of deep foundation pit engineering. Terzaghi and Peck [1] began to study the ultimate bearing capacity of the loose under shear failure and instability. The foundation pit support design calculation method has been widely recognized by scholars and professionals. Based on this method, the theory has been improved and revised so that it can be better applied in engineering practice, and it is still used today [2]. In the 1950s, Italian engineers developed the support technology of piles + underground diaphragm walls, which became a major construction method for foundation pit engineering. In the 1960s, specifications, technologies and methods for the design and construction of deep foundation pit support were gradually established. In the 1970s, Japanese scholars proposed the SWM method (SWM is the abbreviation of Soil mixing wall). After several improvements, this method became mature and has been widely used in practical engineering. The earliest successful application of loose nail wall support technology to a project occurred in France [3], and the widespread application of loose nail wall support technology has promoted the development of related theoretical and experimental research. In the late 1980s, Zhou et al. [4] were used to simulate the pit dewatering through the inversion of permeability parameters based on the field pumping tests. Satty [5] proposed the analytic hierarchy

process. Based on the summary of Qingdao coastal deep foundation pit engineering. Zhu et al. [6] discussed the deep deformation of the deep foundation pit supporting structure in more depth by considering the excavation process. Wei [7] considered the combination of deterministic factors and uncertain factors, an optimization method for foundation pit support schemes that was based on reliability analysis was proposed. Liu and Lei [8] regarded the majorization of the deep foundation pit support of the Guangzhou Metro as the research background, constructed evaluation model for supporting schemes of subway deep foundation pits. Dai et al. [9] studied the mechanical characteristics of deep foundation pit excavation and support in detail. Yu [10] proposed a complex horizontal support form and a supporting structure system for ground walls. Li et al. [11] calculated and analyzed the horizontal displacement of the pile at various excavation depths with the background of the deep foundation pit project of Guiyang West Road Station of Guiyang Metro Line 2. Li et al. [12] focused on the numerical simulation of the foundation pit supporting structure and on the application of analytical theory to improve the results. Zhang et al. [13] used the elastoplastic numerical simulation method to fully consider the coordination relationship of pile-loose deformation. Xiao and Peng [14] analyzed the selection of a deep and large foundation pit support in combination with on-site monitoring data and changes in surrounding environmental conditions. Yu et al. [15] aimed at overcoming the main limitation of the available method in the analysis of the stability of narrow and long foundation pits.

In recent years, the amount of research that has been conducted on deep foundation pit support has gradually increased, but the research on drilling deep foundation pit hole cast-in-place pile + steel support is less and immature. Therefore, this article studies the deformation rule of deep foundation pit bored piles + steel support.

BASIC ASSUMPTIONS AND ENGINEERING OVERVIEW

Basic assumptions

It is highly difficult for a numerical simulation to fully match the established model with the actual project, and it is necessary to impose basic assumptions on the model. The basic assumptions of this model are as follows:

(1) Rock and loose are regarded as homogeneous and isotropic elastoplastic materials, and the influence of precipitation on the loose characteristic and on the rheological effects of the loose is not considered;
(2) The supporting structure is regarded as an ideal elastomer;
(3) The initial crustal stress field is assumed to be the self-gravity stress field.
(4) It is assumed that groundwater is ignored throughout the excavation process. However, in engineering cases, necessary curtain water-stopping measures are often taken for foundation pits; hence, the forecast deviation value is often small.

Project overview

Project scale

The standard section of deep foundation pit of Southwest Jiaotong University Station of Chengdu Metro Line 6, which width is 22.5 m, overall length is 222.1 m, and the excavation depth is 26.64 m. The excavation depth of the foundation pit is an approximately rectangular parallelepiped structure. Figure 1 is a simplified geometric plan of foundation pit. Figure 2 is a picture of the construction pictures.

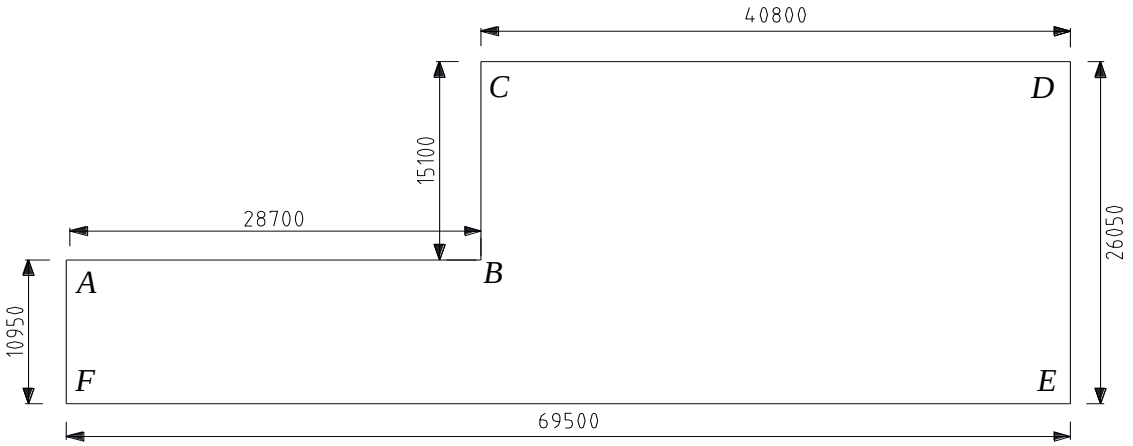

Fig. 1 – Foundation pit plane simplified diagram

Fig. 2 – Construction pictures

Material properties

The material properties of the loose and the supporting system are presented in Tables 1~4.

Tab. 1 - loose parameters

Stratum	Thickness /m	Underlying structural integrity	Natural density ρ / g/cm^3			Cohesion c /kPa	Internal friction angle ϕ /o	Poisson's ratio v	Deformation modulus E_0 / MPa	Severity kN/m^3
Artificial filling	3	Moist and loose	1.8×10^3			15	5	0.30	10.00	18
Silty filling	1	Soft structure	1.9×10^3			20	15	0.30	12.00	19
Fine sand	2	Loose structure	1.9×10^3			/	30	0.28	20.00	19
Slightly dense pebbles	3	Loose structure	2.0×10^3			/	32	0.20	30.64	20
Moderately dense pebbles	20	Loose structure	2.1×10^3			/	36	0.20	38.80	21
Compact pebbles	/	Loose structure	2.2×10^3			/	40	0.20	56.17	22

Tab. 2 - Physical parameters of the envelope structure

Name	Diameter /m	Severity /(kN/m^3)	Elastic modulus /GPa	Poisson's ratio	Pile length /m
Steel support	Φ0.609	78.5	200	0.3	/
A6-type pile	Φ1.2	25	31.5	0.2	31.64 (Pile depth 5)
D6-type pile	Φ1.0	25	31.5	0.2	31.64
E6-type pile	Φ1.0	25	31.5	0.2	31.64
L6-type pile	Φ1.0	25	31.5	0.2	8.7 (Pile depth 3)
LZ-type pile	Φ1.2	25	31.5	0.2	29.74 (Pile depth 8)

Tab. 3 - Design values of the pre-loaded axial force for steel supports

Support position	AB section /kN		BC section /kN		CD section /kN		EF section /kN	
	f	f1	f	f1	f	f1	f	f1
First support (Construction permanent cover)	720	350	220	110	220	110	220	110
First support	/	/	860	400	860	400	860	400
Second support	1370	400	1360	500	1450	500	1430	500
Third support	2420	450	2450	500	2530	500	2430	500
Fourth support	2130	450	2130	500	2140	500	2130	500

Note: f is the design value of the axial force and f1 is the pre-added axial force value. These sections represent the range of design values of the pre-loaded axial force for steel supports.

Tab. 4 - Model parameters of the cover plate and the retaining wall

Name	Thickness /mm	Severity /(kN/m^3)	Elastic modulus /GPa	Poisson's ratio
Cover plate	800	25	31.5	0.2
Retaining wall	300	25	31.5	0.2

Process of foundation pit excavation

The deep foundation pit excavation adopts half cover excavation method. It is designed as two phases and divided into ten working conditions. The excavation process is shown in Table 5.

Tab. 5 - The excavation process

Working condition		Construction process
First phase	I	Establish the initial ground stress balance under the weight of soil.
	II	Setting of bored piles and temporary piles.
	III	Excavate -1.5 m, and install the first support at -0.5 m.
	IV	Excavate to -5.5 m, install permanent cover and concrete retaining wall at -4.5 m.
	V	Remove the first support, and L6 temporary pile and backfill the cover plate.
Second phase	VI	Excavate -4.185 m, and install the first support at -3.185 m.
	VII	Excavation -7.685 m, installation of a second support at -8.685 m.
	VIII	Excavate -17.185 m, and install the third support at -16.185 m.
	IX	Excavate -22.685 m, and install the fourth support at -21.685 m.
	X	Excavation -26.64 m, foundation pit excavation support is completed.

STRESS AND DEFORMATION OF THE FOUNDATION PIT

The foundation pit model is simulated and analyzed by abaqus finite element software, the total number of divided foundation pit grid units is 117012. The loose unit is C3D8R; the retaining pile is simplified as a continuous wall unit; the cover unit is C3D8R; the temporary pile unit is C3D8R; and the diagonal brace and cover pile are T3D2 pole units.

The C3D8R element is an 8-node hexahedral linear reduced integral element, it has the following three advantages: (1) Shear self-locking phenomenon is not easy to occur under bending load; (2) The solution of displacement is more accurate; (3) When the mesh is distorted, the accuracy of the analysis will not be greatly affected. The continuous wall unit is simulated by the solid unit, the spring stiffness element is used to simulate the mutual rubbing between the continuous wall and the soil. The T3D2 pole unit is a three-dimensional beam element defined by two nodes, and it is a lightweight element type that can simulate large deformation.

The contacts relationship of the components are as follows: the support structure and the loose body interact with each other by establishing surface-to-surface contact; the cover plate and the support structure realize a rigid connection between them via common nodes; and the components of the support structure also pass through the common nodes and release the rotational degree of freedom to realize articulation between them.

Change rules of the ground settlement and the pit bottom uplift

(1) Ground settlement outside the pit

Select the points on the section that correspond to the maximum settlement for extraction of the data for analysis, and organize the data into a curve form to better visualize the change trend of loose settlement. The curves are plotted in Figure 3 (a)-(b).

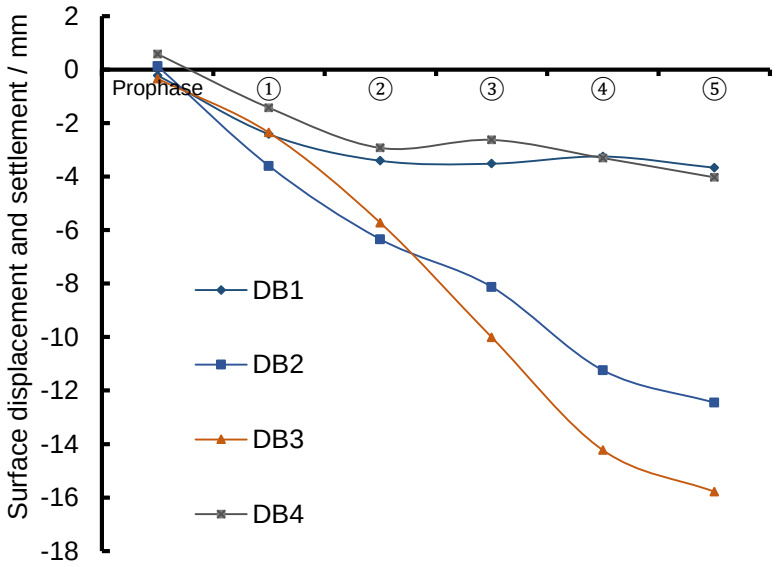

(a) Surface subsidence time-history curves

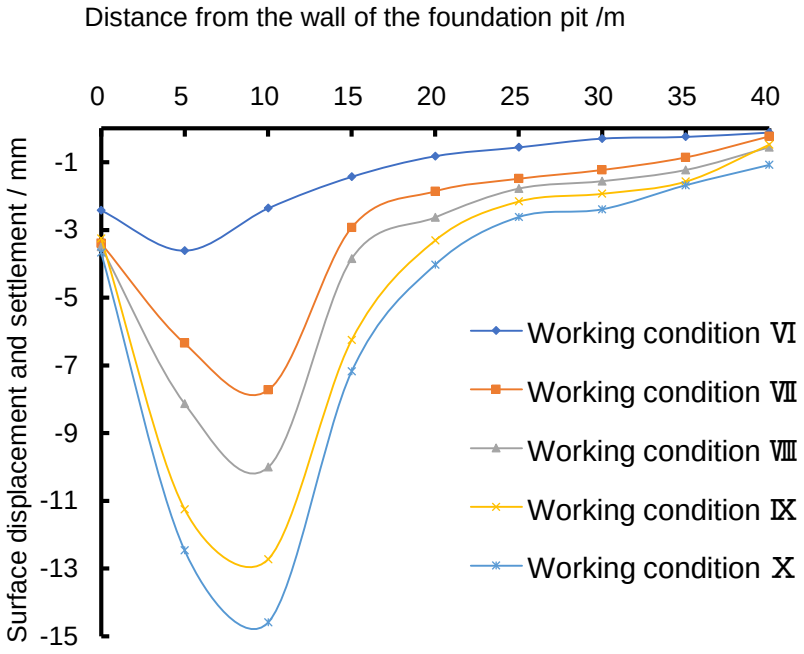

(b) Surface settlement curves from the foundation pit wall

Fig. 3 – Surface subsidence curves

According to Figure 3(a)~(b), the surface settlement curve increases almost linearly. In the later stage of excavation, the settlement curve of the foundation pit tends to be gentle, and the entire settlement curve shows a "parabolic" change. The main settlement occurs approximately 5 ~ 10 m from the foundation pit wall, and the maximum value is approximately 15 mm. After the steel support is erected, the deformation curve of the foundation pit gradually changed from a "triangle" to a "groove shape". The settlement trend of the ground surface outside the pit changed as the ground surface settlement increased rapidly with the distance from the pit wall. When the sedimentation of the foundation pit reaches the maximum settlement value, the ground sedimentation decreases with the increase of the distance from the pit wall, finally, stabilizes and approaches zero. According to the ground settlement map, the width of the impact of the construction of the foundation pit exceeds twice the depth of the construction of the foundation pit.

(2) Loose uplift at the bottom of the pit

The change curve of the pit bottom uplift can well reflect the change of the loose pressure at the bottom of the pit during excavation. A change that is too large demonstrates that the earth pressure on the bottom of the deep foundation pit is too large and, hence, the deformation of the envelope structure is too large, thus, it can easily cause instability of the structure, and it is necessary to study the loose at the bottom of the pit. Select the loose in the middle as the research object, and plot the deformation curve of this loose under each working condition, as shown in Figure 4.

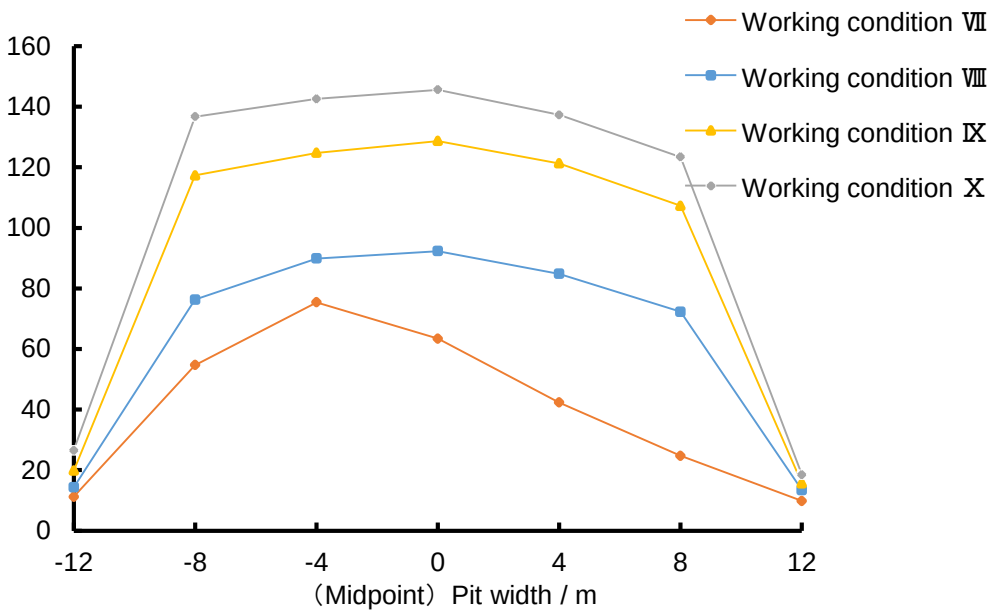

Fig. 4 – Variation of the loose uplift displacement at the bottom of the pit

According to Figure 4, the change in the settlement of the loose bulge is substantially influenced by the excavation of the first phase. The maximum displacement of the uplift of the foundation pit loose occurs at the midpoint of the foundation pit. However, when the deep foundation pit is constructed in the first stage, the loose body has already undergone the uplift phenomenon. Therefore, during the second phase of the excavation process, the maximum displacement of the loose uplift under working condition six occurred at the midpoint of the cover plate. With the continuous excavation of deep foundation pits, this effect is gradually eliminated. The uplift of the loose occurs in the middle of the bottom of the pit. The maximum rise of the foundation pit is approximately 140 mm. In addition, according to the figure, the uplift amount of the foundation pit is constantly increasing over time. Since the deep excavation of the second phase is deeper, the uplift amount of the foundation pit is relatively large. During the third construction process, the uplift amount changed the most. This is because the deep foundation pit has a deeper support interval here, and the pressure on the retaining structure is also the largest, thereby resulting in a sudden increase in the loose uplift.

DISPLACEMENT CHANGES OF THE SUPPORTING STRUCTURE

Variation of the vertical displacement of the envelope structure

In this numerical simulation, the bored cast in situ pile is simplified as an underground continuous wall, therefore, this article will study the change rules of the vertical displacement of the underground continuous wall. Several points at the positive corner are used to analyze the vertical settlement of the wall top. The curves of the displacement and deformation are plotted in Figure 5.

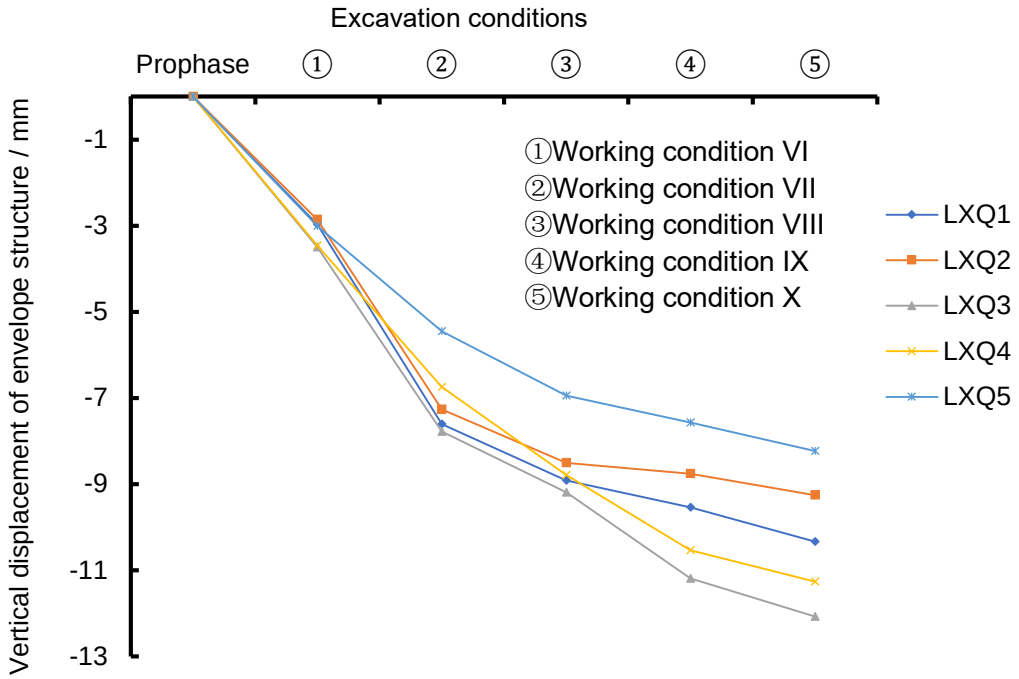

Fig. 5 – Curves of the vertical settlement of the envelope structure

According to the settlement curves in Figure 5, the retaining structure moves downward. Especially prior to the installation of the second steel support, the envelope structure shows a significant downward trend. This is because the first support only supported one side and the other side of the envelope structure is connected to the cover plate. Exerting its supporting role has led to a significant decline in the envelope structure. When the second steel support is installed, the supporting structure and the steel support form a single unit, which fully utilizes its maximum support advantages. Hence, the subsequent settlement trend is slow, and, eventually, the settlement level stabilizes when the loose supports have been finished. The maximum settlement of the retaining structure is approximately 12 mm, which accords with the value that is specified by the foundation pit code.

Axial force of the steel support

The prophase excavation support involves only one steel support, and the support depth is relatively shallow. In addition, it must be removed in the subsequent phase, there is no continuity, and the change rule cannot be studied. Therefore, this article only extracts the four steel supports of the second phase of the deep foundation pit and studies the rule of their axial force change. The oblique rods with relatively high stress and the first crossbar of the standard section are extracted as research objects, and the stress variation rules are analyzed. The variety of the axial force is plotted in Figure 6 (a)~(b).

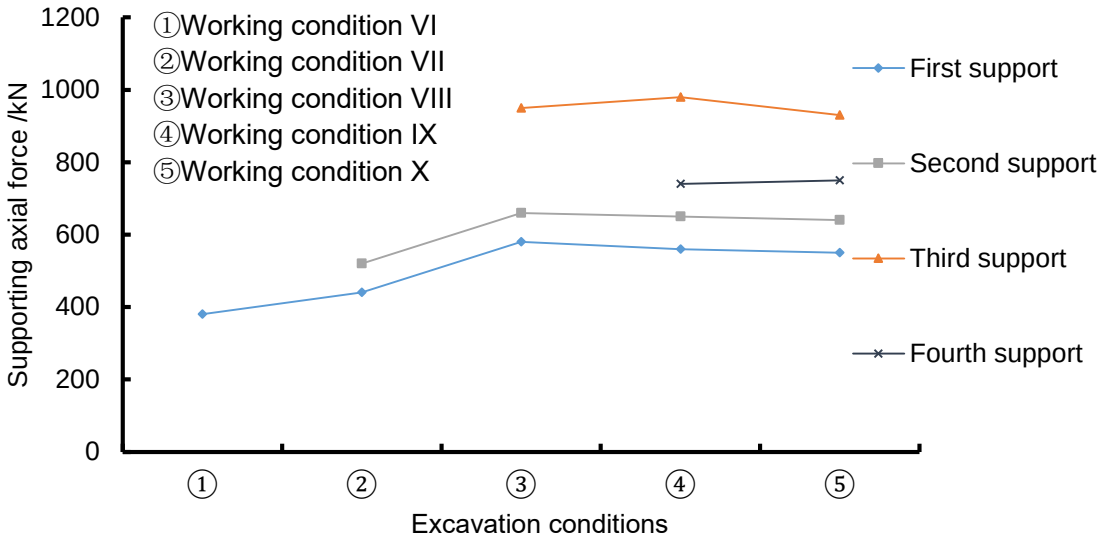

(a) Steel support of the standard section

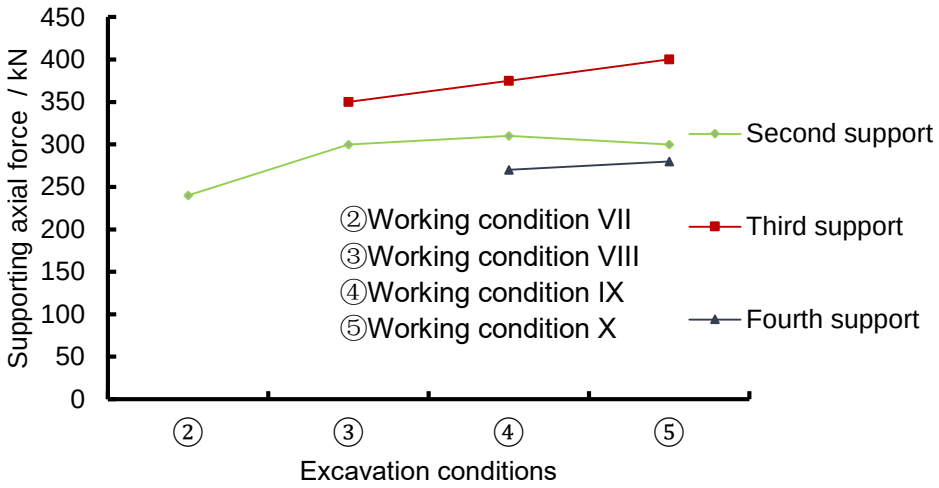

(b) Inclined steel support of the pit angle

Fig. 6 - Axial force changes of the steel support

In Figure 6, the force change rule of the steel support in the standard section is plotted. With the installation of the steel support and the excavation of the loose, the axial forces of the first and second steel supports slowly increase, and they attained their largest values when the third steel support is installed. The third steel support axial force initially increase and subsequently decrease, and the fourth steel support axial force is approximately stable. The axial force of the third steel support is much larger than those of the other three steel supports. This is because the role of the steel support in the support system is resisting the horizontal deformation of the envelope structure. According to the change curve of the deep horizontal displacement of the envelope structure, the maximum point of its horizontal displacement is at the third steel support setting. Hence, the axial force of this support exceeds those of the other supports. In the later stage of deep foundation pit excavation, the axial force of the steel support tends to be stable. Hence, the support system that is composed of the steel support and the surrounding structure is in a safe and reliable state. The support axial force of the pit angle consists of the axial forces of only three steel supports; this is because the upper surface of the second support is a cover plate and the first steel support does not have an inclined support at the pit angle. The axial force deformation of the second steel support

increased initially and subsequently decreased steadily. The variety of the axial force of the three supports is approximately consistent with the change of the supporting axial force of the standard section of the foundation pit. The axial force of the inclined support is lower than that of the standard section. The horizontal deformation of the pit angle retaining structure is smaller than the horizontal deformation of the standard envelope section. The place where the maximum horizontal displacement is attained by the pit angle retaining structure is the same as that of the standard envelope structure, namely, near the setting of the third support.

Analysis of the Pit Angle Effect of the Retaining Structure

The pit angles in the foundation pit are divided into two types: the internal corner and the positive corner. The pit angle has a strong spatial effect, and the positive corner is the most unstable place in the deep foundation pit retaining structure. Therefore, the pit angle should be researched extensively.

According to Figure 1, the maintenance structure has one positive corner B (the positive corner is the angle greater than 180 degrees, point B in this paper is 270 degrees) and multiple internal corners, such as A and C (the internal corners is the angle less than 180 degrees, point A and C in this paper are 90 degrees). Due to the soil pressure of the positive corner in deep foundation pit is relatively large, it is the most unstable force area in the deep foundation pit retaining structure. Therefore, the positive corner should be avoided as much as possible. If the positive corner cannot be avoided, it should be studied via numerical simulations to analyze the reasons for its instability and to provide corresponding guidance for subsequent construction. During the excavation of the first phase, the excavation of the foundation pit is shallow, and the horizontal displacement of the supporting structure is relatively small; hence, the change rule of its horizontal displacement is investigated. The data of the deep horizontal displacement of the underground diaphragm wall with positive corners of 1 m, 4 m, 7 m, 10 m, and 13 m on the AB and BC sections under each working condition are analyzed, and the deformation rules are summarized, as shown in Figure 7(a)~(e).

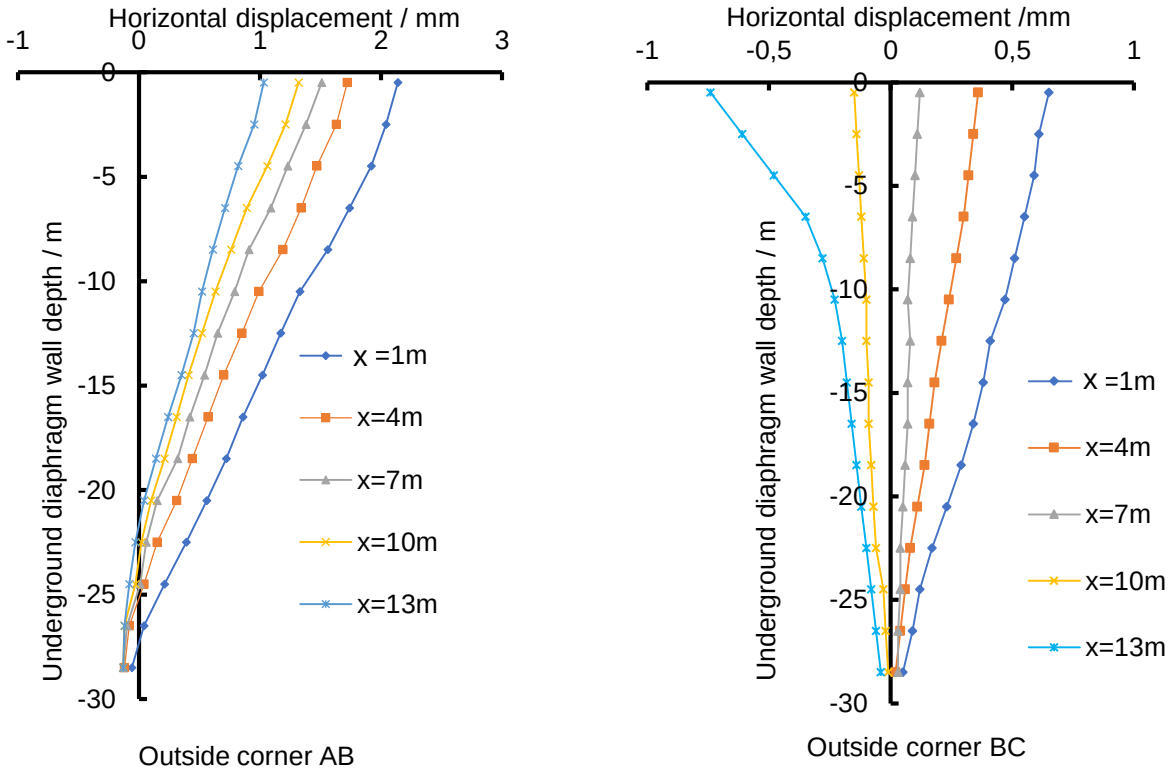

(a) Working condition VI

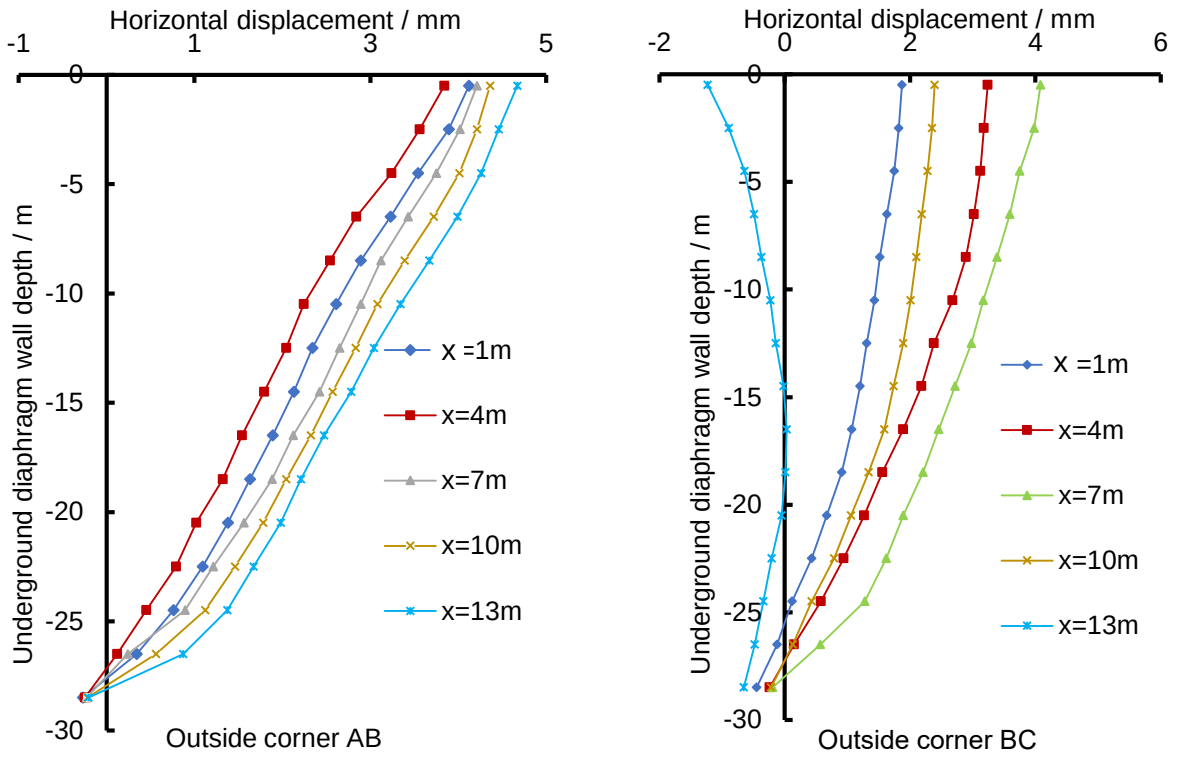

(b) Working condition VII

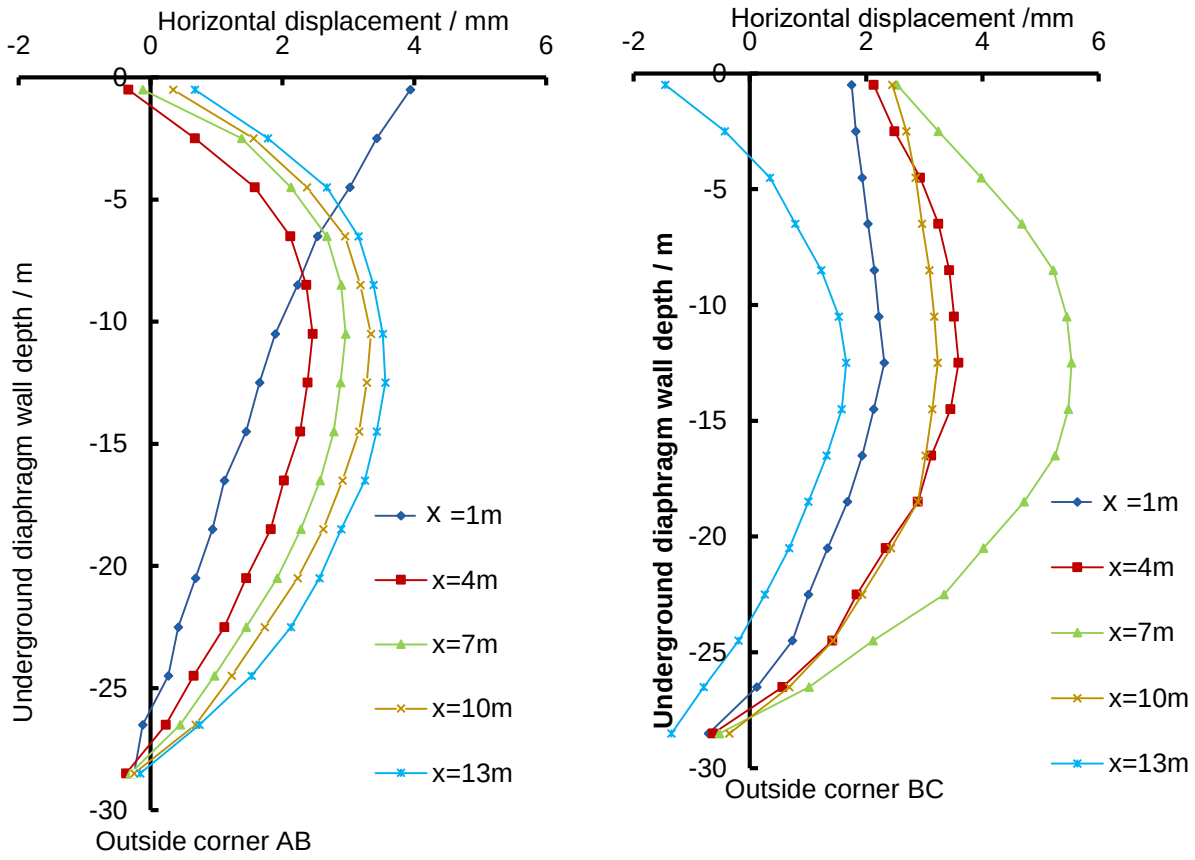

(c) Working condition VIII

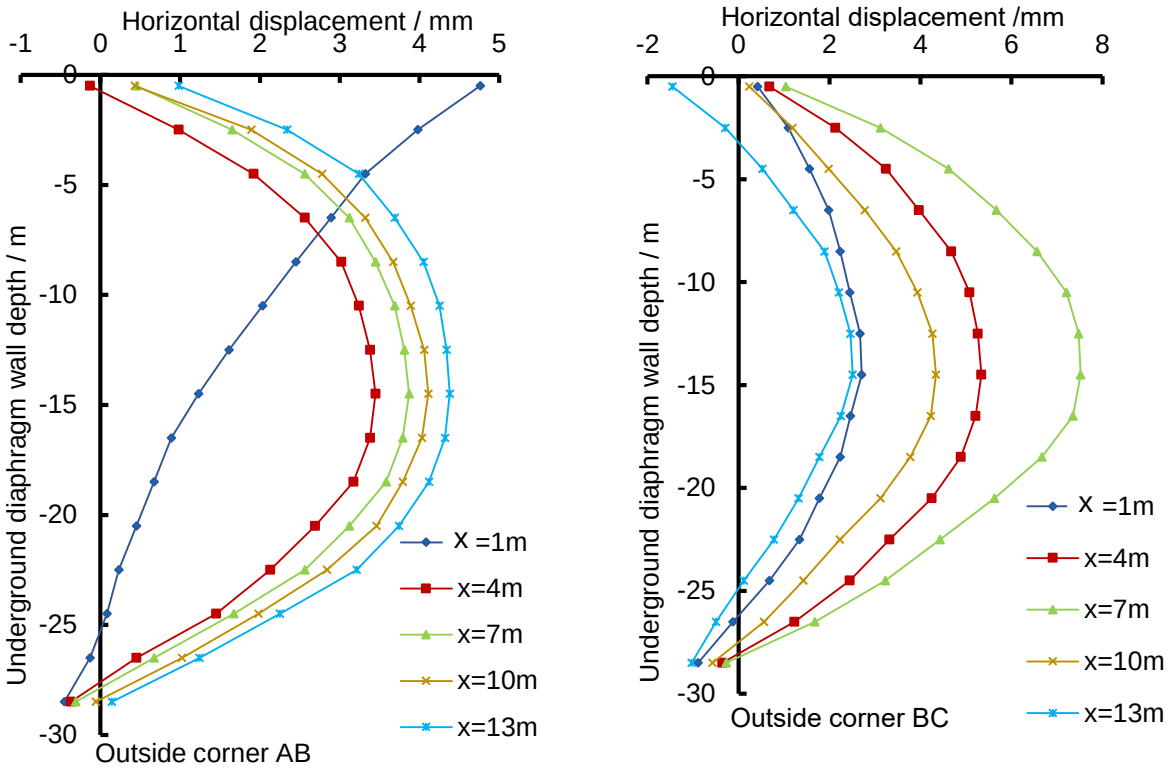

(d) Working condition IX

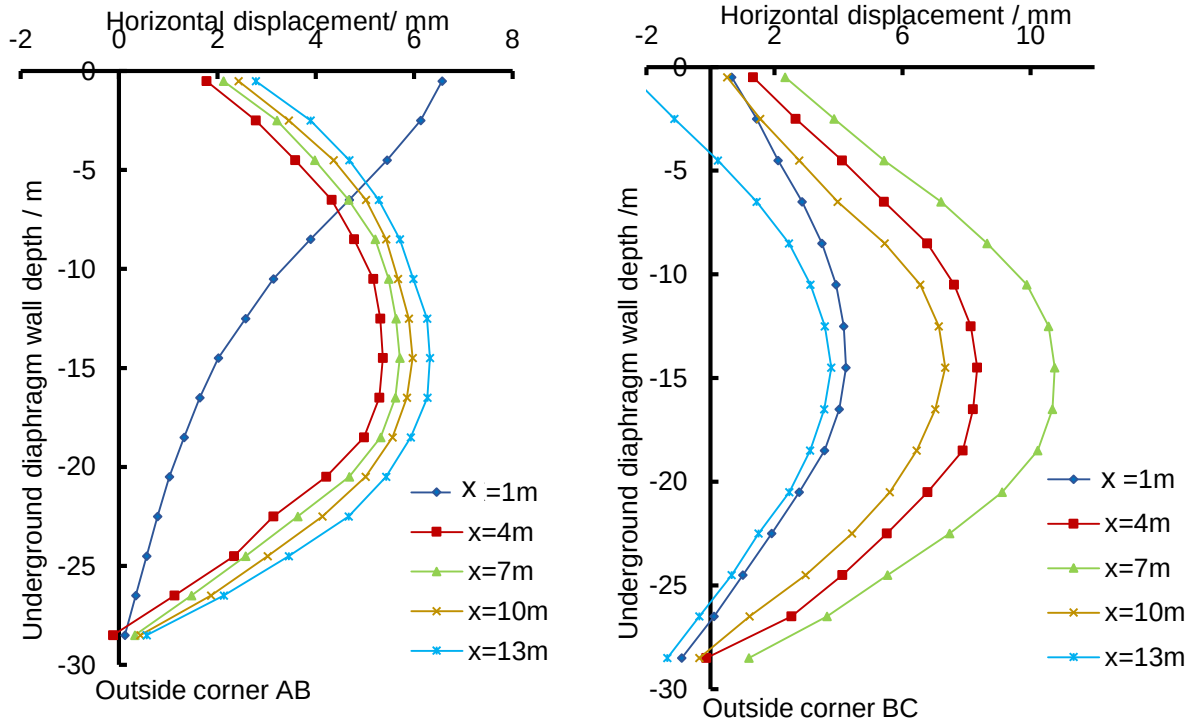

(e) Working condition X

Fig. 7 – Curves of the horizontal displacements of the retaining structure at both ends of the positive corner under various working conditions

According to Figure 7, under working condition VI, the retaining structures of the positive corner AB section are in a cantilever state and almost all move horizontally into the foundation pit. The point with the largest horizontal displacement is not at the positive corner but at approximately 4 m from the positive corner. This is because a horizontal support and multiple inclined supports are set near the positive corner, which effectively prevent the destruction of the positive corner of the foundation pit. The enclosure structure of the positive corner BC section is also in a cantilever state, but the rule of movement to the outside of the pit is farther away from the positive corner of the pit. This is because this place is near the internal corner C. Due to the inclined support and the effect of the CD segment on the internal corner, the retaining structure is subjected to internal forces that exceed the earth pressure outside the deep foundation pit. Therefore, the displacement of the envelope structure corresponds to negative values.

Under working condition VII, the change rule of the envelope structure in section AB is similar to the deformation rule under working condition VI. With the continuous construction of the deep foundation pit, the retaining structure moves horizontally into the pit, and the retaining structure of section BC undergoes a "bending" change. This is because section BC is an inclined support with a large axial force, which can bear most of the lateral pressure of the loose outside the pit. The support structure is no longer in a cantilever state, and the axial force slowly becomes a fixed force at both ends.

Under working condition VIII, the horizontal displacement change rule of the envelope structure in section AB is approximately the same as that of the overall envelope structure, and the envelope structure exhibits a "bulge" phenomenon. However, a different trend is observed near the positive corner. Here, the envelope structure does not follow the rule “a small change in the middle and a large change in the middle”. This is because the positive corner of the deep foundation pit is squeezed by not only the earth pressure but also the pressure that is induced by the horizontal movement of the support structure of the BC section into the pit after being subjected to the axial force of the inclined support. Thus, the supporting axial force is much smaller than the pit pressure on the envelope structure, and the envelope structure is in a cantilever state. With the continuous construction of the deep foundation pit, the variety rule of the BC section's retaining structure shows an increasingly strong "bow step" shape; hence, the BC section exhibits a satisfactory embedding effect. The more complicated force occurs at the place that is connected with the inside corner, and the envelope structure moves outside the pit.

During the excavation under working condition IX, the envelope structures of the positive corner AB and positive corner BC sections continued to increase with the excavation of the deep foundation pit, and the "bulge" phenomenon became increasingly apparent. Hence, the sand pebble geology has a satisfactory embedding effect on the bottom of the envelope structure. The change rule of the horizontal displacement under working condition X is almost the same as those under working conditions VIII and IX. The displacement deformation of the envelope structure attains its maximum value. The displacement of the envelope structure at the positive corner of segment AB reaches 6 mm, which satisfies the maximum deformation displacement that is specified by the code. The maximum point of the envelope structure of the BC section occurs at the third support, and the maximum displacement is approximately 10 mm, which satisfies the maximum deformation displacement that is specified by the code.

In summary, the change rule of the retaining structure at the positive corner pit is similar to the change rule of the overall structure. However, various differences are readily observed: The horizontal displacement change along the short side at the positive corner B differs substantially from that of the ordinary support structure, and according to the preliminary analysis, the pre-loaded axial force of the steel support is too small. However, the negative change in the displacement near the internal corner C indicates that the envelope structure is moving horizontally outside the pit, which may be caused by the excessive axial force of the second inclined support. Thus, the forces at the positive corner and the internal corner of the retaining structure are highly complicated, and this corner is the most unstable place.

CONCLUSIONS

1) The curves of the surface settlement results of the 3D numerical simulation are analyzed, and the ground settlement of the loose body is found to increase continuously with the excavation of the foundation pit. The maximum point of loose surface settlement is not near the pit wall but at a distance of approximately 6-10 m from the pit wall. After erection of steel support, the variation law of the surface settlement curve outside the foundation pit is that the surface settlement increases rapidly with the increase of the distance from the pit wall. When the settlement of foundation pit reaches the maximum settlement value, the surface subsidence decreases with the increase of distance from the pit wall. From Figure 3 (b) we can clearly see this trend.

2) According to the analysis of the envelope structure, the settlement of the envelope structure increases and eventually becomes flat. With the continuous excavation of the deep foundation pit, the retaining structure exhibits a "bulge " phenomenon, which also demonstrates that the two ends of the retaining structure are better restrained and the sand pebble geological retaining structure exhibits a satisfactory embedding effect.

3) Focusing on the pit angles of the supporting structure, the results demonstrate that the positive corner of the supporting structure is the most complicated place, (the positive corner is the angle greater than 180 degrees, point B in this paper is the positive corner). With instability changes, in the support of the foundation pit, the positive corner of the foundation pit should be avoided as much as possible. If it is unavoidable, in-depth study of the positive corner should be conducted to identify the cause of the instability of the positive corner, and the axial force should be adjusted reasonably to transform the envelope structure of the positive corner into a stable state under stress to ensure the safety of foundation pit construction.

ACKNOWLEDGMENTS

This research is supported in part by the National Natural Science Foundation of China (grant number: 51968045), and a part of science and technology project in China Railway 12th Bureau Group Co. LTD. (Grant number: 17C-5).

REFERENCES

[1] Terzaghi K., Peck R.B. Soli Mechanics in engineering practice[M]. New York: John Wiley and Sons,1948.

[2] Whittle A.J., Hashash Y.M.A., Whitman, R.V. 1993, Analysis of deep excavation in boston, Journal of Geotechnical Engineering, 119(1), 69-90. DOI:https://doi.org/10.1061/(ASCE)0733-9410(1993)119:1(69)

[3] Zhu, F.B., Miao, L.C., Gu, H.D., et al (2013), “A case study on behaviors of composite loose nailed wall with bored piles in a deep excavation”, Journal of Central South University, 20(7), 2017-2024. DOI: 10.1007/s11771-013-1703-8

[4] Zhou N.Q., Vermeer P A , Lou R., et al. (2010), Numerical simulation of deep foundation pit dewatering and optimization of controlling land subsidence[J]. Engineering Geology, 114(3-4):251-260. DOI:https://doi.org/10.1016/j.enggeo.2010.05.002

[5] Satty, T.L. The analytic hierarchy process[M]. New York: Mc Graw Hill Inc.,1980.

[6] Zhu, Z.G., Zhao, W., Li, S.G. (2013), “Study on calculation methods of brace construction for metro deep foundation pits”, Chinese Journal of Underground Space and Engineering, 9(5), 1109-1114.

[7] Wei, D.J. (2016), ‘Research on support scheme optimization and risk control of deformation of metro foundation pit nearby buildings”, PhD’s thesis, Xi’an University of Architecture and Technology, Xi’an, China.

[8] Liu, Z.J. and Lei, J.S. (2007), “Fuzzy probability model of supporting scheme for deep foundation pit of metro and its application”, Journal of Railway Science and Engineering, 4(6), 57-60. DOI:10.19713/j.cnki.43-1423/u.2007.06.011

[9] Dai, Y.B., Zhang, S.G., Zhou, Z.S., et al. (2005), “Application of fuzzy consistent matrix theory to optimization of bracing projects for deep foundation pit of metro”, Chinese Journal of Geotechnical Engineering, 27(10), 1162-1165. DOI:10.3321/j.issn:1000-4548.2005.10.010

[10] Yu, C.Y. (2019), Design and deformation monitoring of complex support in deep foundation pit. 4th International Conference on Energy Equipment Science and Engineering, December, Xi'an, China. DOI:10.1088/1755-1315/242/6/062028

[11] Li, T., Shao, W., Zheng, L.F., et al. (2019), “Analytical solution of retaining pile’s deformation for deep loose-stone composite foundation”, Journal of China University of Mining and Technology, 48(03), 511-519. DOI:10.13247/j.cnki.jcumt.001005

[12] Li, D., Zhang, Q.C., Jin, G. et al. (2015), “Analytical solution of earth pressure on supporting structure of deep foundation pit considering arching effects”, Rock and loose Mechanics, 36(S2), 401-405. DOI:10.16285/j.rsm.2015.S2.056

[13] Zhang, J.G., Xiao, S. G., Zou, L. et al. (2013), “Earth pressure on retaining structure of round deep foundation pit in sand-cobble looses”, Journal of Civil Architectural & Environmental Engineering, 35(4), 89-93 DOI:10.11835/j.issn.1674-4764.2013.04.014

[14] Xiao, S.J. and Peng, W.P. (2018), “Scheme selection analysis on design of a deep and large foundation pit”,Journal of Hunan University Natural Sciences, 45(S1),190-196. DOI:10.16339/j.cnki.hdxbzkb.2018.S0.034

[15] Yu, J.L., Long, Y., Xia, X. et al. (2017), “Basal stability for narrow foundation pit”, Journal of Zhejiang University (Engineering Science), 51(11), 2165-2174. DOI:10.3785/j.issn.1008-973X.2017.11.010

CIVIL ENGINEERING JOURNAL

Article no. 23

THE CIVIL ENGINEERING JOURNAL 3-2023

CONSTRUCTION VERIFICATION OF AN ASYMMETRIC ARCH BRIDGE BASED ON CONSTRUCTION MONITORING AND TESTS

Xilong Zheng[1], Dachao Li[2], Kexin Zhang[2], Xiaojie Xue [3] and Fanhua Min[4]

1. *School of Civil and Architectural Engineering, Harbin University, No.109 Zhongxing Road, Harbin, Heilongjiang Province, China; sampson88@126.com*
2. *School of Transportation and Geomatics Engineering, Shenyang Jianzhu University, No. 25 Hunnan Zhong Road, Shenyang, Liaoning Province, China; jt_zkx@sjzu.edu.cn*
3. *Engineering Department, Guangzhou Expressway Co., LTD, No. 17 Fenghuang San Road, Guangzhou, Guangdong Province, China*
4. *Research and Development Center, Liaoning Transportation Planning and Design Institute Co. LTD, No. 42 Lidao Road, Shenyang, Liaoning Province, China*

ABSTRACT

For the three-span continuous tied arch bridge with unequal span, its sagittal span ratio is different, which leads to the design internal force and construction is very complicated. The construction method and installation sequence are closely related to the main beam, arch rib alignment and the internal force state of the structure. For the arch bridge with special structure, the stiffness of the arch ring and the stress of the main beam will affect the stability and deformation of the whole structure. The theoretical and practical deviations of arch bridge construction are cumulative. If not timely and effective control and adjustment according to the actual data, it will endanger the safety of the structure in the construction process. In order to ensure the safety of the bridge construction process, the stress of the main beam, the centring of the arch ring and the temperature are monitored and recorded during the whole construction process. After the completion of the bridge construction, static and dynamic load tests were conducted to verify whether the bridge can meet the design specifications. The construction monitoring results indicated that during the construction of the arch bridge, the stress of the girders was in good agreement with the theoretical values, meeting the design standards and specifications. The actual alignment of arch rings was basically consistent with the theoretical alignment.

KEYWORDS

Tied arch bridge, Through arch bridge, Construction monitoring, Construction verification, Load tests

INTRODUCTION

Arch bridge is a common bridge type, which has a long history in the world. Compared to the beam bridge, the arch bridge is not only beautiful in shape, but also has greater spanning capacity. An arch bridge transmits vertical loads to its arches, which in turn transmits forces to the foundations on either side. The span of arch bridge is restricted by material properties as a flexural component [1-3]. With the progress of the times, the traditional masonry arch bridge was gradually replaced by

reinforced concrete arch bridge. The reinforced concrete (RC) arch bridge has great difficulty in construction method and construction monitoring because of its large dead weight. Tied arch bridges have the general characteristics of arch bridges as well as their own unique characteristics. It is a bridge type that combines the advantages of arch and beam. It combines the two basic structural forms of arch and beam to bear load together. This kind of arch bridge is a statically indeterminate system in the interior and a statically indeterminate system in the exterior. This structural form gives full play to the structural performance and combination function of beam bending and arch compression. The horizontal thrust at the arch end is borne by tension rod, so that the support at the arch end does not generate horizontal thrust [4-5]. Besides, it has two characteristics of large span capacity and strong adaptability to the foundation [6-7]. When the deck elevation is limited, the tied arch bridge can ensure a large clearance under the bridge [8].

As a kind of non-thrust combined system, arch rings stiffness and girders stress of the tied arch bridge will affect the stability and deformation calculation results of the whole bridge structure. The theoretical and practical deviations of arch bridges in construction are cumulative. If it is not controlled and adjusted timely and effectively according to the actual data, it will endanger the safety of the structure during the construction process. Therefore, arch bridge construction monitoring is especially essential [9-11]. The goal of load test is to measure the stress and deflection of the control section of the bridge span structure under the action of test load through the static load, and compare with the theoretical calculation value, to check whether the stress value and deflection value of the control section of the structure are consistent with the design requirements, and to evaluate the current bearing capacity of the bridge span structure. Through the dynamic load test, the overall dynamic performance of the structure and the dynamic performance under the vehicle are evaluated, which provides the original data for the bridge maintenance, management, reinforcement and repair or reconstruction in the future [12-14].

To ensure the safety construction, in the construction monitoring, the arch rings line and stress, the temperature changes before and after the girders pouring were monitored. At the same time, bridges were also experimented with static and dynamic load tests to verify whether the bridge could achieve the designed requirements. This work can offer significant reference for the construction and design of similar tied arch bridges.

BACKGROUND

Wolong River Bridge is located in Dalian City, across the Wolong River, the central axis of the bridge and the river oblique. Wolong River Bridge is a three-span continuous girder arch composite bridge. The vertical section of the completed bridge is shown in Figure 1. It has a total length of 130 m with three spans. The length of each span is 48 m, 43 m and 38.5 m respectively. The width of the bridge deck is 6.0 m (sidewalk) +11.5 m (motor vehicle lane) +4.0 m (cables area) +11.5 m (motor vehicle lane) +6.0 m (sidewalk) = 39 m. The design base period of the bridge structure is 100 years. The design of the bridge's automobile load is highway level one according to Chinese regulations. The upper column of the bridge tower adopts rectangular section, the lower column adopts cylindrical section, and the foundation adopts pile group.

Fig. 1 – Vertical section of Wolong River Bridge

The load-bearing structure consists of five rooms RC box-girders. The box-girder height at the fulcrum is increased to 3.0 m. The edge fulcrum is raised in a straight line, and the girder height in the middle fulcrum is changed in a circular arc. The top edge of the main girder within the 4 m cables area at both ends of the arch feet is increased by 0.4 m C50 concrete is used. Bridge's elevation is shown in Figure 2. The box-girder is 39 m of top width and 26.85 m of bottom width. The bi-directional 1.5% transverse slope of the deck is adjusted by the height change of the main girder web. The hanger rods are arranged within the range of the middle box, and the main girder is set with transverse diaphragms at each anchorage point of the hanger rods, the width of which is 0.35~0.65 m. Prestressed steel beams are arranged in the longitudinal and transverse beam, end beam and middle beam of the main beam. The arch axis equation is a parabolic equation, and the ratio of vector to span is F /L = 1/1.9, 1/2.7 and 1/3.9, respectively. The height of the vector is about 25 m, 16 m and 10 m respectively. The section width of the arch rings is 3 m, and the height of the three spans is 1.5 m, 1.35 m and 1.2 m, respectively. The arch rings are made of C50 concrete with cast-in-place supports. PES7-55 and PES7-73 normal suspenders are used for the suspenders. The distance between the suspenders is 3.5 m, the safety factor of the suspenders is 2.5, and the tension of the single suspenders is 900 kN~1500 kN. The pile foundation is made of bored pile with a diameter of 150 cm, and the whole bridge has a total of 32 piles.

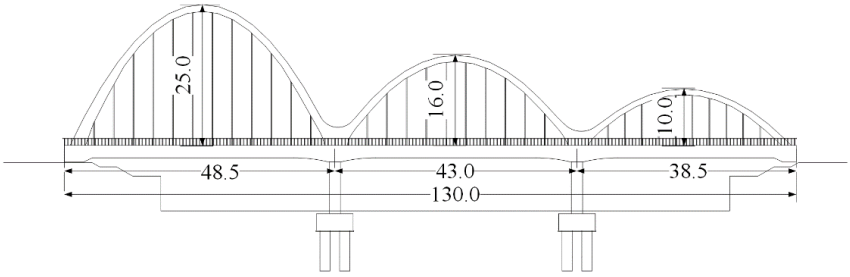

Fig. 2 – Elevation of the arch bridge (unit: m)

The construction process is mainly in group of six steps: (1) Substructure and foundation construction；(2) Set up the main girder support and cast the main girder；(3) Set up arch rings support and pour arch rings；(4) Install the suspender, tension the suspender for the first time, and remove the arch rings support；(5) Remove the main beam bracket and tension the suspender for the second time；(6) Bridge deck construction, boom force adjustment. The specific construction steps are shown in Figure 3.

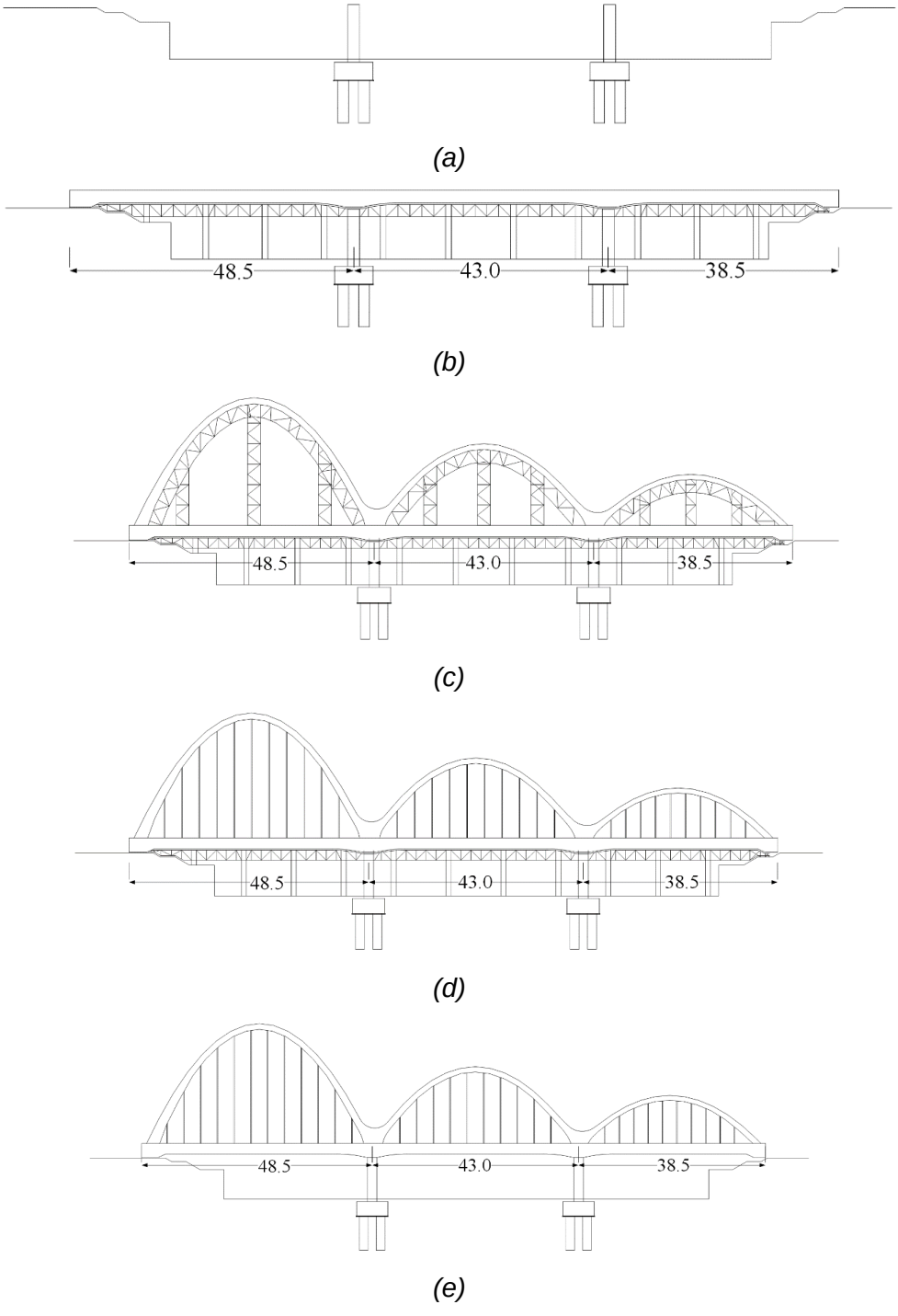

Fig. 3 – The specific construction steps

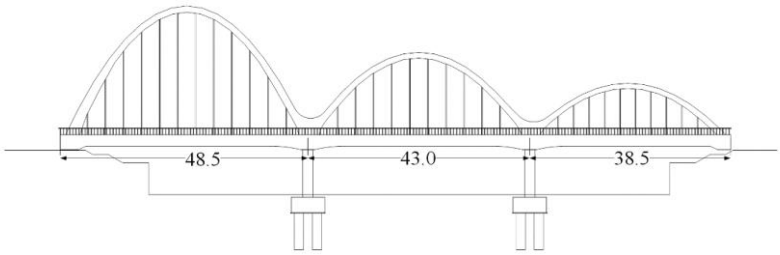

(f)

Fig. 3 – The specific construction steps : (a) Step 1: Substructure and foundation construction; (b) Step 2: Set up the girders brackets and cast the main girder; (c) Step 3: Set up arch rings support and pour arch rings; (d) Step 4: Install the hangers, tension the hangers for the first time, and remove the arch rings support; (e) Step 5: Remove the brackets and tension the hangers for the second time; (f) Step 6: Bridge deck construction, hangers force adjustment

CONSTRUCTION MONITORING AND LOAD TEST

Continuous beam arch composite bridge presents excellent and stable economic indicators and beautiful appearance which is more suitable for soft soil foundation because of its light structure and no horizontal thrust outside [15-16]. The main arch bears the vertical load and the vertical cable force of the bridge span. This is mainly because the design parameters used in the design, such as the elastic modulus of materials, the dead weight of components and the temporary load of construction, are not completely consistent with the parameters in the actual project. The construction of complex bridge is a systematic project. In the system design is the ideal target, and from start to completion of the whole to achieve goals, the design must go through the process, will be a lot of determination and the influence of the uncertainty, including design calculation, material properties and construction precision, load, atmospheric temperature, and many other aspects of the differences between ideal state and actual state. How to find out the relative true value from various parameters distorted by errors in construction and carry out real-time identification (monitoring), adjustment (correction) and prediction of the construction state is crucial to the realization of the design goal [17-18].

Finite element model (FEM)

As a software widely used in civil engineering, Midas/Civil is adopted to build the FEM of the arch bridge. In order to facilitate the calculation, some elements in the model are simplified on the basis of fully considering the construction sequence and the structure stress. Box-girders and arch rings are girder elements, and the suspender is tensile structural elements. Figure 4 shows the FEM of the tied arch bridge.

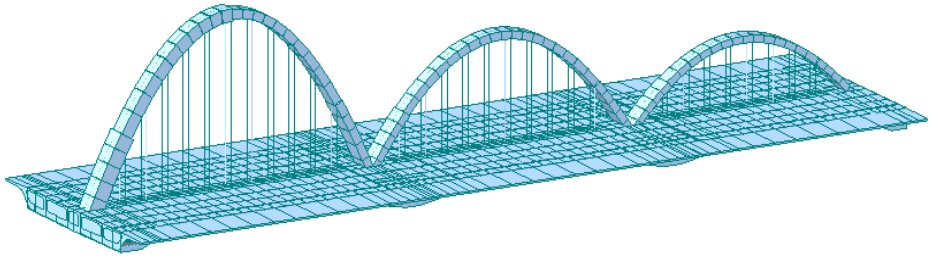

Fig. 4 – FEM of the tied arch bridge

The definition of mechanical properties of different sections of pedestrian arch bridge in the FEM is shown in Table 1. The box girders and arch rings are casted with C50 concrete. The cap and abutment are made of C40 concrete, the pier and foundation are made of C30 concrete, and the elastic modulus E = 3×10^4 MPa. The sling is composed of 61 high-strength steel wires with a tensile strength of 1670 MPa. The standard yield strength of ordinary steel bar is 335 MPa.

Tab. 1 - Mechanical Properties Defined in the FEM

Structural Parts	Material	Compressive Strength （MPa）	Tensile Strength （MPa）	Modulus of Elasticity （MPa）
Box Girders, Arch Rings	C50 Concrete	22.4	1.83	3.45×10^4
Bridge Abutments	C40 Concrete	18.4	1.65	3.25×10^4
Bridge Piers, Foundation	C30 Concrete	13.8	1.39	3.00×10^4
Suspenders	OVM.PES7-61	-	1670	2.05×10^3
Prestressed Reinforcement	Φ15.2 Steel Strand	-	1860	-
Steel Bars	HRB335	-	420	2.10×10^5

Construction monitoring scheme

Position of measuring points

As shown in Figure 5, six test sections are arranged in the arch bridge. Concrete temperature measurement is to test and monitor the temperature distribution of the whole pouring block, to provide guidance for construction.

Measuring point arrangement of arch rings elevation is shown in Figure 6. Elevation observation should be carried out in 33 sections where the arch rings, arch foot and suspender are located. Therefore, there are 66 measuring points in the whole elevation. Permanent observation points are set up at the top and foot of the arch. The data of these observation points are one of the most important data in construction monitoring.

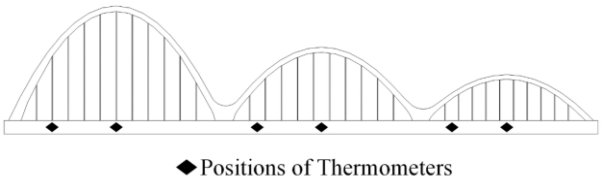

Fig. 5 – Positions of measuring points

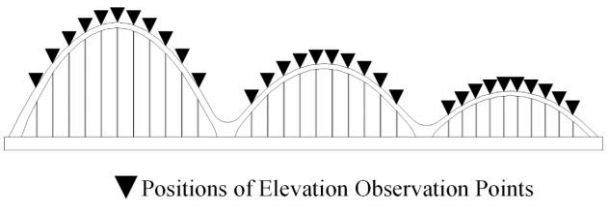

Fig. 6 – Measuring points for elevation of arch rings

Static load tests

Test contents

Based on the stress characteristics of the tied arch bridge, test sections are determined as the

1/2, 1/4, 1/8, 3/4, and 7/8 span section. The test content and measuring points are shown in Table 2. Static load tests include vertical deflection, longitudinal displacement and strains of the girders. In addition, the hangers force is also tested in the experiments. The placement of measuring points in this static load test is shown in Figure 7.

Tab. 2 - Test Contents of Static Load Tests

Measuring Points	Test Contents
N1-N6	Deflection of Girder
M1-M6	Lateral Strain of Girder
M7-M12	Vertical Strain of Girder
D1-D3	Hangers Force

Arrangement of test vehicles and measuring points

The layout of measuring points in static load test is shown in Figure 7. If the actual load of the vehicle is inconsistent with the calculation and analysis, it will be adjusted in the later stage. The test vehicles are planned to be 6 trucks each weighing 450kN, and the specific parameters are shown in Table 3.

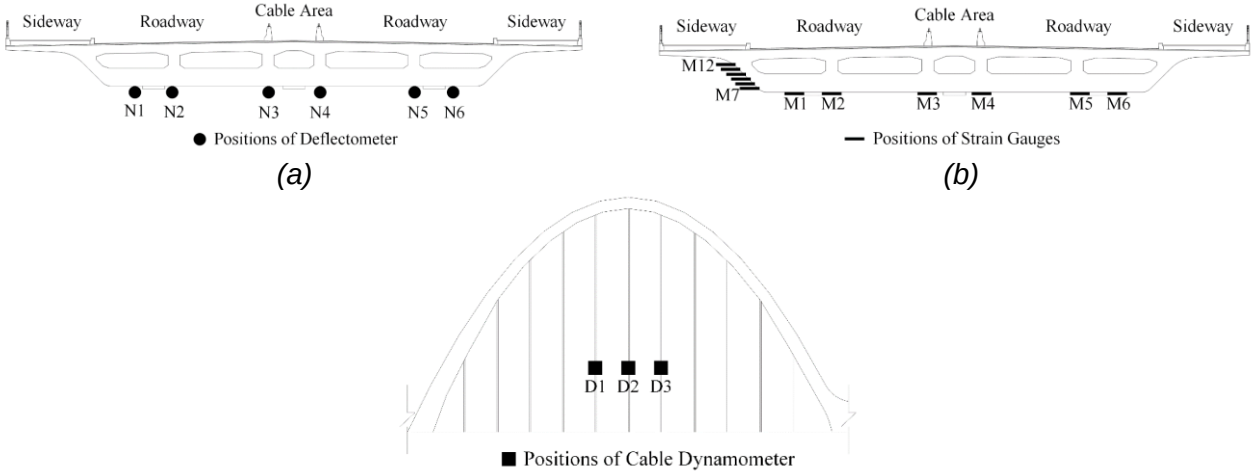

(a) *(b)* *(c)*

Fig. 7 – The layout of measuring points in static load test :(a) Deflection measurement points;(b) Strain measuring points; (c) Hangers force measuring points

Tab. 3 - Detailed Data of The Loading Vehicle

P1	P2	P3	A	B	C	D
Front Axle	Rear 1Axis	Rear 2 Axis	Wheelbase	Wheelbase	Wheelbase	Wheelbase
（kN）	（kN）	（kN）	（cm）	（cm）	（cm）	（cm）
40~80	90~130	90~130	130~145	330~430	300~500	180

The static test load loading method is to use the three-axle truck as the equivalent load. Meanwhile, the equivalent load can generate the stress in the test process. Therefore, for a specific

test section, the number of vehicles required to be loaded will be equivalent converted by the designed load and according to the principal standard.

Test conditions

The static load tests of the tied arch bridge are divided into four working conditions by changing the longitudinal position of the test vehicle on the bridge deck to ensure the load efficiency within the specified range. Four test conditions are shown in Figure 8:

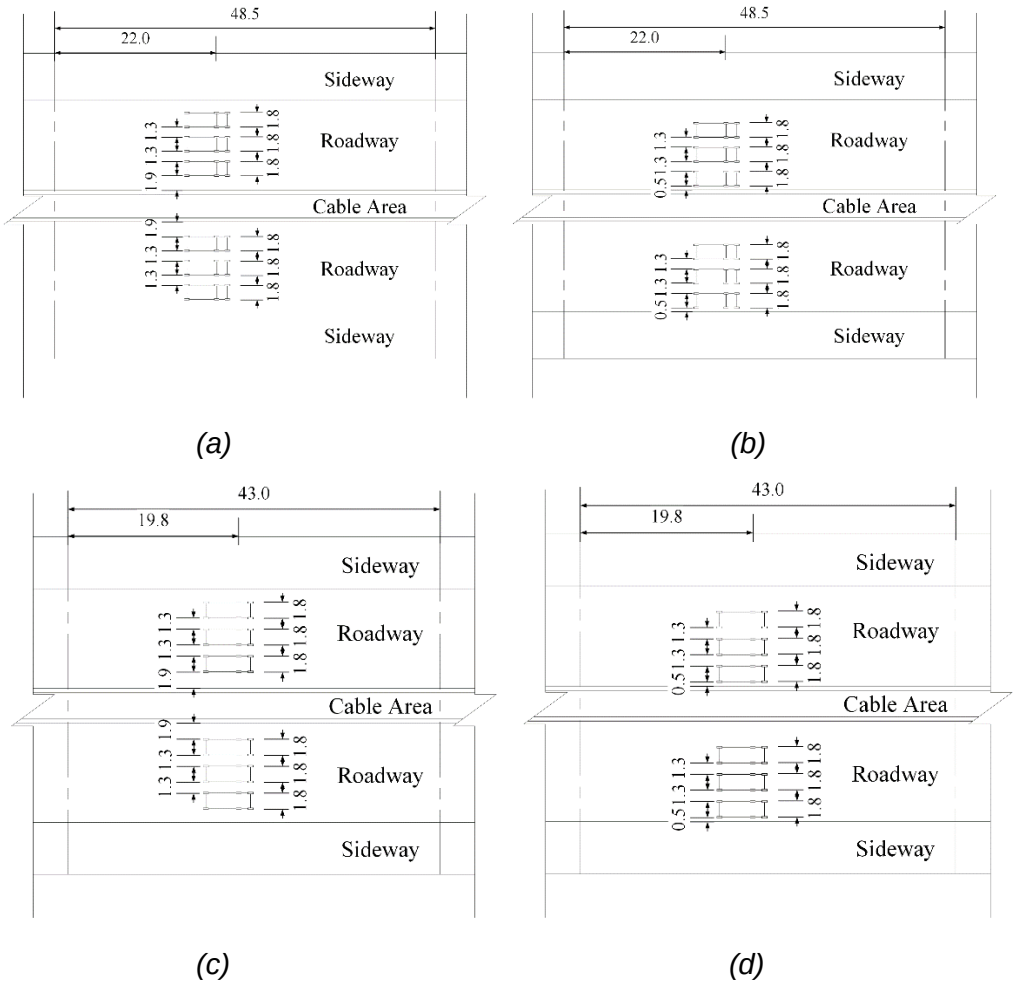

Fig. 8 – Four loading conditions of static load test : (a) Test condition 1: Maximum positive bending moment of the first span under symmetric loading; (b) Test condition 2: Maximum positive bending moment of the first span under eccentric loading; (c) Test condition 3: Maximum positive bending moment of the second span under symmetric loading; (d) Test condition 4: Maximum positive bending moment of the second span under eccentric loading.

Dynamic load test

Dynamic load tests are to understand the dynamic characteristics of the tied arch bridge from many measured data and signals, and comprehensively evaluate the dynamic characteristics of the bridge. The internal laws of bridge structure vibration are revealed to judge the actual working state. Meanwhile, original data are also accumulated for the structural evaluation in the service phase. In addition, the time history curves of various vibration parameters can be obtained. Due to the vibration

of the real bridge structures are often complex, are generally not random, directly according to the signal or data to analyze and judge the regularity of structural vibration is difficult, usually need to analyze the vibration waveform and processing, in order to do further analysis for structure dynamic performance, can draw such as amplitude, parameters such as damping ratio, coefficient of vibration mode, impact [19-23]. Frequency domain analysis is to reveal the frequency of the signal components and transfer characteristics of vibration system. Then the distribution of vibration energy can be found by frequency, so as to determine the frequency and frequency distribution characteristics of the bridge. It is concluded that the vibration quantity after, can be in accordance with the relevant index comprehensive evaluation of the dynamic properties of bridge structure. The layout of dynamic load test points is shown in Figure 9. Bridge dynamic load test adopts the bridge dynamic data acquisition system produced by Donghua Test Technology Co., LTD. The acquisition system model is DH5937.

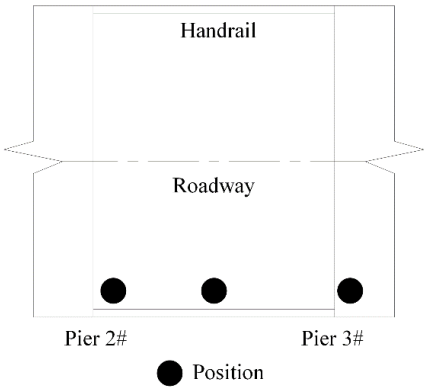

Fig. 9 – Layout of dynamic load test points

CONSTRUCTION MONITORING RESULTS

Temperature monitoring results

The test results of temperature monitoring are shown in Figure 10. The observed maximum temperature of the main girder can reach 34.4 °C and the lowest temperature is 0.2 °C; the observed maximum temperature of the roof can reach 38.1 °C and the lowest temperature is -3.8 °C. The temperature change trend is very regular after the girders concrete poured. After the arch rings concrete poured, the temperature of the tied arch bridge varied within a reasonable range. The temperature changes of the whole bridge are in accordance with the natural conditions, and the structure of the whole bridge is safe and stable.

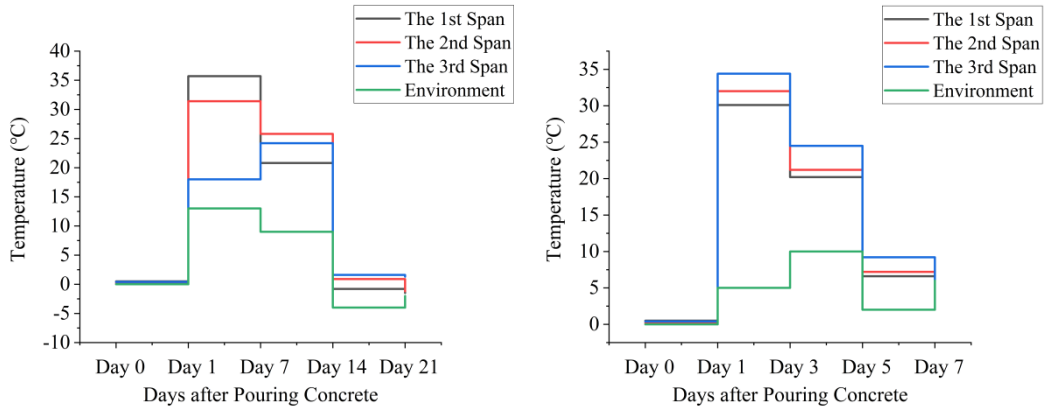

(a) *(b)*

Fig. 10 – Temperature monitoring test results

Arch rings linear monitoring results

Monitoring results of arch rings elevation are shown in Figure 11. The figure shows the elevation data of the arch rings before and after the disassembly of the arch rings support. The largest elevation difference of the arch rings is at the 1-3# suspender section, the 1-2# suspender section and the 2-3# suspender section in turn, of which the difference of the 1-2# suspender is 1.4cm at most, followed by the 1-3# with 1.3 cm and the 2-3# with 1.2cm respectively. Generally speaking, the elevation of the arch rings changes little before and after the disassembly of the support, which meets the requirements of design and construction safety.

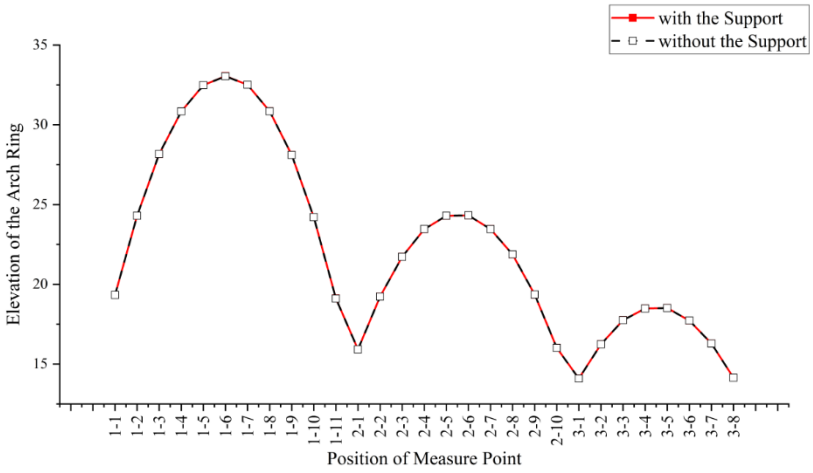

Fig. 11 – Monitoring results of arch rings elevation

Monitoring results of hangers' force

Comparison of measured hangers force and target force under bridge completion is shown in Figure 12. The hangers force line of the suspender is similar to the elevation curve of the arch rings, and it can be clearly seen that the column chart presents three arcs. The hanger force of D6 is the largest, reaching 824.8 kN, slightly less than the target force of 828.6 kN. The hanger force of the D29 is the smallest, only 325.1 kN, which is also smaller than the target cable force of 325.9 kN. In the second span, the measured force is slightly larger than the target force. But in general, there is minor division between the measured force and the designed force in the completed bridge.

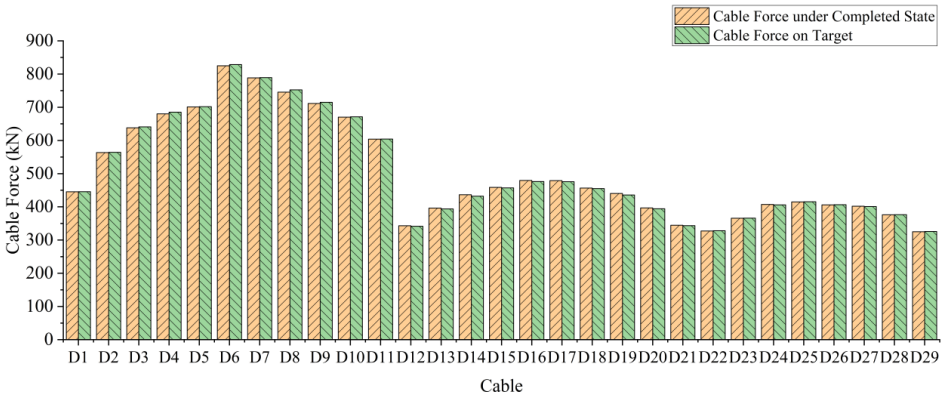

Fig. 12 – Monitoring results of hangers' force

LOAD TEST RESULTS

Static load test results

Girder deflection test results

Test results of main girder deflection are shown in Figure 13. From the direction of the deflection measurement points, the measured value reaches the maximum at N3 under working condition 1, which is 2.9 mm, lower than the theoretical value of 3.06 mm. The deflection curves under working conditions 2 and 4 decrease in turn in the direction of the transverse bridge under the test load, and reach the minimum deflection of 2.54 mm and 1.54 mm at N6, and the maximum deflection of 3.77 mm and 2.69 mm at N1, respectively. Under working condition 3, the measured deflection at N3 has a maximum value of 2.2 mm. The measured deflection values of the mid-span section of the main girder of the test holes are all less than the theoretical calculated values, and the deflection check coefficient is between 0.53 and 0.89, which indicates that the bearing capacity of the structure meets the design requirements. Besides, the residual deflection is less than 20%.

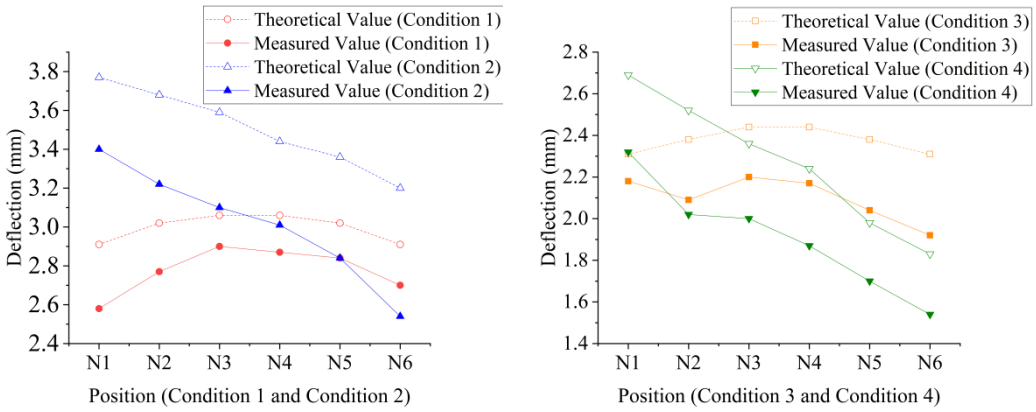

(a) *(b)*

Fig. 13 – Comparison of measured and theoretical values of main girder deflection

Strain test results of girder

As shown in Figure 14, four curves represent the variation rule of main girder strain under four

working conditions. Under the load of test conditions 1 and 3, the transverse strain of the main girder presents a trapezoidal distribution. Under test condition 1, the measured values of M3 and M4 are the largest, which are 55 and 60 respectively, less than the theoretical value 86. Under working condition 3, the transverse strain of measuring points M3 and M4 is also larger than that of other measuring points upward of the main girder transverse bridge. However, the measured value is still less than the theoretical value. Under the four working conditions, the measured values of the transverse strain of the main girder are all less than the theoretical values. As a result, all tested girders are in the state of tension, which meets the designed requirements.

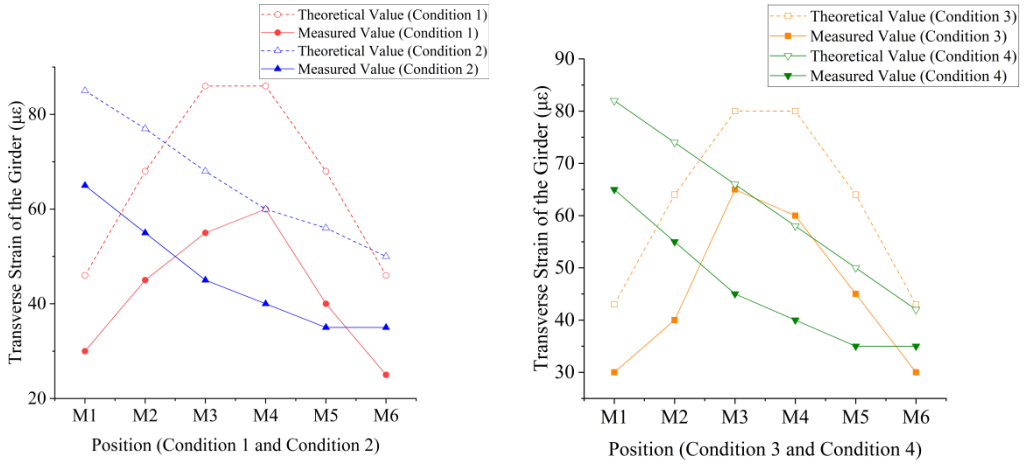

(a) *(b)*

Fig. 14 – Comparison between measured and theoretical values of transverse strain of main girder

Test results of vertical strain of main girder are shown in Figure 15. The measured and theoretical values of M7~M12 are decreasing under the four working conditions. The maximum measured vertical strain of measuring point M7 under four working conditions is 30, 65, 35, 65, 65 respectively. Under working condition 1, the minimum vertical strain of the main girder is -60 of the measuring point M12, indicating that the measuring point is under pressure at this time. The strains the vertical measuring point is between -60 and 65 under the test condition 2. The measured minimum value of the measuring point M12 is -20, and the maximum value is 35 of the measuring point M7 in the test condition 3. Under the test condition 4, the measured minimum strain of M12 is -60, and the maximum strain is 65. Under the four test conditions, the measured transverse strains are less than the theoretical strains. Besides, the decline rate of test conditions 2 and 4 is greater than that of conditions 1 and 3.

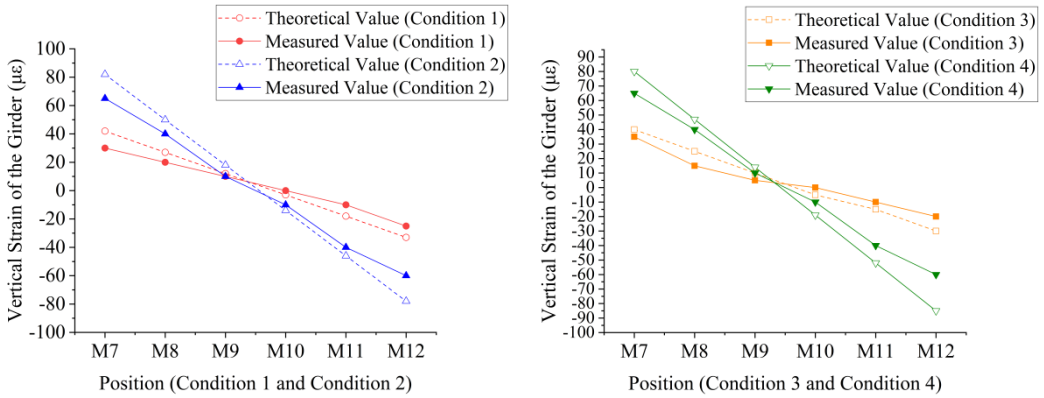

(a) *(b)*

Fig. 15 – Comparison of measured and theoretical vertical strain values of main girder

Test results of hangers' force

Test results of hangers' force are shown in Table 4. Under test condition 2, the difference between the measured and theoretical values of D2 is the largest. Compared with the theoretical value of 93 kN, the measured value of D2 suspender is only 66 kN, and its difference is 27 kN. Meanwhile, the check coefficient of hangers' force increment is 0.71. The second is the hanger force at position D2 under test conditions 1 and 3 respectively. In these two test conditions, the check coefficient at positions D1 and D2 is 0.73. Then the difference between the theoretical force and the measured force is 26 kN and 21 kN, respectively. In the whole static load test, the difference between the theoretical value and the measured value of the hanger force is obvious, but the increment check coefficient of the cable force at several measuring points is between 0.71 and 0.83, which achieves the designed standards.

Tab. 4 -Test Results of Suspender Force

Working Condition	Position	Theoretical Value (kN)	Measured Value (kN)	Testing Coefficients
Condition 1	D1	92	72	0.78
	D2	95	69	0.73
	D3	94	77	0.82
Condition 2	D1	90	75	0.83
	D2	93	66	0.71
	D3	92	74	0.8
Condition 3	D1	80	60	0.75
	D2	78	57	0.73
	D3	80	65	0.81
Condition 4	D1	77	58	0.75
	D2	81	60	0.74
	D3	80	66	0.83

Dynamic load test results

The test results of dynamic load test including pulsation test, 5 km/h, 10 km/h and 20 km/h are shown in Figure 16. The pulsation curve and frequency waveform are measured by velocity sensor on the deck of tied arch bridge. The third span natural vibration frequency was in 12.55 Hz~17.10 Hz. The measured frequency is all larger than the theoretical frequency of 10.93 Hz, which proves that the tied arch bridge has a adequate stiffness actually.

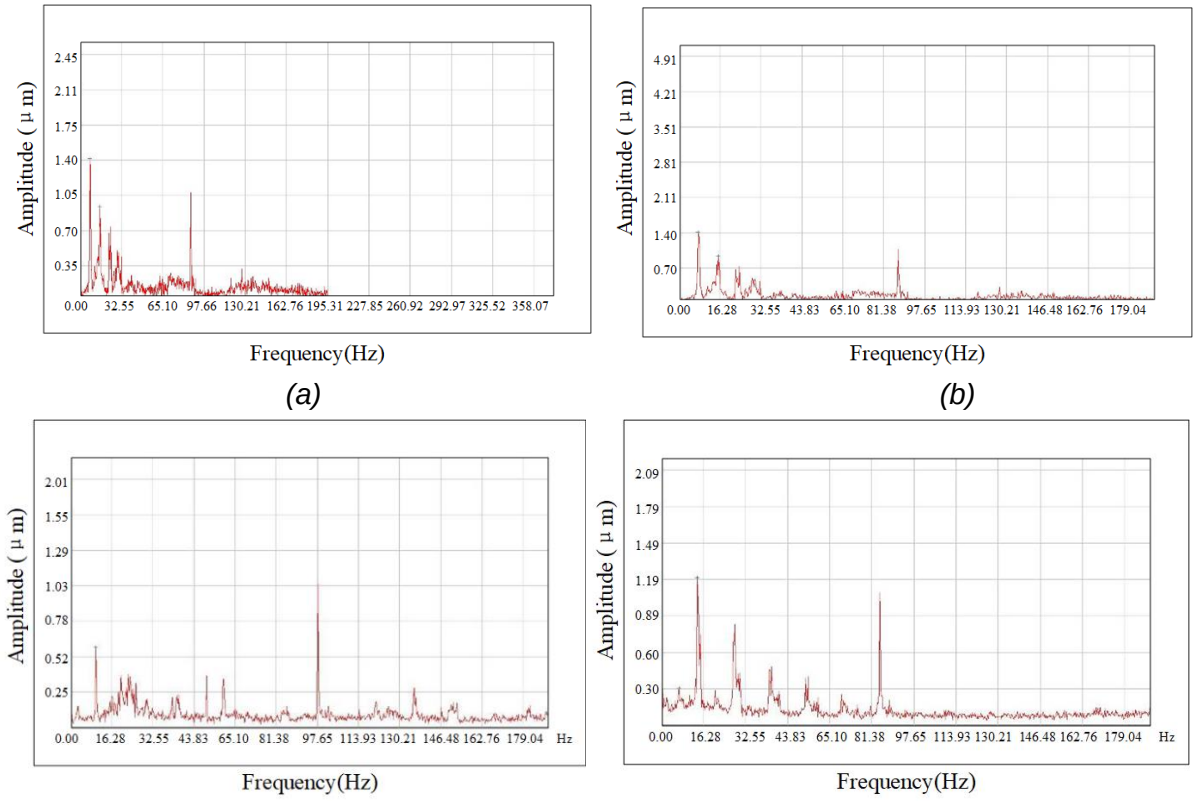

Fig. 16 – The test results of dynamic load tests:(a) Natural frequency spectrum of the second span of the west bridge in the pulsation test; (b) Natural spectrum diagram of bridge in the 5 km/h running test (F =14.63 Hz); (c) Natural spectrum diagram of bridge in the 5 km/h running test (F = 16.31Hz); (d) Natural spectrum diagram of bridge in the 5 km/h running test (F = 17.10 Hz)

CONCLUSION

(1) The largest elevation difference of the arch rings is at the 1-3# suspender section, the 1-2# suspender section and the 2-3# suspender section in turn, of which the difference of the 1-2# suspender is 1.4cm at most, followed by the 1-3# with 1.3 cm and the 2-3# with 1.2cm respectively. The arch ring elevation changes little before and after the removal of the support, indicating that the weight of the main beam is borne by the derrick and the main beam.

(2) The hangers force line of the suspender is similar to the elevation curve of the arch rings, and it can be clearly seen that the column chart presents three arcs. The hanger force of D6 is the largest, reaching 824.8 kN, slightly less than the target force of 828.6 kN. The hanger force of the D29 is the smallest, only 325.1 kN, which is also smaller than the target cable force of 325.9 kN. In the second span, the measured force is slightly larger than the target force. There is minor division between the measured force and the designed force in the completed bridge.

(3) Measured strain of the bridge under the test conditions is basically linear in the direction of the beam height, indicating that the structure basically conforms to the assumption of the plane section when working. The measured deflection of the mid-span girder is always less than the calculation values, and the deflection is between 1.54~3.40 mm, indicated that the stiffness of the box-girders meets the designed standards. Natural vibration frequency of the tied arch bridge was

measured between 12.55 Hz and 19.55 Hz by the pulsation test. At the same time, the measured data are all greater than the theoretical value of 10.93 Hz. The dynamic load test shows that the stiffness meets the requirements. The load tests have achieved an expected purpose.

REFERENCE

[1] He M, Fu X , Chen S . Evaluation of bearing capacity of reinforced concrete box ribbed arch bridge based on static load test[J]. E3S Web of Conferences, 2021, 233(3):01024.
[2] R Ceravolo, Coletta G , Lenticchia E , et al. In-Operation Experimental Modal Analysis of a Three Span Open-Spandrel RC Arch Bridge[M]. 2020.
[3] Kolla A, Kurapati R , Meka S , et al. Health Assessment and Modal Analysis of Historical Masonry Arch Bridge[M]. 2021.
[4] Benedetti A, Tarozzi M , Pignagnoli G , et al. Dynamic Investigation and Short-Monitoring of an Historic Multi-span Masonry Arch Bridge[M]. 2020.
[5] Zhou Y. The suspender construction error and control of a through tube tied arch bridge[J]. Shanxi Architecture, 2010.
[6] Ammendolea D, Greco F , Blasi P N , et al. Strategies to improve the structural integrity of tied-arch bridges affected by instability phenomena[J]. Procedia Structural Integrity, 2020, 25:454-464.
[7] Zong Z H, Jaishi B , Ge J P , et al. Dynamic analysis of a half-through concrete-filled steel tubular arch bridge[J]. Engineering Structures, 2005, 27(1):3-15.
[8] Chen H, Dong J H . Practical Formulae of Vibration Method for Suspender Tension Measure on Half-through and Through Arch Bridge[J]. China Journal of Highway & Transport, 2007, 20(3):66-70.
[9] Jing-xian, SHI, Zhuo-yin, et al. Simulation Calculation and Monitoring of Deformation of Concrete-Filled Steel Tube Arch Bridge[C]// 2018.
[10] Nonaka T, Ali A . DYNAMIC RESPONSE OF HALF-THROUGH STEEL ARCH BRIDGE USING FIBER MODEL[J]. Journal of Bridge Engineering, 2001, 6(6):482-488.
[11] Li J B, Ge S J , Chen H . Seismic behavior analysis of a 5-span continuous half-through CFST arch bridge[J]. World Information on Earthquake Engineering, 2005.
[12] Shao Y, Sun Z G , Chen Y F , et al. Impact effect analysis for hangers of half-through arch bridge by vehicle-bridge coupling[J]. Structural Monitoring and Maintenance, 2015, 2(1):65-75.
[13] Wang H. Study on deformation monitoring of continuous through concrete-filled steel tube arch bridge[J]. IOP Conference Series: Materials Science and Engineering, 2019, 592(1):012005 (7pp).
[14] Meixedo A G, Ribeiro D , Santos J P , et al. Progressive numerical model validation of a bowstring-arch railway bridge based on a structural health monitoring system[J]. Journal of Civil Structural Health Monitoring, 2021.
[15] Lu W, Li J , Yu L , et al. Force Analysis of Arch rings of Half-Through Irregular CFST Tied Arch Bridge during Construction Stage[J]. International Journal of Critical Infrastructures, 2021, 17(4):1.
[16] Yao G W, Chao Y , Wu H J , et al. Construction Control of Hoisting and Installation of Arch rings of a Half-Through CFST Stiff Skeleton Arch Bridge[J]. Bridge Construction, 2017, 47(5):107-111.
[17] Guan J W, Wang C J . Analysis of In-pipe Concrete Grouting Process for Arch ringss in Half-through Concrete-filled Steel Tubular Arch Bridge[J]. Western China Communications Science & Technology, 2018.
[18] Farahmand-Tabar S, Barghian M . Seismic assessment of a cable-stayed arch bridge under three-component orthotropic earthquake excitation[J]. Advances in Structural Engineering, 2020, 24(2):227–242.
[19] Elewa M. Numerical Investigation on the Behavior of Skewed Concrete Tied Arch Bridges[M]. 2020.
[20] Senatore G, Reksowardojo A P . Force and Shape Control Strategies for Minimum Energy Adaptive Structures[J]. Frontiers in Built Environment, 2020, 6:105.

[21] T Forgács, Sarhosis V , S Dány. Shakedown and dynamic behaviour of masonry arch railway bridges[J]. Engineering Structures, 2020, 228.
[22] Ma L. Study on Stress Properties and Optimization of Critical Nodes of Long-span Steel Truss Arch Bridge[J]. Urban Roads Bridges & Flood Control, 2018.
[23] Karieta V. THE ANALYSIS OF RATIONAL COMPONENT PARAMETERS FOR STRESS RIBBON THROUGH STEEL ARCH FOOTBRIDGES[J]. Engineering Structures and Technologies, 2018, 10(2):72-77.

CIVIL ENGINEERING JOURNAL

Article no. 24

THE CIVIL ENGINEERING JOURNAL 3-2023

HISTORICAL RETAINING WALLS MONITORING: A CASE STUDY OF DEBOSQUETTE WALL OF KYIV-PECHERSK LAVRA

Roman Shults[1], Mykola Bilous[2] and Andrii Khailak[3]

1. *King Fahd University of Petroleum and Minerals, Interdisciplinary Research Center for Aviation and Space Exploration, Dhahran, Academic Belt, Bld. 76, Saudi Arabia; roman.shults@kfupm.edu.sa*
2. *Kyiv National University of Construction and Architecture, School of GIS and Territory Management, Department of Applied Geodesy, Povitroflotskij Ave, 31, Kyiv, Ukraine; bilous.mv@knuba.edu.ua*
3. *Research Institute of Building Production named after V.S. Balitsky, Department of Instrumental Control of Construction and Mounting Works, Sector of research, geodetic engineering development and implementation of control methods in construction Lobanovskyi Ave, 51, Kyiv, Ukraine; akhailak79@gmail.com*

ABSTRACT

Geospatial monitoring of historic buildings has a valuable meaning for their restoration and preservation measures. The preparation and accomplishment of such monitoring have their features and cannot be standardized. Therefore, in each particular case, monitoring is carried out for specific requirements and conditions. The paper presents the results of geospatial monitoring for a part of the UNESCO object Kyiv-Pechersk Lavra. The primary subject of geospatial monitoring is a retaining wall known as the Debosquette Wall. The wall was built in the XVIII century and underwent restoration in 2014. A geospatial monitoring system has been established to prevent undesirable damage and displacements. Assigning the necessary observation accuracy for such a complex object is difficult. In the paper, the modern approach to observation accuracy calculation has been suggested and studied. The approach is based on the application of structural mechanics principles. The structural analysis of the Debosquette Wall has been accomplished. The output of the analysis was applied to calculate the required observation accuracy. The geospatial network and monitoring scheme were developed based on the calculated accuracy. The monitoring proceeded for half a year in 2012-2013, was interrupted for one year, and kept on in 2015. The primary stress was made on the horizontal displacements in that these displacements are the primary threats to the wall stability. The in-depth analysis of the monitoring results has been accomplished. It was found that the displacements have stayed within the allowable values. The developed monitoring approach is recommended for similar projects.

KEYWORDS

Retaining wall, Geospatial monitoring, Observation accuracy, Horizontal displacement, Displacement direction

INTRODUCTION

Geospatial monitoring has become an essential part of most engineering projects. The role and goal of geospatial monitoring depend on the studied structure. Particular attention should be paid to monitoring tasks for historic buildings, especially at the restoration stage. Numerous studies have investigated various monitoring methods depending on the displacements to be measured (vertical, horizontal, or spatial). These methods include different types of leveling, traverses, GNSS, laser scanning, photogrammetry, InSAR, sensors, and their combinations [1-13]. The application of these methods has its pros and cons. However, a number of recent studies have shown that any of these methods can be successfully applied to monitor historic buildings [14-25]. In general, geospatial monitoring of engineering structures contains well-known stages, namely design, target setup, geodetic network creation, observations, data processing, and analysis. This list of stages is well-described in a bunch of papers, reports, and textbooks, e.g., [26,27]. In the case of historic building monitoring, the first stage requires special attention. The design stage supposes the development of recommendations for observation accuracy, network geometry, and observation scheme. Historic buildings stand out in their complex geometry, different and even unknown construction materials, and adverse construction conditions (poorly understood geology, unaccounted loads, etc.). Such conditions lead to an issue of correct accuracy assignment for observations. The traditional approach for accuracy assignment was worked out for typical structures with preliminary known geometry, construction scheme, materials, and loads. Obviously, this case is not applicable to historic buildings. The conditions get complicated in the case of monitoring such complex structures as retaining walls. Retaining walls are used to protect the surrounding structures from possible hill collapse and serve to support the structures placed on the hill. Mostly, retaining walls are considered a kind of anti-landslide structure. Typically, the same methods and approaches are applied for monitoring retaining walls as in a general case. Different studies of monitoring methods for retaining walls have been considered in [28-36]. In our case, the main challenge is monitoring the historic retaining wall. The main theoretical issue that has to be solved is the correct observation accuracy assignment. This task has not been addressed yet in the considered publications. The correct accuracy also serves for the analysis of monitoring results, being that by comparing the allowable accuracy with measured displacements, we may infer the significance of the displacements. Therefore, the paper aimed at the theoretical study of accuracy assignment for monitoring historical retaining walls and practical implementation of the obtained accuracy for monitoring results analysis. The rest of the paper contains a description of the study object, theoretical background for the suggested accuracy assignment approach, a description of monitoring workflow, results of accuracy calculation by the suggested approach, and, finally, the analysis of monitoring results.

MATERIAL AND METHODS

Monitoring object

Kyiv-Pechersk Lavra is one of the astonishing structures of Kyiv city and a world-renowned center of Orthodox Christianity. The Lavra is a complex of various historical structures, including churches, towers, caves, overpasses, and retaining walls. In total, more than fifty structures (Figure 1).

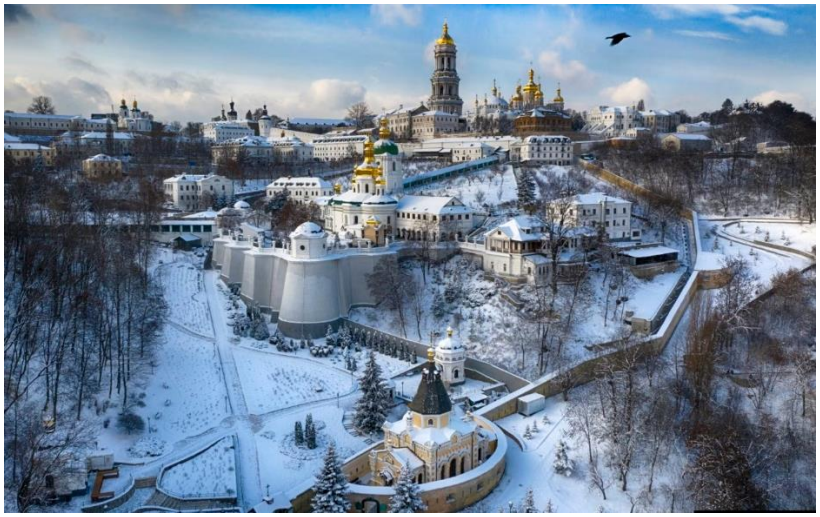

Fig. 1 – General view of the Kyiv-Pechersk Lavra with the Debosquette Wall in front [37]

The history of the Lavra commenced in 1051 when the first complex of cave monasteries was built. The complex developed over many centuries until XIX C. In 1990, the Lavra complex was listed by UNESCO. The main buildings of the Lavra ensemble are the Dormition Cathedral, the Trinity Gate Church, the Great Bell Tower, the Church of All Saints, the Refectory Church, the monastery fortified walls with towers, the cave complexes of St. Anthony (Near) and St. Theodosy (Far) with surface churches, the Exaltation of the Cross and the Nativity of the Virgin and the Church of the Saviour on Berestove [38]. Among the fortified walls, the Debosquette Wall is of great interest [39] (Figure 2).

Fig. 2 – General view of the Debosquette Wall [39]

The wall was built in XVIII C. The total length of the wall exceeds 100 m (Figure 3). Initially, the wall was intended to reinforce the southeast hill of the Near Caves territories. In 1816, two made of bricks rotundas were built at the top of the Debosquette Wall [40].

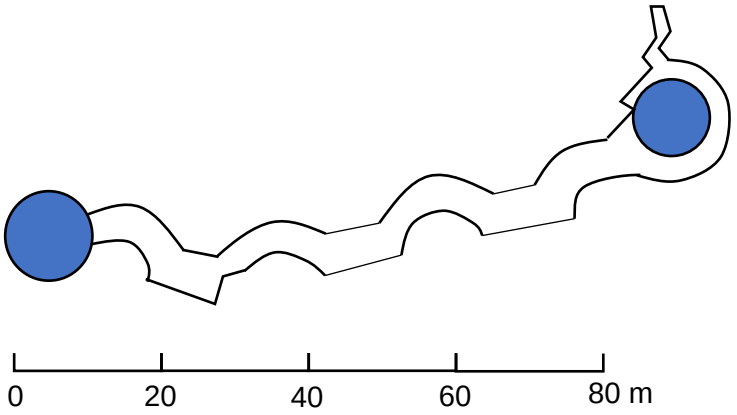

Fig. 3 – Horizontal sketch of the Debosquette Wall

Since its construction as a fortified structure, the primary purpose of the wall has changed. Today, the primary role of the Debosquette Wall is the anti-landslide structure. Therefore, by its functionality, the Debosquette Wall can be treated as a retaining wall that bears the load from a hill, structures emplaced on the hill and prevents them from collapsing. In 2011, the Ukrainian government decided to reconstruct and restore the Debosquette Wall. According to the reconstruction project, complex geospatial monitoring of the wall was envisaged. The goal of the monitoring was to establish the possible displacements of the wall during and right after the restoration works with appropriate accuracy.

Method for monitoring accuracy assignment

Insofar as the monitoring must be accomplished with necessary accuracy, the correct assignment of the accuracy is of great importance. On the other hand, any historical structure is unique, and there is no general approach to monitoring accuracy determination. This is why, before geospatial monitoring works, the appropriate method for accuracy determination has to be developed. It is worth mentioning that the primary attention has to be paid to horizontal displacements for retaining walls. Vertical displacements are typically insignificant. Thus, the method considered below is intended for the accuracy of horizontal displacement determination.

Let us consider the suggested approach for accuracy determination. The right way is the application of structural mechanics principles and approaches. The method presented below further develops the concept suggested in [41,42]. We may consider the wall a vertical cantilever beam clamped at one side and free on another. Under this premise, the deflection will have a maximum value at the top of the wall. Different loads affect the retaining wall. One may find a detailed description of the loads and their relationships in [43]. For our case, we may use the simple model where the main forces are given in Figure 4.

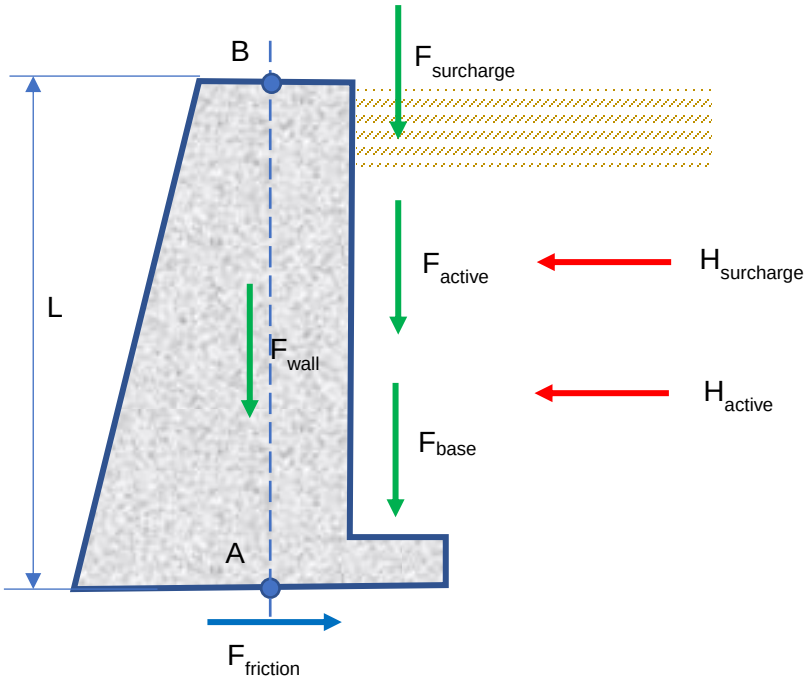

Fig. 4 – Forces acting on a retaining wall

A cantilever retaining wall in Figure 4 must resist both overturning and sliding. In structural mechanics, the normative loads are multiplied by the reliability coefficient. On average, the value of the reliability coefficient can be accepted equals 1.2. In other words, it means that standard loads can exceed the normative loads by 20%. The loads' effect can be presented throughout the overturning moment M_O, which tends to overturn the wall, and sliding force F_S, which tends to move the wall. In terms of the moment, force, and reliability coefficient, we may write down the conditions for allowable deviations in the overturning moment and sliding force. In general, the inequalities

$$M_O \le M_R, F_S \le F_R, \tag{1}$$

establish the stability conditions, where M_R, F_R are resisting moment and resisting force. On the other hand, by applying the reliability coefficient, we get

$$\Delta M_O^{max} \le 0.2 M_O, \Delta F_S^{max} \le 0.2 F_S \tag{2}$$

Therefore, the values ΔM_O^{max} and ΔF_S^{max} can be treated as additional unpredictable loads that lead to the structure displacement. If we convert the additional loads to displacements δ, we may calculate the necessary accuracy m by using the expression

$$m \le 0.2\delta. \tag{3}$$

The value m in (3) ensures the observation accuracy for which we can reliably determine the displacements invoked by the additional loads. Thus, the determined displacements will not be distorted by observation accuracy. To calculate the displacement δ, the expressions for the cantilever beam can be used with sufficient accuracy. For the case of distributed force q, given

Young's modulus E and the moment of inertia of the wall's cross-section I, we have [43,44] for the maximum displacement:

$$\delta = \frac{qL^4}{8EI}, \tag{4}$$

for the displacement at any point:

$$\delta(l) = \frac{ql^2(6L^2-4Ll+l^2)}{24EI}, \tag{5}$$

for a slope at any point:

$$\theta(l) = -\frac{ql(3L^2-3Ll+l^2)}{6EI}. \tag{6}$$

For the case of moment, we have a maximum displacement:

$$\delta = \frac{Ma(2L-a)}{2EI}, \tag{7}$$

for the displacement at any point:

$$\delta(l) = \begin{cases} -\frac{Ml^2}{2EI}, l \le a \\ -\frac{Ma^2}{EI}\left(l-\frac{a}{2}\right), l > a, \end{cases} \tag{8}$$

for a slope at any point:

$$\theta(l) = \begin{cases} \frac{Ml}{EI}, l \le a, \\ \frac{Ma^2}{EI}, l > a, \end{cases} \tag{9}$$

where a is a lever arm distance for the moment.

The figures obtained by the expressions (2), (3), (4), (6), (7), and (9) will be provided in the next section.

Accuracy calculation

In the previous section, the method for monitoring accuracy assignment has been suggested. The method allows assigning the accuracy for horizontal displacement determination. Using the necessary initial parameters, one is able to calculate the overturning moment and sliding force for the particular wall. Based on these values, we may calculate the allowable displacement. Let us find out how the suggested method works for the Debosquette Wall. The main initial parameters for calculation are outlined in Table 1. The backfill soil type is stiff clay.

Tab. 1 - Initial data for analysis

Parameter	Value	Parameter	Value
Moment of inertia	1125 m^4	Soil unit weight	13 kN/m^3
Young's modulus	50 MPa	Soil friction angle	30 deg
Wall height	15 m	Wall material strength	20 MPa

Using these data, the overturning moment and sliding force and their allowable deviations were calculated:

$$M_O = 3130\ kN \cdot m,\ F_S = 655\frac{kN}{m},$$

$$\Delta M_O^{max} = 626\ kN \cdot m, \Delta F_S^{max} = 131\frac{kN}{m}.$$

Now, it is possible to use the expressions (4), (6), (7), and (9) to calculate the displacements due to the overturning moment and sliding force. The displacement and slope graphs for the overturning moment and sliding force are presented in Figure 5 and Figure 6, as well as the moment diagrams for both cases.

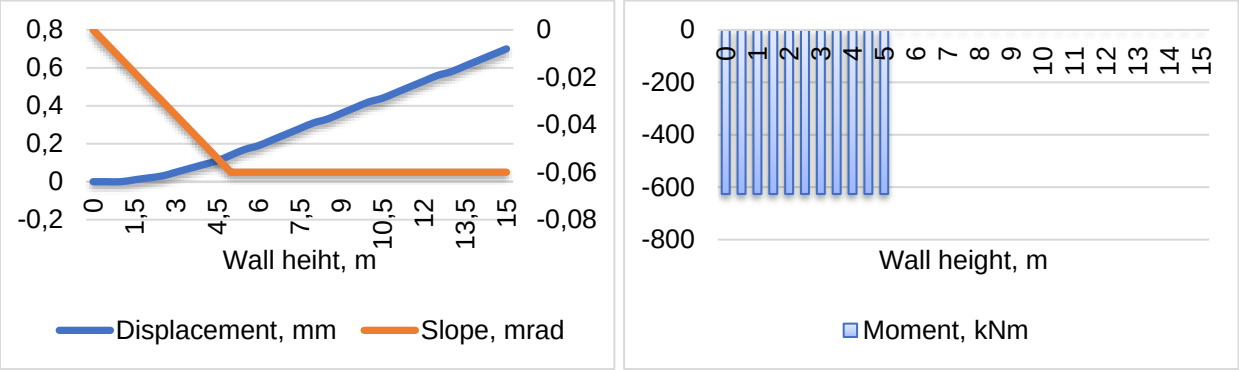

Fig. 5 – Overturning moment effect

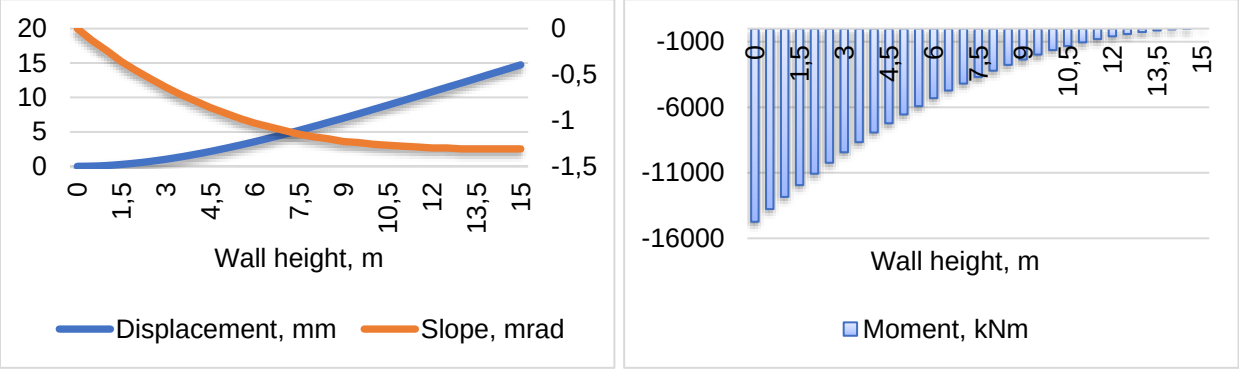

Fig. 6 – Sliding force effect

We may apply the superposition method to calculate the final displacement, which gives a preliminary result for a displacement of 15.44 mm. For monitoring accuracy calculation, this approximation provides reasonable output. Therefore, the observation accuracy will

$$m = 0.2 \cdot 15.44 = 3.1\ mm.$$

This value was used as reference accuracy for developing the observation scheme and measurement equipment choice. The chosen equipment for measurements is capable of ensuring the determined accuracy. The estimated value of the total displacement δ was applied for measurement result analysis.

Monitoring scheme

Geospatial monitoring has been accomplished separately for vertical and horizontal displacements. To these aims, two different monitoring networks were created. For the horizontal monitoring network, the Kyiv city coordinate system was adopted. GNSS observations referenced the point of beginning for the horizontal network to the city coordinate system. In what follows, the initial coordinates were accepted unchanged. All points of the horizontal monitoring network were permanently mounted by tube pillars with screw holes for precise centering of total stations and targets. The scheme of the horizontal network is given in Figure 7. The distances and angles were measured by Leica TCR 1201+ R400 total station, which has an angle measurement error ±1 sec, and distance measurement error ±1 mm + 1.5 ppm. The distances and angles were measured with six repetitions. The network was checked with control measurements for each observation epoch to control network point displacements. Deformation targets were mounted onto the wall along three levels (see Figures 8 and 9). The bottom-level targets (Rp1 – Rp23) were used both for vertical and horizontal displacement determination. In total, sixty-three targets were mounted.

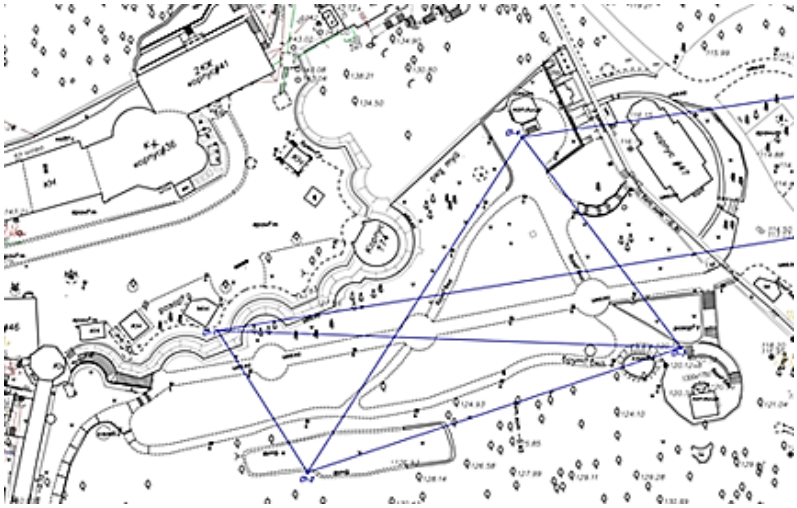

Fig. 7 – Scheme of the horizontal monitoring network

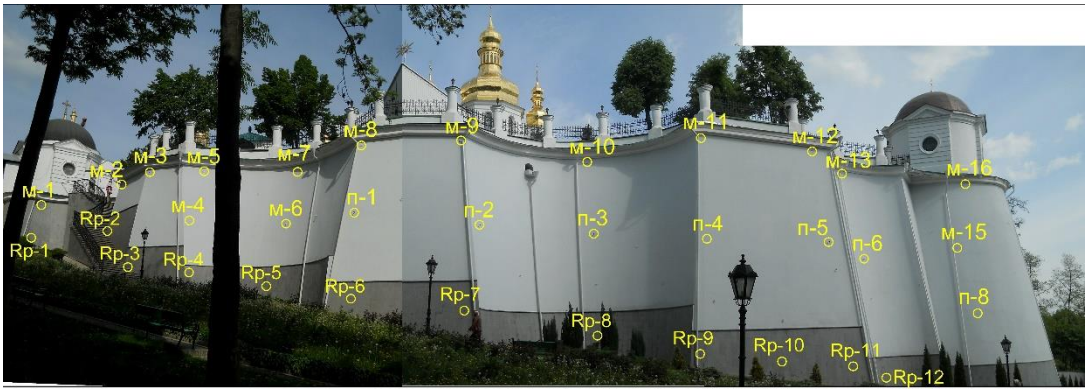

Fig. 8 – Scheme of the deformation targets (southern facade)

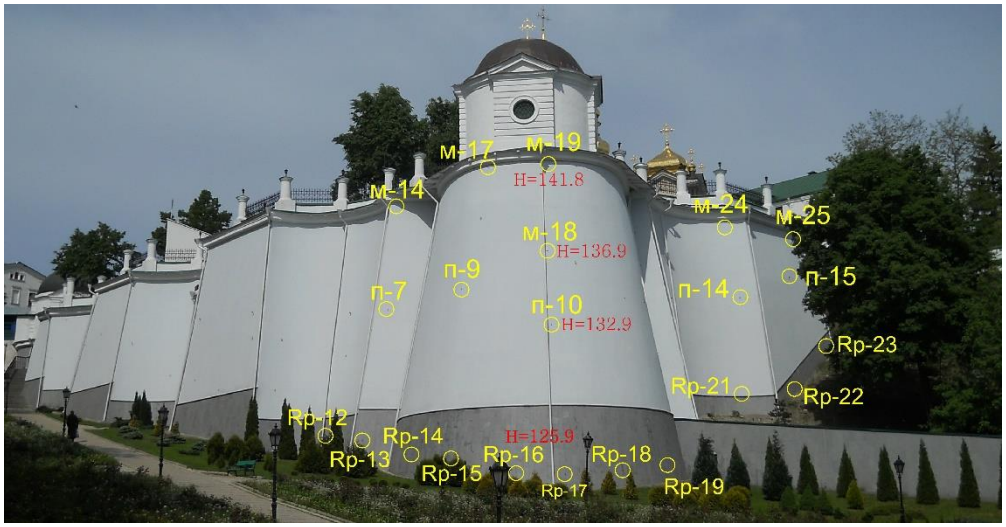

Fig. 9 – Scheme of the deformation targets (southeastern facade)

The vertical monitoring network was referenced to the benchmarks of the city height system using standard leveling procedures. The scheme of the vertical monitoring network is given in Figure 10.

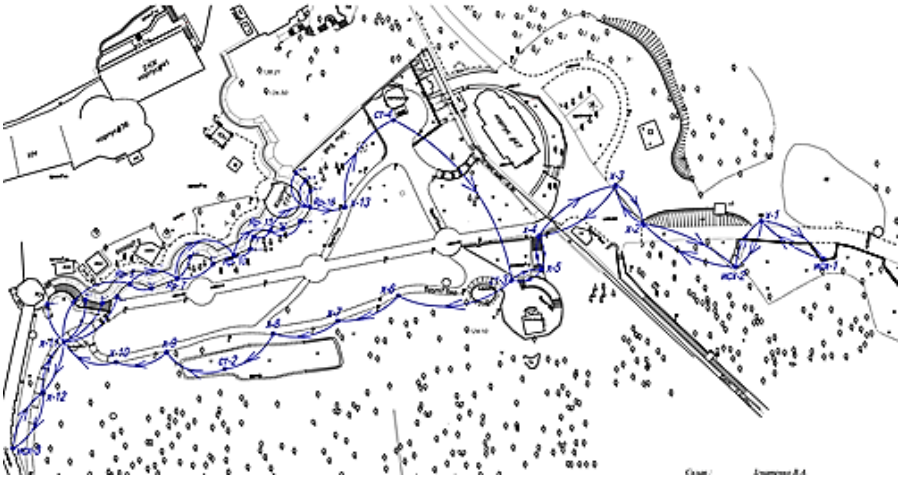

Fig. 10 – Scheme of the vertical monitoring network

Points of beginning for the vertical network were placed outside the region of possible deformations. Levelling lines were run in forward and inverse directions. The precise level DL-101C (levelling error for one kilometer of a double run is ± 0.4 mm) and coded invar level rods were used. Lines of sight were in a range of 25 m.

The results of monitoring will be presented in the next section. But one remark has to be provided. It was determined that vertical displacements were insignificant during the monitoring period. The maximum value was detected for target Rp 23 and equals -3 mm. That is why only horizontal displacements will be considered and analyzed in what follows.

RESULTS

Monitoring results

The monitoring was carried out according to the schemes considered in the previous section. The observation accuracy corresponded to the value calculated before. The dataset for monitoring the Debosquette Wall spans the period from 05.11.2012 until 13.05.2015p. During that time interval, twenty observations were accomplished. As it was mentioned, the main concern was horizontal displacements. Below, the horizontal displacements for different deformation targets are presented.

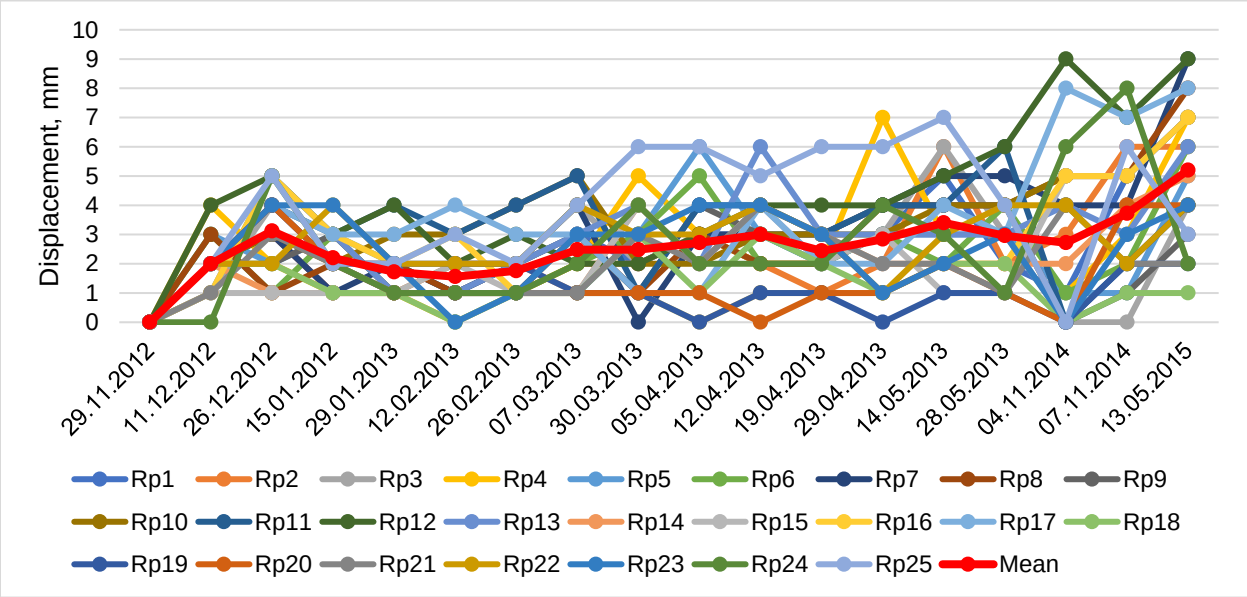

Fig. 11 – Horizontal displacements for deformation targets Rp1 – Rp25

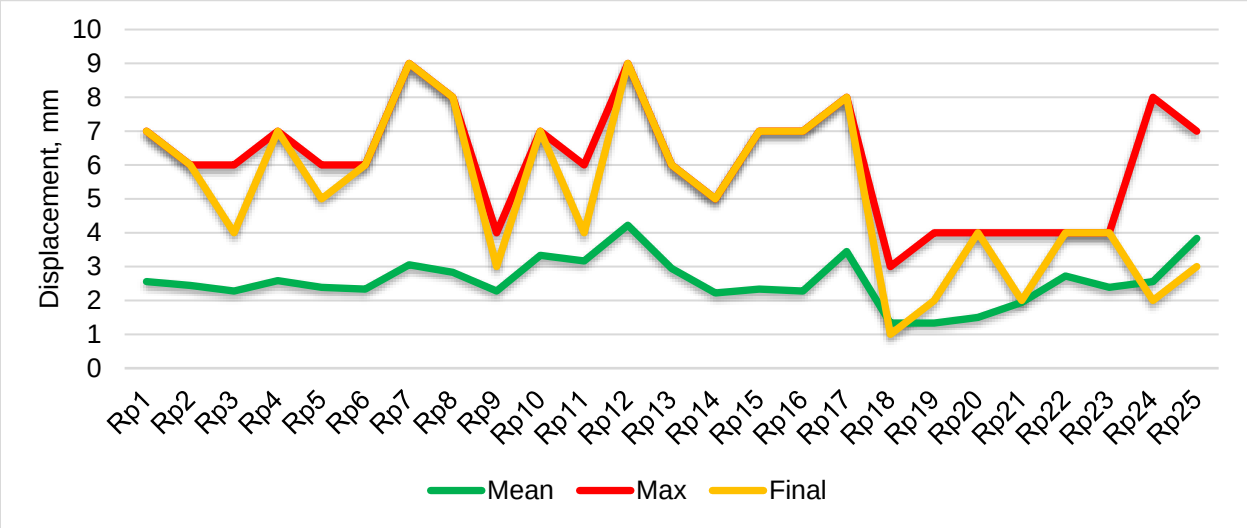

Fig. 12 – Main characteristics of the deformation process for targets Rp1 – Rp25

In Figure 11, the mean displacement for each observation epoch is given aside from the horizontal displacements. Figure 12 shows each deformation target's mean, maximum, and final displacement. The same content is given in Figure 13 – Figure 16 but for different deformation targets.

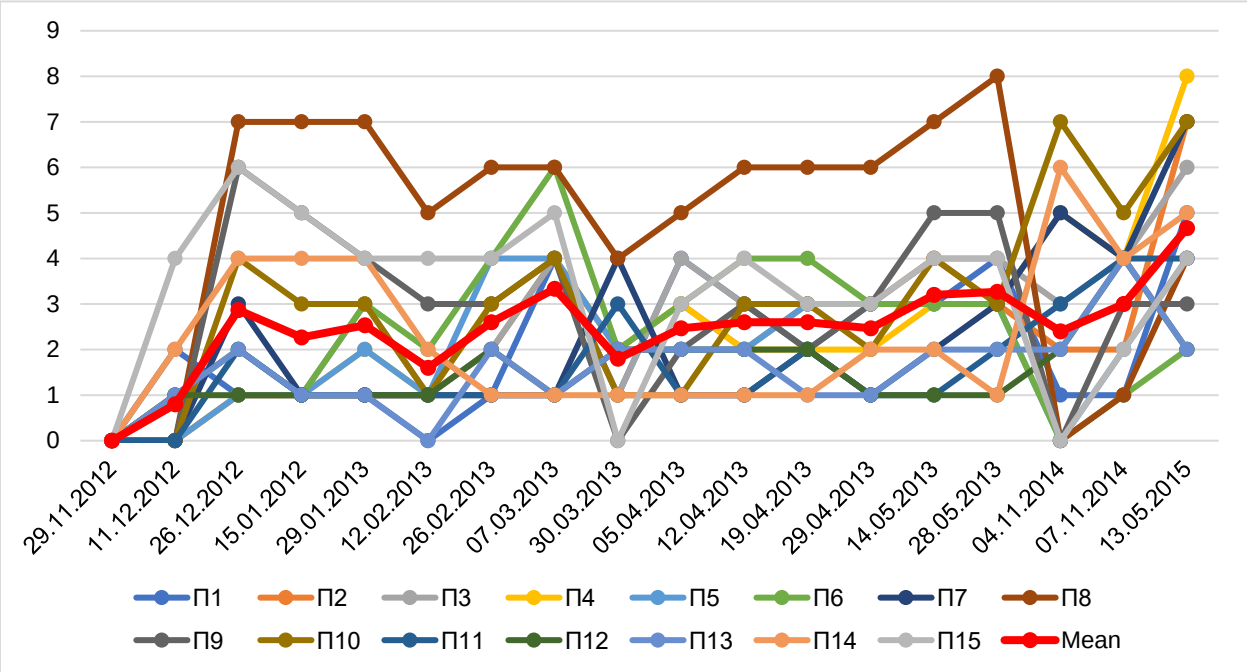

Fig. 13 – Horizontal displacements for deformation targets П1 – П15

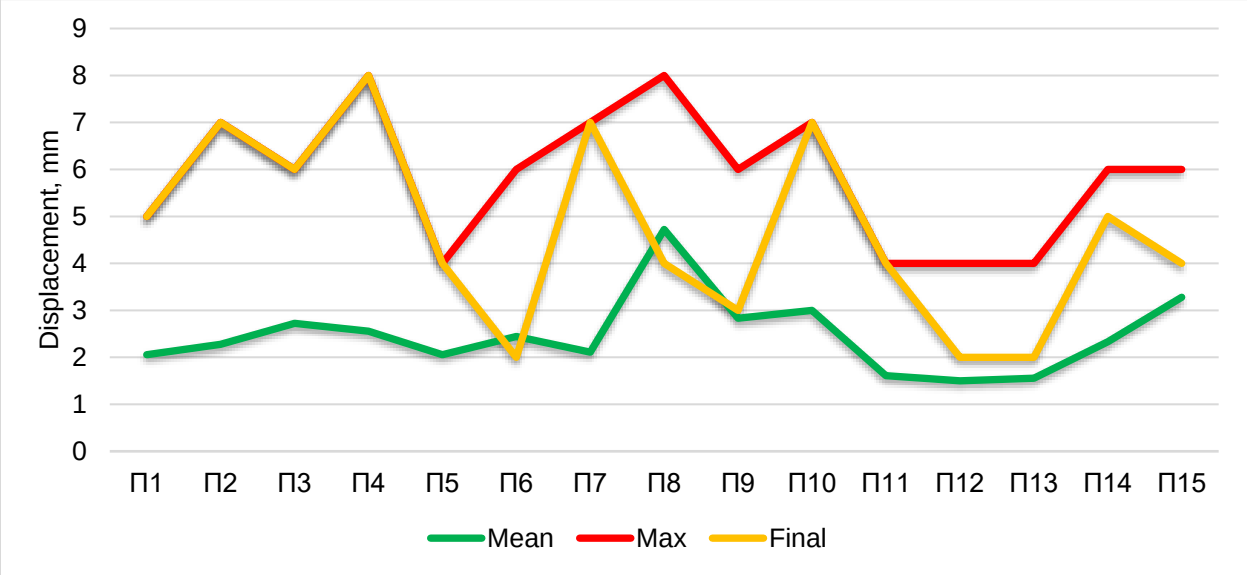

Fig. 14 – Main characteristics of the deformation process for targets П1 – П15

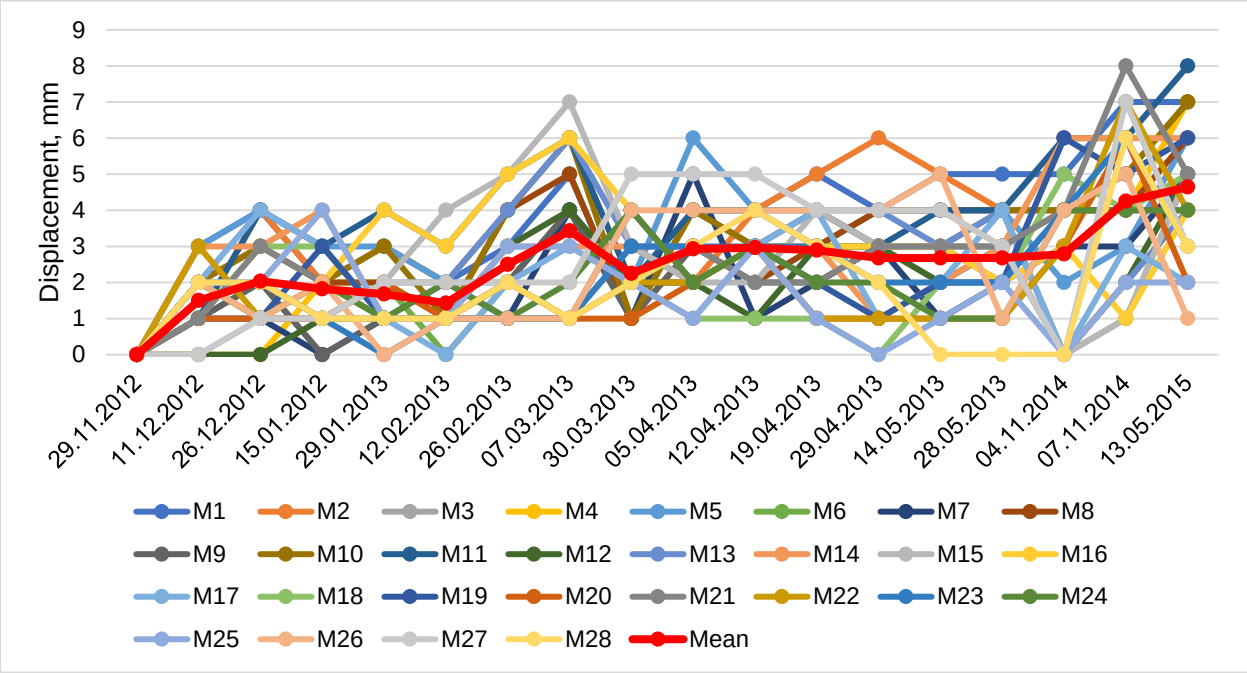

Fig. 15 – Horizontal displacements for deformation targets M1 – M28

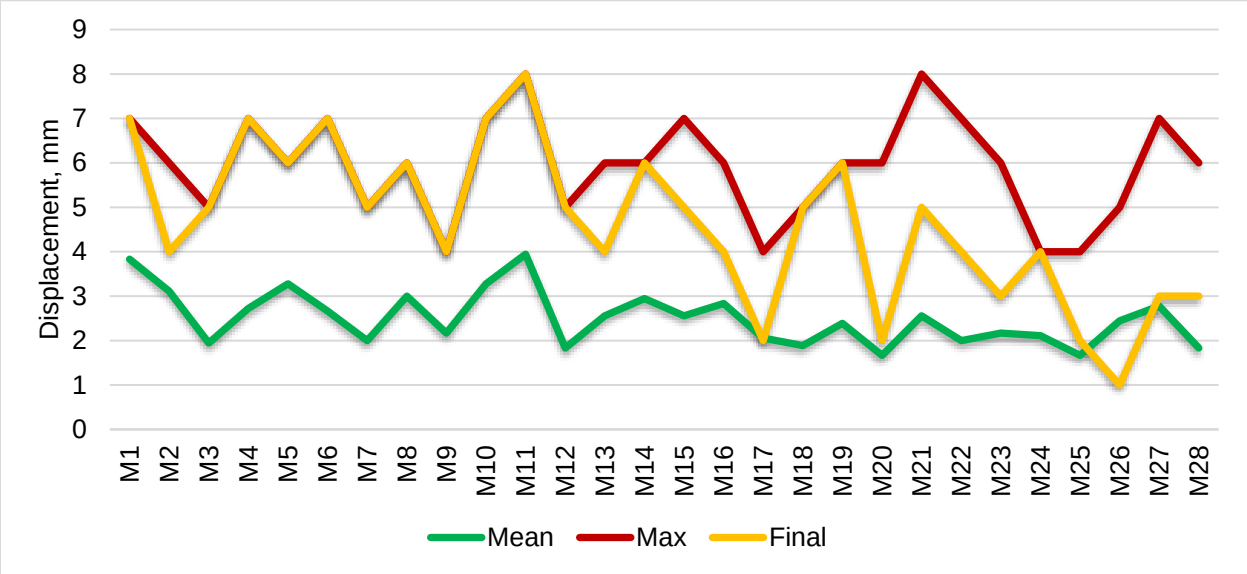

Fig. 16 – Main characteristics of the deformation process for targets M1 – M28

The results presented in Figure 11 – Figure 16 yielded some interesting findings. Firstly, the largest displacements have reached the targets in the bottom of the Debosquette Wall, namely 7 mm for the targets Rp1, Rp4, Rp10, Rp15, Rp16; 8 mm for the targets Rp8, Rp17, and 9 mm for the targets Rp7, Rp12. Just a few targets in the middle and at the top of the retaining wall had significant horizontal displacements, specifically 7 mm for the targets П2, П7, M1, M6, M10, M18, and 8 mm for the targets П4, M11. Secondly, none of the displacements reached the critical value

of 15 mm. Thirdly, the last observation epochs have shown that the displacements tend to increase after the reconstruction. That is especially clear in Figure 11 and Figure 13. The latter inference makes indispensable further monitoring both for vertical and horizontal displacements.

CONCLUSION

Current research appears to validate the view that the geospatial monitoring of historic structures is a unique process. Performing geospatial monitoring needs a neat approach and correct estimation of the task and solutions. The paper considered the particular case of the geospatial monitoring of historic retaining walls before and after their reconstruction. The crucial point of such monitoring is a correct observation accuracy assignment. It was suggested to assign the proper accuracy using principles of structural mechanics. The aim of this approach is twofold: to determine the necessary observation accuracy and to obtain the correct criterion for monitoring data analysis. The appropriate monitoring workflow was suggested and implemented based on the calculated accuracy. Thanks to the correct choice of monitoring accuracy, the high reliability of the measurements was ensured. The results of monitoring have confirmed the relative stability of the studied historic structure. However, the displacements tend to increase, which requires monitoring to keep on. Future studies will have to further the fusion of structural mechanics and applied geodesy for monitoring tasks.

REFERENCES

[1] Acosta L.E., De Lacy, M.C., Ramos, M.I., Cano, J.P., Herrera, A.M., Avilés, M., Gil, A.J. 2018. Displacements study of an earth fill dam based on high precision geodetic monitoring and numerical modeling. Sensors, 18(5): 1369-1384. https://doi.org/10.3390/s18051369

[2] Aminjafari S. 2017. Monitoring of Masjed-Soleiman embankment dam's deformation using a combination of interferometric synthetic aperture radar (InSAR) and finite element modeling. Journal of Geodesy and Cartography, 43(1): 14-21. https://doi.org/10.3846/20296991.2017.1299842

[3] Janowski A., Kaminski W., Makowska K., Szulwic J., Wilde K. 2015. The method of measuring the membrane cover geometry using laser scanning and synchronous photogrammetry. In: Proccedings of the 15th International Multidisciplinary Scientific GeoConference - SGEM2015. 1-11.

[4] Shen N., Chen L., Liu J., Wang L., Tao T., Wu D., Chen R. 2019. A review of global navigation satellite system (GNSS)-based dynamic monitoring technologies for structural health monitoring. Remote Sensing, 11: 1001-1046. https://doi.org/10.3390/rs11091001

[5] Taşçi L. 2015. Deformation monitoring in steel arch bridges through close-range photogrammetry and the finite element method. Experimental Techniques, 39: 3-10. https://doi.org/10.1111/ext.12022

[6] Jiménez-Martínez M.J., Quesada-Olmo N., Zancajo-Jimeno J.J., Mostaza-Pérez T. 2023. Bridge Deformation Analysis Using Time-Differenced Carrier-Phase Technique. Remote Sensing, 15: 1458. https://doi.org/10.3390/rs15051458

[7] Caldera, S., Barindelli S., Sansò F., Pardi L. 2022. Monitoring of Structures and Infrastructures by Low-Cost GNSS Receivers. Applied Sciences, 12: 12468. https://doi.org/10.3390/app122312468

[8] Sztubecki J., Topoliński S., Mrówczyńska M., Bağrıaçık B., Beycioğlu A. 2022. Experimental Research of the Structure Condition Using Geodetic Methods and Crackmeter. Applied Sciences, 12: 6754. https://doi.org/10.3390/app12136754

[9] Xiao P., Zhao R., Li D., Zeng Z., Qi S., Yang X. 2022. As-Built Inventory and Deformation Analysis of a High Rockfill Dam under Construction with Terrestrial Laser Scanning. Sensors, 22: 521. https://doi.org/10.3390/s22020521

[10] Kovačič B., Doler D., Topolšek D. 2021. Optimization and Development of the Model for Monitoring the Deformations on the Airport Runways. Processes, 9: 833. https://doi.org/10.3390/pr9050833

[11] Stiros S.C. 2021. GNSS (GPS) Monitoring of Dynamic Deflections of Bridges: Structural Constraints and Metrological Limitations. Infrastructures, 6: 23. https://doi.org/10.3390/infrastructures6020023
[12] Scaioni M., Marsella M., Crosetto M., Tornatore V., Wang J. 2018. Geodetic and Remote-Sensing Sensors for Dam Deformation Monitoring. Sensors, 18: 3682. https://doi.org/10.3390/s18113682
[13] Erol B. 2010. Evaluation of High-Precision Sensors in Structural Monitoring. Sensors, 10: 10803-10827. https://doi.org/10.3390/s101210803
[14] Barazzetti L., Banfi F., Brumana R., Gusmeroli G., Previtali M., Schiantarelli G. 2015. Cloud-to-BIM-to-FEM: Structural simulation with accurate historic BIM from laser scans. Simulation Modelling Practice and Theory, 57: 71-87. http://dx.doi.org/10.1016/j.simpat.2015.06.004
[15] Castagnetti C., Cosentini R.M., Lancellotta R., Capra A. 2017. Geodetic monitoring and geotechnical analyses of subsidence induced settlements of historic structures. Struct Control Health Monitoring, 24: 1-15. https://doi.org/10.1002/stc.2030
[16] Rossi M., Bournas D. 2023. Structural Health Monitoring and Management of Cultural Heritage Structures: A State-of-the-Art Review. Applied Sciences, 2023: 13, 6450. https://doi.org/10.3390/app13116450
[17] Casula G., Fais S., Cuccuru F., Bianchi M.G., Ligas P. 2023. Diagnostic Process of an Ancient Colonnade Using 3D High-Resolution Models with Non-Invasive Multi Techniques. Sensors, 23: 3098. https://doi.org/10.3390/s23063098
[18] Bačová D., Ižvoltová J., Šedivý Š., Chromčák J. 2023. Different Approach for the Structure Inclination Determination. Buildings, 13: 637. https://doi.org/10.3390/buildings13030637
[19] Costanzo A., Falcone S., La Piana C., Lapenta V., Musacchio M., Sgamellotti A., Buongiorno M.F. 2022. Laser Scanning Investigation and Geophysical Monitoring to Characterise Cultural Heritage Current State and Threat by Traffic-Induce Vibrations: The Villa Farnesina in Rome. Remote Sensing, 14: 5818. https://doi.org/10.3390/rs14225818
[20] Patrucco G., Gómez A., Adineh A., Rahrig M., Lerma J.L. 2022. 3D Data Fusion for Historical Analyses of Heritage Buildings Using Thermal Images: The Palacio de Colomina as a Case Study. Remote Sensing, 14: 5699. https://doi.org/10.3390/rs14225699
[21] Miano A., Di Carlo F., Mele A., Giannetti I., Nappo N., Rompato M., Striano P., Bonano M., Bozzano F., Lanari R., et al. 2022. GIS Integration of DInSAR Measurements, Geological Investigation and Historical Surveys for the Structural Monitoring of Buildings and Infrastructures: An Application to the *Valco San Paolo* Urban Area of Rome. Infrastructures, 7: 89. https://doi.org/10.3390/infrastructures7070089
[22] Giuffrida D., Bonanno S., Parrotta F., Mollica Nardo V., Anastasio G., Saladino M.L., Armetta F., Ponterio R.C. 2022. The Church of S. Maria Delle Palate in Tusa (Messina, Italy): Digitization and Diagnostics for a New Model of Enjoyment. Remote Sensing, 14: 1490. https://doi.org/10.3390/rs14061490
[23] Del Soldato M., Farolfi G., Rosi A., Raspini F., Casagli N. 2018. Subsidence Evolution of the Firenze–Prato–Pistoia Plain (Central Italy) Combining PSI and GNSS Data. Remote Sensing, 10: 1146. https://doi.org/10.3390/rs10071146
[24] Sánchez-Aparicio L.J., Villarino A., García-Gago J., González-Aguilera D. 2016. Photogrammetric, Geometrical, and Numerical Strategies to Evaluate Initial and Current Conditions in Historical Constructions: A Test Case in the Church of San Lorenzo (Zamora, Spain). Remote Sensing, 8: 60. https://doi.org/10.3390/rs8010060
[25] Fregonese L., Barbieri G., Biolzi L., Bocciarelli M., Frigeri A., Taffurelli L. 2013. Surveying and Monitoring for Vulnerability Assessment of an Ancient Building. Sensors, 13: 9747-9773. https://doi.org/10.3390/s130809747
[26] Eichhorn A. 2007. Tasks and newest trends in geodetic deformation analysis: a tutorial. In Proceedings of the 15th European Signal Processing Conference (EUSIPCO 2007), Poznan, Poland, 1156-1160.
[27] Welsch W.M., Heunecke O. 2001. Models and terminology for the analysis of geodetic monitoring observations - Official Report of the Ad-Hoc Committee of FIG Working Group 6.1. In Proceedings of the 10th FIG International Symposium on Deformation Measurements, Orange, California, USA. 390-412.

[28] Oats R.C., Escobar-Wolf R., Oommen T. 2017. A Novel Application of Photogrammetry for Retaining Wall Assessment. Infrastructures, 2: 10. https://doi.org/10.3390/infrastructures2030010
[29] Sestras P., Bilașco Ș., Roșca S., Veres I., Ilies N., Hysa A., Spalević V., Cîmpeanu S.M. 2022. Multi-Instrumental Approach to Slope Failure Monitoring in a Landslide Susceptible Newly Built-Up Area: Topo-Geodetic Survey, UAV 3D Modelling and Ground-Penetrating Radar. Remote Sensing, 14: 5822. https://doi.org/10.3390/rs14225822
[30] Peduto D., Oricchio L., Nicodemo G. et al. 2021. Investigating the kinematics of the unstable slope of Barberà de la Conca (Catalonia, Spain) and the effects on the exposed facilities by GBSAR and multi-source conventional monitoring. Landslides, 18: 457–469. https://doi.org/10.1007/s10346-020-01500-9
[31] Kaartinen E., Dunphy K., Sadhu A. 2022. LiDAR-Based Structural Health Monitoring: Applications in Civil Infrastructure Systems. Sensors, 22: 4610. https://doi.org/10.3390/s22124610
[32] Scotland I., Dixon N., Frost M.W., Wackrow R., Fowmes G.J., Horgan G. Measuring Deformation Performance of Geogrid Reinforced Structures Using a Terrestrial Laser Scanner; Loughborough University Institutional Repository: Leicestershire, UK, 2014.
[33] Tung S.H., Weng M.C., Shih M.H. 2013. Measuring the in situ deformation of retaining walls by the digital image correlation method. Engineering. Geology, 166: 116–126. https://doi.org/10.1016/j.enggeo.2013.09.008
[34] Scaioni M., Alba M., Roncoroni F., Giussani A. 2010. Monitoring of a SFRC retaining structure during placement. Eur. J. Environ. Civ. Eng., 14: 467–493 https://doi.org/10.1080/19648189.2010.9693237
[35] Laefer D., Lennon D. 2008. Viability Assessment of Terrestrial LiDAR for Retaining Wall Monitoring. GeoCongress, 310: 247-254. https://doi.org/10.1061/40971(310)
[36] Oskouie P., Becerik-Gerber B., Soibelman L. 2016. Automated measurement of highway retaining wall displacements using terrestrial laser scanners. Autom. Constr., 65: 86–101. https://doi.org/10.1016/j.autcon.2015.12.023
[37] Inside Kyiv's Sacred Cave Monastery As 'Eviction' Deadline Looms. Available online: https://www.rferl.org/a/kyiv-monastery-lavra-eviction-crisis/32319718.html (accessed on 01 August 2023)
[38] Report of Joint World Heritage Centre/ICOMOS Reactive Monitoring Mission to the World Heritage property. Kyiv: Saint-Sophia Cathedral and Related Monastic Buildings, Kyiv-Pechersk Lavra (Ukraine). Available online: http://kyiv-heritage.com/sites/default/files/Ukraine-Kyiv-RM%20mission%20WHC-ICOMOS-14FEB20%20332c%20(ALL).pdf (accessed on 01 August 2023)
[39] Kyiv-Pechersk Lavra. Part 9. Other objects. Available online: https://ukrainaincognita.com/kyivska-oblast/kyiv/kyevo-pecherska-lavra/kyevo-pecherska-lavra-chastyna-9-inshi-obekty (accessed on 01 August 2023)
[40] Debosquette wall. Available online: https://uk.wikipedia.org/wiki/%D0%9C%D1%83%D1%80_%D0%94%D0%B5%D0%B1%D0%BE%D1%81%D0%BA%D0%B5%D1%82%D0%B0 (accessed on 29 July 2023)
[41] Shults, R., 2021. The Models of Structural Mechanics for Geodetic Accuracy Assignment: A Case Study of the Finite Element Method. In Contributions to International Conferences on Engineering Surveying. Springer Proceedings in Earth and Environmental Sciences. Springer, Cham, edited by A. Kopáčik, P. Kyrinovič, J. Erdélyi, R. Paar, A. Marendić, 187-197. https://doi.org/10.1007/978-3-030-51953-7_16
[42] Shults, R., 2022. Structural analysis of monitoring results of long-span roof structures. In: Proceedings of the 5th Joint International Symposium on Deformation Monitoring (JISDM), Valencia, Spain, 431-438. http://doi.org/10.4995/JISDM2022.2022.13893
[43] Connor, J.J., & Faraji, S. 2016. Fundamentals of structural engineering (2nd ed). Springer. https://doi.org/10.1007/978-3-319-24331-3
[44] Clayton C.R., Woods R.I., Bond A.J., Milititsky J. 2014. Earth Pressure and Earth-Retaining Structures. CRC Press.

CIVIL ENGINEERING JOURNAL

Article no. 25

THE CIVIL ENGINEERING JOURNAL 3-2023

A NEW HYBRID FRAMEWORK OF MACHINE LEARNING TECHNIQUE IS USED TO MODEL THE COMPRESSIVE STRENGTH OF ULTRA-HIGH-PERFORMANCE CONCRETE

Xin Zuo[1], Die Liu[1], Yunrui Gao[1], FengJing Yang[2] and Gohui Wong[3]*

1. *Business School of Chongqing Institute of Humanities and Science and Technology, Chongqing, China*
2. *School of Architecture and Art, Chongqing Institute of Humanities and Technology, Chongqing, China*
3. *College of Civil Engineering, Architecture, and Environment, Wuhan, China, email: hbwh0314@163.com*

ABSTRACT

To calculate the compressive strength (CS) of concrete, it is necessary to investigate Ultra-High-Performance Concrete $(UHPC)$ in terms of its components and their quantities. Empirical analysis of relationships between constituents can be more time- and money-consuming. The CS can now be evaluated based on the composition of the ingredients thanks to intelligent systems. Additionally, it is advisable to promote the use of eco-friendly materials in concrete, one of the most commonly used materials in the world. The CS of $UHPC$ was attempted to model in this study. The CS of concrete has been simulated using Support Vector Regression (SVR), a Machine Learning (ML) technique that is compatible with Particle Swarm Optimisation (PSO) and Henry's Gas Solubility Optimisation $(HGSO)$, based on various materials used in the construction present article. The CS values were determined through the testing of eight components. The modeling process was evaluated using a variety of metrics. In this regard, the test phase modeling's root-mean-square error $(RMSE)$ for $SVR-HGSO$ was 8.45, while it was 9.23 for $SVR-PSO$. $SVR-HGSO's\ RMSE$ rate for the training phase was calculated at 10.15, which is 3.3 percent higher than $SVR-PSO's\ RMSE$ of 10.49.

KEYWORDS

Compressive strength, Support vector regression, Ultra-High-Performance Concrete, Particle swarm optimization, Henry's Gas Solubility Optimization

INTRODUCTION

Superior mechanisms and persistence capabilities, like self-compactness, in constructions, compressive strength (CS) of more than $150\ Mpa$, and exceptional durability in any challenging environments, use Ultra-High-Performance Concrete $(UHPC)$ as a suitable material [1]–[4]. Reducing the cement and micro-silica content significantly lowers costs and $CO2$ emissions, even despite the high initial cost and negative environmental impact, the practical qualities and extended service life compared to conventional or high-strength concrete are justifiable. Cement reduction, which is crucial in this regard, can boost the construction industry's sustainability by resulting in more environmentally friendly structures [5]. Numerous studies have recently examined $UHPC$ usage and behaviour [6], where $UHPC$ typically displays CS that range from $150\ MPa$ to $810\ MPa$ [7]–[9]. Researchers are interested in using materials like micro-silica, fly ash, metakaolin, and nano-silica in the design of concrete mixtures. Furthermore, since the assets are used to address various

aspects of the concrete and the design of the concretes is primarily based on CS, comparing their effects on the mechanical features of concrete has the greatest interest [10], [11].

The Portland cement-like fly ash helps produce concrete with less water by having a shape and size similar to Portland cement. Fly ash and superplasticizers are best blended to enhance the mechanical properties of concrete, particularly its CS. The cost, durability, workability, and water permeability of concrete, on the other hand, are all significantly impacted by the addition of fly ash. Fly ash is frequently used to replace sticky substances in construction projects. While highlighting the environmental advantages, using fly ash in concrete mixtures lowers the risk of contamination [12]–[14]. Fly ash can replace $20-50\%$ of the total adhesion of concrete and can even be increased to 60% if the initial strength of the concrete is a crucial factor [15], [16].

Concrete with a similar shape to pozzolan is mixed with a different amount of cement, changing how practical concrete behaves [17]–[20]. Because of the silica fumes' small particle size, it can serve as both a filler and a pozzolan in the concrete mixture [21]. The concrete's short-term $(28-day)$ CS would be improved despite the increasing proportion of silica fume inside the concrete that reduces the concrete's ability to be worked [22]. It is not always possible to determine with absolute certainty which silica fume will achieve the best CS. To increase the CS of concrete, researchers substitute various percentages of silica fume [23], [24]. Since the particles are smaller than those of cement, the silica vapour reaction improves the properties of concrete similarly to pozzolan [25]–[30]. Micro-silica with superplasticizers improves CS in the context of fly ash by lowering porosity [31].

The use of Machine Learning (ML) techniques in civil engineering is very widespread. Such solutions have the researchers' view for appraising concrete properties [32]–[35]. The $UHPC$ presence entails more progress in modeling with Artificial Intelligence (AI) for knowing the behavior of concrete overloading. Many methods to model the performance of $UHPC$ have been successfully introduced by experts in several studies [36]–[38]. These techniques depend on a dataset to create a trustworthy model, and the accuracy of their results depends on the species discovered through experimentation or the dataset drawn from the literature. One study included sugarcane bagasse ash and used a gene expression program to estimate the CS of concrete [39]. By contrasting the model's output with empirical strength measurements, the accuracy of the model was determined. In other research, a framework for evaluating the compressive strength of cement made of nano- and micro-silica was developed using genetic programming [40]. One study proposed a silica fume-based model for predicting the CS of concrete [41]. To lessen the expense and complexity of the developed model, they used Artificial Neural Networks (ANN) and had the grey wolf optimisation algorithm (GWO) algorithm optimise their model.

In the current study, a ML method based on the Support Vector Regression (SVR) method is investigated. This method makes use of the algorithms to predict the CS of concrete. In this regard, Particle Swarm Optimisation (PSO) and Henry's Gas Solubility Optimisation $(HGSO)$, two novel optimization algorithms, are used to more accurately model the CS of $UHPC$. R^2, VAF, OBJ, and MAE are four indices that are used to assess the modeling process; they are thoroughly introduced in Table 3.

From a paper on $UHPC$, CS studies, an experimental research dataset with numerous parameters is gathered [42]–[44]. Ingredients needed to produce high $UHPC$ is 1) fine powders (silica fume crushed, nano-silica, and quartzite), 2) lower water/binder ratio (below 0.2), 3) cement (more than 800 kg/m^3); 4) high range water-reducing admixture, and 5) steel fibers as well as polyethylene fibers [45].

Therefore, coupled frameworks of $SVR-PSO$ and $SVR-HGSO$ attempt to feed on data of ingredients of concrete and target values of CS and then generate the $UHPC$ persistence rates with various ingredients. The specific information needed for modeling is displayed in the following section.

MATERIALS AND METHODOLOGY

The clear methods provided in this sector are required for the probe of models that attempt to the results of ingredient compositions should be estimated in terms of CS for $UHPC$. Two potent optimization algorithms work in tandem with the capable SVR to avoid estimating the necessary parameters while locating the best modeling framework. To improve the accuracy of simulating the CS of various sample compositions, the $SVR-PSO$ and $SVR-HGSO$ have been developed. For samples, the data published in [42]–[44] are available. Table 1 provides a brief overview of the information gathered from 110 experimental samples in this regard. The various CSs of each sample are produced by combining the aforementioned ingredients in different amounts.

Simulating their resistance is modeled with the mathematical solutions elaborated on in this section. Also, Fig. 1 exhibits the CS derived from the various mixtures of items presented in Table 1, in which each colorful string represents one sample out of 110 samples.

Tab.1 - Input and target data for predictive models

Ingredient	$Unit$	$Symbol$	Statistical measurements				
			Min	Max	$Mean$	$Median$	$St.dev$
$Cement$	(kg/m^3)	CE	383	1600	879.7	786	329.8
$Silica\ fume$	(kg/m^3)	SI	30	367.95	192	196	94.6
$Fly\ ash$	(kg/m^3)	FA	120	448	33	120	72.7
$Sand$	(kg/m^3)	SA	292	1898	980	1107	513.8
$Steel\ fiber$	(kg/m^3)	SF	2	470	39	8	74.8
$Quartz\ powder$	(kg/m^3)	QP	203.3	750	36.9	211	125.9
$Water$	(kg/m^3)	WA	109	334.5	197.1	185.3	54.3
$Admixture$	(kg/m^3)	AD	4	185	31.9	30.1	28.2
$Compressive\ strength$	(MPa)	CS	95	240	152.2	147.9	31.5

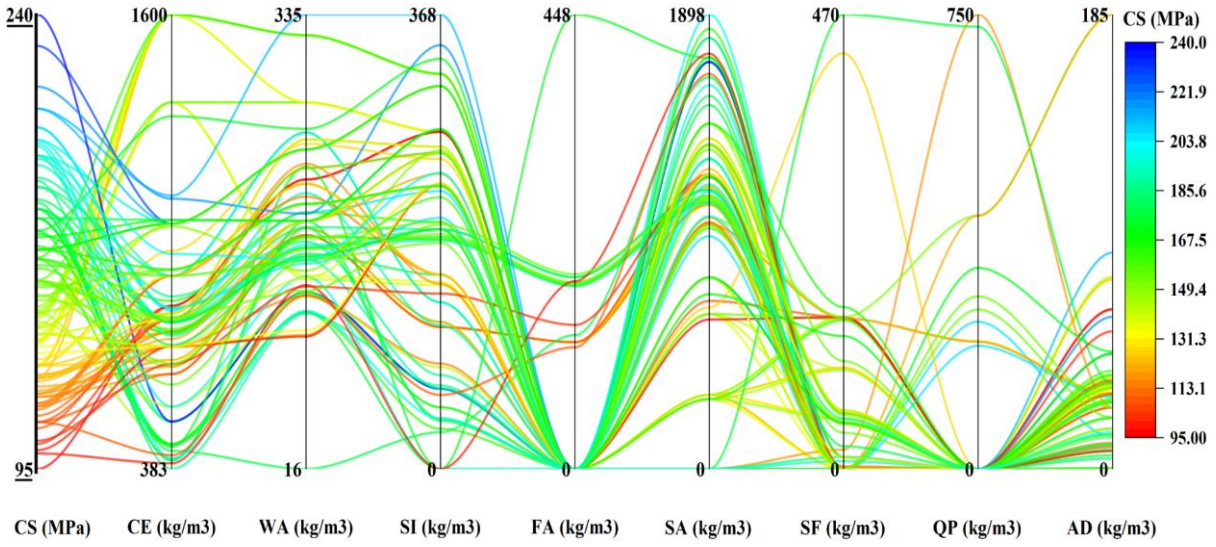

Fig. 1 – The compressive strength of various mixtures of ingredients

Henry's gas solubility optimization algorithm, $HGSO$

Henry's Law of Physics is used to construct the $HGSO$ [46]. The aforementioned regulation was developed by the maximum amount of dissolved solute envisioned at a specific pressure and temperature level [47]. Applying the aforementioned rule makes it possible to demonstrate the

solubility of low-soluble gases in the unique solvent. The ability of solubility has been largely influenced by temperature and pressure; for gases, the pressure parameter is reduced by increasing the temperature variable, and the relationship is appropriate for solids. Pressure's incremental trend contributes to an increase in solubility [48]. The gas and the pertinent solubility were used in the study by Hashemian et al. to develop the Henry law [46]. The following lists the steps needed for $HGSO$:

1- Establishing the precise location and quantity of gases (creating the initial population).

2- Creating population classes based on gas type characteristics.

3- figuring out the cost of the classes, selecting them, and selecting the ones with the best results to assign appropriate conditions.

4- Updating the coefficients of Henry's law.

$$H_j(t+1) = H_j(t) \times e^{\left(-C_j\left(\frac{T^\theta - T(t)}{T(t)\times T^\theta}\right)\right)} \quad (1)$$

$$T(t) = e^{\left(\frac{t}{iter}\right)} \quad (2)$$

In which the H_j shows the Henry law coefficient for class j .C_j and T^θ Alternatively, exhibit a random and constant number of $[0\ to\ 1]$. Also, the variables of $iter$ and t represent, respectively, the number of iterations in the queue and temperature.

5- Update of the factor of solubility using Eq. (3).

$$S_{i,j}(t) = K \times H_j(t+1) \times P_{i,j}(t) \quad (3)$$

where K displays a constant value; $P_{i,j}(t)$ and $S_{i,j}$ represent the solubility and pressure of gas i^{th} in the class of j, alternatively.

6- Next, the location of the primitive population is updated using Eq.s $(4, 5)$.

$$X_{i,j}(t+1) = X_{i,j}(t) + F \times r \times \gamma \times \left(X_{i,best}(t) - X_{i,j}(t)\right) + F \times r \times \alpha \times \left(P_{i,j}(t) \times X_{best}(t) - X_{i,j}(t)\right) \quad (4)$$

$$\gamma = \beta \times e^{\left(-\frac{F_{best}(t)+\varepsilon}{F_{i,j}(t)+\varepsilon}\right)} + \varepsilon \quad (5)$$

In which $X_{i,j}$ describes where the gas of i in the class of j. Variables of $F_{i,j}$ and F_{best} demonstrates the population in cluster j and the best cost of petrol i. Parameters of $X_{i,best}$ and X_{best} indicate, instead, the preferred gas in the class of j and the population. Additionally, the r parameter displays a random number between $[0\ and\ 1]$. α and β , as a fixed number, are determined 1 as well as ε, which is 0.05. γ additionally displays the probable interaction between the gases.

7- To satisfy the regional minimum trapping standards, the worst petrol number is assigned.

$$N_w = N \times (rand(C_2 - C_1) + C_1) \quad (6)$$

In which, C_1 and C_2 are fixed, as 0.1 and 0.2, alternatively, and the N shows the population.

8- The worst gas location can be calculated with Eq. (7).

$$G_{i,j} = G_{Min(i,j)} + r \times \left(G_{Max(i,j)} - G_{Min(i,j)}\right) \quad (7)$$

In which G_{Min} and G_{Max} are, respectively, the lower and upper boundaries. The variable of $G_{i,j}$ denotes the gas i location in the class of j.

Particle swarm optimization algorithm, PSO

Known as a population-based solution, the PSO algorithm. PSO was created with an eye toward the feedback of animal group interactions. Essentially, this approach was proposed in a study that $Kennedy\ et\ al.$ [49], who elaborated it extensively [50]–[53]. This makes the location and the velocity parameter essential components of population control. The first of two scoring schemes is taken into consideration, and the best global position is the one that best fits the placement of the particles. To reach the maximum number of iterations, particle location, and velocity are determined iteratively. Updates to the locations and velocities are made by the equations below.

$$P.v_{ij}^{new} = WP.v_{ij}^{current} + C_1 r_1 (P.p.best_{ij}^{new} - P.p_{ij}^{current}) + C_2 r_2 (Global.best_{ij}^{current} - P.p_{ij}^{current}) \quad (8)$$

$$P.p_{ij}^{new} = P.p_{ij}^{current} + P.v_{ij}^{new} \quad (9)$$

where W stands for the inertia factor. $P._v$ and $P._p$ display the position and speed of the particles. The accidental number of $(0\ to\ 1)$ is represented by the variables r_1 and r_2. C_1 and C_2 are used to calculate the acceleration factors for local and global learning, respectively. The best solutions from all swarms are represented by the Global best variable.

Support Vector Regression, SVR

SVR, was introduced to classify regression problems [54]. Support vector machine (SVM) regression refers to a SVR machine that uses a tolerance region (ε) to determine a regression. In the SVR approach, regression class classification is utilized to design a hyperplane optimized. To find answers to questions about regression and to create the following features, SVR was combined with supervised learning techniques [55]:

$$min_{w,b} = \frac{1}{2}\|w\|^2 + C\sum_{i=1}^{m}(\xi_i + \xi_i^*) \quad (10)$$

$$s.t. \quad \begin{Bmatrix} y_i - (w^T x_i + b) \le \varepsilon + \xi_i \\ (w^T x_i + b) - y_i \le \varepsilon + \xi_i^* \\ \xi_i, \xi_i^* \ge 0 \end{Bmatrix}$$

The specifications of w, C, b, ξ, and ε, alternately represent the bias, amount of boundary exceeding, coefficient weight, queue regularisation factor, and rate of deviation from the hyper-plane. Two concepts are included in the function of fitness:

$$\frac{1}{2}\|w\|^2 \quad (11)$$

$$C\sum_{i=1}^{m}(\xi_i + \xi_i^*) \quad (12)$$

Equation (11) was used to maintain the distance between the sample and the hyperplane while modifying Equation (12) to widen the gap between the sample and the hyperplane. When creating a function with a hyperplane target, appropriate values of b and w were gathered. To achieve the desired outcome for this study, a quadratic objective function was used [56]. The main responsibility of the SVR has been to determine the defining parameters in the optimal levels (ε, $sigma$, and C) that are indicated in Table 2.

Tab. 2 – The determining variables' magnitudes of each optimizer

		$SVR-HGSO$	$SVR-PSO$
Training phase	C	3.050	0.05
	$EPSILON$	139.302	1298.62
	$GAMA$	0.066	0.05
Testing Phase	C	0.301	3.781
	$EPSILON$	28.094	2981
	$GAMA$	0.070	2

SVR was combined with a variety of optimizers, including $HGSO$ and PSO, to estimate parameters at the best level to locate pertinent parameters.

Criteria for evaluation of developed $SVR-HGSO$ and $SVR-PSO$

The various evaluators for measuring the CS of concrete samples using predictive frameworks are defined in Table 3.

Tab. 3 – The metrics used to evaluate models

$Indexes$	$Codes$	$Relations$	$Status$
Variance account factor	VAF	$\left(1-\frac{var(t_n-y_n)}{var(t_n)}\right)*100$	A high value means desirable
Mean absolute error	MAE	$\frac{1}{N}\sum_{n=1}^{N}\lvert p_n-t_n\rvert$	A low value means desirable.
Root mean squared error	$RMSE$	$\sqrt{\frac{1}{N}\sum_{n=1}^{N}(p_n-t_n)^2}$	$A\ low\ value\ means\ desirable.$
Pearson's correlation coefficient	R^2	$\left(\frac{\sum_{n=1}^{N}(t_n-\bar{t})(p_n-\bar{p})}{\sqrt{[\sum_{n=1}^{N}(t_n-\bar{p})^2][\sum_{n=1}^{N}(p_n-\bar{p})^2]}}\right)^2$	$A\ high\ value\ means\ desirable$
Statistical parameters, including the various error indices	OBJ	$\left(\frac{n_{train}-n_{test}}{n_{train}+n_{test}}\right)\frac{RMSE_{train}+MAE_{test}}{R^2_{train}+1}+\left(\frac{2n_{train}}{n_{train}+n_{test}}\right)\frac{RMSE_{test}-MAE_{test}}{R^2_{test}+1}$	A low value means desirable [57]

In mentioned relations, p_N exhibits the magnitude of predicted CS; t_n is the n^{th} target value (as measured); $\bar{t}$ is the measured data as calculated averagely; $\bar{p}$ represent the averaged target values of CS and the variables for the phases of training and testing, respectively, the n_{train} and n_{test} which are the collected number of CS relevant steps of train or testing.

RESULTS AND DISCUSSIONS

The results of modeling $UHPC$ in 110 compound samples were produced using both frameworks. In addition, to better understand the capabilities of each proposed model, the performance evaluation indices evaluated the $SVR-HGSO$ and $SVR-PSO$ modeling processes. In the initial step, the simulated results of each sample's CS are shown in front of the actual numbers. In this regard, Fig. 2 displays the CSs that S$VR-HGSO$ modeled.

The aforementioned optimization algorithms and the SVR model are created independently in the Matlab software before being combined to create the hybrid framework. The optimization algorithm is viewed as the primary function in the modeling process, and the SVR model is taken to be the cost function. The optimization algorithm defines the input variables, target variables, and the hey parameter of SVR in each step, and the SVR model provides predictions corresponding to these variables. The maximum iteration serves as the stopping criterion, and the $RMSE$ value is used to determine which model is best developed. Additionally, Appendix A now includes a brief program of the $SVR-PSO$ model development.

Tab. 4 - Comparison of present study results with recently published articles with similar datasets.

$Work\ ID$	$Model$	R^2
Wu [1]	$FDA-RBF$	0.916
$R.Abuodeh\ et\ al.$ [2]	$BPFNN$	0.8
$Alabduljabbar\ et\ al$ [3]	$Gene\ expression$	0.969
$Present\ Work$	$SVR-HGSO$	0.964

A comparison of the present study with published articles that studied similar fields is presented in Table 4. This table is presented as an identifier of the developed hybrid model performance and workability compared to recent studies. The results obtained from the $SVR-HGSO$ show its higher capability in predicting the CS of $UHPC$.

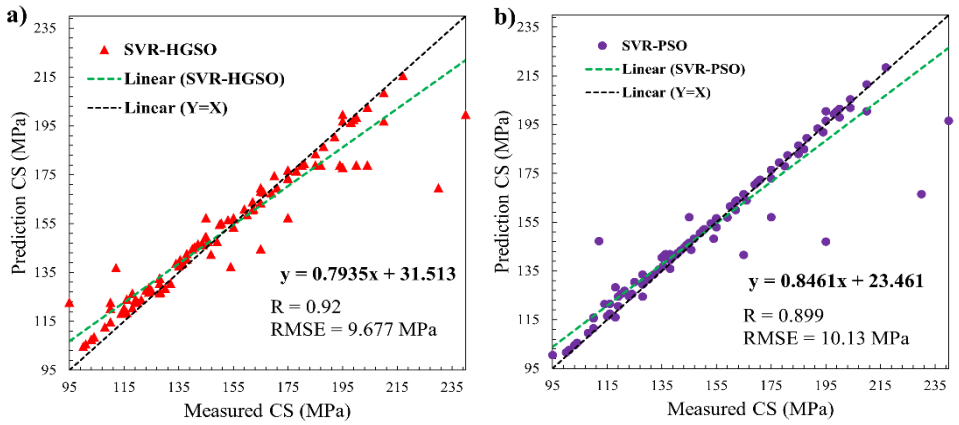

Fig. 2 – Estimated CS by: a) $SVR-HGSO$ and b) $SVR-PSO$

As seen in Figure 2, the results of each model are at an acceptable rate. $SVR-HGSO$ was able to model the CS variables 2.31 percent better than $SVR-PSO$ due to its higher R^2 at the level 0.92. Similar to this, the other model performed this task better, with a 4.69 percent lower $RMSE$ index, and was able to model the compounds' CS factor with a 10.13 MPa error. The slope of the trendline for the PSO-owned model, however, could be found to be better with a value of 0.84, this is 6.33 percent higher than SVR-HGSO, indicating that certain points between the samples with numbers 195 to 210 that are outside the best-fit line may have been the source of this event.

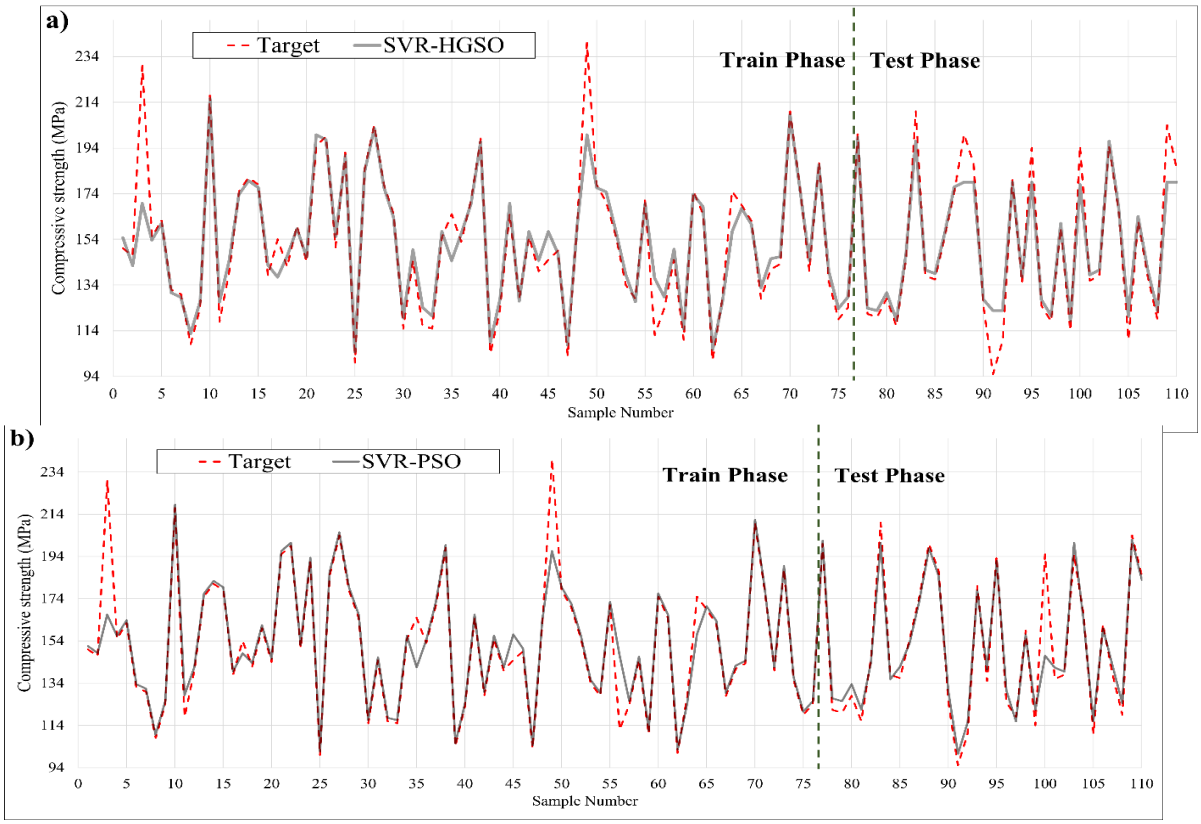

Fig. 3 –Estimated and Target values CS appraised by: a) $SVR-HGSO$ and b) $SVR-PSO$

Surveying Figure 3, the training stages are approximately identical to each other except for some parts, such as samples with the numbers 32 and 33, which are modeled more accurately by the $SVR-PSO$ with errors of 1.31% and 1.32%, respectively, while by the $SVR-HGSO$ the errors are 7% and 4.7%. With an error of 1.28 percent in $SVR-PSO$ versus 3.96 percent in $HGSO$, the sample of 75 also produced better modeling results. In the testing phase, $PSO's$ grey lines could be used to demonstrate that, when compared to $SVR-HGSO$, $SVR-PSO's$ grey lines are more closely aligned with the target red dashed lines. $SVR-HGSO$, on the other hand, better models the sample size of 100 with an error of 8.70%, whereas $SVR-PSO$ models this sample with an underestimation error of 24.61%. In order to better comprehend the disagreement in modelling CS values, Figure 4 makes an attempt to illustrate the variations in CS magnitudes between the two proposed models.

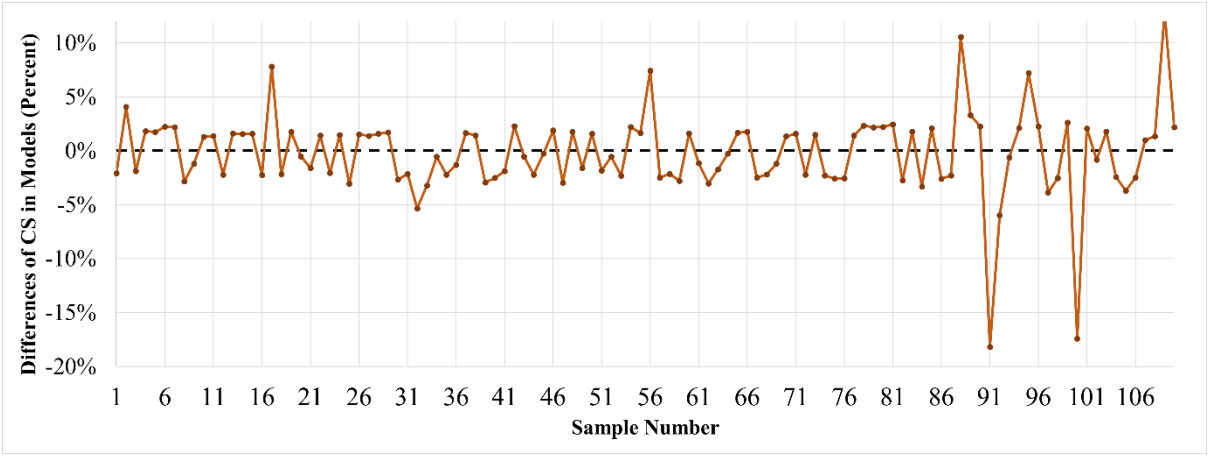

Fig. 4 – Difference between estimated CSs and developed frameworks.

It is noteworthy that Figure 4 was produced in the first stage by dividing the CS values modeled from $SVR-PSO$ by $SVR-HGSO$. Overall, the majority of the samples (samples 1 to 77) are modeled similarly, with a difference of 5% in the training phase. However, some examples in the testing phase, like 17, 32, and 56 samples, could be simulated with more than a five percent difference. On the other hand, samples $88, 91, 95, 100$, and 109 were modeled with different rates for the testing phase.

Figure 5 attempts to indicate the errors involved in modeling the CS of samples at the next stage. Any deviations from the measured $CS's$ target value lead to a gap from the zero line. Based on Figure 5 (a), the capability of $SVR-HGSO$ to model In contrast to $SVR-PSO$, the compressive resistance of samples is modeled with high-rate fluctuations. In place of $SVR-HGSO$, the smoother error line can be seen in the Training section. Every single point in the highlighted area is incorrect that are between -15% and $+23\%$ lower than $SVR-PSO$, despite the third sample of $SVR-HGSO$ having more errors of 27% during the training phase.

Additionally, the $SVR-HGSO$ 0-line does not have as many points as the $SVR-PSO$ 0-line that are touched by the evaluation indices. The $SVR-HGSO$ model includes a large number of samples for the testing phase. In contrast to $SVR-PSO$, which gave the Testing section a smoother line around the 0 error line, they are far from the 0 error line. The $SVR-HGSO$ in the sample of 91 exhibits the highest error rate in Figure 4, with a 29.28 percent error. The outcomes of the model's performance should be examined, as was already mentioned. Four assessment criteria that were used in the current study to evaluate models are shown in Figure 5.

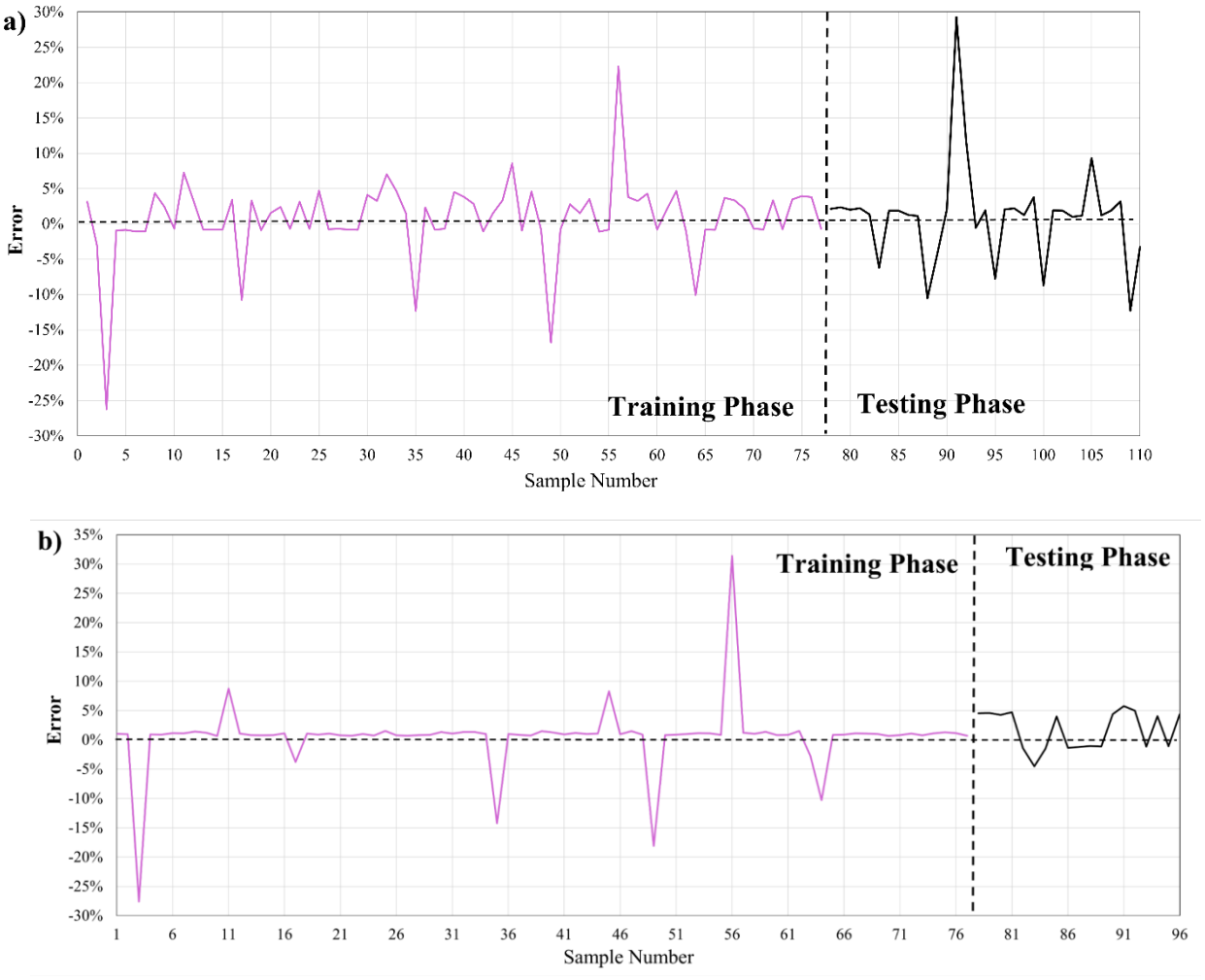

Fig. 5 – Error rates of CS modeling by a) $SVR-HGSO$ and b) $SVR-PSO$

$SVR-HGSO$ has demonstrated improved performance for the three statuses of training, testing, and total in the index R^2 for models. With a value of 0.96, the testing phase has a higher R^2 value, which is 3.84% higher than $SVR-PSO$. $SVR-PSO$ in the Training section could achieve the worst circumstance for the $RMSE$ error index with a value of 10.492 MPa, which is 3.33 percent higher than the rest. However, during the Testing section, $SVR-HGSO$ could only obtain 8.451 MPa while $SVR-PSO$ obtained 9.23 MPa; this represents a 9.25% difference between the two models' simulations of the CS values under better conditions contrast to the $RMSE$ indicator, the $SVR-HGSO's$ performance from the MAE viewpoint from the $SVR-PSO's$ according to Fig. 6, performance for three conditions is ranked higher from an MAE perspective. $SVR-HGSO's$ testing phase had a CS calculation error of 5.644 MPa, which is 20% more than $SVR-PSO's$. The VAF criterion also demonstrated how closely the outcomes of the two models matched one another. With a difference of 2.22% for both the training and testing phases, the $SVR-HGSO$ could outperform the $SVR-PSO$ when the entire data set is taken into account. With rates of 92.21 and 96.33, the differences are roughly two percent in favour of $SVR-HGSO$. Except for the VAF index, $SVR-HGSO$, and $SVR-PSO$, the OBJ indicator that encompasses all of the criteria mentioned in both phases obtained magnitudes of 7.575 and 6.747, indicating the $SVR-HGSO's$ superior performance with a 12.27% advantage over other models.

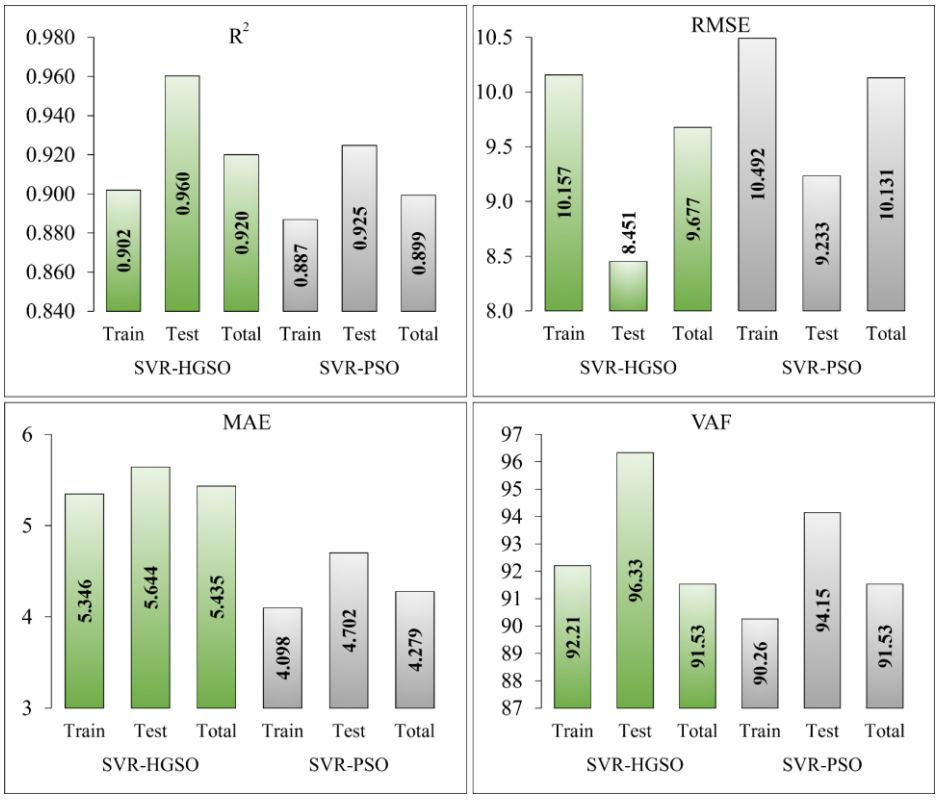

Fig. 6 – Evaluation indices' results for the performance of the proposed model

In the next stage, the distribution of errors for both models has been shown through Figure 7 that for $SVR-HGSO$, the errors are non-regularly spread over the horizontal axis with low concentrations around the 0 point of error. However, for $SVR-PSO$, this condition seems better with a suitable distribution of errors around 0 error. The bell-shaped normal distribution curves of error also show the thinner $SVR-PSO$ in front of the flatter $SVR-HGSO$ curve.

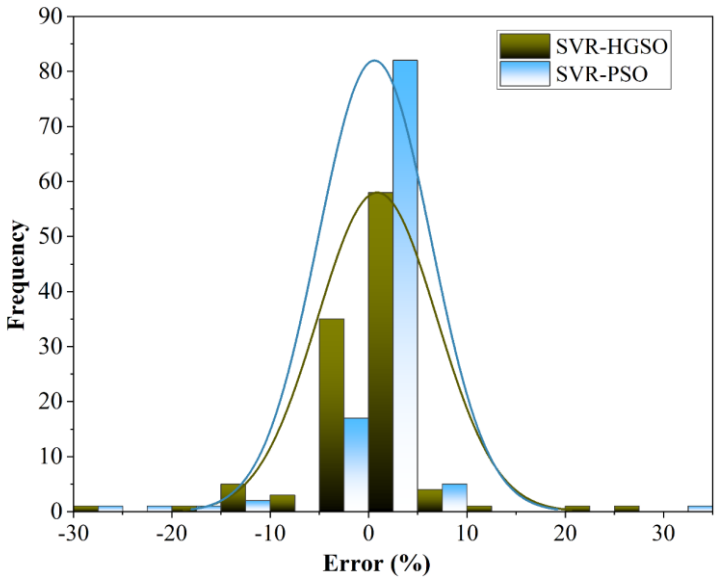

Fig. 7 – Error distribution of CS modeled via developed $SVR-HGSO$ and $SVR-PSO$

CONCLUSION

Ultra-high-performance concrete $(UHPC)$ is a widely used substance that produces buildings with exceptional performance, capabilities, and remarkable durability in any challenging environment. Reducing the cement and micro-silica content significantly lowers costs and $CO2$ emissions, even though the useful qualities and extended service life in comparison to regular or high-strength concrete compensate the pricey initial investment and negative environmental effects. Numerous studies have looked at the behavior of $UHPC$, which typically exhibits a CS of between $150\ MPa$ and $810\ MPa$. In some recent studies, various models were used to predict the CS of $UHPC$ concrete. Regarding these studies, it made sense that there wasn't a hybrid automated framework of predictive models. Consequently, a novel hybrid framework was created in the current study, and the presented models made a significant contribution is defined as follows:

- The SVR method, which employed the algorithms to predict concrete CS, was examined as a ML technique.
- $SVR-HGSO$ and $SVR-PSO$, two novel optimization algorithms, are used to more accurately model the CS of $UHPC$.
- With a difference of 2.31 percent, the $SVR-HGSO$ framework was able to model the CSs more accurately than $SVR-PSO$ thanks to its higher R^2 at the level of 0.92. $SVR-PSO$ was able to model the compounds' CS factor using the $10.13\ MPa$ error for the $RMSE$ index. While the other model performed this task more effectively than $SVR-HGSO$, with an $RMSE$ of 4.69 percent lower.
- Both models accurately predicted the CS values in the testing phase compared to the training phase. The $RMSE$ for $SVR-HGSO$ was $8.451\ MPa$, while the $RMSE$ for $SVR-PSO$ was $9.23\ MPa$, a difference of 9.25%.
- The VAF criterion also demonstrated how closely the outcomes of the two models matched one another. With a difference of 2.22% for VAF in both the training and testing phases, the $SVR-HGSO$ could outperform the $SVR-PSO$. The rates were 92.21 and 96.33, with differences of about 2% in favour of $SVR-HGSO$. The VAF index, the $SVR-HGSO$, and all of the other parameters specified in both phases were not included in the OBJ indication and the $SVR-PSO$, respectively, obtained values of 7.575 and 6.747, indicating that the $SVR-HGSO$ performed 12.27% better than the $SVR-PSO$.

- On the other hand, it is obvious that the search process of the $HGSO$ model in the exploration and exploitation outperformed compared to the PSO model, and delaying in local minimal for $HGSO$ is less than the PSO model.

To sum up, the $SVR - HGSO$ managed the error rates better than the $SVR - PSO$ visible in Figure 6 despite the accepted level of accuracy in modeling for both developed frameworks.

REFERENCES

[1] B. A. Graybeal, "Compressive behavior of ultra-high-performance fiber-reinforced concrete," *ACI materials journal*, vol. 104, no. 2, p. 146, 2007.

[2] P. Richard and M. Cheyrezy, "Composition of reactive powder concretes," *Cement and concrete research*, vol. 25, no. 7, pp. 1501–1511, 1995.

[3] Y. L. Voo and S. J. Foster, "Characteristics of ultra-high performance 'ductile'concrete and its impact on sustainable construction," *The IES Journal Part A: Civil & Structural Engineering*, vol. 3, no. 3, pp. 168–187, 2010.

[4] P. C. AITCIN, "Arts e scienza del calcestruzzo ad alte prestazioni," *L'Industria italiana del cemento*, vol. 68, no. 731, pp. 350–365, 1998.

[5] F. P. Torgal and S. Jalali, "Cement composites reinforced with vegetable fibres," in *Eco-efficient Construction and Building Materials*, Springer, 2011, pp. 143–156.

[6] C. Shi, Z. Wu, J. Xiao, D. Wang, Z. Huang, and Z. Fang, "A review on ultra high performance concrete: Part I. Raw materials and mixture design," *Construction and Building Materials*, vol. 101, pp. 741–751, 2015.

[7] Z. Yunsheng, S. Wei, L. Sifeng, J. Chujie, and L. Jianzhong, "Preparation of C200 green reactive powder concrete and its static–dynamic behaviors," *Cement and Concrete Composites*, vol. 30, no. 9, pp. 831–838, 2008.

[8] W. Zheng, B. Luo, and Y. Wang, "Compressive and tensile properties of reactive powder concrete with steel fibres at elevated temperatures," *Construction and Building Materials*, vol. 41, pp. 844–851, 2013.

[9] A. A. Pishro and X. Feng, "Experimental Study on Bond Stress between Ultra High Performance Concrete and Steel Reinforcement," *Civil Engineering Journal*, vol. 3, no. 12, pp. 1235–1246, 2018.

[10] Y. K. Cho, S. H. Jung, and Y. C. Choi, "Effects of chemical composition of fly ash on compressive strength of fly ash cement mortar," *Construction and Building Materials*, vol. 204, pp. 255–264, Apr. 2019, doi: 10.1016/j.conbuildmat.2019.01.208.

[11] M. Lezgy-Nazargah, S. A. Emamian, E. Aghasizadeh, and M. Khani, "Predicting the mechanical properties of ordinary concrete and nano-silica concrete using micromechanical methods," *Sādhanā*, vol. 43, no. 12, p. 196, Dec. 2018, doi: 10.1007/s12046-018-0965-0.

[12] J.-S. Chou and A.-D. Pham, "Smart Artificial Firefly Colony Algorithm-Based Support Vector Regression for Enhanced Forecasting in Civil Engineering," *Computer-Aided Civil and Infrastructure Engineering*, vol. 30, no. 9, pp. 715–732, Sep. 2015, doi: 10.1111/mice.12121.

[13] M. H. Rafiei, W. H. Khushefati, R. Demirboga, and H. Adeli, "Supervised Deep Restricted Boltzmann Machine for Estimation of Concrete.," *ACI Materials Journal*, vol. 114, no. 2, 2017.

[14] M. Castelli, L. Trujillo, I. Goncalves, and A. Popovic, "An evolutionary system for the prediction of high performance concrete strength based on semantic genetic programming," *Computers and Concrete*, vol. 19, no. 6, pp. 651–658, 2017.

[15] L. Lam, Y. L. Wong, and C. S. Poon, "Effect of Fly Ash and Silica Fume on Compressive and Fracture Behaviors of Concrete," *Cement and Concrete Research*, vol. 28, no. 2, pp. 271–283, Feb. 1998, doi: 10.1016/S0008-8846(97)00269-X.

[16] K. Ganesh Babu and G. Siva Nageswara Rao, "Early strength behaviour of fly ash concretes," *Cement and Concrete Research*, vol. 24, no. 2, pp. 277–284, 1994, doi: 10.1016/0008-8846(94)90053-1.

[17] L. G. Li, J. Zhu, Z. H. Huang, A. K. H. Kwan, and L. J. Li, "Combined effects of micro-silica and nano-silica on durability of mortar," *Construction and Building Materials*, vol. 157, pp. 337–347, Dec. 2017, doi: 10.1016/j.conbuildmat.2017.09.105.

[18] H. Eskandari, A. M. Nic, and A. Ghanei, "Effect of Air Entraining Admixture on Corrosion of Reinforced Concrete," *Procedia Engineering*, vol. 150, pp. 2178–2184, 2016, doi: 10.1016/j.proeng.2016.07.261.

[19] Z. Zhang, B. Zhang, and P. Yan, "Comparative study of effect of raw and densified silica fume in the paste, mortar and concrete," *Construction and Building Materials*, vol. 105, pp. 82–93, Feb. 2016, doi: 10.1016/j.conbuildmat.2015.12.045.

[20] A. Madadi, H. Eskandari-Naddaf, and M. Gharouni-Nik, "Lightweight Ferrocement Matrix Compressive Behavior: Experiments Versus Finite Element Analysis," *Arabian Journal for Science and Engineering*, vol. 42, no. 9, pp. 4001–4013, Sep. 2017, doi: 10.1007/s13369-017-2557-4.

[21] B. B. Sabir, “Mechanical properties and frost resistance of silica fume concrete,” *Cement and Concrete Composites*, vol. 19, no. 4, pp. 285–294, Jan. 1997, doi: 10.1016/S0958-9465(97)00020-6.
[22] M. Mazloom, A. A. Ramezanianpour, and J. J. Brooks, “Effect of silica fume on mechanical properties of high-strength concrete,” *Cement and Concrete Composites*, vol. 26, no. 4, pp. 347–357, May 2004, doi: 10.1016/S0958-9465(03)00017-9.
[23] S. Bhanja and B. Sengupta, “Influence of silica fume on the tensile strength of concrete,” *Cement and Concrete Research*, vol. 35, no. 4, pp. 743–747, Apr. 2005, doi: 10.1016/j.cemconres.2004.05.024.
[24] M. Y. Mansour, M. Dicleli, J. Y. Lee, and J. Zhang, “Predicting the shear strength of reinforced concrete beams using artificial neural networks,” *Engineering Structures*, vol. 26, no. 6, pp. 781–799, May 2004, doi: 10.1016/j.engstruct.2004.01.011.
[25] Z. Bajja, W. Dridi, A. Darquennes, R. Bennacer, P. Le Bescop, and M. Rahim, “Influence of slurried silica fume on microstructure and tritiated water diffusivity of cement pastes,” *Construction and Building Materials*, vol. 132, pp. 85–93, Feb. 2017, doi: 10.1016/j.conbuildmat.2016.11.097.
[26] M. Rostami and K. Behfarnia, “The effect of silica fume on durability of alkali activated slag concrete,” *Construction and Building Materials*, vol. 134, pp. 262–268, Mar. 2017, doi: 10.1016/j.conbuildmat.2016.12.072.
[27] H. Li, H. Xiao, J. Yuan, and J. Ou, “Microstructure of cement mortar with nano-particles,” *Composites Part B: Engineering*, vol. 35, no. 2, pp. 185–189, Mar. 2004, doi: 10.1016/S1359-8368(03)00052-0.
[28] L. P. Singh, S. R. Karade, S. K. Bhattacharyya, M. M. Yousuf, and S. Ahalawat, “Beneficial role of nanosilica in cement based materials – A review,” *Construction and Building Materials*, vol. 47, pp. 1069–1077, Oct. 2013, doi: 10.1016/j.conbuildmat.2013.05.052.
[29] A. K. Mukhopadhyay, “Next-generation nano-based concrete construction products: a review,” *Nanotechnology in civil infrastructure*, pp. 207–223, 2011.
[30] L. G. Li, J. Y. Zheng, J. Zhu, and A. K. H. Kwan, “Combined usage of micro-silica and nano-silica in concrete: SP demand, cementing efficiencies and synergistic effect,” *Construction and Building Materials*, vol. 168, pp. 622–632, Apr. 2018, doi: 10.1016/j.conbuildmat.2018.02.181.
[31] M. Jalal, A. Pouladkhan, O. F. Harandi, and D. Jafari, “Comparative study on effects of Class F fly ash, nano silica and silica fume on properties of high performance self compacting concrete,” *Construction and Building Materials*, vol. 94, no. 90, p. 104, 2015.
[32] D. De Domenico and G. Ricciardi, “Shear strength of RC beams with stirrups using an improved Eurocode 2 truss model with two variable-inclination compression struts,” *Engineering Structures*, vol. 198, p. 109359, Nov. 2019, doi: 10.1016/j.engstruct.2019.109359.
[33] L. Sadowski, M. Nikoo, and M. Nikoo, “Concrete compressive strength prediction using the imperialist competitive algorithm,” *Computers and Concrete*, vol. 22, no. 4, pp. 355–363, 2018.
[34] S. Czarnecki, M. Shariq, M. Nikoo, and Ł. Sadowski, “An intelligent model for the prediction of the compressive strength of cementitious composites with ground granulated blast furnace slag based on ultrasonic pulse velocity measurements,” *Measurement*, vol. 172, p. 108951, Feb. 2021, doi: 10.1016/j.measurement.2020.108951.
[35] Ł. Sadowski, M. Piechówka-Mielnik, T. Widziszowski, A. Gardynik, and S. Mackiewicz, “Hybrid ultrasonic-neural prediction of the compressive strength of environmentally friendly concrete screeds with high volume of waste quartz mineral dust,” *Journal of Cleaner Production*, vol. 212, pp. 727–740, Mar. 2019, doi: 10.1016/j.jclepro.2018.12.059.
[36] C. T. G. Awodiji, D. O. Onwuka, C. Okere, and O. Ibearugbulem, “Anticipating the Compressive Strength of Hydrated Lime Cement Concrete Using Artificial Neural Network Model,” *Civil Engineering Journal*, vol. 4, no. 12, p. 3005, Dec. 2018, doi: 10.28991/cej-03091216.
[37] J. Kasperkiewicz, J. Racz, and A. Dubrawski, “HPC Strength Prediction Using Artificial Neural Network,” *Journal of Computing in Civil Engineering*, vol. 9, no. 4, pp. 279–284, Oct. 1995, doi: 10.1061/(ASCE)0887-3801(1995)9:4(279).
[38] E. Ghafari, M. Bandarabadi, H. Costa, and E. Júlio, “Design of UHPC using artificial neural networks,” in *Brittle Matrix Composites 10*, Elsevier, 2012, pp. 61–69. doi: 10.1533/9780857099891.61.
[39] M. F. Javed *et al.*, “Applications of Gene Expression Programming and Regression Techniques for Estimating Compressive Strength of Bagasse Ash based Concrete,” *Crystals*, vol. 10, no. 9, p. 737, Aug. 2020, doi: 10.3390/cryst10090737.
[40] S. A. Emamian and H. Eskandari-Naddaf, “Genetic programming based formulation for compressive and flexural strength of cement mortar containing nano and micro silica after freeze and thaw cycles,” *Construction and Building Materials*, vol. 241, p. 118027, Apr. 2020, doi: 10.1016/j.conbuildmat.2020.118027.
[41] A. Behnood and E. M. Golafshani, “Predicting the compressive strength of silica fume concrete using hybrid artificial neural network with multi-objective grey wolves,” *Journal of Cleaner Production*, vol. 202, pp. 54–64, Nov. 2018, doi: 10.1016/j.jclepro.2018.08.065.

[42] M. Hassan and K. Wille, “Experimental impact analysis on ultra-high performance concrete (UHPC) for achieving stress equilibrium (SE) and constant strain rate (CSR) in Split Hopkinson pressure bar (SHPB) using pulse shaping technique,” *Constr Build Mater*, vol. 144, pp. 747–757, Jul. 2017, doi: 10.1016/j.conbuildmat.2017.03.185.
[43] H.-O. Jang, H.-S. Lee, K. Cho, and J. Kim, “Experimental study on shear performance of plain construction joints integrated with ultra-high performance concrete (UHPC),” *Construction and Building Materials*, vol. 152, pp. 16–23, Oct. 2017, doi: 10.1016/j.conbuildmat.2017.06.156.
[44] K. Wille and C. Boisvert-Cotulio, “Material efficiency in the design of ultra-high performance concrete,” *Construction and Building Materials*, vol. 86, pp. 33–43, Jul. 2015, doi: 10.1016/j.conbuildmat.2015.03.087.
[45] K.-Q. Yu, J.-T. Yu, J.-G. Dai, Z.-D. Lu, and S. P. Shah, “Development of ultra-high performance engineered cementitious composites using polyethylene (PE) fibers,” *Construction and Building Materials*, vol. 158, pp. 217–227, 2018.
[46] F. A. Hashim, E. H. Houssein, M. S. Mabrouk, W. Al-Atabany, and S. Mirjalili, “Henry gas solubility optimization: A novel physics-based algorithm,” *Future Generation Computer Systems*, vol. 101, pp. 646–667, Dec. 2019, doi: 10.1016/j.future.2019.07.015.
[47] V. Mohebbi, A. Naderifar, R. M. Behbahani, and M. Moshfeghian, “Determination of Henry’s law constant of light hydrocarbon gases at low temperatures,” *The Journal of Chemical Thermodynamics*, vol. 51, pp. 8–11, Aug. 2012, doi: 10.1016/j.jct.2012.02.014.
[48] T. L. Brown, *Chemistry: the central science*. Pearson Education, 2009.
[49] R. Eberhart and J. Kennedy, “A new optimizer using particle swarm theory,” in *MHS’95. Proceedings of the Sixth International Symposium on Micro Machine and Human Science*, IEEE, pp. 39–43. doi: 10.1109/MHS.1995.494215.
[50] A. Maleki, “Optimal operation of a grid-connected fuel cell based combined heat and power systems using particle swarm optimisation for residential sector,” *International Journal of Ambient Energy*, vol. 42, no. 5, pp. 550–557, Apr. 2021, doi: 10.1080/01430750.2018.1562968.
[51] G. Perampalam, K. Poologanathan, S. Gunalan, J. Ye, and B. Nagaratnam, “Optimum Design of Cold-formed Steel Beams: Particle Swarm Optimisation and Numerical Analysis,” *ce/papers*, vol. 3, no. 3–4, pp. 205–210, Sep. 2019, doi: 10.1002/cepa.1159.
[52] F. Masoumi, S. Najjar-Ghabel, A. Safarzadeh, and B. Sadaghat, “Automatic calibration of the groundwater simulation model with high parameter dimensionality using sequential uncertainty fitting approach,” *Water Supply*, vol. 20, no. 8, pp. 3487–3501, Dec. 2020, doi: 10.2166/ws.2020.241.
[53] M. B. Patil, M. N. Naidu, A. Vasan, and M. R. R. Varma, “Water distribution system design using multi-objective particle swarm optimisation,” *Sādhanā*, vol. 45, no. 1, p. 21, Dec. 2020, doi: 10.1007/s12046-019-1258-y.
[54] L. Wang, *Support vector machines: theory and applications*, vol. 177. Springer Science & Business Media, 2005.
[55] V. Vapnik, *The nature of statistical learning theory*. Springer science & business media, 2013.
[56] A. Al-Fugara, M. Ahmadlou, A. R. Al-Shabeeb, S. AlAyyash, H. Al-Amoush, and R. Al-Adamat, “Spatial mapping of groundwater springs potentiality using grid search-based and genetic algorithm-based support vector regression,” *Geocarto International*, pp. 1–20, 2020.
[57] G. Pazouki, E. M. Golafshani, and A. Behnood, “Predicting the compressive strength of self-compacting concrete containing Class F fly ash using metaheuristic radial basis function neural network,” *Structural Concrete*, Feb. 2021, doi: 10.1002/suco.202000047.

APPENDIX A:

```
% PSO-SVR for UHPC Compressive Strength Prediction

% Step 1: Load and preprocess the data
data = load('uhpc_data.mat');
X = data.features; % Input features
y = data.labels; % Compressive strength labels

% Step 2: Split the data into training and testing sets
ratio = 0.8; % Training-testing data ratio
splitIdx = round(ratio * size(X, 1));
X_train = X(1:splitIdx, :);
y_train = y(1:splitIdx);
X_test = X(splitIdx+1:end, :);
y_test = y(splitIdx+1:end);

% Step 3: Define the objective function for SVR
objective = @(x)svrObjective(x, X_train, y_train);

% Step 4: Define the PSO parameters
nParticles = 50; % Number of particles
nVariables = size(X_train, 2); % Number of variables (dimensionality)
maxIterations = 100; % Maximum number of iterations

% Step 5: Initialize the PSO parameters
particlePositions = rand(nParticles, nVariables); % Initialize positions randomly
particleVelocities = zeros(nParticles, nVariables); % Initialize velocities to zero
personalBestPositions = particlePositions; % Initialize personal best positions
personalBestValues = inf(nParticles, 1); % Initialize personal best values
globalBestPosition = zeros(1, nVariables); % Initialize global best position
globalBestValue = inf; % Initialize global best value

% Step 6: Perform PSO iterations
for iteration = 1:maxIterations
    % Evaluate current positions
    particleValues = objective(particlePositions);

    % Update personal best positions and values
    updateIndices = particleValues < personalBestValues;
    personalBestPositions(updateIndices, :) = particlePositions(updateIndices, :);
    personalBestValues(updateIndices) = particleValues(updateIndices);

    % Update global best position and value
    [minValue, minIndex] = min(personalBestValues);
    if minValue < globalBestValue
        globalBestPosition = personalBestPositions(minIndex, :);
        globalBestValue = minValue;
    end

    % Update particle velocities and positions
    inertiaWeight = 0.9; % Inertia weight
    cognitiveWeight = 2; % Cognitive weight
    socialWeight = 2; % Social weight
```

```
    r1 = rand(nParticles, nVariables);
    r2 = rand(nParticles, nVariables);
    particleVelocities = inertiaWeight * particleVelocities ...
        + cognitiveWeight * r1 .* (personalBestPositions - particlePositions) ...
        + socialWeight * r2 .* (globalBestPosition - particlePositions);
    particlePositions = particlePositions + particleVelocities;

    % Perform boundary handling (if necessary)
    % e.g., particlePositions = max(min(particlePositions, upperBounds), lowerBounds);
end

% Step 7: Predict the compressive strength using the trained SVR model
predictedValues = svrPredict(X_test, globalBestPosition);

% Step 8: Evaluate the prediction performance
mse = mean((predictedValues - y_test).^2); % Mean Squared Error
rmse = sqrt(mse); % Root Mean Squared Error
mae = mean(abs)
```

CIVIL ENGINEERING JOURNAL

Article no. 26

THE CIVIL ENGINEERING JOURNAL 3-2023

INFLUENCE OF CONSTRUCTION PERIOD OF BRIDGE ACROSS RESERVOIR ON OPERATION OF ADJACENT POWER STATION

Xi Mao[1], Hongyu Qiu[2], Rui Wang[4], Peiyu Huang[1], Shuiqian Wang[2], Nengzhong Lei[1], Weimin Wu[2], Songliang Chen[1], Lele Wang[3], Jiawen Huang[1] and Zhongquan Xu[1]

1. *School of Civil Engineering and Architecture, Wuyi University, 358 Baihua Road, Wuyishan, Fujian, China*
2. *Water Conservancy Management Center of Fujian Province, 34 Wushan Road, Fuzhou, Fujian, China*
3. *Fujian Key Laboratory of Hydrodynamics and Hydraulic Engineering, 158 Dongda Road, Fuzhou, Fujian, China*
4. *POWERCHINA Chengdu Engineering Corporation Limited, Chengdu, Sichuan, China; 270231694@qq.com*

ABSTRACT

The influence of the construction period of the bridge project across the reservoir on the adjacent power station includes not only the direct impact on the hydropower hub but also the impacts on the reservoir area, flood discharge, power station head, water diversion and sediment prevention, power generation operation, and other factors. In this paper, from the aspects of the power station operation, an evaluation index for the influence of the construction period of a bridge across a reservoir on the adjacent power station is developed, and an evaluation system is constructed. Based on the constructed evaluation system, the influence of the bridge construction period on the adjacent power stations is analyzed. This evaluation system provides a reference for the impact assessment of cross-reservoir bridge engineering on adjacent hydropower stations.

KEYWORDS

Bridge engineering, Construction stage, Environment, Influence, Reservoir

INTRODUCTION

The smooth road is inseparable from the connection of the bridge, and the bridge has become a common and special part of the road building. It is common because crossing rivers and valleys cannot be separated from bridges, every river on the way is crossed by bridges. It is special because the bridge is actually the road in the air. If the road is in the air, the structure and material of the road will become complex and special, and need special scientific support and process production [1][2]. Today, with the rapid development of science and technology, there are talents and universities specializing in the study and study of bridge construction, With the support of advanced technology and a variety of powerful machines, the construction of Bridges under various conditions has become convenient, and ultra-long and ultra-high bridges have become easier and easier [2][3].

Bridges are one type of historically representative engineering structure in the process of human history. The San Francisco Golden Gate Bridge in the United States, the Sydney Harbour Bridge in Australia, London Bridge in the United Kingdom, the Stone Strait Bridge in Japan, the Yangpu Bridge in Shanghai, and the Hangzhou Bay Cross-sea Bridge, the Nanjing Yangtze River Bridge, the Hong Kong Qingma Bridge, and the Hong Kong-Zhuhai-Macao Bridge in China are all

valuable works of art and have become regional landmarks and landscape highlights [4][5]. Due to the need for highway construction in various terrains and landforms, including construction in mountainous areas and of reservoir bridges, the construction of some highways has encountered more complex terrain and geological conditions. The main manifestations are as follows: the ground height difference in mountainous areas varies greatly, each span is large, the height of the bridge pier is generally required to be large, and the terrain is steep [6].

For railways that encounter a large number of reservoir dams, the interaction between their construction and the reservoir dams distributed along the line cannot be avoided. It is extremely urgent to find ways to evaluate the impact of the railway bridge construction period on adjacent power stations and to solve the dispute between railway constructors and the owners of hydropower projects along the line. Currently, few studies have been conducted on the impact assessment of cross-reservoir bridge projects on power stations. The Southern Sichuan Railway Company has evaluated the impact of the Fushun Tuojiang River Bridge on the Huangnitan Hydropower Station from the aspects of the power station structure safety, flood discharge, power generation operation, and bank slope [7]. In addition, Huang [8] and Zhang [9] conducted relevant research on the impact of bridge vibration on the surrounding environment and achieved certain results. However, research in this field is still in the supplementary improvement stage, and impact assessments of bridges on reservoir power stations are also very scarce.

Therefore, in this study, a super-large bridge on a railway across a reservoir is taken as an example, and the impacts of bridge construction on all of the aspects of the adjacent power station are determined. Furthermore, the potential impact indicators of the bridge on the power station are determined as much as possible, and an evaluation system is developed to provide a reference for the impact assessment of bridges across reservoirs on adjacent power station projects.

PROJECT PROFILE

The railway is located in Shiyang Town, Tianquan County, Ya'an City, Sichuan Province. It crosses the Xinzhong Hydropower Station via the Xinzhong Power Station Bridge. The bridge obliquely crosses the reservoir area of the Xinzhong Power Station approximately 50 m to the south of the dam, and the bridge axis is 47° obliquely crossing the dam (Figure 1). The bridge is a double-track curved railway. The bridge scheme is a 5-unit 2 × 68 m T-shaped continuous girder bridge. The total length of the bridge is 796.62 m, and the maximum height of the bridge is approximately 33.5 m. The nearest distance between the bridge and the power station is approximately 50 m. Piers 4–12 of the bridge are wading piers. The wading pier 4 is located closest to the power station and is 175 m upstream of the power station water intake.

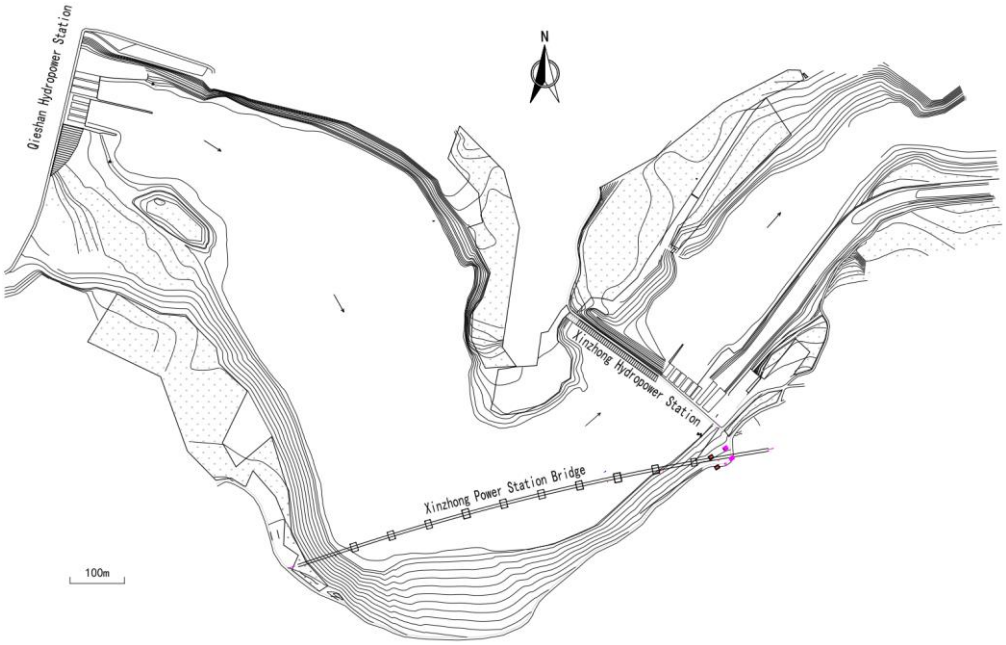

Fig. 1 – Schematic showing the relationship between the location of the Xinzhong railway bridge line and the power station

The Xinzhong Hydropower Station is located on the main stream of the Tianquan River in Tianquan County Town, approximately 11 km from Tianquan County Town (Figure 2). The Xinzhong Hydropower Station is a riverbed power station, and the project consists of a retaining dam, power plant, and tailrace. The installed capacity of the power station is 21 MW (3 × 7 MW), and the designed water head is 13 m. The normal water level of the reservoir is 656.50 m, and the adjustable reservoir capacity is 680,000 m³. The designed flood standard of the power station is a 50-year flood (flow rate of 3560 m /s), and the check flood standard is a 300-year flood (flow rate of 4620 m³/s). The reservoir operation mode is as follows: during the flood season (June to October), when the inflow is less than 500 m³/s, the reservoir is maintained within the normal water level; when the storage flow is greater than 500 m³/s, the gate is opened and flushing is stopped [10].

The construction and operation of the power station are as follows: the construction of the Xinzhong Hydropower Station began in October 2005 and was completed in December 2010. Through operation, inspection, and rectification over the years, it has been determined that the Xinzhong Hydropower Station hub project is in good health and running normally.

Fig. 2 – Site photos of Xinzhong Hydropower Station

CONSTRUCTION OF IMPACT ASSESSMENT SYSTEM

The impacts of similar cross-reservoir bridges such as the Xinzhong Railway Bridge on the power station are not limited to the impact on the hub project itself. Under the long-term operation of the reservoir, the impact also includes many problems such as erosion and deposition in the reservoir area, flood discharge, power station head, water diversion and sediment prevention, and power generation operation [11]. In this study, a total of nine impact assessment indices were selected from the three aspects of the reservoir impact, the power station hub impact, and the power generation operation impact in the impact assessment of the Xinzhong Railway Bridge on the adjacent Xinzhong Hydropower Station to construct an assessment system for the impact assessment of the power station. The construction of the impact assessment system is illustrated in Figure 3.

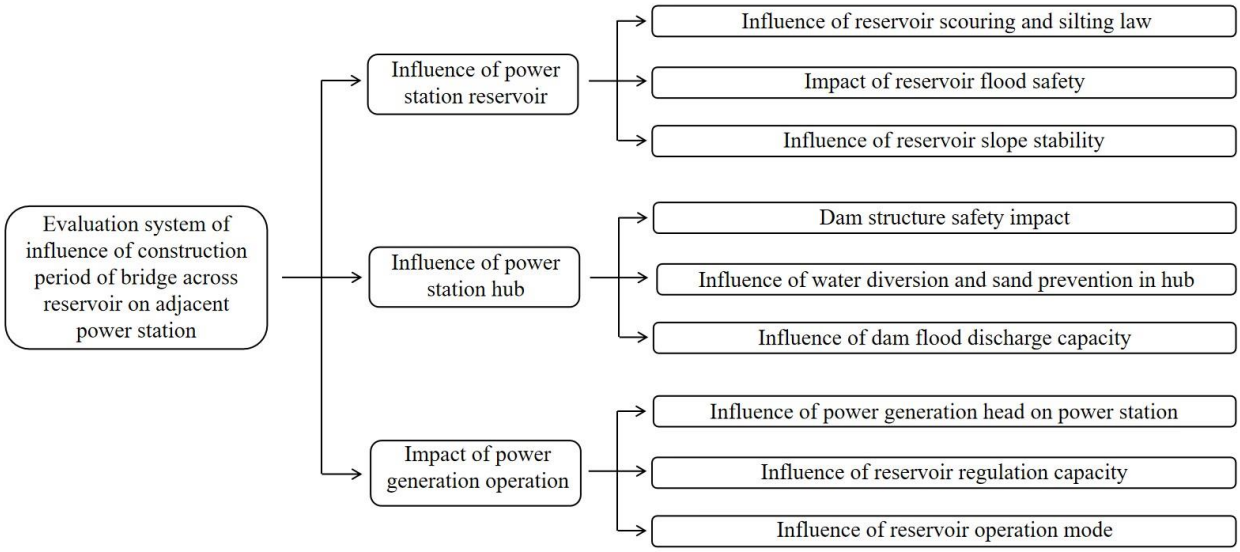

Fig. 3 – The impact assessment system of the construction period of the cross-reservoir bridge on the adjacent power station

RESULTS: IMPACT ASSESSMENT OF XINZHONG POWER STATION

Status evaluation of Xinzhong Power Station

The Xinzhong Power Station was commissioned in 2010. During the first 10 years of reservoir operation, all of the hydraulic structures were in normal operation without major reconstruction or expansion. According to the analysis presented in the External Deformation Monitoring Report of the Xinzhong Power Station, the reservoir and dam of the Xinzhong Power Station have good safety conditions without obvious external deformation.

Reservoir impact

The influence of the bridge construction on the reservoir area of the power station was mainly caused by the construction of the wading bridge pier, including the change in the flow field in the reservoir area caused by the cofferdam of the wading bridge pier, the rise of the water level, and the disturbance of the riverbed by construction. In this study, the influence of the Xinzhong Railway Bridge on the Xinzhong Power Station reservoir area was evaluated. Using the Mike21FM two-dimensional hydraulic calculation software, the hydraulic calculations were performed for the cofferdam of the wading pier during the construction period, and the influence of the bridge on the

reservoir area during the construction period was evaluated based on the changes in the flow field, water level, and sediment deposition [12].

Change in the reservoir flow field

There are nine wading piers on the Xinzhong Railway Bridge. The flow field analysis was performed as follows: the flow velocity in the main flow area of the bridge section was between 2.00 and 3.20 m/s, and the main flow in the river section was located on the right side of the center of the riverbed under natural conditions. Due to the large size of the steel cofferdam during the construction period (maximum size of 11.1 × 14.9 m), the influence of the bridge pier cofferdam on the flow field in the river section during the construction period was obvious. Under the action of the bridge pier cofferdam, the water flow was pushed to the central part of the area. The main stream of the river was completely located in the middle of the riverbed, and the flow velocity in the middle of the riverbed area was significantly increased compared with the current situation.

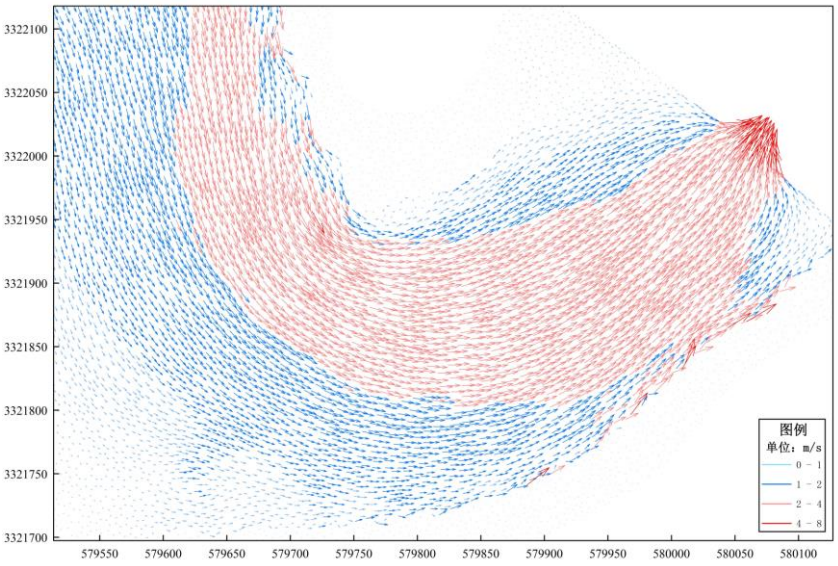

(a) Current flow field

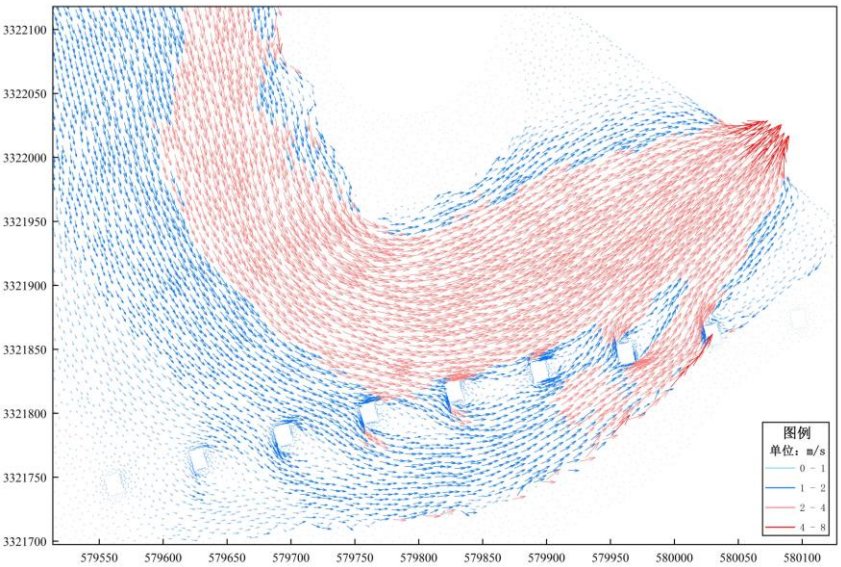

(b) Flow field during construction

Fig. 4 – Comparison of the flow fields in the reservoir area during and after bridge construction (designed flood flow conditions)

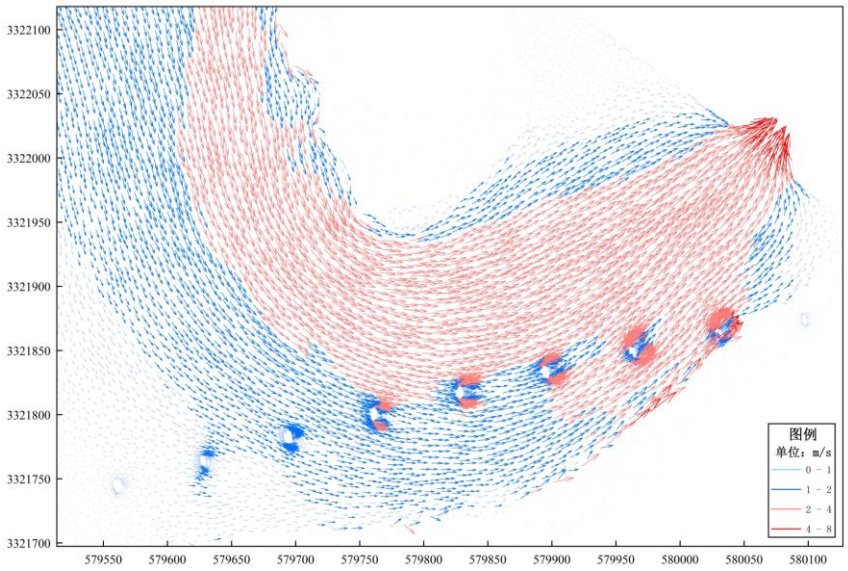

(c) Operating flow field

Fig. 4 – Comparison of the flow fields in the reservoir area during and after bridge construction (designed flood flow conditions)

Effect of reservoir erosion

The river section of the bridge is a typical river bend section. The sediment transport forms a bent circulation phenomenon. The right concave bank is dominated by erosion, and the left convex bank is dominated by deposition. During the bridge construction period, when the inflow was less than the boundary flow of 500 m3/s, due to the operation of the water level in front of the power station dam at a higher normal storage level, the flow velocity in the reservoir area was small, and the sediment carrying capacity of the water flow was weak. Under these conditions, the change in the flow velocity caused by the construction of the pier was also very small. Therefore, when the inflow was small, the pier construction had little effect on the riverbed siltation. When the inflow was greater than the demarcation flow of 500 m3/s, the water level of the power station was a lower open water level, and the flow velocity of the river section increased and returned to the natural river state. Under the action of the bridge pier steel cofferdam, the sediment, which was originally moving with the main stream of the river on the right side, was pulled to the riverbed area on the left by the flow, resulting in the change in the local riverbed deposition pattern. However, because the construction period was only 32 months, the influence of the change in the riverbed sedimentation on the long-term operation of the power station was controllable.

Impact of reservoir flood safety

The steel cofferdam of the bridge pier is located in the main stream area of the river, occupying the flood area of the river, and it has a certain water-blocking effect, resulting in a certain rise in the water level of the reservoir area. The results of the hydraulic calculation revealed that under the condition of a 50-year flood flow in the design standard, the maximum water level of the river section would rise by 0.64 m. However, there would be no important flood control object or flood control sensitive point in the Xinzhong reservoir area, and the rise in the water level would have little effect on the flood control in the reservoir area.

Effect of bank slope stability

The reservoir area of the Xinzhong Power Station mainly exposes the Oligocene Lushan Formation (E3l), which is composed of silty mudstone interbedded with thin argillaceous siltstone and a small amount of sandstone. The bank slopes on both sides are composed of bedrock, and there is no unfavorable fracture combination. Although a small amount of collapse occurs under the action of dynamic water processes, it has little effect on the whole bank, and the bank slopes on both sides are stable.

The pier is located near the right bank slope. During the foundation excavation stage of the construction, the excavation was controlled, the support was well done, blasting was strictly prohibited to prevent instability of the bank slope, and slope observation and early warning were also well done. If the bank slope collapses or loses stability, it should be repaired before the flood season.

The river section of the bridge is a typical curved river section. During the flood season, the main stream of the river is located on the right side of the river. The right bank of the river section belongs to the top scour part of the river. Under the action of the steel cofferdam of the bridge pier, the main stream area was shifted from the right side of the river to the center of the riverbed. Therefore, the pier steel cofferdam of the bridge construction reduced the risk of water erosion of the right bank.

Influence of power station hub

The influence of the construction of this new railway bridge in China on the power station hub was a direct dominant influence, which was mainly manifested as direct damage to the power station dam by the bridge construction and a negative effect on the safety of the engineering structure. The bridge construction resulted in water diversion and sediment problems caused by the power station shutdown, and the influence of the bridge construction on the dam discharge capacity caused dam flood control safety problems.

Influence of dam structure

The retaining dam, flood discharge sluice, power plant, and other buildings are the most important facilities of the dam. The bridge needs to be carefully evaluated before construction, and protection should be strengthened during construction. The construction of the Xinzhong Railway Bridge included trestle construction, bored pile construction, cofferdam construction, bridge structure construction, and other procedures. There were no violent construction activities such as blasting in these construction procedures, and there were small vibrations during the bored pile steel casing and pier cofferdam insertion processes. However, the riverbed overburden medium between the bridge and the power station had an obvious buffering effect on the construction vibrations. Under the condition of a reasonable construction scheme and other control measures, the influence of the vibrations on the dam could be effectively controlled. Therefore, during the bridge construction period, the direct safety threat to the structure of the retaining dam, flood discharge sluice, power plant, and other buildings of the Xinzhong Power Station was low.

Influence of water diversion and sand prevention in hub

The Xinzhong Power Plant is located on the right side of the riverbed. The bridge construction period had little effect on the change in the flow field near the sand trap of the plant, and the effect of the sand trap in front of the plant was not significantly changed by the bridge construction.

The foundation construction directly disturbed the sediment of the riverbed cover, which caused an increase in the suspended sediment content of the water flow for a short period, increasing the sediment amount passing the power station and threatening the operation safety of the generator set. To ensure the safe operation of the power station unit, when the bridge construction had a great influence on the riverbed disturbance, the power station needed to be shut down in time to avoid the sand peak.

Influence of dam flood discharge capacity

The flood discharge capacity of the hydropower station is mainly controlled by the orifice size of the flood discharge facility and the downstream water level flow relationship. The Xinzhong Railway Bridge is located upstream of the Xinzhong Hydropower Station. The bridge does not affect the orifice size of the flood discharge facilities or the relationship between the downstream water level and flow. Therefore, the construction period of the Xinzhong Railway Bridge did not affect the flood discharge capacity of the Xinzhong Hydropower Station and did not affect the flood control safety of the hub.

Influence of power station operation

Compared with the direct impact of the bridge on the power station hub, the impact of the bridge on the power generation operation of the power station was more indirect and implicit. For example, the backwater caused by the bridge construction led to a decrease in the water head or a decrease in the regulating reservoir capacity and forced the management to change the reservoir operation mode, resulting in the hidden loss of power generation by the hydropower station.

Impact of power generation head

The power generation head of the power station is mainly controlled by the tailwater level flow relationship of the power station when the water level in front of the dam is constant. The bridge project was generally located downstream of the power station and could raise the tailwater level and reduce the power generation loss of the power station. In this case study, the Xinzhong Power Station Bridge is located upstream of the Xinzhong Power Station. The bridge does not affect the downstream water level flow relationship and does not affect the power generation head of the Xinzhong Power Station.

Adjusting the storage impact

The normal reservoir level of the Xinzhong Hydropower Station is 656.50 m, the regulating reservoir capacity is 680,000 m³, and the total reservoir capacity is 1.47 million m³. The total steel cofferdam volume during the construction period of the wading bridge was approximately 75,000 m³, accounting for approximately 0.5% of the total reservoir capacity of the reservoir, so it had little effect on the regulating reservoir capacity of the reservoir.

Influence of reservoir operation mode

The reservoir operation mode is mainly related to the reservoir scouring, silting rule, regulating storage capacity, tail water level, and flow. If the above indices change significantly, the operation mode of the reservoir needs to be adjusted. According to the analysis, the construction period of the Xinzhong Railway Bridge did not cause significant changes in these indicators and did not cause adjustment of the operation mode of the power station reservoir.

Construction of evaluation system of Xinzhong power station

According to various influencing factors, the evaluation index system includes 3 first-level indicators and 10 second-level indicators. According to the characteristics of Xinzhong Power Station, the weight of each index is set. For different environmental characteristics, the choice of index weight can also be different. The evaluation index system is shown in Table 1.

Fig. 1 - Xinzhong power station evaluating indicator system table

First-level indicators		First-level indicators	
Name of indicator	Weight	Name of indicator	Weight
Reservoir impact	0.4	Change in the reservoir flow field	0.25
		Effect of reservoir erosion	0.25
		Impact of reservoir flood safety	0.25
		Effect of bank slope stability	0.25
Influence of power station hub	0.3	Influence of dam structure	0.30
		Influence of water diversion and sand prevention in hub	0.30
		Influence of dam flood discharge capacity	0.40
Influence of power station operation	0.3	Impact of power generation head	0.30
		Adjusting the storage impact	0.30
		Influence of reservoir operation mode	0.40

The calculation formula of the influence index of the power station is as follows:

$$RHI = \sum_{i=1}^{n}(ZB_{nw} \times ZB_{nr}) \quad (1)$$

In Formula (1): RHI is the comprehensive score; ZB_{nw} is the weight of the nth index in the index layer; ZB_{nr} is the score of the nth index of the index layer.

The power station impact assessment level is divided into three levels according to the evaluation index score from high to low, namely level I (safe), level II (relatively safe), and level III (unsafe). The scoring range and evaluation grade of the impact index of the power station are shown in Table 2.

Tab. 2 - Power station impact index classification standard table

Assignment range	Evaluation grade
[85.00，100]	Grade I
[60.00，85.00)	Grade II
[0，60.00)	Grade III

Loss evaluation

The loss estimation of the impact of railway bridges on power stations mainly includes the inundation loss of the reservoir area, the structural loss of the power station hub, and the power loss. The inundation loss of the reservoir area is the compensation cost of the new inundated object caused by the bridge construction. The structural loss of the power station hub is that when the bridge construction causes structural damage to the power station hub, it is necessary to evaluate the degree of structural damage and to calculate the compensation cost according to the amount of reconstruction or repair work. The electric quantity loss is calculated according to the electric quantity loss caused by the decrease in the water head of the power station, the shutdown of the station to avoid the sand peak during the construction period, and the change in the reservoir operation mode.

According to the above analysis, the Xinzhong Railway Bridge had no compensation for new submerged objects in the reservoir area, no compensation for structural losses to the power station hubs, and no compensation for power losses caused by a decrease in the power station head and

changes in the reservoir operation mode. However, there was compensation for power losses caused by the disturbance of the riverbed during bridge construction, which required shutting down the power station to avoid the sand peak. However, the influence of the sediment on the operation of the unit was more complex. Whether it was necessary to stop the machine to avoid sediment depended on the sediment content, grain type, the effect of the unit itself on the sediment adaptability, the bridge construction period, and other factors. Therefore, it is necessary to strengthen the sediment monitoring of the intake of the power station during the bridge construction period, to dynamically adjust the operation period of the unit according to the situation, and to carry out statistical analysis of the power generation loss according to the actual power station shutdown days after the construction is completed.

Problems that may be encountered during construction

There are relatively few regulations for mountainous areas and reservoir areas, and the corresponding schemes should be adopted in combination with different landforms. Many research aspects need to be refined and improved.

(1) The transportation of bridge materials in mountainous areas has always been a difficult problem in the construction process. Due to the poor linear shape of the access channel, it is difficult for large vehicles to enter and exit, and thus, the transportation of beams and plates or large materials becomes a technical problem.

(2) There are many factors affecting the type of bridge constructed in mountainous areas and reservoirs, so it is necessary to monitor the mid- and long-term stress and deformation of the bridge in the later operation process to study the wind load, temperature, concrete shrinkage and creep, and the influence of materials on the durability of the structure.

CONCLUSIONS

In this paper, the impact assessment system of the railway bridge across the reservoir on the adjacent power station is constructed, the impact assessment factors are constructed, and the analytical weight value of each factor is determined. Taking the construction of railway bridge for Xinzhong Hydropower Station as an example, the impact of the bridge on the construction period and the whole life of the bridge is evaluated systematically. According to the calculation, the evaluation value of the railway bridge to the power station is 86, and the evaluation impact is small.

The construction of the evaluation system can provide a powerful negotiation basis for resolving the disputes between the railway construction side and the hydropower project owners along the line, and help to quickly resolve the differences between the parties and promote the project process.

ACKNOWLEDGEMENTS

This research was supported by Wuyi University (grant number: YJ202216), the Education Department of Fujian Province (grant number: JAT220379), the Department of Science and Technology of Fujian Province (grant number: 2023J011046), and Sichuan University (grant number: SKHL2117). The authors declared that they have no conflicts of interest to this research.

REFERENCES

[1] Zhou X H, Zhang X G. Thoughts on the Development of Bridge Technology in China[J]. Engineering, 2019, 5(6): 1120-1130, DOI: 10.1016/j.eng.2019.10.001.

[2] Kang C, Schneider S, Wenner M, Marx S. Development of design and construction of high-speed railway bridges in Germany[J]. Engineering Structures, 2018, 163(may15): 184-196, DOI: 10.1016/j.engstruct.2018.02.059.

[3] Su M, Wang J, Peng H, Cai C S, Dai G L. State-of-the-art review of the development and application of bridge rotation construction methods in China[J]. Science China Technological Sciences, 2021, 64(6): 1137-1152, DOI: 10.1007/s11431-020-1704-1.
[4] Delan Yin. Brief Discussion of Bridge Engineering History[J]. Journal of Engineering Studies, 2016, 08(06):654-660, DOI: 10.3724/SP.J.1224.2016.00654.
[5] Han Z Y. Aesthetics Innovation and Practice of Urban Bridge Design[J]. Structural Engineering International, 2021(4): 31, DOI: 10.1080/10168664.2020.1848368.
[6] Malekly H, Mousavi S M, Hashemi H. A fuzzy integrated methodology for evaluating conceptual bridge design[J]. Expert Systems with Applications, 2010, 37(7):4910-4920, DOI: 10.1016/j.eswa.2009.12.024.
[7] Tian Z X, Chen Q. Tuojiang Bridge Construction Monitoring Stress Analysis[J]. Gansu Science and Technology, 2012, 28(1): 118-120, DOI: 10.3969/j.issn.1000-0952.2012.01.045. (in Chinese)
[8] Huang J, Ding Y, Shi Z L, Li Z X. Seismic responses of long-span cable-stayed bridges under different patterns of earthquake excitations[J]. China Journal of Highway and Transport, 2005, 18(3): 48-53, DOI: 10.3321/j.issn:1001-7372.2005.03.010. (in Chinese)
[9] Ding Y, Li Z X, Zhang Y. Seismic analysis and isolation for station-bridge structures of light railways[J]. Earthquake Engineering and Engineering Vibration, 2003, 23(6): 163-168, DOI: 10.3969/j.issn.1000-1301.2003.06.026. (in Chinese)
[10] Shu S. Emergency plan for flood control of reservoir hydropower station[J]. Architectural Engineering Technology And Design, 2016, 13: 1937, DOI: 10.3969/j.issn.2095-6630.2016.13.857. (in Chinese)
[11] Huang H. Evaluation of the impact of the impoundment of the hydropower station in the Hengjiang River Basin on the safety of the bridge in the reservoir area[D]. Southwest Jiaotong University, 2014. (in Chinese)
[12] Stevens R F. Substation Design Standards and Short Cuts Save Manpower[J]. IEEE Transactions on Power Apparatus and Systems, 1957, 76(3):627-632, DOI: 10.1109/AIEEPAS.1957.4499625.

CIVIL ENGINEERING JOURNAL

Article no. 27

THE CIVIL ENGINEERING JOURNAL 3-2023

$PM_{2.5}$ ESTIMATION IN THE CZECH REPUBLIC USING EXTREMELY RANDOMIZED TREES: A COMPREHENSIVE DATA ANALYSIS

Saleem Ibrahim[1], Martin Landa[1], Eva Matoušková[1], Lukáš Brodský[2] and Lena Halounová[1]*

1. *Department of Geomatics, Faculty of Civil Engineering, Czech Technical University in Prague, 166 29 Prague, Czech Republic, email: saleem.ibrahim@fsv.cvut.cz, martin.landa@fsv.cvut.cz; eva.matouskova@fsv.cvut.cz; lena.halounova@fsv.cvut.cz*
2. *Department of Applied Geoinformatics and Cartography, Faculty of Science, Charles University, 128 43 Prague, Czech Republic, email: lukas.brodsky@natur.cuni.cz*

ABSTRACT

The accuracy of artificial intelligence techniques in estimating air quality is contingent upon a multitude of influencing factors. Unlike our previous study that examined PM2.5 over whole Europe using unbalanced spatial-temporal data, the focus of this study was on estimating PM2.5 specifically over the Czech Republic using more balanced dataset to train and evaluate the model. Moreover, the spatial autocorrelation between PM2.5 measurements was taken into consideration while building the model. The feature importance while developing the Extra Trees model revealed that spatial autocorrelation had greater significance in comparison to commonly used inputs such as elevation and NDVI. We found that R2 of the 10-CV for the new model was 16% higher than the previous one. Where R2 reached 0.85 with RMSE=5.42 µg/m3, MAE=3.41 µg/m3, and bias=-0.03 µg/m3. The developed spatiotemporal model was employed to generate comprehensive daily maps covering the entire study area throughout the period 2018–2020. The temporal analysis showed that the levels of PM2.5 exceeded recommended limits during the year 2018 in many regions. The eastern part of the country suffered from the highest concentrations especially over Zlín and Moravian-Silesian Regions. Air quality improved during the next two years in all regions reaching promising levels in 2020. The generated dataset will be available for other future air quality studies.

KEY WORDS

Air quality, PM2.5, Artificial intelligence, Spatial autocorrelation, Czech Republic

INTRODUCTION

Atmospheric Particulate Matter (PM) with a diameter smaller than or equal to 2.5 microns (PM2.5) is small enough to be inhaled deeply in the lungs and are able to reach the bloodstream and reduce the immune system's capacities [1]. The exposure of high PM2.5 levels could cause serious health problems especially in densely populated areas that produce enormous amounts of pollution into the atmosphere due to increased combustion sources and human activities [2]. PM has an effect on mortality even at concentrations that are in compliance with the European annual regulation [3]. In Europe, around 300,000 premature deaths are caused by PM annually and more than 330 billion Euros of economic cost, that encouraged the Directive 2008/50/EC to limit the yearly average of PM2.5 to 20 µg/m3 since the first of January 2020 [4].

In this study, we focused on the Czech Republic (CZ). Based on previous studies, CZ suffered from low air quality in some regions throughout last decades. The estimated additional social costs

resulting from the poor air quality in Ostrava city for children aged 0-15 amounted to approximately 20 million Euros per year [5]. In 2012 winter, the mean value of PM2.5 over Ostrava was 159 μg/which caused a smog episode [6]. When studying causes of air pollution in Teplice within the framework of the Teplice Program, initiated around 1970, researchers found that around 70% of PM2.5 fine particles came from the local heating sources that used brown coal with a high SO2 content [7]. As a result of this discovery, the Czech government supported a transition from coal to natural gas for local heating in mining districts in 1994 [7]. The north-eastern part of CZ that shares borders with Poland, which is highly polluted due to its long history of coal mining, heavy industry, traffic infrastructure and the dense population [8]. In 2018, around 1.2% of the CZ's total area, which is home to roughly 6.1% of the population, exceeded 25 μg/m3 [9]. Approximately 20% of households in CZ use individual heating systems that burn solid fuels [10]. During 2013 winter in the residential district of Mladá Boleslav, wood burning was found to be the primary source of PM10 mass, with coal combustion following as the second most significant source [11]. Coal remains a key energy source in CZ, accounting for one-third of the country's total energy supply in 2019 [12]. Coal also accounted for 46% of the country's electricity generation and more than 25% of residential heating [12]. The Czech government is currently exploring strategies for removing coal from its energy mix, including potential timelines for this transition. To support this effort, the government established a Coal Commission in 2019, which presented its recommendations in December 2020. The Commission advised that coal should be phased out no later than 2038 [12]. The data from April 2018 to March 2019 collected in the Moravian-Silesian Region has verified that during the winter season, the inflow of PM cross-border pollution from Poland is a key factor contributing to air pollution levels [13].

In recent decades, numerous studies have utilized the capabilities of artificial intelligence (AI) in estimating PM2.5 concentrations. These studies have focused on developing various types of models to increase the limited spatial coverage that is provided by PM2.5 ground monitors. Covering more auxiliary data as inputs helped to improve the performance of the models when compared to the typical interpolation methods which rely solely on the observations from the monitors [14]. The auxiliary inputs for the models usually include a combination of satellite data, meteorological modeled data, topography, and land cover data. Satellite-based Aerosol Optical Depth (AOD) is a valuable indicator of aerosol levels in the Earth's atmosphere and since PM2.5 is a type of aerosol, there is generally a positive correlation that made AOD a crucial factor in predicting PM2.5 levels [15,16]. Meteorological data such as the planetary boundary layer height (PBLH) that is the vertical extent of the lowest part of the Earth’s atmosphere, Relative Humidity (RH) which represents the total amount of water vapor that exists in the atmosphere relative to the maximum amount water vapor that air can hold at particular temperature, the Total Column Water Vapor (TCWV) that is the measurement of the total amount of water vapor present in the vertical column of the Earth’s atmosphere, Wind Speed (WS), Temperature (T), Total Precipitation (TP), and Evaporation (E) have shown that significance varies depending on the region when PM2.5 is estimated [14,17,18]. Moreover, a few studies considered the Spatial Autocorrelation (SA) of PM2.5 when developing predictive models. Inspired by the first law of geography which proposes that all features present on a geographic surface have a connection with each other, and that geographic entities have a stronger association with nearby entities as compared to those that are located far away [19]. In a study spanning from 1999 to 2016, the yearly average PM2.5 levels in Chinese cities exhibited a typical autocorrelation [20]. In another study, including SA improved the performance of the Random Forest (RF) model and decreased the Root Mean Square Error (RMSE) by ~18% when estimating PM2.5 over Sichuan Basin in 2019 [21]. Adding the spatial lag variable (SLV) as a virtual input in the neural network model for estimating the yearly PM2.5 concentrations increased the coefficient of determination (R2) by ~9% [22].

In this study, we aimed to estimate the concentrations of PM2.5 over the CZ during the years 2018, 2019, and 2020. CZ is a landlocked country that covers an area of 78870 square kilometres located in central Europe bordering Germany, Poland, Slovakia, and Austria.

MATERIALS AND METHODS

Dependent variable and primary independent variables

Daily PM2.5 concentrations for 2018, 2019, and 2020 were collected from the Czech Hydrometeorological Institute (CHMI). The total number of stations and observations after removing the outlier values were 54 and 54,495 respectively. The number of observations per year is 18330 in 2018, 18022 in 2019, and 18144 in 2020.

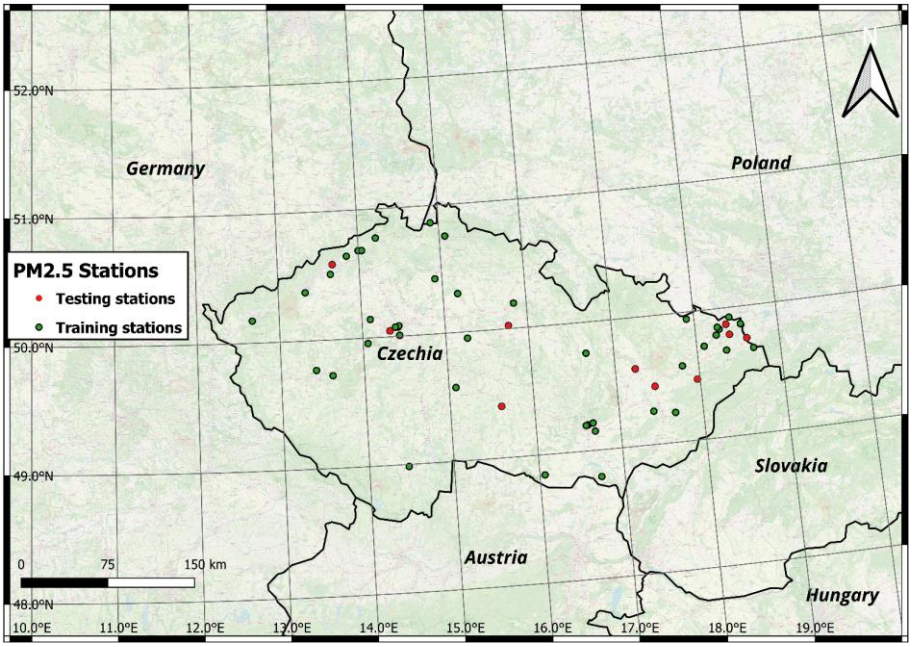

Fig. 1 - Study area with ground stations. The red dots represent the stations that were used to test the model and the green dots represent the stations that were used to train the model

We explored the following data as primary inputs in our study, AOD data over CZ was collected from the Geo-Harmonized Atmospheric Dataset for Aerosols (GHADA) which is a full coverage dataset over Europe with 1 km spatial resolution that was built based on the MCD19A2 MODIS product [23] and modelled AOD from Copernicus Atmosphere Monitoring Service (CAMS) [24]. This dataset showed good results when validated with NASA's Aerosol Robotic Network (AERONET) observations [25]. Meteorological data like PBLH, WS calculated based on the u and v wind components, temperature at 2m (T2m), TP, E, TCWV, and RH were collected from the European Centre for Medium-Range Weather Forecasts ERA5 climate reanalysis [26], and then reprojected to the grid using the bilinear interpolation; monthly NDVI from the MODIS MOD13A3 product [27]; the percentage of artificial surfaces and air pollution resources for each 1km2 cell were calculated from the CORINE Land Cover (CLC) of 2018 which was built based on ortho-rectified satellite images with a spatial resolution ranging from 5-60 m, and were aggregated to 100 m; Open Street Map (OSM) data was processed to calculate the total road lengths (RL) within each cell of the grid; elevation (H) was extracted from the Japan Aerospace Exploration Agency (JAXA) digital surface model [28], and population data was estimated from the monthly Visible Infrared Imaging Radiometer Suite (VIIRS) nighttime lights of 2019 [29]. The linear analysis between the primary inputs and PM2.5 showed that PBLH and T2m were the most negatively correlated variables to PM2.5 with Pearson correlation of -0.25 and -0.22 respectively. NDVI, TCWV, WS, RH, H, and TP also had negative correlations with PM2.5. Whereas, E, AOD, NL, and RL had positive correlations with PM2.5. The following table shows the primary data that was used

in our study. All primary data was reprojected to the European Terrestrial Reference System 1989 (EPSG:3035) with a grid of 1 km2 that covers the study area using bilinear interpolation for meteorological data and the cubic convolution for the elevation model.

Tab. 1 - The primary inputs that were explored in this study

Name		Variable	Unit	Spatial resolution	Source
Aerosol optical depth		AOD	-	1 km	GHADA
Meteorological	Planetary boundary layer height	PBLH	m	0.1°×0.1°	ERA5-Land
	Wind speed	WS	m/s		
	Temperature at 2m	T2m	K		
	Total precipitation	TP	mm		
	Evaporation	E	mm		
	Total column water vapor	TCWV	Kg/m^2		
	Relative humidity	RH	%	0.25°×0.25°	ERA5
Land cover	Normalized Difference Vegetation Index	NDVI	-	1 km	MODIS MOD13A3
	CORINE Land Cover	CLC	-	100 m	Corine LC 2018
	Road length	RL	m	~10 m	Open street maps
Topography		H	m	~30 m	JAXA
Population		NL	$nW/cm^2/sr$	500 m	VIIRS

Model development

A machine learning algorithm was used with feature engineering techniques that were applied to train the PM2.5 predictive model.

We used the Extra Trees (ET) algorithm which is an ensemble learning method that combines the predictions of several decision trees to make the final prediction [30]. It is an extension of the widely used RF algorithm where in both, the final prediction is the majority of predictions in classification problems and the arithmetic average in regression problems. ET reduces overfitting by introducing additional randomness during the construction of the trees and it uses the entire dataset while training without performing any pruning which decreases the required time for training compared to the RF that applies pruning techniques. A deeper explanation of this algorithm was provided in our previous work [25,31].

Feature engineering and model training

The temporal inputs were represented by the radian day and the year. The radian day will help the model understand the cyclic nature of time and enables it to capture the seasonal patterns in the data. Whereas, adding the year will capture long-term trends that occur over the years of the

study period. The spatial inputs were represented by longitude, latitude, and elevation. Adding the spatial inputs will allow the model to capture the inherent spatial heterogeneity in the data. In addition to the mentioned inputs, SA of the dependent variable was calculated based on the training set. We used the Local Moran Index (LMI) that was based on the foundation of the Moran's I statistic [32]. LMI is a spatial autocorrelation statistic used in geography and other disciplines to identify local clusters or spatial patterns of similar or dissimilar values in a dataset [33]. Positive values for LMI indicate that the observation at the station is a part of a cluster of similar observations from surrounding stations and vice versa, the magnitude of the LMI value represents the strength of SA [34]. For each day of the study period, LMI was calculated for each station considering the closest three neighboring stations using the K-nearest neighbors (KNN) weight matrix with k=3.

$$\boldsymbol{LMI_i} = \frac{\boldsymbol{z_i - \bar{z}}}{\boldsymbol{\sigma^2}} \sum_{\boldsymbol{j=1, i \neq j}}^{\boldsymbol{n}} [\boldsymbol{w_{ij}}(\boldsymbol{z_j} - \boldsymbol{\bar{z}})] \quad (1)$$

Where, Zi is the value of the observation at the location i; $\bar{z}$ is the average value of z with the sample number of n; zj is the value of the observation at all other stations where i≠j; σ2 is the variance of the observation z; and wij is the weight matrix for the locations i and j.

The whole dataset was split into a training set (80% of the dataset) and a test set (20% of the dataset), Figure 1 represents the distribution of the stations. LMI was calculated based on the training set only to assure that the test set remains unseen for the model. The feature importance for each input was calculated and based on that some features were removed to generalize the model and to reduce complexity. CLC, OSM, and population had low importance because these inputs are not real time data. Figure 2 shows feature importance of the primary inputs in the training set.

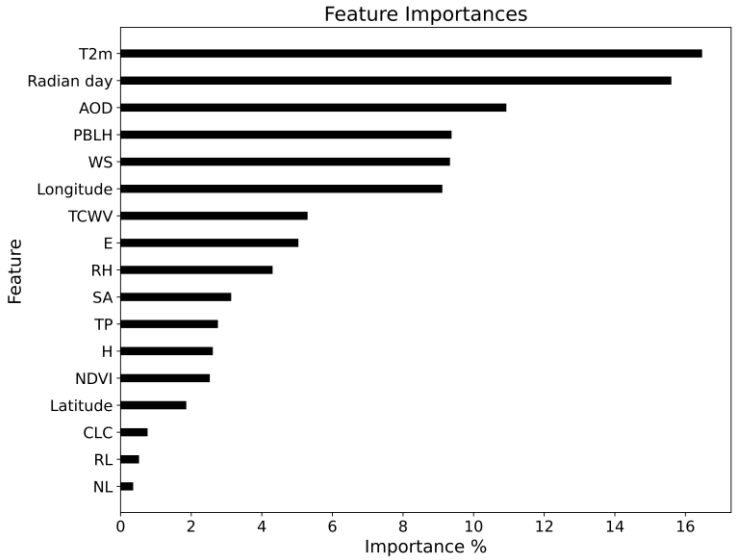

Fig. 2 - Feature importance calculated based on the training data.

The widely used grid search technique with 10-fold Cross Validation (10-CV) was used for hyperparameters tuning. In this process, the training data was split into 10 equal-sized folds, where each fold was used as a validation set while training the model on the remaining 9 folds. We employed R^2, the RMSE, and the Mean Squared Error (MAE) as evaluation matrices. R^2 measures the proportion of variance in $PM_{2.5}$ that can be explained by the model. RMSE quantifies the average difference between the predicted and observed $PM_{2.5}$ values. MAE measures the average absolute difference between the predicted and observed $PM_{2.5}$ values. Utilizing these three metrices together is commonly used in regression problems to provide a comprehensive evaluation of the model. The maximum depth of the trees, the minimum number of samples required to split an internal node and

the minimum number of samples required at a leaf node were the main parameters to fine-tune the model. While applying the 10-CV on the training data, we tested how the performance will drop when excluding some inputs. We found that NDVI did not noticeably affect the performance of the model and it was excluded as well.

Model validation

This section was dedicated to the validation process to assess the reliability and accuracy of our findings.

Validation on the test set

We tested the model on the test set that was taken from the stations in unseen locations for the model. This validation showed the model ability to predict values in new locations that were not used to generate the LMI. The model showed good results when estimating $PM_{2.5}$ in the new locations with R^2 = 0.86, RMSE=5.61 μg/m^3, and MAE=3.37 μg/m^3.

Validation on all data

It is a common approach in $PM_{2.5}$ studies to apply 10-CV of the whole dataset [35–37]. In order to do this validation, we generated LMI based on the data from all stations, then we applied a sample based 10-CV. The model showed similar results compared to the validation on the test set with R^2=0.85, RMSE=5.42 μg/m^3, MAE=3.41 μg/m^3 and, bias=-0.03 μg/m^3. Figure 3 shows the results of the sample based 10-CV.

A negative bias indicates that, on average, the model tends to underpredict $PM_{2.5}$ values. However, a value of -0.03 appears to align reasonably well with the characteristics of the data where the values range between 2 and 200 with an average of 17 μg/m^3.

R^2 values indicate that the model explains around 86% and 85% of the variance in $PM_{2.5}$ values, which suggests that the model is performing well and generalizing reasonably to unseen data.

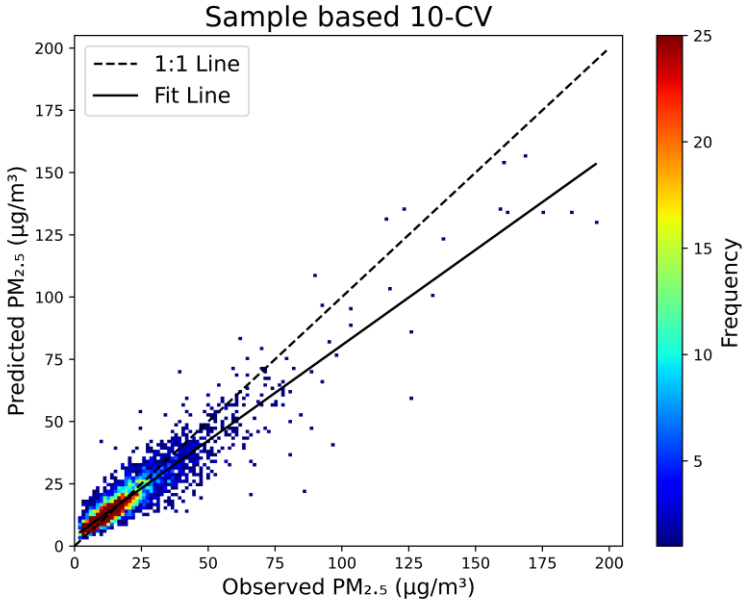

Fig 3 - Density scatter plot for the 10-CV applied on all data.

Results

Model deployment

We utilized the model to generate daily full coverage $PM_{2.5}$ maps over CZ. To validate the deployment of the model we extracted values of the estimated $PM_{2.5}$ at station locations and compared their temporal profiles with observed values. Figure 4 represents the temporal profile for three stations with high, normal, and low $PM_{2.5}$ levels.

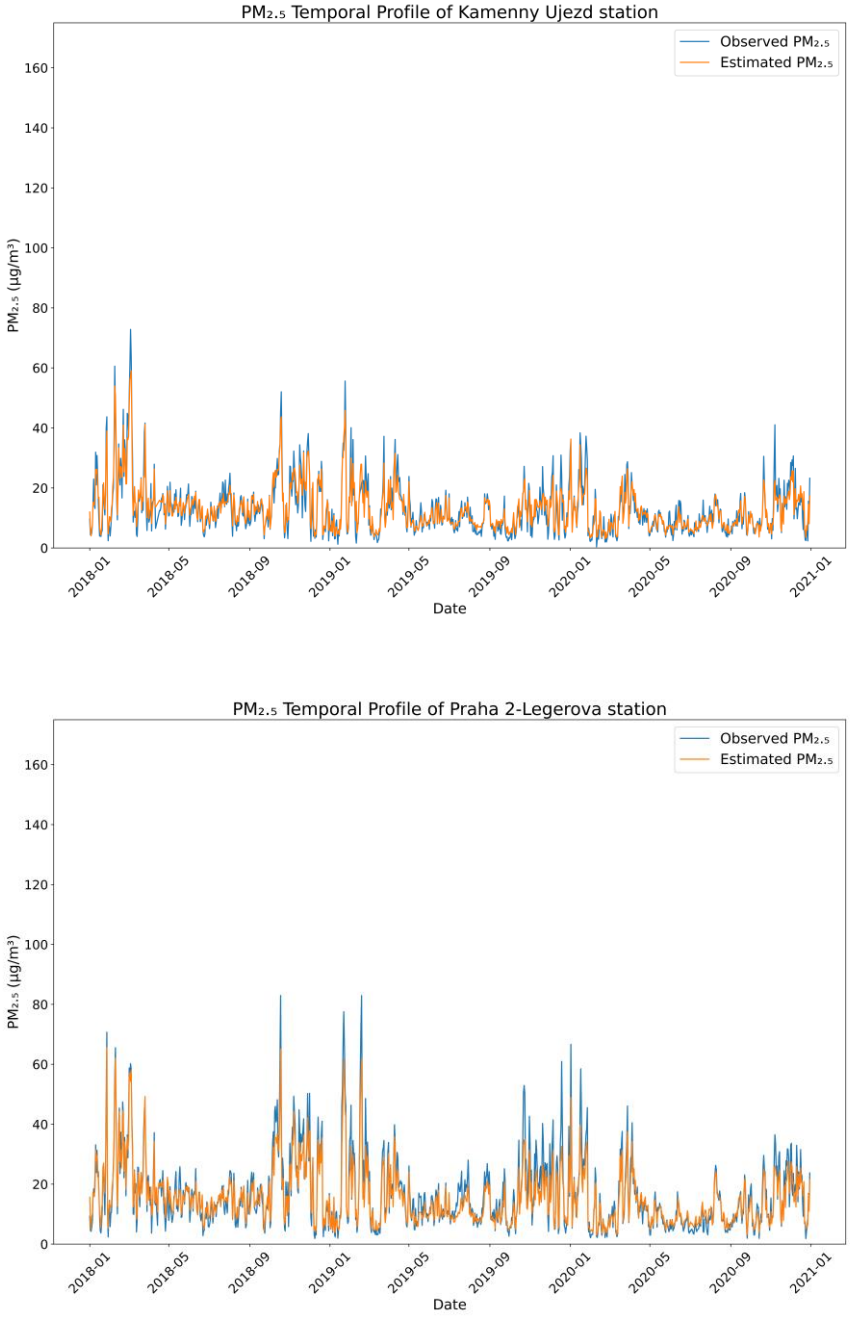

Fig. 4 - $PM_{2.5}$ temporal profile over three stations

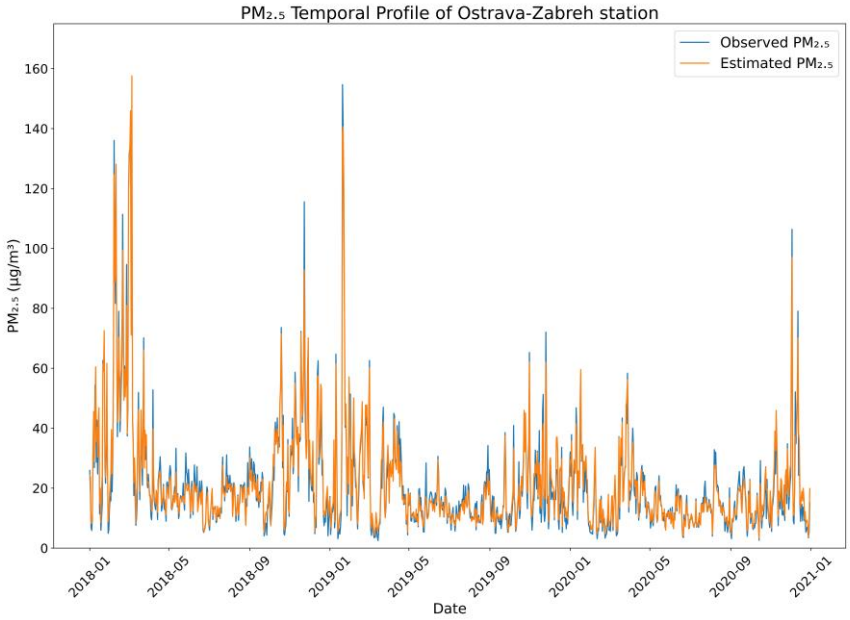

Fig. 4 - $PM_{2.5}$ temporal profile over three stations: Kamenny Ujezd station, Praha 2-Legerova station, and Ostrava-Zabreh station.

The results in all stations show nearly perfect overlap, which confirms not only high general accuracy of the model but also temporal clarity of the predictions. They also show slight bias of the model in the peaks' predictions, small underestimation in high values and slight underestimation in down-peaks. It can be noticed that $PM_{2.5}$ values are higher during winter compared to other seasons in the three chosen stations.

Temporal and regional analysis

We calculated the average $PM_{2.5}$ levels for each year during the study period. In Figure 5 we show the yearly average levels. $PM_{2.5}$ decreased gradually throughout the study period. The eastern part of CZ had the highest $PM_{2.5}$ levels. The Moravia-Silesian Region was the most polluted region with an average $PM_{2.5}$ level of 25.2 µg/m^3 in 2018, 18 µg/m^3 in 2019 and 15.8 µg/m^3 in 2020. Karlovy Vary Region had the lowest $PM_{2.5}$ values with 16.4 µg/m^3 in 2018, 11.1 µg/m^3 in 2019, and 10.2 µg/m^3 in 2020. Besides, the Moravia-Silesian Region, $PM_{2.5}$ values exceeded 20 µg/m^3 in Zlín and Olomouc Regions with average values of 22.7 µg/m^3 and 22.2 µg/m^3 respectively during 2018. Good $PM_{2.5}$ levels <= 12 µg/m^3 were found in six regions in 2020, these regions are Plzeň, Karlovy Vary, Southern Bohemia, Vysočina, Central Bohemia, and Liberec.

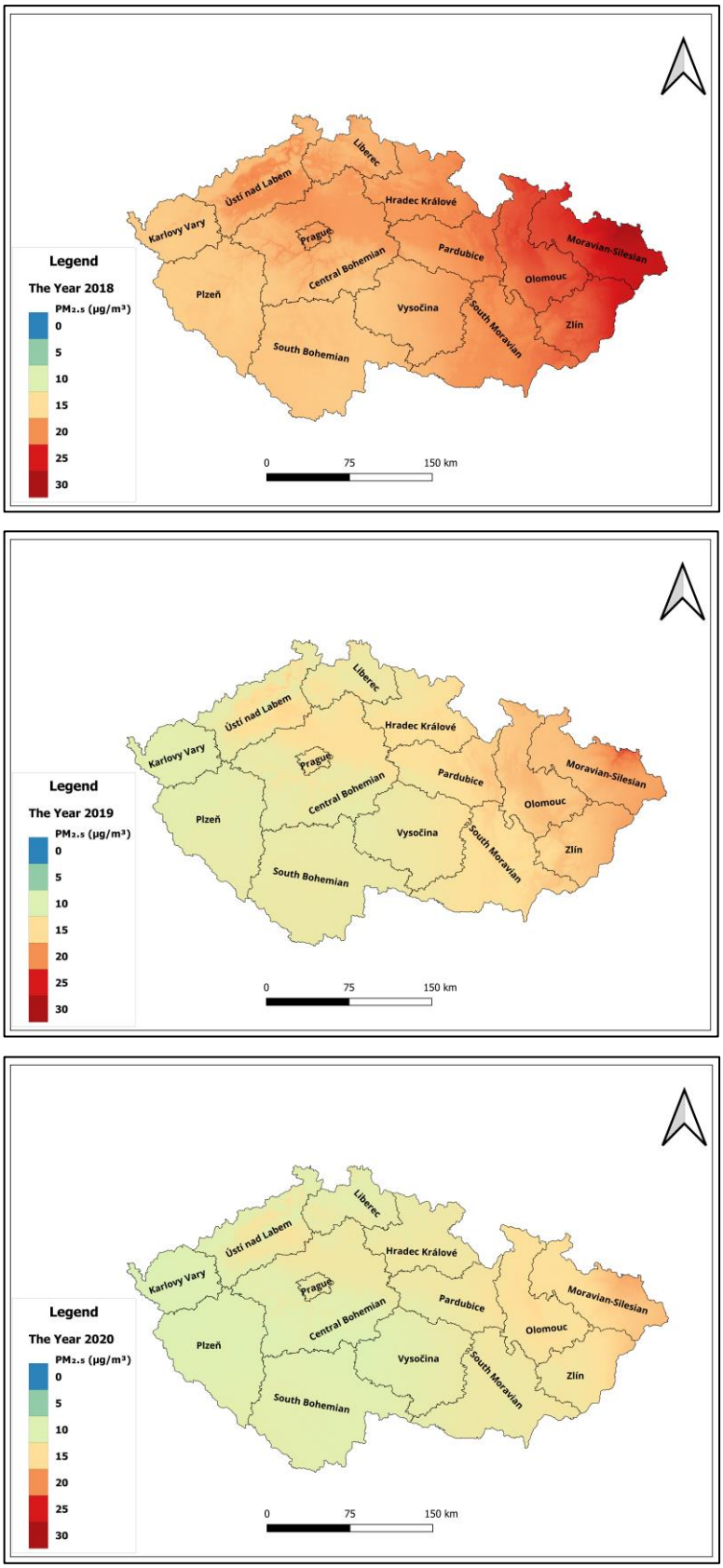

Fig. 5 - The average $PM_{2.5}$ levels over the Czech Republic in the years 2018, 2019, and 2020.

Seasonal analysis

In this analysis, we delved into the seasonal patterns of $PM_{2.5}$ concentrations of 2018–2020. By examining the fluctuations across different seasons and analyzing the variations in $PM_{2.5}$ levels over time, we aimed to gain valuable insights into the underlying factors influencing pollution levels during specific seasons of the study period. Winter was represented by January, February, and December; summer encompasses June, July, and August; spring spans from March through May; and autumn extends from September to November. We calculated the average $PM_{2.5}$ levels for each region in CZ in the different seasons. Figure 6 shows the results we conducted.

The average $PM_{2.5}$ levels in summer are relatively consistent for each year across the entire country. $PM_{2.5}$ concentrations exhibit significant variations during winter seasons. In winter, the average $PM_{2.5}$ was the highest in all regions except two in 2018 where Prague had the highest values during autumn and Karlovy Vary had the highest levels during spring. The eastern part of CZ was highly polluted during 2018 winter with average values of 30 μg/m^3 over Olomouc Region, 31 μg/m^3 over Zlín Region, and 35 μg/m^3 over the Moravian-Silesian Region. Pardubice, Karlovy Vary, and South Moravian Regions also had average concentrations higher than 25 μg/m^3 during this season. In 2019, only the eastern part of CZ had an average concentration higher than 25 μg/m^3. Air quality improved throughout the study period; the Moravian-Silesian Region recorded the highest average value of 20 μg/m^3 in 2020 winter.

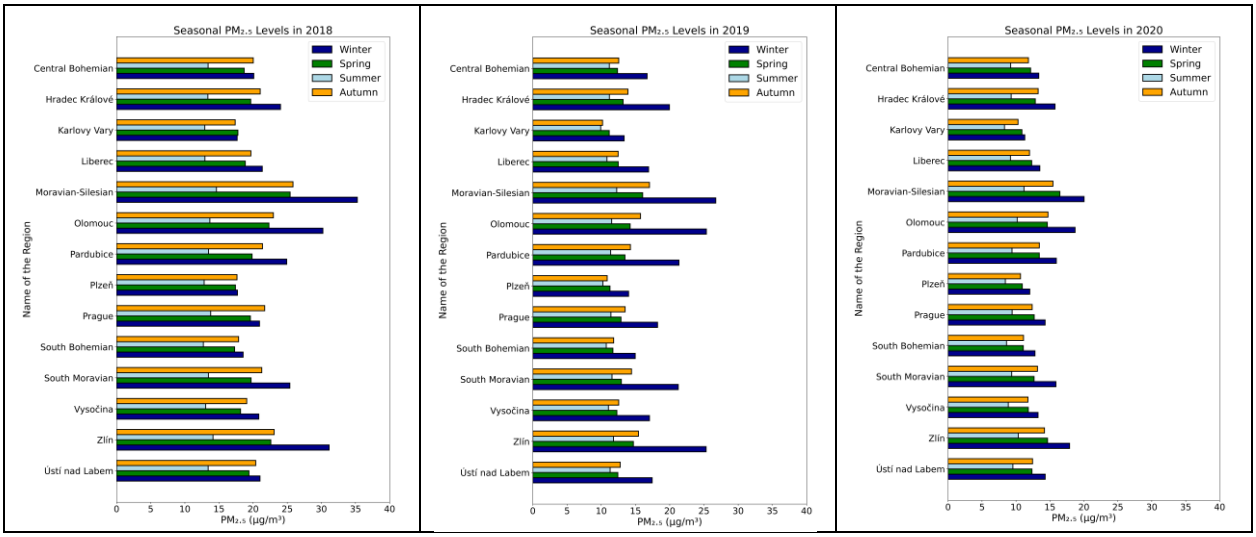

Fig. 6 - $PM_{2.5}$ seasonal analysis over the Czech Republic in 2018, 2019, and 2020.

DISCUSSION

In this study, we used a tree-based machine learning algorithm called the Extra Trees to estimate PM2.5 over CZ with a high spatial resolution of 1 km during 2018–2020. In contrast to our prior study, which concentrated on the entire Europe [31], we discovered that incorporating more balanced data in terms of spatial and temporal distribution enhances the overall accuracy of the model and simplifies the modeling approach. The R2 obtained from the 10-fold cross-validation of the model developed specifically for CZ was 0.85, whereas the corresponding R2 for the model developed for the entire European region was 0.69 [31]. Dividing the data according to stations, ensured that the model can accurately forecast the absent PM2.5 values in new locations, achieving a high R2 of 0.86 and a low RMSE of 5.61 μg/m3.

The spatial autocorrelation we calculated based on the Local Moran Index had higher feature importance than other spatial independent variables like elevation. Calculating the Local Moran Index can give different results due to factors like the K value and the data's distribution, which are important to consider when using it in machine learning models. It should be noted that

the spatial autocorrelation must be generated from the training data only without including the test data, so the test set remains totally unseen to the model to evaluate its performance in an unbiased way.

Confirming the findings from our earlier study, the independent variables which exhibit a high degree of invariance over the duration of the study, like land cover data or the length of the roads in every 1 km of the grid, will have a lower importance on the model. Unlike other studies that included all input features regardless to their importance in generating the model [38], we showed that excluding these inputs will better generalize the model leading to improved estimations. We believe that the inclusion of temporally varying data will enhance the training process of the model, resulting in increased accuracy. For instance, including road traffic intensity yields more refined estimations compared to relying solely on static factors such as the length of roads. For each year during the study period, the yearly averages were computed by taking a simple average of all the available values per pixel.

The results showed that PM2.5 levels were above the recommended limits in many regions of CZ in 2018. The eastern part suffered from the highest values especially during the winter season where the concentrations reached unhealthy levels with values higher than 30 μg/m3. The part located on the Czech-Polish border is characterized as a significant industrial zone with abundant coal deposits and a long-standing presence of factories involved in power generation and manufacturing of coal specifically used for steel-making purposes. PM2.5 levels found to exceed the limits over Polish cities in winter seasons [39], airborne transport facilitate the inflow of particulate matter from Poland across borders, making it a crucial factor in contributing to elevated air pollution levels in the eastern part of CZ. The average concentrations of PM2.5 during summer season were almost consistent for all regions each year and lower than average concentrations during winter, which indicates high effects of heating on PM2.5 levels of especially over the regions that count on burning coal as the main heating source. The measures that were taken by the government to reduce the usage of coal played an important role in improving air quality in recent years. Moreover, the COVID-19 lockdown had a positive effect on PM2.5 levels in the year 2020 due to decreased industrial activities and reduced transportation emissions [31]. The concentrations of PM2.5 in 2020 were less than 20 μg/m3 in all regions except the Moravian-Silesian Region during winter months. The yearly average PM2.5 concentrations calculated over CZ during 2018–2020 in this study align well with our previous findings [31], this serves as validation for the reliability of the dataset we generated using open PM2.5 data for conducting air quality studies throughout Europe. Even though the western part of the country had low concentrations of PM2.5, we recommend augmenting the number of ground monitors in this part to establish a more extensive network that can be utilized for subsequent analysis. We strongly encourage the ongoing reduction of coal usage for local heating, acknowledging the progress that has already been made in this regard. Besides using green energy especially in the eastern part of the country where the highest concentrations were found.

CONCLUSION

In this study, we estimated daily PM2.5 concentration over the Czech Republic with a high spatial resolution of 1 km throughout 2018-2020. A comprehensive data analysis was applied to tune and generalize the spatiotemporal PM2.5 predictive model. The model achieved high accuracy in estimating missing PM2.5 values with R2 of 0.85, RMSE of 5.42 μg/m3, MAE of 3.41 μg/m3, and bias of -0.03 μg/m3. Leveraging machine learning techniques and incorporating auxiliary data in model construction can enhance our comprehension of both the temporal and spatial fluctuations in PM2.5 concentrations. Based on our findings, the eastern part of the country suffered from the highest concentrations especially over Zlín and Moravian-Silesian Regions where the values for 2018 winter, reached risky average concentrations of 30 μg/m3 and 35 μg/m3 respectively. In contrast to 2018, PM2.5 levels dropped over the whole Czech Republic during the next two years reaching acceptable levels that are less than 20 μg/m3 in almost all regions during

the year 2020. The COVID-19 lockdown played a role in improving air quality due to reduced human activities. The generated dataset can be used to obtain a better understanding of the regional and seasonal PM2.5 concentrations throughout the study period.

FUNDING

This work is co-financed by the Grant Agency of the Czech Technical University in Prague, grant No. SGS23/050/OHK1/1T/11 and by the Grant Agreement Connecting Europe Facility (CEF) Telecom project 2018-EU-IA-0095 by the European Union.

ACKNOWLEDGEMENT

The authors sincerely thank the Czech Hydrometeorological Institute for providing PM2.5 observations, NASA EOSDIS for providing the daily MCD19A2 product that is available from the Land Processes Distributed Active Archive Centre (LPDAAC), the European Centre for Medium-Range Weather Forecasts (ECMWF) for providing global reanalysis of atmospheric composition, and the Japan Aerospace Exploration Agency (JAXA) for providing the digital surface model used in this study.

DATA AVAILABILITY

The datasets generated during and/or analyzed during the current study are available from the corresponding author on reasonable request.

REFERENCES

1. Martins NR, Carrilho da Graça G. Impact of PM2.5 in indoor urban environments: A review. Sustain Cities Soc. 2018;42. doi:10.1016/j.scs.2018.07.011
2. Baklanov A, Molina LT, Gauss M. Megacities, air quality and climate. Atmos Environ. 2016;126. doi:10.1016/j.atmosenv.2015.11.059
3. Pascal M, Falq G, Wagner V, et al. Short-term impacts of particulate matter (PM10, PM10-2.5, PM2.5) on mortality in nine French cities. Atmos Environ. 2014;95. doi:10.1016/j.atmosenv.2014.06.030
4. European Commission. Directive 2008/50/EC of the European Parliament and of the Council of 21 May 2008 on Ambient Air Quality and Cleaner Air for Europe (OJ L 152, 11.6.2008, Pp. 1-44).; 2008. https://environment.ec.europa.eu/topics/air/air-quality/eu-air-quality-standards_en
5. Tóthová D. Respiratory diseases in children and air pollution - The cost of - Illness assessment in Ostrava City. Cent Eur J Public Policy. 2020;14(1):43-56. doi:10.2478/CEJPP-2020-0003
6. Mikuška P, Křůmal K, Večeřa Z. Characterization of organic compounds in the PM2.5 aerosols in winter in an industrial urban area. Atmos Environ. 2015;105:97-108. doi:10.1016/J.ATMOSENV.2015.01.028
7. Sram RJ. Impact of Air Pollution on the Health of the Population in Parts of the Czech Republic. Int J Environ Res Public Heal 2020, Vol 17, Page 6454. 2020;17(18):6454. doi:10.3390/IJERPH17186454
8. Seibert R, Nikolova I, Volná V, Krejčí B, Hladký D. Air Pollution Sources' Contribution to PM2.5 Concentration in the Northeastern Part of the Czech Republic. Atmos 2020, Vol 11, Page 522. 2020;11(5):522. doi:10.3390/ATMOS11050522
9. Hůnová I. Erratum: Hůnová, I. Ambient Air Quality in the Czech Republic: Past and Present. Atmosphere 2020, 11, 214. Atmos 2021, Vol 12, Page 720. 2021;12(6):720. doi:10.3390/ATMOS12060720
10. Horák J, Hopan F, Šyc M, et al. Estimation of selected pollutant emissions from solid-fuel combustion in small heating appliances. Chem Sheets. 2011;105(11):851-855. Accessed June 11, 2023. http://www.chemicke-listy.cz/ojs3/index.php/chemicke-listy/article/view/1028
11. Hovorka J, Pokorná P, Hopke PK, Křůmal K, Mikuška P, Píšová M. Wood combustion, a dominant source of winter aerosol in residential district in proximity to a large automobile factory in Central Europe. Atmos Environ. 2015;113:98-107. doi:10.1016/J.ATMOSENV.2015.04.068
12. IEA. Czech Republic 2021 – Analysis - IEA. Published 2021. Accessed June 11, 2023. https://www.iea.org/reports/czech-republic-2021

13. Pavlíková I, Hladký D, Motyka O, Vergel KN, Strelkova LP, Shvetsova MS. Characterization of PM10 Sampled on the Top of a Former Mining Tower by the High-Volume Wind Direction-Dependent Sampler Using INNA. Atmos 2021, Vol 12, Page 29. 2020;12(1):29. doi:10.3390/ATMOS12010029
14. Lee HJ. Advancing Exposure Assessment of PM2.5 Using Satellite Remote Sensing: A Review. Asian J Atmos Environ. 2020;14(4). doi:10.5572/ajae.2020.14.4.319
15. Wang J, Christopher SA. Intercomparison between satellite-derived aerosol optical thickness and PM2.5 mass: Implications for air quality studies. Geophys Res Lett. 2003;30(21):2095. doi:10.1029/2003GL018174
16. Liu Y, Park RJ, Jacob DJ, et al. Mapping annual mean ground-level PM2.5 concentrations using Multiangle Imaging Spectroradiometer aerosol optical thickness over the contiguous United States. J Geophys Res Atmos. 2004;109(D22):1-10. doi:10.1029/2004JD005025
17. Liu B, Ma X, Ma Y, et al. The relationship between atmospheric boundary layer and temperature inversion layer and their aerosol capture capabilities. Atmos Res. 2022;271. doi:10.1016/j.atmosres.2022.106121
18. Li X, Feng YJ, Liang HY. The Impact of Meteorological Factors on PM2.5 Variations in Hong Kong. In: IOP Conference Series: Earth and Environmental Science. Vol 78. ; 2017. doi:10.1088/1755-1315/78/1/012003
19. Tobler WR. A Computer Movie Simulating Urban Growth in the Detroit Region. Econ Geogr. 1970;46:234. doi:10.2307/143141
20. Wang H, Chen Z, Zhang P. Spatial Autocorrelation and Temporal Convergence of PM2.5 Concentrations in Chinese Cities. Int J Environ Res Public Heal 2022, Vol 19, Page 13942. 2022;19(21):13942. doi:10.3390/IJERPH192113942
21. Zhang Y, Zhai S, Huang J, et al. Estimating high-resolution PM2.5 concentration in the Sichuan Basin using a random forest model with data-driven spatial autocorrelation terms. J Clean Prod. 2022;380:134890. doi:10.1016/J.JCLEPRO.2022.134890
22. Wang W, Zhao S, Jiao L, et al. Estimation of PM2.5 Concentrations in China Using a Spatial Back Propagation Neural Network. Sci Reports 2019 91. 2019;9(1):1-10. doi:10.1038/s41598-019-50177-1
23. Lyapustin A, Wang Y, Laszlo I, et al. Multiangle implementation of atmospheric correction (MAIAC): 2. Aerosol algorithm. J Geophys Res Atmos. 2011;116(3). doi:10.1029/2010JD014986
24. Inness A, Ades M, Agustí-Panareda A, et al. The CAMS reanalysis of atmospheric composition. Atmos Chem Phys. 2019;19(6). doi:10.5194/acp-19-3515-2019
25. Ibrahim S, Landa M, Pešek O, Pavelka K, Halounová L. Space-time machine learning models to analyze COVID-19 pandemic lockdown effects on aerosol optical depth over europe. Remote Sens. 2021;13(15). doi:10.3390/rs13153027
26. Muñoz-Sabater J, Dutra E, Agustí-Panareda A, et al. ERA5-Land: A state-of-the-art global reanalysis dataset for land applications. Earth Syst Sci Data. 2021;13(9). doi:10.5194/essd-13-4349-2021
27. Didan K. MOD13A3 MODIS/Terra vegetation Indices Monthly L3 Global 1km SIN Grid V006. NASA EOSDIS L Process DAAC. Published online 2015.
28. Tadono T, Ishida H, Oda F, Naito S, Minakawa K, Iwamoto H. Precise Global DEM Generation by ALOS PRISM. ISPRS Ann Photogramm Remote Sens Spat Inf Sci. 2014;II-4. doi:10.5194/isprsannals-ii-4-71-2014
29. Elvidge CD, Zhizhin M, Ghosh T, Hsu FC, Taneja J. Annual Time Series of Global VIIRS Nighttime Lights Derived from Monthly Averages: 2012 to 2019. Remote Sens 2021, Vol 13, Page 922. 2021;13(5):922. doi:10.3390/RS13050922
30. Geurts P, Ernst D, Wehenkel L. Extremely randomized trees. Mach Learn. 2006;63(1):3-42. doi:10.1007/s10994-006-6226-1
31. Ibrahim S, Landa M, Pešek O, Brodský L, Halounová L. Machine Learning-Based Approach Using Open Data to Estimate PM2.5 over Europe. Remote Sens 2022, Vol 14, Page 3392. 2022;14(14):3392. doi:10.3390/RS14143392
32. Moran PAP. Notes on Continuous Stochastic Phenomena. Biometrika. 1950;37(1/2):17. doi:10.2307/2332142
33. Anselin L. Local Indicators of Spatial Association—LISA. Geogr Anal. 1995;27(2):93-115. doi:10.1111/J.1538-4632.1995.TB00338.X
34. Zhang C, Luo L, Xu W, Ledwith V. Use of local Moran's I and GIS to identify pollution hotspots of Pb in urban soils of Galway, Ireland. Sci Total Environ. 2008;398(1-3):212-221. doi:10.1016/J.SCITOTENV.2008.03.011

35. Schneider R, Vicedo-Cabrera AM, Sera F, et al. A satellite-based spatio-temporal machine learning model to reconstruct daily PM2.5 concentrations across great britain. Remote Sens. 2020;12(22). doi:10.3390/rs12223803
36. Li T, Shen H, Zeng C, Yuan Q, Zhang L. Point-surface fusion of station measurements and satellite observations for mapping PM2.5 distribution in China: Methods and assessment. Atmos Environ. 2017;152. doi:10.1016/j.atmosenv.2017.01.004
37. Wei J, Huang W, Li Z, et al. Estimating 1-km-resolution PM2.5 concentrations across China using the space-time random forest approach. Remote Sens Environ. 2019;231. doi:10.1016/j.rse.2019.111221
38. Stafoggia M, Bellander T, Bucci S, et al. Estimation of daily PM10 and PM2.5 concentrations in Italy, 2013–2015, using a spatiotemporal land-use random-forest model. Environ Int. 2019;124:170-179. doi:10.1016/J.ENVINT.2019.01.016
39. Czernecki B, Marosz M, Jędruszkiewicz J. Assessment of Machine Learning Algorithms in Short-term Forecasting of PM10 and PM2.5 Concentrations in Selected Polish Agglomerations. Aerosol Air Qual Res. 2021;21(7):200586. doi:10.4209/AAQR.200586

CIVIL ENGINEERING JOURNAL

Article no. 28

THE CIVIL ENGINEERING JOURNAL 3-2023

EMPIRICAL VULNERABILITY ANALYSIS OF RAILWAY BRIDGE SEISMIC DAMAGE BASED ON 2022 MENYUAN EARTHQUAKE

Jing He and Yong Huang

Key Laboratory of Earthquake Engineering and Engineering Vibration, Institute of Engineering Mechanics, China Earthquake Administration, Key Laboratory of Earthquake Disaster Mitigation, Ministry of Emergency Management, Harbin 150080, China；huangyong@iem.ac.cn

ABSTRACT

A 6.9 magnitude earthquake at a depth of 10 km struck Menyuan County, Haibei Prefecture, Qinghai Province, China, on January 8, 2022. This earthquake damaged some railway bridges on the Lanzhou-Xinjiang Passenger Dedicated Line. This study combines relevant historical earthquake damage experience, considers the effects of earthquake intensity, site soil classification, superstructure type, foundation failure factor, number of spans, and total bridge length, and develops empirical formulas for seismic damage prediction of railway bridges using ordinal logistic regression model in SPSS software. Since the accuracy of both predictions for seismic damage is practically the same, using this regression to predict seismic damage to railway bridges is considered valid. The predicated seismic damage matrix, as were the anticipated multi-intensity mean damage index and the empirical vulnerability curve based on the two-parameter lognormal distribution function, were generated on this basis. We get a risk assessment of future seismic damage for regional bridges when they experience different intensities or peak ground acceleration. According to the conclusions, although the suggested particular equations and vulnerability curves do not apply to the remainder of the region owing to geographical uniqueness, the technical approach is valid. It may be used as a reference for seismic damage prediction and vulnerability evaluation in other regions. The earthquake damage prediction matrix derived from the regression analysis can provide reasonable and fast forecasts before the next earthquake.

KEYWORDS

Railway bridges, Empirical vulnerability, Seismic damage prediction, Ordinal logistic regression

INTRODUCTION

As a lifeline project, it is necessary to strengthen and improve the seismic capacity of bridges before earthquakes and to enable them to meet the needs of traffic and emergency resource deployment after earthquakes during their service phase. The seismic damage prediction and vulnerability study of railway bridges in the region is an effective and realistic technique to achieve these criteria. The predicted damage and vulnerability curves allow for a general estimation of which bridges in the region require targeted strengthening to improve seismic capacity. Bridge damage prediction methods are classified into four types: Empirical Statistical Methods, Code Calibration Methods, Pushover, and Integrated Qualitative and Quantitative Evaluation Approaches for big-span bridges. The empirical-statistical method is a seismic safety evaluation method that selects the main factors affecting bridge damage based on historical seismic experience, bridge seismic knowledge, and information provided by bridge samples and then performs statistical regression of the influence mode and weights of each influencing factor based on a large number of samples to establish an empirical bridge damage prediction formula [1].

In 1956, Keisaburo Kubo [2] defined the vulnerability index and counted thirty highway bridges based on ten influencing parameters, such as seismic intensity, site characteristics, and liquefaction. In 1986, Japan [1] proposed an updated method for vulnerability analysis of highway bridges by analyzing 124 earthquake-damaged bridges, considering 15 influencing factors such as design codes, superstructure type, and bridge axis slope, and using an empirical formula obtained by statistical methods. In 1994, Zhu Meizhen [3] developed an empirical formula for predicting nonlinear seismic damage to highway bridges based on the seismic damage of more than 100 bridges in China's Tangshan, Haicheng, and Tonghai earthquakes using statistical methods. In 1994, Wang Tianwei [4] published an empirical method for forecasting earthquake damage to railway bridges using linear regression analysis and the principle of least squares to construct a prediction formula. In 2003, Longjun Xu [5] provided a straightforward approach to forecast earthquake damage for railway bridges and illustrated the cumulative damage probability curves of railway bridges under various earthquake intensities. In 2013, Yang Fan [6] proposed a hierarchical weighted synthesis method based on the hierarchical analysis method applicable to assessing earthquake damage to railway bridges. In 2021, Y.J. Xu et al. [7] proposed a real-time regional seismic damage assessment framework based on Long Short-Term Memory neural network architecture. In 2022, Li WS et al. [8] established a probabilistic seismic demand model for a typical regular continuous-girder bridge and provided suggestions for seismic damage prediction and seismic insurance risk evaluation. Although railway and highway bridges' seismic damage phenomena differ, the forecast methodologies are identical. These approaches give a theoretical foundation for employing regression analysis to anticipate earthquakes. Still, they are no longer relevant to today's railway bridges due to changes in building technology and seismic design.

Currently, there are three broad groups of systems for quick seismic damage assessment assumptions based on historical earthquake damage data, information from earthquake intensity records, and fundamental structural features of bridges. The first one is the system formed by the seismic damage presumption process for highway bridges proposed by Kuan Kobayashi et al. [9], which has been widely used in Japan [10] and modified after the Kumamoto earthquake [11]. The second one is Murano Gallon et al. [12] proposed a software system [13] for forming a presumptive design chart for seismic damage with the ratio of the predominant period of ground motion to the intrinsic period of the structure as the horizontal coordinate and the ratio of the maximum acceleration of ground motion to the yield seismicity of the structure as the vertical coordinate, which has been used in the Japanese railway sector. The third one is the vulnerability curve approach, represented by the HAZUS earthquake damage assessment system in the United States [14]. These approaches, however, need a large and diverse sample of seismic data, and are computationally demanding. Among these three methods, the design codes of Chinese and Japanese bridges differ, so the seismic factors differ, and their evaluation systems cannot be used. In the Menyuan earthquake, the lack of specific ground motion data at the bridge site made it challenging to get the predominant period quickly. The HAZUS evaluation system used in the United States collects seismic hazard data of bridges in the United States, and the geological conditions and construction methods at the bridge site are so different that it does not apply to China.

This work aims to apply ordinal logistic regression to forecast seismic damage on the northeast edge of Qinghai, derive empirical vulnerability curves, and validate the method's broad applicability.

THEORETICAL FOUNDATION

The analysis data of vulnerability that can be obtained is of utmost importance, and the methods used are subject to specific restrictions depending on the data information. The prediction of bridge damage has seismic uncertainty, structural insecurity, and regional character. Bridge vulnerability is the probability distribution of all limit states, and the degree of seismic damage to bridge structures is defined in terms of a number of limit states using probability distribution theory. This assessment is frequently based on ground shaking parameters or macroscopic fuzzy physical

quantities, takes structural strength stochasticity into account, and uses arbitrary resistance or limit state strength assessment of bridge structures [15].

While the seismic vulnerability of bridge structures is an important component of the probabilistic theory of seismic hazard analysis, which can effectively quantify a reasonable estimate of the seismic capacity of bridge structures, the northeastern edge of the Qinghai-Tibet Plateau is seismically prone. It has significant railways and infrastructure passing through it. As a result, it is important to study the risk assessment of railway bridges in this region. The seismic hazard matrix for the area can be obtained using the empirical equation for earthquake hazard prediction, and the vulnerability curve can be fitted using the seismic hazard matrix. Though Menyuan has experienced numerous earthquakes throughout its history, only the 6.9 in 2022 caused serious seismic damage to the railway system. The seismic vulnerability analysis of a few railway bridges on the Lanzhou-Xinjiang Passenger Dedicated Line for the magnitude 6.9 Menyuan earthquake in 2022 is significant for the future seismic risk assessment of the railway system in the northeastern margin of the Qinghai-Tibet Plateau due to the regional nature of seismic vulnerability assessment. Meanwhile, while high-speed railway bridge bearings were damaged by the Luzhou earthquake in 2021, the seismic damage of the Lanzhou-Xinjiang Passenger Dedicated Line bridge caused by the Menyuan earthquake was the first time that a high-speed railway bridge on China's mainland was subjected to a real earthquake assessment. The analysis of its seismic damage pattern characteristics is critical for the seismic design of future high-speed railway bridges.

This paper considers the effects of seismic intensity, site soil classification, superstructure type, foundation failure coefficient, number of spans, and total bridge length on bridge damage. The ordinal logistic regression model is used. The specific technical route is first establishing the empirical formula for predicting the earthquake damage to railway bridges, getting the damage matrix, and drawing the empirical vulnerability curve to achieve the empirical vulnerability analysis of the earthquake damage to railway bridges in the Menyuan earthquake. The technical flowchart is shown in Figure 1.

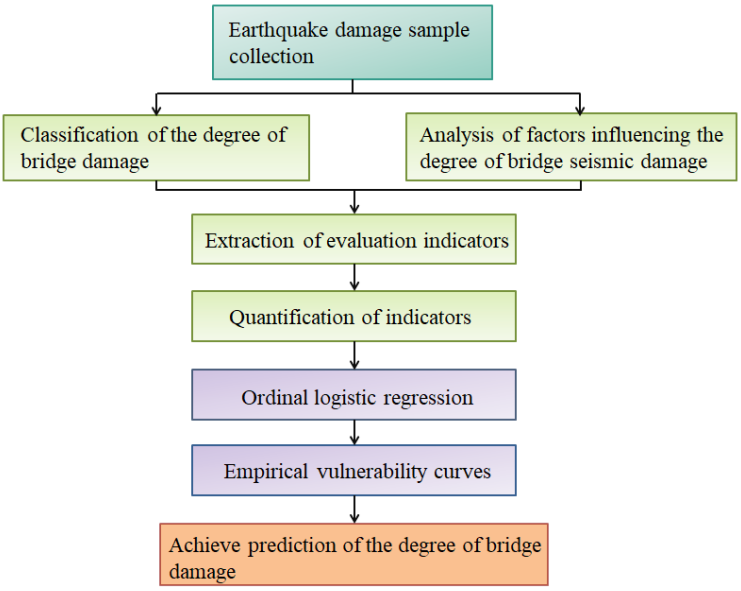

Fig.1 – Technical flowchart

RAILWAY BRIDGE SEISMIC DAMAGE

On January 8, 2022, a 6.9 magnitude earthquake occurred in Menyuan County, Haibei Prefecture, Qinghai Province, China, with a depth of 10 km. The left-slip type earthquake occurred in the Lenglongling fault zone with a maximum intensity of IX degrees. In the IX degree zone, the girders were significantly displaced and slanted, the tracks were severely twisted and partially

broken, fractures formed on the road surface in several places, fissures and misalignments in the bedrock were evident, and the mountain fell. The severe earthquake damage to the bridges was mostly exhibited as lateral sliding of the major girders, damage to the bearings and retaining blocks, track system distortion, and tilting of the electric poles. Other bridges on the Lanzhou-Xin Passenger have earthquake damage, including pier fractures, bearing anchorages sliding off, and rail sleeper concrete cracking. The Liu Huanggou Bridge, for example, was the first true bridge of seismic damage in China's high-speed railway [16]. Figure 2 depicts typical railway bridge seismic damage.

(a)Sleeper crack

(b) Bearing damaged

(c) Pier cracked

(d) Girder large horizontal displacement

Fig.2 –Typical railway bridge seismic damage

Extraction and quantification of evaluation indicators

The seismic damage of railway bridges was divided into five degrees [3, 4] based on the collected seismic samples and associated experiences, as indicated in Table 1.

Tab. 1 - The defines of the degree of earthquake damage

degree of seismic damage	destruction phenomenon
Collapsed (D)	The bridge cannot be used.
Severely Damaged (C)	The main load-bearing structure is severely damaged and needs significant repair or reconstruction.
Moderately Damaged (B)	The main load-bearing structures suffer damage or local damage.
Slightly Damaged (A)	Non-load-bearing structures suffer damage.
No Damaged (A0)	No seismic damage.

The railway bridge damage sample was drawn from 135 railway bridges in the Menyuan earthquake area, which included 111 simply supported girder bridges, 23 continuous girder bridges and continuous rigid frame bridges, and one girder-arch combination bridge. According to the earthquake damage assessment in Table 1, there were no collapsed bridges, one severely damaged

bridge, seven moderately damaged bridges, four slightly damaged bridges, and 123 generally undamaged bridges, as indicated in Figure 3.

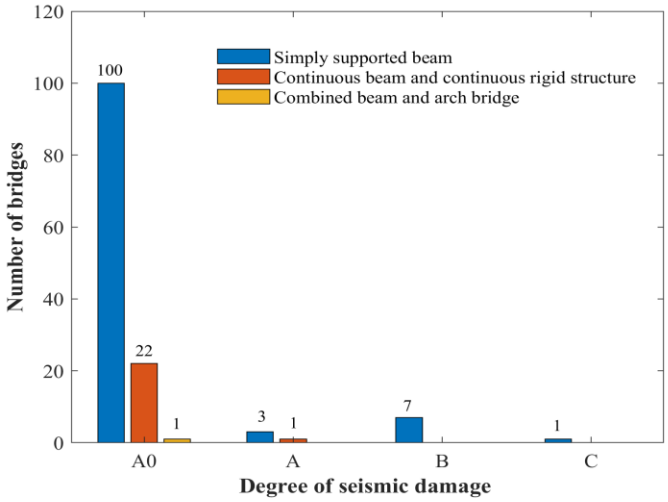

Fig. 3 – Earthquake damage statistics of railway bridges in Menyuan earthquake

Meizhen Zhu [3] believed that the coefficient values of each element are derived from mathematical statistics and offered the recommended coefficient values of the main influencing factors for highway bridges. Tianwei Wang [4] presented different coefficients for qualitative and quantitative factors for seismic damage prediction of railway bridges, and the connection between the coefficients is consistent with the general principles of seismic engineering. Based on the collected bridge seismic data and the relevant historical seismic experience, the following six factors are listed as the main factors affecting bridge seismic damage, as shown in Table 2.

Tab. 2 - Statistical value of impact coefficient of earthquake damage

No.	Main influencing factors	Categories	Statistical coefficient
1	Intensity	Ⅵ	1.0
		Ⅶ	1.1
		Ⅷ	1.2
		Ⅸ	1.3
		Ⅹ	1.4
		Ⅺ	1.5
2	Superstructure	girder-arch combination bridge	1.0
		continuous girder bridges and continuous rigid frame bridge	1.1
		simply supported girder bridge	1.4
3	Site soil classification	1	1.0
		2	1.1
		3	1.2
		4	1.3
4	Foundation failure	none	1.0
		slight	1.2
		heavy	1.6
5	Number of hole spans	=1	1.0
		1~6	1.1
		6<	1.2
6	Total length of bridge	<200m	1.0
		>200m	1.2

We discovered that the region's bridges have enormous spans during the statistical process. The overall length of bridges may approach 5200m, with varied superstructure shapes and site types, and the real seismic damage is dispersed in various intensity zones. These are connected to the bridges' location on the Qinghai-Tibet Plateau, which has a high concentration of permafrost, varied seismic protection for bridges, and various bridge spans owing to topography and geomorphological variations. As a result, this seismic damage index's division is irrelevant to the remainder of the plain area. It should be changed based on regional topography and bridge structural features.

THE ORDINAL LOGISTIC REGRESSION MODEL

In order to represent the connection between the degree of bridge damage and its numerous influencing factors, this study on bridge damage prediction seeks a model of functional relationship class, describing this relationship either qualitatively or quantitatively. Regression analysis is a mathematical technique used to determine the law of interrelationship between dependent and independent variables from a large amount of data, as well as to perform factor analysis and determine the degree of prediction and influence by one or more variables on the value of the dependent variable. To analyze the factors influencing the degree of bridge damage and understand the law of bridge damage, an ordinal logistic regression model is established in this paper using each factor affecting bridge damage as the independent variable and the degree of individual bridge damage as the dependent variable. The projected outcomes are also contrasted with the actual harm to confirm that the regression model is accurate.

The logistic model belongs to nonlinear regression analysis, and its study is mainly aimed at a multiple regression method between the results of dichotomous or multi-categorical variables of the dependent variable and certain influencing factors. This study employs ordinal logistic regression since the different seismic levels are the dependent variable.

Let there be k classifications of the dependent variable and the probabilities of each classification denoted as P1, P2... Pk, the following k-1 logistic regression equations can be fitted to the n independent variables [17]:

$$P_1 = \frac{\exp(\alpha_1+\beta_1X_1+\beta_2X_2+\cdots+\beta_nX_n)}{1+\exp(\alpha_1+\beta_1X_1+\beta_2X_2+\cdots+\beta_nX_n)} \quad (1)$$

$$P_2 = \frac{\exp(\alpha_2+\beta_1X_1+\beta_2X_2+\cdots+\beta_nX_n)}{1+\exp(\alpha_2+\beta_1X_1+\beta_2X_2+\cdots+\beta_nX_n)} - P_1; \quad (2)$$

…

$$P_{k-1} = \frac{\exp(\alpha_{k-1}+\beta_1X_1+\beta_2X_2+\cdots+\beta_nX_n)}{1+\exp(\alpha_{k-1}+\beta_1X_1+\beta_2X_2+\cdots+\beta_nX_n)} - P_1 - P_2 \ldots - P_{k-2}; \quad (3)$$

The kth class is used as the reference class. Where: α1, α2... α k-1 are the constant terms of the regression equation; Xi (i=1, 2... n) is the influence factor; βi represents the regression coefficient.

Model building and results

This study employed the parameters affecting seismic intensity, site soil classification, superstructure type, foundation failure factor, number of spans, and overall bridge length as independent variables. The dependent variable was the seismic damage index of railway bridges. The data were imported into the statistical analysis program SPSS [18], and multiple logistic regression analysis was carried out with the help of the equation above to produce the regression model and coefficients for predicting the degree of bridge seismic damage, which are displayed in Table 3. As shown in Table 3, only these three components pass the significance test because their p-values for the intensity coefficient, site coefficient, and foundation failure coefficient are all less than 0.05.

Tab. 3 - Regression coefficients of each variable in Logistic regression

Model		Coefficient	Std. Error	Wald χ2	Significance P-value
Threshold	[A0]	181.820	89.872	4.093	0.043
	[A]	189.465	93.545	4.102	0.043
	[C]	190.480	93.694	4.133	0.042
Independent variables	1(Intensity)	89.939	42.416	4.496	0.034
	2(Superstructure)	28.250	23.263	1.475	0.225
	3(Site)	-108.005	47.073	5.264	0.022
	4(Foundation failure)	113.793	55.937	4.138	0.042
	5(Span)	88.912	58.658	2.298	0.130
	6(Bridge length)	-56.794	46.791	1.473	0.225

Model Testing

The goodness-of-fit test shows that the significance p-values for both Pearson and Deviation tests are greater than 0.1, as shown in Table 4, and the model is considered to fit relatively well.

Tab. 4 - goodness-of-fit of Logistic regression

Model	Chi-Square	Degree of freedom	Significance P-value
Pearson	4.717	69	1.000
Deviation	5.239	69	1.000

The parallelism hypothesis test determines if the effect of each independent variable value level on the dependent variable is the same in each regression equation. Because the parallelism test's initial premise is that the model fulfils parallelism, if the P-value is larger than 0.05, the model accepts the original hypothesis, i.e., it passes the parallelism test. In contrast, if the P-value is less than 0.05, the model rejects the initial hypothesis and fails the parallelism test. As shown in Table 5, the findings reveal that P=1.0>0.1, which is compatible with proportionate dominance, i.e., the individual regression equations of the models are parallel.

Tab. 5 - Logistic regression parallel line test

Model	-2*Log Likelihood	Chi-Square	Degree of freedom	Significance P-value
Original hypothesis	0.000	-	-	-
Conventional	0.000	0.000	12	1.000

The model fit information test determines if the partial regression coefficients of all independent variables in the model are valid, as given in Table 6, with P<0.05 in the findings indicating that the model is valid.

Tab. 6 - Fitting information of Logistic regression mode

Model	-2*Log Likelihood	Chi-Square	Degree of freedom	Significance P-value
Intercept Only	99.075	-	-	-
Final	0.000	99.075	6	0.000

The anticipated values were compared to the actual statistical values, and the results are displayed in Table 7. The predicted earthquake damage rates are identical to the actual earthquake damage rates. The ordered logistic regression model has high discriminative performance and can forecast the bridge damage level more accurately.

Tab. 7 - Comparison of Logistic regression predicted earthquake damage rate and actual earthquake damage rate

Seismic damage	A0	A	B	C
Actual/%	91.11	2.96	5.19	0.74
Prediction/%	91.11	2.22	6.67	0
Error/%	0	25	27	100

Example

Since the accuracy of both predictions for seismic damage is practically the same, using this regression to predict seismic damage to railway bridges is considered valid. Ordinal logistic regression can predict each bridge damage stage at a given intensity, and some of the findings are displayed in Table 8.

For example, the probability of A0 for bridge No. 69 is 0, the probability of A is 0.09, the probability of B is 0.79, and the probability of C is 0.12. As a result, the anticipated category is "B," indicating the greatest likelihood of injury.

Although the ordered logistic regression effectively predicts bridge seismic damage, some errors exist, such as bridge No. 67 in Table 8. The predicted object often cannot be entirely consistent with the background information of the bridge at the time of statistics, and sometimes even significant differences, which will affect the prediction accuracy to a certain extent [3]. In addition, some secondary factors will lead to a specific error in predicting seismic damage to bridges. However, this error will not make the seismic damage level show a significant difference, which can only be a difference of one neighbouring level.

Tab. 8 - Schematic table of ordered logistic regression calculation (part)

Bridge No.	Influence factor coefficient						Real		A0	A	B	C	Prediction
	1	2	3	4	5	6							
	……												
67	1.2	1.4	1.0	1.0	1.2	1.2	A		0.00	0.09	0.79	0.12	B
68	1.2	1.4	1.2	1.2	1.2	1.2	B		0.00	0.03	0.92	0.05	B
69	1.2	1.4	1.0	1.0	1.2	1.2	B		0.00	0.09	0.79	0.12	B
	……												
73	1.2	1.4	1.0	1.0	1.0	1.0	A		0.03	0.96	0.01	0.01	A
74	1.2	1.4	1.0	1.0	1.1	1.0	B		0.00	0.01	0.98	0.01	B
75	1.2	1.4	1.0	1.0	1.1	1.0	B		0.00	0.01	0.98	0.01	B
	……												

BRIDGE SEISMIC EMPIRICAL VULNERABILITY

Railway bridge seismic vulnerability can be expressed by vulnerability curves that reflect the conditional likelihood of the structural reaction surpassing the structural load-bearing capacity defined by the damage phase under varying intensities of seismic action. Empirical and analytical approaches can be used to calculate bridge vulnerability curves. The vulnerability curves obtained through empirical methods are generally based on damage reports from previous earthquakes [19].

The damage probability matrices of various types of bridges were calculated through statistical regression after collecting damage data from regions where earthquakes have occurred. These matrices are then used as the foundation for the empirical vulnerability curve. Yamazaki et al. proposed an empirical vulnerability model and used the least squares regression method to obtain the log-normal distribution parameters; Tanaka used a two-parameter normally distributed vulnerability function [20].

Bridges in different intensity zones will present different degrees of damage, and it is difficult to judge their vulnerability to earthquake damage in the region by only analyzing their damage at a particular intensity. This paper presents the prediction statistics of bridge structures in different intensity zones and establishes a damage prediction matrix based on multiple intensity zones, as shown in Table 9. The actual seismic damage in this Menyuan earthquake is shown in parentheses.

Tab. 9 - Seismic predicated matrix of railway bridges %

Intensity / Damage	Ⅵ	Ⅶ	Ⅷ	Ⅸ	Ⅹ	Ⅺ
A0	100(100)	82.22(100)	0(8.34)	0(0)	0(0)	0(0)
A	0(0)	17.78(0)	91.85(33.33)	3.70(0)	0(0)	0(0)
B	0(0)	0(0)	8.15(58.33)	88.15(0)	3.70(0)	0(0)
C	0(0)	0(0)	0(0)	8.15(100)	96.30(0)	91.85(0)
D	0(0)	0(0)	0(0)	0(0)	0(0)	8.15(0)

The outcomes of the forecast demonstrate that the bridge damage's severity increases with the earthquake's magnitude. In the earthquake intensity zone of magnitude VI, all railway bridges exhibited basic intactness; in the earthquake intensity zone of magnitude VII, 17.78% of the bridges suffered minor damage; in the earthquake intensity zone of magnitude VIII, virtually no bridges were intact and showed minor and moderate damage; in the earthquake intensity zone of magnitude IX, 88.15% fewer bridges were slightly damaged; 80% more moderate damage; and 8.15% more severely damaged bridges; in the earthquake intensity zone of magnitude X, bridges essentially occurred Bridges in the X degree zone sustained 96.30% major damage, but there was no destruction; in the XI degree zone, 8.15% of bridges were destroyed.

Average seismic damage model for multi-intensity areas

The damage to the bridge at each seismic level was calculated as shown in Table 9, with the corresponding damage indices within the different levels, as shown in Table 10, to analyze the overall damage of the bridge at different intensities. A weighted average was then performed to obtain the parameter known as the mean damage index (MSDI) % [21], as shown in equation (4):

$$[\mathrm{MSDI}] = \sum_{i=1}^{5} d_i \, \delta_i \quad (4)$$

Where:$[\mathrm{MSDI}]$ represents the average damage index of railway bridges in the region；$\mathrm{d_i}$ represents the normalization of the damage index to obtain a continuous value between 0 and 1, representing the damage degree of the structure from intact to destroyed；δ_i damage level is the damage ratio of the bridge structure for i(i=1,2,3,4,5).

Tab. 10 - Earthquake damage index of different grades

Damage / Value	A0	A	B	C	D
highest value（h）	0	1.6	2.4	3	4
mean value（m）	0.8	2	2.7	3.5	4.5
lowest value（l）	1.6	2.4	3	4	5

Equation (4) is matrixed with the existing seismic vulnerability matrix in order to obtain the damage of bridge structures in various intensity zones. Equations (5) through (7) then build a vulnerability matrix model based on the average seismic damage index.

$$[\mathrm{MSDI}]\alpha = [d_i]^T \left[\delta_{ji}\right] \quad (5)$$

$$[\mathrm{MSDI}]\alpha = \begin{bmatrix} d_1 \\ d_2 \\ \vdots \\ d_i \end{bmatrix}^T \begin{bmatrix} \delta_{61} & \cdots & \delta_{6i} \\ \vdots & \cdots & \vdots \\ \delta_{j1} & \cdots & \delta_{ji} \end{bmatrix} \quad (6) \qquad [\mathrm{MSDI}]\alpha = \begin{bmatrix} \mathrm{MSDI}_6 \\ \mathrm{MSDI}_7 \\ \mathrm{MSDI}_8 \\ \vdots \\ \vdots \\ \mathrm{MSDI}_j \end{bmatrix} \quad (7)$$

Where δ_{ji} denotes the damage ratio (number of damage ratio) of the structure subjected to the ith seismic damage level in the j (j=6, 7, 8, 9, 10, 11) intensity zone, $[\mathrm{MSDI}]\alpha$ indicates the average seismic damage index limit，α indicates h、m、l.

The average seismic damage index matrix of the bridges in the region is obtained as shown in equations (8) - (10):

$$[\mathrm{MSDI}]\mathrm{S_h} = \begin{bmatrix} 0 \\ 5.69 \\ 33.30 \\ 48.39 \\ 59.56 \\ 61.63 \end{bmatrix} \quad (8) \quad [\mathrm{MSDI}]\mathrm{S_m} = \begin{bmatrix} 16.00 \\ 20.27 \\ 41.14 \\ 54.79 \\ 69.41 \\ 71.63 \end{bmatrix} \quad (9) \quad [\mathrm{MSDI}]\mathrm{S_l} = \begin{bmatrix} 32.00 \\ 34.84 \\ 48.98 \\ 61.19 \\ 79.26 \\ 81.63 \end{bmatrix} \quad (10)$$

Figure 4 depicts the vulnerability curve of the average seismic damage of bridges for multi-intensity areas. When the region suffered an earthquake of magnitude VII, the probability of bridge damage was 33% at the highest value, 19% at the mean value, and 4% at the lowest value. The predicted vulnerability curve of bridges under MSDI parameters can predict the minimum to maximum level of bridge seismic damage at different intensities. This is a very conservative approach.

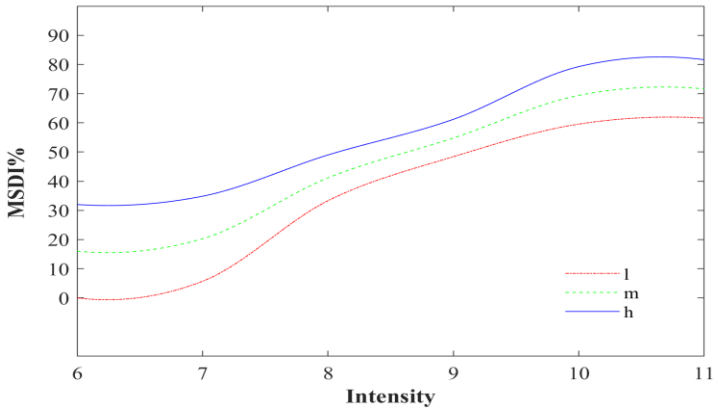

Fig. 4 –Predicted vulnerability curve of bridges under MSDI parameters

Vulnerability curves based on two-parameter log-normal distribution functions

Each seismic damage class was assigned its own vulnerability curve. To guarantee precise prediction, C and D were classed as the same class in this earthquake due to the lack of damage in the destroyed condition.

Assuming a two-parameter log-normal distribution for the vulnerability curve:

$$F_j(\mathrm{a}, c_j, \zeta_j) = \Phi\left[\frac{\ln(a/\theta_j)}{\zeta_j}\right] \quad (11)$$

where $\mathrm{F_j}(\mathrm{a}, \theta_\mathrm{j}, \zeta_\mathrm{j})$denotes the probability that the bridge reaches or exceeds the jth damage state; $\Phi(\cdot)$is the standard normal distribution function; a is the PGA value; θ_j and ζ_j are the median and

logarithmic standard deviation of the damage state corresponding to the vulnerability curve (j=1, 2, and 3 denote "A", "B", "C、D", respectively).

From the China Intensity Table [22], the relationship between intensity and PGA is shown in Table 11.

Tab. 11 - Correlation between intensity and PGA

Intensity	Ⅵ	Ⅶ	Ⅷ	Ⅸ	Ⅹ	Ⅺ
PGA(m/s2)	0.63	1.25	2.50	5.00	10.00	20.00
PGA(g)	0.064	0.128	0.255	0.510	1.020	2.041

With the seismic damage ratio matrix in Table 9, the corresponding transcendence probabilities can be obtained from equation (12) as shown in Table 12.

$$F_j(I_i) = \sum_{k=1}^{j} P_k\,(I_i) \tag{12}$$

Where, $P_j(I_i)$ indicates the probability of being in the jth damage state under intensity i, that is, the damage ratio of being in the jth damage state under intensity i.

Tab. 12 - Exceedance probability F of bridges with different earthquake damage grades

Damage / PGA(g)	A0	A	B	C、D
0.064	1	0	0	0
0.128	1	0.1778	0	0
0.255	1	1	0.0815	0
0.510	1	1	0.963	0.0815
1.020	1	1	1	0.963
2.041	1	1	1	1

The vulnerability curves corresponding to the damage states "A", "B", "C、D" obtained by using the cumulative function of the lognormal distribution is shown in Figure 5. When the PGA in the region is 0.5g, bridges are largely destroyed, more than 95% of the bridges are slightly damaged and 70% suffer moderate and severe damage. In addition, from this curve, we can know the possible magnitude of PGA in the region when 20% of the bridges exceed some damage state.

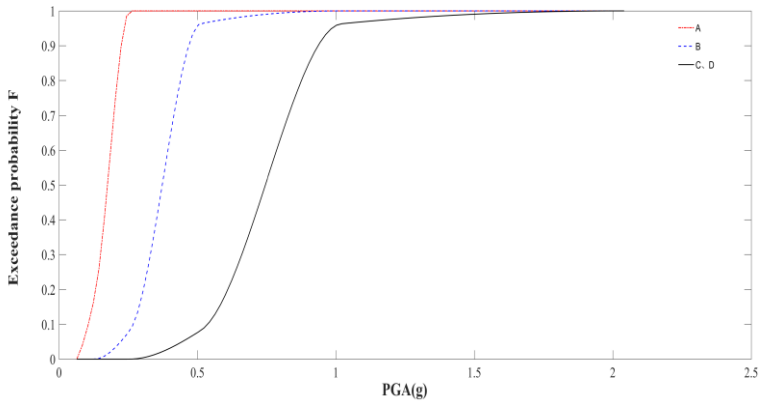

Fig.5 –Predicted vulnerability curve based on a two-parameter log-normal distribution function

CONCLUSION

This study presents a seismic damage prediction formula based on ordinal logistic regression in SPSS. The method can predict the damage index of a single bridge and its likelihood of occurring in different damage states. On the base, the predicated empirical vulnerability curve may be used to quickly analyze the total damage of bridges in the region at various intensities and damage states.

The predicted vulnerability curve of bridges under MSDI parameters is a very conservative approach that can know the minimum to the maximum level of bridge seismic damage at different intensities. The predicted vulnerability curve based on a two-parameter log-normal distribution function can visualize the probability of damage for various seismic damage states of the bridge when the PGA is what and the possible PGA in the region when the bridge is damaged to a certain extent. Moreover, this method can serve as a reference for analyzing the risk assessment of railway bridges in the region and give some foundation for later prediction of bridge damage in the region with some reliability to make realistic forecasts before the next earthquake. It is important to note that the regression equation proposed in this paper does not apply to other regions because the defined damage index is based on a summary of the damaged bridges in the 2022 Menyuan earthquake, and the topography and climate of bridges in different regions vary greatly, as do their site classification and traditional structure types. The Lanzhou-Xinjiang Passenger Dedicated Line is located in the Qinghai-Tibet Plateau, with permafrost zones, a cold temperature, and more mountains, so there are some differences in the seismic design of bridges. As a result, when an earthquake happens, the seismic damage displayed is inconsistent. However, this work's technical line of study gives some pointers for other places to use when assessing vulnerability and risk. The findings of this study have substantial significance for the seismic risk assessment of bridges on Qinghai's northeastern border.

ACKNOWLEDGEMENTS

Supported by: Scientific Research Fund of Institute of Engineering Mechanics, China Earthquake Administration (Grant No. 2021EEEVL3013)

REFERENCES

[1] Wang DS, Feng QM. Prediction Method of Bridge Earthquake Damage [J]. Journal of Natural Disasters, 2001(03): 113-118.

[2] Keizaburo Kubo, Zhang SS. Earthquake Damage Prediction of Bridges [J]. World Earthquake Engineering, 1984(05): 8-11.

[3] Zhu MZ. Practical Methods of Earthquake Damage Prediction for Highway Bridges [J]. Journal of Tongji University (Natural Science Edition), 1994(03): 279-283.

[4] Wang TW, Yang CH. Earthquake Damage Prediction and Seismic Reinforcement of Railway Bridges [J]. Railway Construction, 1991(08): 4-9.

[5] L. J. Xu, Q. Zhang. Prediction of earthquake damage of railway bridges [J]. Journal of Shandong College of Construction Engineering, 2003(01): 27-31.

[6] F. Yang, M. B. Su. Techniques for earthquake damage assessment of railway bridges [J]. Journal of Natural Hazards, 2013(03): 213-220.

[7] Y. J. Xu et al.. Real-time regional seismic damage assessment framework based on long short-term memory neural network [J]. Computer-Aided Civil and Infrastructure Engineering, 36(4) (2021)504-521.

[8] W. S. Li, Y. Huang, Z. K. Xie. Machine Learning-Based Probabilistic Seismic Demand Model of Continuous Girder Bridges [J]. Advances in Civil Engineering, (2022).

[9] Kobayashi HIROSHI, etc. The method of deducing the degree of disaster of the road and bridge in Okeo during the great earthquake [J]. Technical Information on Civil Engineering, 2005, 47(12): 48-53.

[10] Kazuhiro NAGAYA, Shojiro KATAOKA, Takaaki KUSAKABE, etc. A Research on Immediate Damage Estimation Technology to Improve Crisis Management for MEGA-Earthquakes [J]. Journal of Japan Society of Civil Engineers, Ser. A1 (Structural Engineering & Earthquake Engineering), 2017, 72(4): 966-974.

[11] Omichi KAZUHO, Shojiro KATAOKA, etc. Verification and Improvement of Structure Damage Estimation Method for Highway Bridges Based on Damage Data of the 2016 Kumamoto Earthquake [J]. Journal of Japan Society of Civil Engineers, Ser. A1 (Structural Engineering & Earthquake Engineering), 2020, 76(4): 765- 773.

[12] Murano YOSHITAKA, NOGAMI YUTA, MIYAMOTO TAKEFUMI. Simple Method to Predict Outline of Seismic Damages of Railway Structures and Running Vehicles [J]. Journal of Japan Society of Civil Engineers, Ser. A, 2010, 66(3): 535-546.
[13] Naoto Iwata, Tojun Sakai, Tojun Yamamoto, etc. Earthquake Countermeasures for Railway Stations in Railway Systems Development of a Railway Earthquake Damage Estimation Information Distribution System for Quick Resumption of Operations [J]. Railway Architecture News, 2020, 77(2): 30-33.
[14] Zong L, Wang YQ, Yang SN et al. Research on Earthquake Damage Assessment Model of Highway and Bridge in China Based on HAZUS Platform [J]. Journal of Civil Engineering, 2014, 47(S1):263-268.
[15] Hu Y. Earthquake Engineering [M]. Beijing: Seismological Press, 2006:354-400.
[16] Cai LW, HUANG Yong, HE Jing et al. Transportation System Damage from the 2022 M6.9 Menyuan Earthquake in Qinghai Province and its implications[J]. Earthquake Engineering and Engineering Vibration, 2022. 42(04): 8-16.
[17] Gao WD. Discrimination and Classification of Expansive Soil Based on Logistic Regression Model [J]. Journal of Yangtze River Scientific Research Institute, 2020. 37(06): 153-155.
[18] Wang DH et al. Multivariate Statistical Analysis and SPSS Application [M]. Shanghai: East China University of Science and Technology Press Co., LTD, 2018:150-220.
[19] H. Hwang, Liu JB. Vulnerability Analysis of Reinforced Concrete Bridge Structures under Earthquake [J]. Journal of Civil Engineering, 2004(06): 47-51.
[20] Chen LB, Zhen KF et al. Vulnerability Analysis of Bridges in Wenchuan Earthquake [J]. Journal of Southwest-Jiao tong University, 2012. 47(04): 558-566.
[21] Li SQ, Yu TL, Zhang M. Comparative analysis of vulnerability of typical structures in different intensities [J]. Journal of South China University of Technology (Natural Science Edition), 2020. 48(03): 67-75.
[22] GB/T 17742-2008 China Intensity Table[S].Beijing: Standards Press of China, 2008.

CIVIL ENGINEERING JOURNAL

Article no. 29

THE CIVIL ENGINEERING JOURNAL 3-2023

RESEARCH ON UNBALANCED WEIGHING EXPERIMENT OF MULTI-POINT BRACED SWIVEL CABLE-STAYED BRIDGE

Zhipeng Tang, Quansheng Sun, Zifeng Gu, Yafeng Zhao and Haoyang Zhang

Department of Civil Engineering, Northeast Forestry University, Harbin， 150040, China; sunquansheng@nefu.edu.cn

ABSTRACT

Rotating bridge structures encounter numerous challenges during the rotation process, and the pre-rotation weighing experiment is the key to addressing these difficulties. Therefore, in order to resolve the obstacles and provide reference for future bridge rotation construction in the context of dependent projects, this study focuses on a prestressed concrete cable-stayed bridge with twin towers and twin cable planes. It proposes a multi-point braced rotation weighing experiment, where both the arm-brace and the spherical hinge are subjected to simultaneous loading. Firstly, theoretical formulas for the weighing experiments under various conditions were derived. The field test results were then utilized to calculate the jacking force at the limit state during the jacking process. Subsequently, these values were substituted into the corresponding formulas to determine the relevant parameters of the weighing experiment. Finally, the counterweight was adjusted based on the weighing results to facilitate the structural rotation. Throughout the swiveling process, the angular velocity remained stable, resulting in the successful rotation of the structure. The successful implementation of a multi-point braced swivel weighing experiment, considering the joint force of the arm-brace and the spherical hinge, can serve as a valuable reference for the design and construction of similar bridges.

KEYWORDS

Cable-stayed bridge, Swivel construction, Multi-point braced, Spherical hinge rotation method, Weighing experiment

INTRODUCTION

Bridge construction in China is currently undergoing rapid development. In addition to spanning ravines, valleys, rivers, and seas, many new bridges must cross over busy transportation lines. Fortunately, the swivel construction method offers an effective solution, offering several advantages such as simplified construction procedures, accelerated construction speed, reduced material usage, and minimal disruption to existing infrastructure. These advantages yield significant economic and social benefits [1]~[4].

The swivel construction method can be classified into three categories based on the swivel direction: horizontal swivel, vertical swivel, and a combination of horizontal and vertical swivel methods [5]~[9]. The horizontal swivel method is widely used in road and railway engineering projects [9]. However, when the bridge constructed by the horizontal swivel method is faced with a swivel across existing lines, a specific obstacle in the process of swivelling, or a slight elevation difference between the bottom of the beam and the obstacles, the traditional single point braced swivel method no longer meets the complex construction conditions, which makes more and more horizontal swivel constructions constantly innovate. Based on this, this article proposes a multi-point braced swivel weighing experiment, which is based on the single-point braced swivel and involves the joint force of the arm-brace and the spherical hinge.

BRIDGE OVERVIEW AND FINITE ELEMENT MODEL

The project-based bridge is on a north-south urban trunk road in Harbin, Heilongjiang Province. It features a twin-tower, double-cable prestressed concrete swivel cable-stayed bridge with a combined span length of (118 + 198 + 118) meters and a semi-floating structural support system. Tower nine rotated 79.31 degrees counter clockwise, while Tower ten rotated 96.12 degrees clockwise; the swivel weight of both towers is approximately 28,000 tonnes. Due to the bridge's location, the bridge spans 48 existing railways at an intersection angle of 80.4°. Furthermore, the main beams of Tower ten's side span must cross the railway catenary during the swivel process. The distance between the bottom of the beams and the railway catenary at its closest position is only 151 mm. In order to increase the distance between the main beams of Tower ten's side span and the railway catenary while maintaining the safety of the swivel process, the multi-point braced swivel method was used for Tower ten. In contrast, the traditional single-point braced swivel method was still used for Tower nine.

Through the finite element method to solve the problem, is the use of mathematical approximation method to simulate the actual physical system (geometry and load conditions). It approximates the real system of infinite unknowns with a finite number of unknowns using simple and interacting components (i.e. cells). Finite element analysis is inextricably linked to the solution of nonlinear issues. Based on actual construction stages and parameters, a static rod system model for the twin-tower, double-cable swivel cable-stayed bridge was developed using Midas Civil to provide theoretical data for the overall structure and precise substitute moments for simplifying the upper structure of the local model. Midas Civil, a general structural analysis and design system for bridges within the Midas suite of software components, incorporating current Chinese design standards, is frequently used by engineering firms for project design and academic structural calculations.

Midas Civil was used to constructing the Danyang Road overpass and the Lekai Street swivel cable-stayed bridge in Heze, China [10]. In his study of the mechanical behaviour of an inter-railway overpass in Zoucheng City subject to the coupled action of multiple elements, Guo [11] also used Midas Civil to create the static rod system model of the swivel cable-stayed bridge.

1. Nodes and units' creation

The nodes and units are created under the bridge's size and location. The overall model has 416 nodes and 393 units, with beam units for the main tower, main girder, and bearing platform; and truss units for the stay cable.

2. Material selection

According to the field experiment, material-related parameters refer to the corresponding material parameters in the Chinese specification database [12] and are given to the corresponding unit.

3. Boundary setting

Because the rod system model is not required to provide seismic and other dynamic data for this paper, the "pile-soil" effect is not considered, and the bottom of the lower foundation slab is fully restrained by general support; the anchoring effect of the anchor on the stay cable and the bridge tower and main beam is simplified and replaced by a rigid connection. The tower beam before the swivel is temporarily consolidated by prestress, which is also replaced by a rigid connection. The tower beam and pier bearings are simulated by elastic supporting.

4. Construction stage

The construction phases of the model are divided into 47 stages, based on the engineering design documents and adjusted in real time according to the actual construction conditions on site.

The overall rod system model omits the detailed structures such as spherical hinges and arm-brace. The bridge layout is shown in Figure 1, and the Midas Civil model is shown in Figure 2.

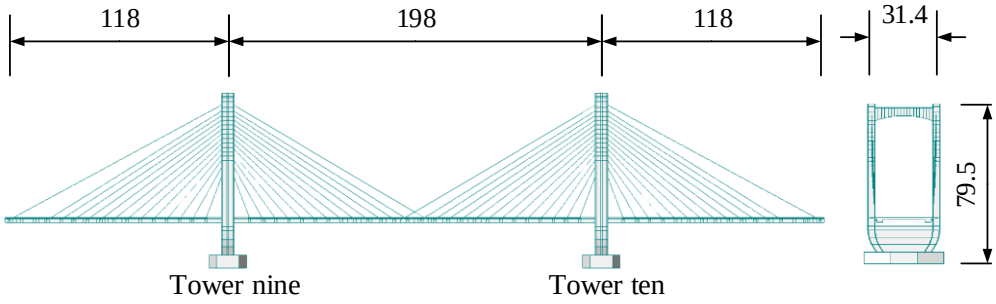

Fig.1 - Bridge layout diagram (unit：m)

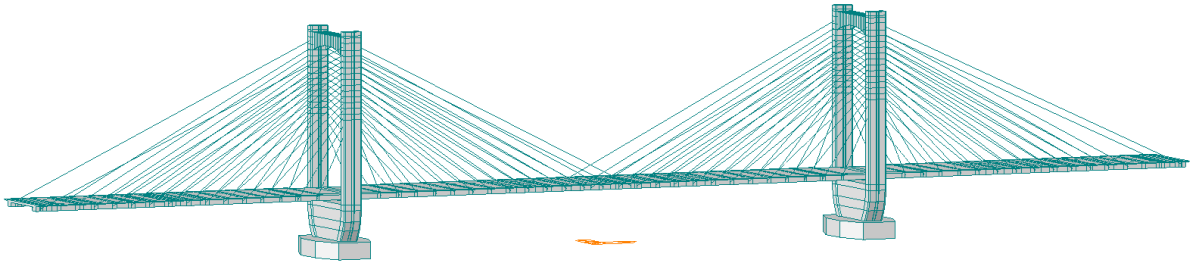

Fig.2 - Midas model diagram.

THEORY RELATED TO MULTI-POINT BRACED SWIVEL WEIGHING EXPERIMENTS

Test method of unbalanced moment of swivel

It is impossible to achieve complete symmetry on both sides of the swivel's spherical hinge during the construction process of a now-poured beam, so an unbalanced moment may occur, which is not conducive to the safe construction of a swivel. To ensure construction safety, it is essential to conduct an unbalanced moment test before swiveling, followed by a counterweight design based on the tested unbalance moment [13]. The test methods of unbalanced moment are as follows: (i) the method based on the stress difference at the root of the main beam; (ii) the method utilizing deflection estimation; and (iii) the spherical hinge rotation test method.

1. The method based on the stress difference at the root of the main beam

The method based on the stress difference at the root of the main beam uses the principle that when pure bending occurs in the main beam, the bending normal stress varies linearly along the height of the beam. The unbalanced moment of the swivel structure is calculated using the stress difference at the root of the main beam.

2. The method utilizing deflection estimation

The fundamental principle of deflection estimation is that after constructing a bridge using the horizontal swivel method, before and after the demolition of the brackets, the beam bodies on both cantilevers ends only produce elastic rotation around the spherical hinge and no other rotation parameters; thus, it is assumed that the difference in deflection between the two cantilever ends is due to the difference in the self-weight of the concrete.

3. The spherical hinge rotation test method

Currently, the bridges constructed by the horizontal swivel method generally use the spherical hinge rotation test method to predict the unbalanced moment and the friction moment of the spherical hinge [14]~[16]. The fundamental principle is the theory of rigid body displacement mutation. This approach

solely considers the rigid body's displacement mutation, ignoring the effect of other factors, and has a high degree of precision, which satisfies the swivel's requirements.

Liu Jian [17] compared all three methods and concluded that the spherical hinge rotation test method is the most accurate. Combined with the construction situation, this project uses the spherical hinge rotation test method for weighing experiments.

Derivation of weighing experiment formula based on spherical hinge rotation method

The spherical hinge rotation method is widely used as a test method for weighing experiments. The specific derivation process of its equation is as follows:

After demolishing the temporary consolidation of the upper swivel structure, which was generated by the boost counterforce seat, the following circumstances will be faced:

1. Calculation of the moment when the spherical hinge frictional moment Mz > the rotational unbalance moment Mg:

As shown in Figure 3, an example of a single point braced swivel weighing.

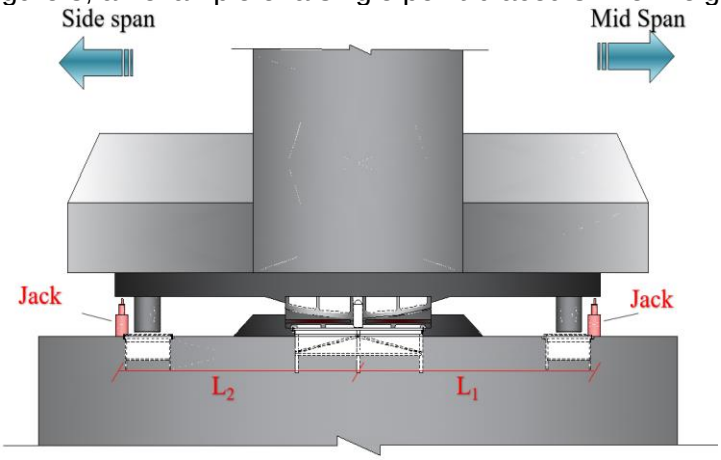

Fig.3 - Schematic diagram of single point braced swivel weighing

In Figure 3 *L1* is the distance from the jack to the spherical hinge centre in mid–span; *L2* is the distance from the jack to the spherical hinge centre in the side–span; Jack is used to apply jacking force; The jack's loading point is situated in the upper foundation slab part on the outside of the arm-brace.

It is assumed that the centre of rotation is biased towards the mid-span direction, and the jacking force *P1* is applied to the foundation slab in the mid-span direction. When the jacking force *P1* is progressively increased to the moment when the spherical hinge experiences a slight rotation, that is, *Mz* and *Mg* in different direction, it will be obtained according to the principle of moment balance that:

$$P_1L_1+M_g=M_z \quad (1)$$

It is assumed that the centre of rotation is biased towards the side-span direction, and the jacking force *P2* is applied to the foundation slab in the side-span direction. When the jacking force *P2* is progressively increased to the moment when the spherical hinge experiences a slight rotation, that is, *Mz* and *Mg* in the same direction, it will be obtained according to the principle of moment balance:

$$P_2L_2=M_g+M_z \quad (2)$$

Combining the (1) and (2) equations, we can obtain:

$$M_g=\frac{P_2L_2-P_1L_1}{2} \quad (3)$$

$$M_z=\frac{P_2L_2+P_1L_1}{2} \quad (4)$$

2. Calculation of the moment when the spherical hinge frictional moment Mz < the rotational unbalance moment Mg:

The counterweights of the single-point and multi-point braced swivel are not the same. Before the weighing experiment, the multi-point braced swivel needs a larger counterweight to raise one end of the main beam.

Because of the giant counterweight of the multi-point braced swivel, only one instance exists, the spherical hinge frictional moment *Mz* < the rotational unbalance moment *Mg*. As a result, it is challenging to balance the structure with the spherical hinge frictional moment *Mz* alone. However, the structure will be re-balanced when the two arm-braces on the mid-span counterweight side contact with the lower foundation slab's slideway to provide the support moment for the structure. Therefore, the arrangement of the jacks is different from the single point braced swivel, which only needs to be arranged on one side, as shown in Figure 4.

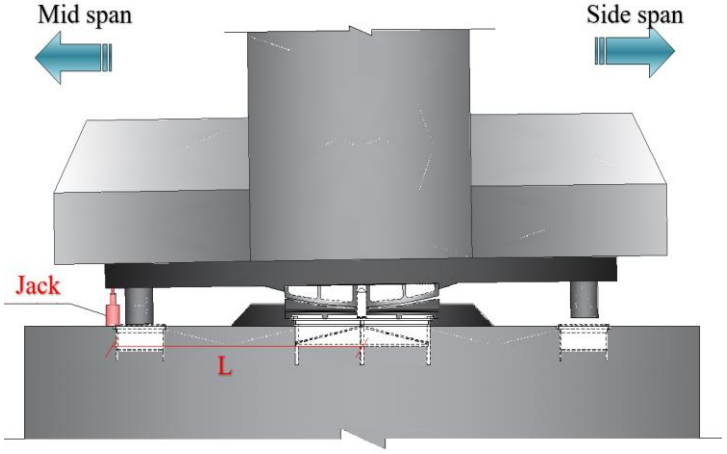

Fig.4 - Schematic diagram of multi-point braced swivel weighing

In Figure 4 L is the distance from the jack to the spherical hinge centre in mid–span.

The theoretical derivation is as follows:

(1) When the jack is loaded on the mid-span side to cause the mid-span side to rise to a slight rotation, that is, *Mz* and *Mg* in the same direction, according to the principle of moment balance, it will be obtained:

$$PL=M_g+M_z \quad (5)$$

In the formula: *P* is the critical force when the jack is loaded to the point of slight rotation, kN.

(2) When the jack is unloaded on the mid-span side to cause the mid-span side to drop down to a slight rotation, that is, *Mz* and *Mg* in the different directions, according to the principle of moment balance, it will be obtained:

$$P_3L=M_g-M_z \quad (6)$$

In the formula: *P3* is the critical force when the jack is unloaded to the point of slight rotation, kN. Combining the (5) and (6) equations, we can obtain:

$$M_g=\frac{(P+P_3)L}{2} \quad (7)$$

$$M_z=\frac{(P-P_3)L}{2} \tag{8}$$

There were partial minor vertical rotations because the Tower ten of the bridge needed counterweights before the weighing experiment. The model of spherical hinge frictional moment [18] is shown in Figure 5.

As shown on the right-hand side of Figure 5., the spherical surface of the spherical hinge is differentiated into tiny circles, and the moments of several circles to the centre O of the upper spherical hinge are summed, yielding the moment equation:

$$dM_z=R\cos\theta dF \tag{9}$$

Integrating Formula (9), we can obtain:

$$M_z=\int_0^{\alpha}\frac{2\mu_0 GR}{\sin^2\alpha}\sin\theta\cos^2\theta\, d\theta=\frac{2(1-\cos^3\alpha)}{3\sin^2\alpha}\mu_0 GR \tag{10}$$

In the formula: μ_0 is the maximum static friction coefficient of the spherical hinge; α is half of the central angle of the spherical hinge, °; R is the radius of the spherical hinge, m.

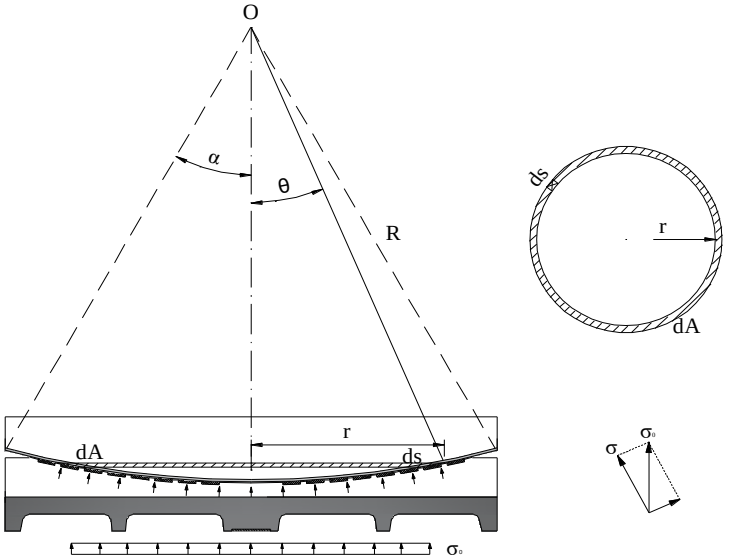

Fig.5 - Model for the frictional moment of a spherical hinge

The eccentricity of the rotating system is calculated as follows:

$$e=\frac{M_g}{G} \tag{11}$$

In the formula: e is the eccentricity of the rotating system, m; G is the weight of the swivel, kN.
After counterweighting, the moment provided by the counterweight is added to the unbalanced moment, and the eccentricity of the rotating system is calculated as follows:

$$e'=\frac{G_1 l+M_g}{G+G_1} \tag{12}$$

In the formula: e' is the eccentricity of the rotating system after the weighing experiment, m; $G1$ is the weight of the counterweight of the weighting experiment, kN.

MULTI-POINT BRACED SWIVEL UNBALANCED WEIGHING EXPERIMENT

Preparation before weighing experiment

Based on the actual conditions of this bridge, the distance between the main beams of Tower ten's side span and the metal catenaries of the high-speed rail below it at their closest point is only 151 mm, posing a collision risk during rotation; thus, the distance between the main beams and the metal catenaries must be increased. As a result, it is calculated that 1,603 tons of concrete heavy blocks must be placed on the main beam of Tower ten's midspan side before the weighing experiment. Because spherical hinges and arm-braces were not simulated in Midas Civil, a comparison of the values in the overall rod system model before and after balancing the counterweights, taking only the rigidity of the main beams into account, revealed that the height of the main beams of the side span of Tower ten and the metal catenaries of high speed rail at their closest point increased by 57mm. Assuming that the integral rigidity is infinite, according to the similar triangle principle, when the arm-braces dropped 20mm to contact the slideway, the closest point of the metal catenaries of the high speed rail and the main beams of Tower ten would rise 20/6500×90630≈279mm (by measuring, the distance from the nearest point of the metal catenaries and the main beams to the centre line of Tower ten of the bridge is 90.63m, the radius of the slideway centre is 6.5m). In conclusion, the closest point of the metal catenaries of the high-speed rail and the main beams of the side-span was lifted by a total of 336 mm by placing 1,603 tons of concrete heavy blocks on the main beams of the mid-span side of Tower ten before the weighing experiment and considering the factors of the contact between the drop of the arm-braces and the slideway and the stiffness of the main beam. The photographs of the counterweight on site in Tower ten are shown in Figure 6.

Fig. 6 - Photographs of the counterweight on site in Tower ten

After Tower ten's counterweight was completed, the temporary loads were taken from the beam body, the steel tube brackets were removed, and the closure facilities were installed. Following the principle of symmetry, the temporary consolidation of the spherical hinge was eliminated, including the brackets of the spherical hinge, the brackets of the arm-braces, the sand bucket, etc., to ensure the free fall of the swivel structure in the vertical direction and avoid the artificial eccentricity and the beam body in the inclined state. During the process of removing the temporary consolidation, the status of the swivel structure was determined by monitoring the displacement of the beam end and the change in the space between arm-braces in real-time. After the removal was complete, monitoring data were used to assess whether the beam body was in equilibrium; the weighing experiment could be performed only when it was in equilibrium [19].

Test loading and measuring point arrangement

Considering a series of factors such as site conditions, before the weighing experiments, eight sets of 5000 kN jacks were symmetrically placed on both sides of the swivel of Tower nine, with the centerline of the bridge as the axis of symmetry. Four sets of 5000 kN jacks were symmetrically placed on the mid-span side of the swivel of Tower ten, with the centerline of the

bridge as the axis of symmetry, which were used to jack up the swivel and to test the values of the reaction force of the temporary fulcrum during the weighing experiments. The layout of the weighing experiment test devices for Tower nine and Tower ten are shown in Figure 7 and Figure 8 respectively.

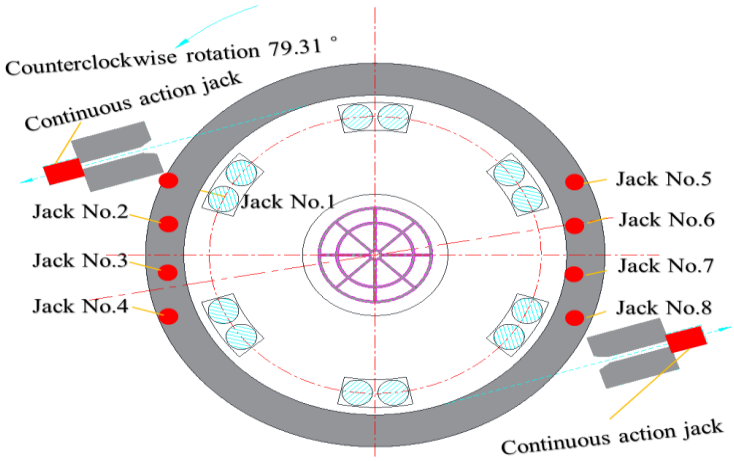

Fig.7 - The layout of the weighing experiment test instruments for Tower nine

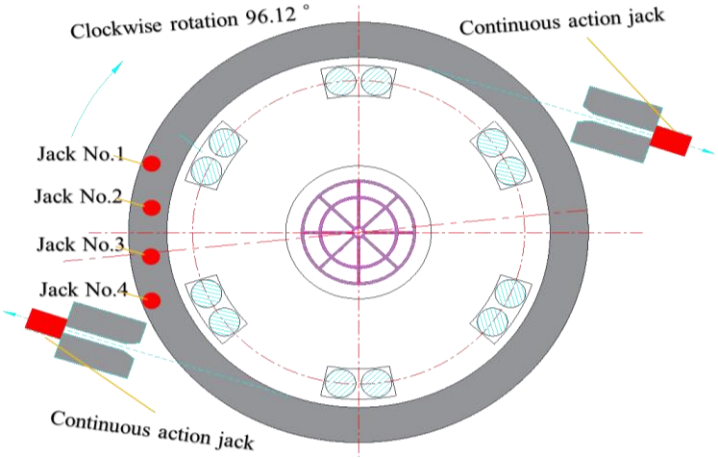

Fig.8 - The layout of the weighing experiment test instruments for Tower ten

Four displacement sensors were placed on both sides of the arm-braces to measure the vertical displacement at each loading stage to ensure the accuracy of the experiment results. Four horizontal displacement sensors were placed on adjacent positions to record the corresponding horizontal displacement at each loading stage, which was used to comprehensively judge the critical state of spherical hinge rotation and reasonably determine the value of critical force. The displacement sensors adopted wireless displacement sensors (range: 0-50 mm, resolution: 0.01/0.005, measuring force: < 2.2 N). The layout of displacement sensors is shown in Figure 9 and Figure 10.

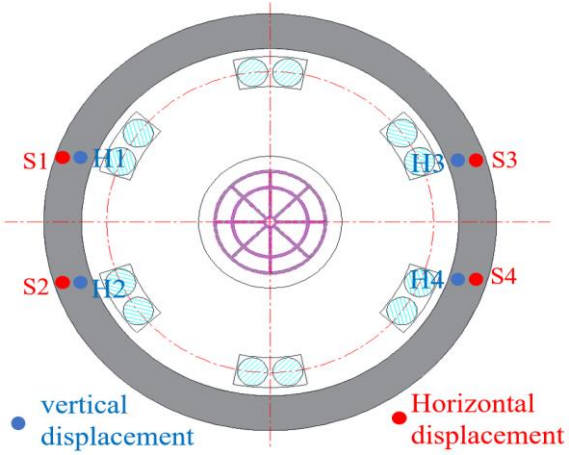

Fig.9 - The layout of displacement sensor

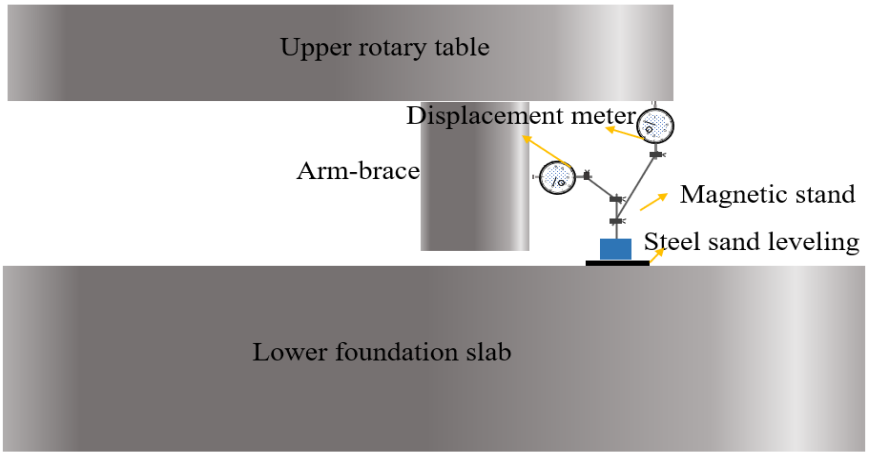

Fig.10 - Side view of displacement sensor arrangement

Experimental procedure

All displacement sensors were reset to zero after the device was set up. After the initial readings were taken, the jacking equipment was synchronously jacked up and held load when loaded to 100 kN. At that point, the values of the horizontal and vertical displacement sensors were read, and the corresponding jacking forces were recorded simultaneously. Following the preceding method, the displacement and load values were read every 100 kN until there was a sudden change in the vertical and horizontal displacement sensor readings. At that point, the critical load (the value of *P1*) and displacement were recorded, followed by continued loading and counting at 100 kN per level and unloading after three-level loading. If the swivel was to be carried out in the conventional way, the remaining four jacking equipment would need to be positioned in jacking positions 5 to 8, loaded and counted according to the preceding method, and the critical force (the value of *P2*) and displacement would be recorded. The multi-point swivel, on the other hand, needed only that the jack be placed in positions 1 to 4, and the critical force (the values of *P* and *P3*) could be determined by loading and unloading the jack. The jack positions are shown in Figure 7 and Figure 8 The flow chart of the weighing experiment is shown in Figure 11.

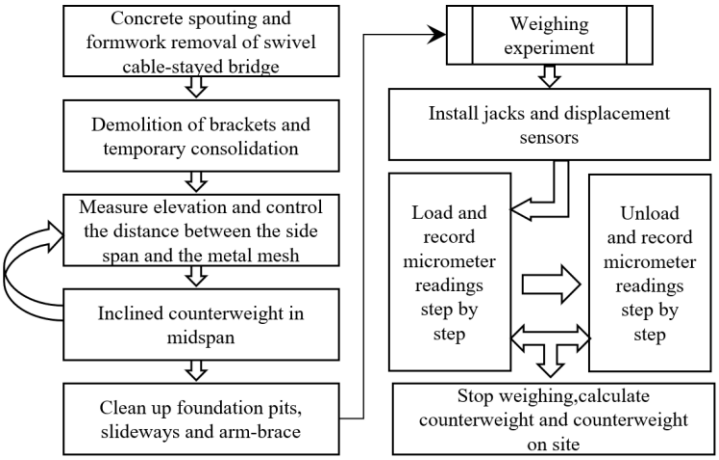

Fig.11 - Flow chart of weighing experiment

RESULTS ANALYSIS

Weighing experiment data are analyzed to determine the rotational unbalance moment *Mg*, the spherical hinge frictional moment *Mz*, and the friction coefficient of the spherical hinges *u*.

Experimentation results

The jacking force at the limit state is determined using the weighing experiment's jacking force-vertical displacement curve. When performing a comprehensive evaluation, it is necessary to use the jacking force-horizontal displacement curve and the jacking force-vertical displacement curve to minimize errors in determining the jacking force when the experimental data is more complicated. Occasionally, during the weighing experiments, it is necessary to combine the disturbance of the beam body and the stability of the sustained load of the jacks [19].

This study focuses on the analysis of the multi-point braced swivel weighing experiment based on the traditional single-point braced swivel weighing experiment.

1. Results of the weighing experiment at Tower nine

The weighing results of Tower nine under a single-point braced swivel were documented based on the on-site weighing situation. According to the records, the mutation value *P2* during the jacking-up process in the mid-span side of Tower nine is 4200 kN, and the mutation value *P1* during the jacking-up process in the side-span side of Tower nine is 1700 kN.

Tower nine used the single-point braced swivel weighing method, and the relevant parameters of the weighing experiment are shown in Table 1.

Tab. 1 - Parameters for weighing experiment on Tower nine

Parameters		Units	Remarks
L_2	8.00	m	Distance from jack to spherical hinge center in side - span
L_1	8.00	m	Distance from jack to spherical hinge center in mid - span
P_2	4200	kN	Critical force when the jack is loaded to the point of slight rotation in side-span
P_1	1700	kN	Critical force when the jack is loaded to the point of slight rotation in mid-span
G	280000	kN	Total weight of the swivel
R	9	m	Spherical radius of the spherical hinge

Parameters		Units	Remarks
α	13.59	°	Half of the central angle of the spherical hinge

By substituting the values from Table 1. into equations (3), (4), (10) and (11).

The results of the weighing experiment calculations are collated in Table 2.

Tab. 2 - Data analysis from weighing results of Tower nine

Parameters		Units	Remarks
Mg	10000.0	kN·m	
Mz	23600.0	kN·m	
e	0.036	m	Bias towards the mid-span side
u	0.0095		

2. Results of the weighing experiment at Tower ten

Unlike the traditional single-point braced swivel weighing experiment, the multi-point braced swivel weighing experiment only required jacks to be placed on one side for loading and unloading. The weighing results of Tower ten under a multi-point braced swivel were documented based on the on-site weighing situation. During the loading procedure, the jacking force and the values of displacement meters S and H on both sides were recorded in real-time. Four displacement meters, two by two on each side, are accordingly divided into four groups, numbered loading groups 1 to 4, and their jacking force and displacement changes are plotted as shown in Figure 12 and Figure 13.

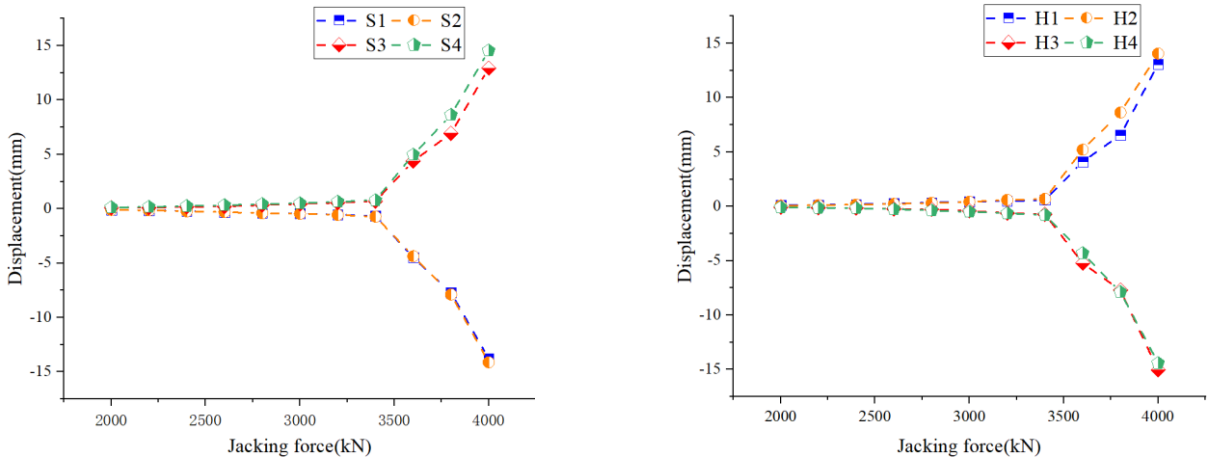

（a）horizontal displacement *（b）vertical displacement*

Fig.12 - Jacking force-displacement diagram for the mid-span side of Tower ten after jacks loading

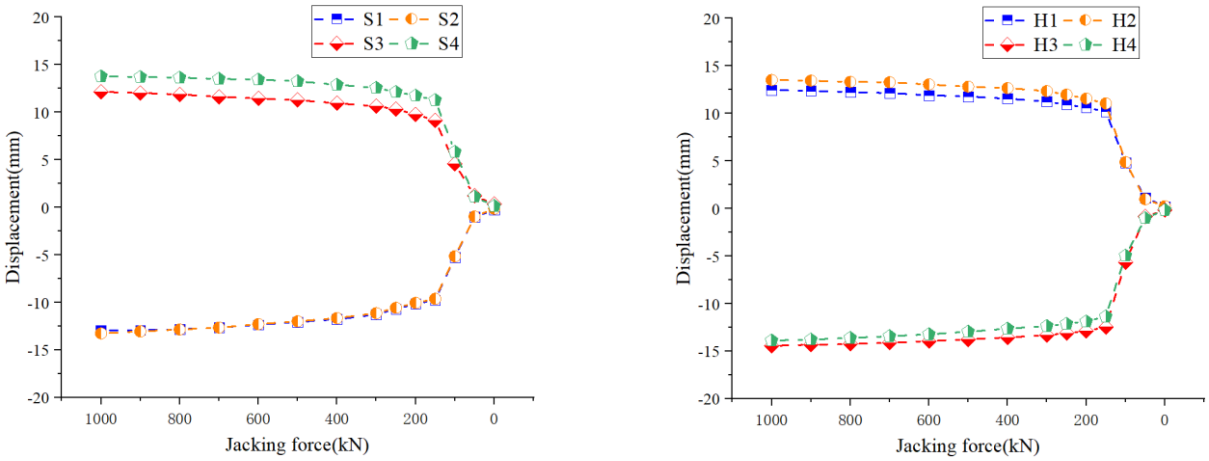

（a）horizontal displacement　　（b）vertical displacement

Fig.13 - Jacking force-displacement diagram for the mid-span side of Tower ten after jacks unloading

From the above loading displacement diagrams, it can be seen that the mutation value P in the process of the jacking-up in the mid-span side of tower ten is 3400 kN, and the mutation value P3 in the process of the jacking-up in the side-span side of tower ten is 150 kN.

Tower ten used the multi-point point braced swivel weighing method, and the relevant parameters of the weighing experiment are shown in Table 3.

Tab. 3 - Parameters for weighing experiment on Tower ten

Parameters		Units	Remarks
L	8.00	m	Distance from jack to spherical hinge center
P	3400	kN	Critical force when the jack is loaded to the point of slight rotation
P_3	150	kN	Critical force when the jack is unloaded to the point of slight rotation
G	280000	kN	Total weight of the swivel
R	9	m	Spherical radius of the spherical hinge
α	13.59	°	Half of the central angle of the spherical hinge

By substituting the values from Table 3 into equations (7), (8), (10) and (11).

The results of the weighing experiment calculations are collated in Table 4.

Tab. 4 - Data analysis from weighing results of Tower ten

Parameters		Units	Remarks
Mg	14200.0	kN·m	
Mz	13000.0	kN·m	
e	0.051	m	Bias towards the mid-span side
u	0.0052		

Setting of the eccentricity of the center of gravity and adjustment of the counterweight

According to the results of the unbalanced weighing and the actual situation on site, Tower nine adopted a balanced counterweight scheme for the beam, with the eccentric distance generally controlled at 0~5 cm, the calculated eccentric distance based on the findings of the weighing

experiment is approximately 0.036 m (bias towards the mid-span side), which satisfies code requirements [20]. Hence no counterweight is carried out.

The beam of Tower ten adopted a longitudinal tilt counterweight arrangement, with eccentric distances generally controlled at 5~15 cm. It is calculated that the bridge is counterweighted by 20 tons at 80 m from the centreline of the bridge at mid-span. After counterweighting, the system can be recalculated using Equation (12) to produce a new eccentricity of approximately 0.108 m (bias towards the mid-span side), which satisfies code requirements [20].

CONSLUSION

A twin-tower and double-cable prestressed concrete swivel cable-stayed bridge with a span combination of (118 + 198 + 118)m was used for the project. A combination of single-point braced, and multi-point braced swivelling weighing experiments was used to determine the spherical hinge frictional moment Mz, the rotational unbalance moment Mg, the eccentricity of the rotating system e, and the maximum static friction coefficient of the spherical hinge u, and the structural counterweight was adjusted based on the experiment results. Finally， Tower nine successfully rotated counterclockwise 79.31°, with a rotational angular velocity ranging from 0.015 rad/min to 0.023 rad/min. Tower ten successfully rotated clockwise 96.12°, with a rotational angular velocity ranging from 0.015 rad/min to 0.024 rad/min. Both towers demonstrated stable rotational angular velocities throughout the swiveling process, guaranteeing the successful completion of the structural swivel and uninterrupted operation of the existing line. Therefore, the multi-point braced swivel weighing experiment, involving the combined forces of the arm-braces and spherical hinges, can be effectively applied in scenarios where a horizontally swiveled bridge encounters rotation across existing lines, specific obstacles, or slight elevation differences between the bottom of the beam and the obstacles. Accordingly, this method also provides an important reference value for the construction of similar bridges in the future.

ACKNOWLEDGMENTS

The research in this paper was supported by the [Heilongjiang Provincial Science and Technology Tackling Project] (Department of Transportation of Heilongjiang Province, China) under Grant [No. 2021HLJ053].

REFERENCES

[1] Zhang L. Y., 2003, Rotating Construction of Bridge : Summary of Rotation Construction of Balanced Rotation System. China Communications Press: Beijing.

[2] Yang H. P. et al., 2017, “Review of China's Rotation Cable-Stayed Bridge Development”, Modern Transportation Technology, 14(06): 34-39.DOI: 10.3969/j.issn.1672-9889.2017.06.010.

[3] Guo W., 2021, “Optimum Design of Spherical Hinge Structure and Rotation State Evaluation of Horizontal Swivel Bridge”, Master thesis of Jilin University, Jilin, China. DOI:10.27671/d.cnki.gcjtc.2022.000336.

[4] Yu P. H., 2022, “Research on Construction Control and Parameter Analysis of Spherical Joints for Large Tonnage Swivel Cable-Stayed Bridge”, Master thesis of Chongqing Jiaotong University, Chongqing, China. DOI:10.27671/d.cnki.gcjtc.2022.000336.

[5] Li L. P., 2009, “Plane Swivel Construction Technology of Continuous Box Girder Bridge”, Railway Standard Design, (08): 55-57.DOI: 10.3969/j.issn.1004-2954.2009.08.017.

[6] Ren H et al., 2008, “Construction Control for Gushan Bridge of Shitai Passenger Line”, Journal of Shijiazhuang Railway Institute(Natural Science), 21(04): 52-56.DOI: 10.3969/j.issn.2095-0373.2008.04.012.

[7] Zhang J. F., 2006, “Construction Technology of Level Swing Method of a T-Rigid Frame Bridge”, Journal of Shijiazhuang Railway Institute, (04): 114-117.DOI: 10.3969/j.issn.2095-0373.2006.04.028.

[8] Zhang W. X. et al., 2012, “Analysis of Influencing Factors of Continuous Box-girder Bridge in the Process of Horizontal Rotation”, Journal of Shijiazhuang Railway Institute, 25(04): 30-33.DOI: 10.3969/j.issn.2095-0373.2012.04.007.

[9] Cheng F. et al., 2011, “Development Status and Prospect of Bridge Swivel Construction Technology

in China", Railway Standard Design, (06): 67-71.DOI: 10.3969/j.issn.1004-2954.2011.06.018.
[10] Wang Z. B. et al., 2011, "Monitoring Technology for Rotation Construction of Cable Stayed Bridge in Baoding City Lekai Street", Railway Engineering, 60(09): 53-56.DOI: 10.3969/j.issn.1003-1995.2020.09.13.
[11] Guo X. G., 2012, "Research on the Mechanical Behavior of Rotation Construction of Cable-Stayed Bridge under Multi-Variable Coupling Effects", Master thesis of Northeast Forestry University, Heilongjiang, China.
[12] MOT (Ministry of Transport of the People's Republic of China) . 2018. Specifications for Design of Highway Reinforced Concrete and Prestressed Concrete Bridges and Culverts. JTG 3362-2018. Beijing, China: MOT
[13] Yang Y. Q., 2013, "Study on Swivel Weighing Experiment of Xingheng Expressway Overpass Crossing Existing Line", Railway Engineering, (08): 41-43.DOI: 10.3969/j.issn.1003-1995.2013.08.13.
[14] Wang S. J. and Zhu X., 2011, "Application of CAD and Finite Element Method in the Gravity Center Analysis of Body Rotating Cable-Stayed Bridge", Advanced Materials Research, (1269): 243-249.DOI: 10.4028/www.scientific.net/AMR.243-249.1549.
[15] Niu Y. Z. et al. 2015, "The Type Research on Super Large Tonnage Hinge of Horizontal Rotating Stayed Bridge", Journal of Railway Engineering Society, 32(06): 34-39.DOI: 10.3969/j.issn.1006-2106.2015.06.008.
[16] Liu X. M., 2016, "Construction Technique of Synchronized Rotation of Twin T Frames for a Continuous Rigid Frame Bridge", World Bridges, (01): 25-29.DOI: 10.3969/j.issn.1671-7767.2016.01.006.
[17] Liu J., 2019, "Force analysis and unbalanced torque prediction of spherical hinge in parallel swivel bridge construction", Master thesis of Shandong University, Shandong, China.
[18] Luo L. J., 2020, "Accurate Calculation Method of Vertical Friction Moment of Spherical Hinge in Bridge Rotation Construction", Railway Engineering, 60(01): 27-30.DOI: 10.3969/j.issn.1003-1995.2020.01.07.
[19] Luo L. J., 2019, "Unbalanced Weighing Test for Changfeng Avenue Viaduct in Wuhan", World Bridges, 47(06): 46-50.DOI: 10.3969/j.issn.1671-7767.2019.06.010.
[20] MOT (Ministry of Transport of the People's Republic of China) . 2020. Specifications for Design of Highway Cable-stayed Bridge. JTG/T 3365-01-2020. Beijing, China: MOT

CIVIL ENGINEERING JOURNAL

Article no. 30

THE CIVIL ENGINEERING JOURNAL 3-2023

ANALYSIS OF THE INFLUENCE OF SIDE WALL OPENING ON THE ARCH STRUCTURE OF METRO STATION USING THE PILE-BEAM-ARCH METHOD

Yongxing Dai[1], Xingkai Pei[1], Zekun Chen[2], Bolun Shi[1], Huijian Zhang[2], Yujie Yang[2] and Wei Chen[2]

1. *Guangzhou Metro Design & Research Institute Co., Ltd, Guangzhou, Guangdong 510010, China; 2873385923@qq.com; 1758584210@qq.com; 1017299784@qq.com*
2. *Key Laboratory of Transportation Tunnel Engineering, Ministry of Education, School of Civil Engineering, Southwest Jiaotong University, 610031, Chengdu, China; 1374309382@qq.com; 695174032@qq.com; 962246504@qq.com, huijianz@163.com*

ABSTRACT

In order to meet the traffic and commercial needs, it is sometimes necessary to open the side wall of the metro station, while the current research on the mechanical properties and safety of the arch caused by the opening of the side wall of the station by pile-beam-arch (PBA) method is rarely involved. In this paper, based on the Tianhe East Station project of Guangzhou Metro Line 11 located in soft-hard uneven stratum using PBA method, the settlement law and mechanical characteristics of the arch under different side wall opening conditions are analyzed, and the influence of opening construction and opening span on the safety of arch is also further studied. The results show that the settlement caused by the opening of the side wall is mainly concentrated in the upper part of the opening area, and gradually expands around the opening area with the increase of opening span, and the maximum settlement occurs in the middle part of the arch. Opening leads to the differential settlement at both ends of the arch. With the increase in opening span, the settlement growth trend of the right side of the arch is greater than that of the left side. The opening of the side wall leads to the increase of the safety factor of the arch body and the decrease of the safety factor of the right arch foot, while the change of the safety factor of the left arch foot is not obvious, and the safety factor meets the specification requirements.

KEYWORDS

PBA method, Side wall openings, Differential settlement, Safety factor; Numerical calculation

INTRODUCTION

In recent years, the pressure on urban public transport is increasing with the acceleration of urbanization and economic development [1-2]. As a relatively environmentally friendly and low-carbon public transport with a large volume of traffic, metro travel has attracted much attention [3-4]. At present, researches on the PBA method mainly focus on the variation law of ground settlement and stratum deformation at each stage of construction [5-10]. After the completion of the metro station, due to the new line transfer or the installation of the attached structure, the demolition construction of the side wall of the station is often required. While the demolition construction will inevitably affect the mechanical system and security of the station structure, it is necessary to analyze the deformation as well as internal force change law of the side wall and the arch in the

opening process of the side wall. It is worth mentioning that the mechanical properties and deformation laws of underground structures have always been the focus of scholars [11-13].

Based on this, scholars have conducted some research on the mechanical behavior of the station with side wall openings [14]. Zhang [15] took the transfer station of a subway station in Beijing as an example and found that the removal of walls by sections and the erection of temporary linings at the same time had a better control effect on the deformation and internal force about the existing structure. Du and Guo [16] found that the demolition stage of the side wall was the most sensitive construction step to the internal force and settlement changes of the existing side wall, and put forward corresponding control measures. Xu [17] analyzed the deformation and stress characteristics of the existing subway structures using the covered excavation method and pointed out that reinforcement measures should be taken before the opening of the side wall. Yuan [18] found that the opening of the side wall can cause the local deformation of the existing station structure but has little impact on the maximum deformation about the whole structure. Wang [19] pointed out that the opening of the side wall would lead to the redistribution of internal forces in the existing station structure, and it was necessary to control the opening size and the clear distance between adjacent openings to reduce the adverse effects brought by the side wall opening. Hu *et al.* [20] analyzed the influence of side wall opening on the force and deformation of station structure and found that the deformation increment met the requirements while the stress increment was higher than the control requirements and suggested that the limit opening span of side wall should be 5.75m when there was no reinforcement. On the other hand, scholars have also studied the influence of reconstruction and expansion construction of existing stations on the force of the original structure and put forward corresponding construction suggestions [21-25]. Although some studies have analyzed the deformation and internal force distribution characteristics of the side wall caused by the opening of the side wall, few studies focused on the change characteristics of the mechanical behavior of the arch caused by the opening of the side wall using PBA method.

Therefore, in this paper, based on the Tianhe East Station project of Guangzhou Metro Line 11, a study on the evolution law of the mechanics and deformation of station arch with the PBA method caused by side wall opening is carried out, and the safety of arch under different opening conditions is also analyzed. The research results of this paper can provide some important references for similar metro construction of side wall openings.

PROJECT OVERVIEW

Tianhe East Station is the seventh station of the Guangzhou Metro Line 11 project, connecting the South China Normal University Station in the east and Guangzhou East Station in the west. The station is located on the east side of the intersection of Tianhe North Road and Longkou West Road. The line is arranged along the east-west direction and construction is carried out by the PBA method, as shown in Figure 1.

The Tianhe East Station is a two-story underground station with a standard section width of 21.3m and an excavation depth of 26.05m. The cross-section of the station is shown in Figure 2. The diameters of the side pile and steel pipe column are 1.2m and 1.8m, respectively; and the thickness of the preliminary lining and secondary lining are 0.3m and 0.9m, respectively. The calculation parameters about the lining structure are displayed in Table 1.

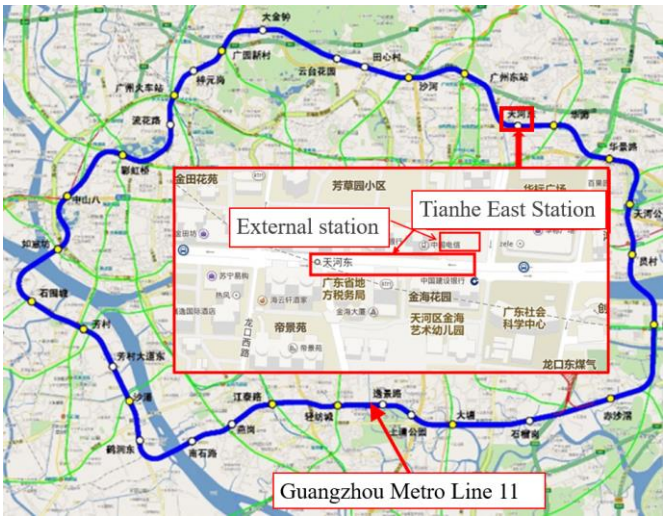

Fig. 1 - Plane view and position about the Tianhe East Station

Tab. 1 - Calculation parameters about the lining structure

Name	Elastic modulus E /MPa	Poisson's ratio μ	Density ρ /(kg/m^3)
Preliminary lining	25000	0.2	2500
Secondary lining	32500	0.2	2700
Crown beam	32500	0.2	2700
Steel pipe column	33500	0.2	2700
Side pile	20000	0.2	2300
Middle plate	32500	0.2	2700
Bottom plate	32500	0.2	2700

Considering that the main body of the station locating in a busy commercial area, to effectively improve the transfer passenger flow capacity of Tianhe East Station, openings are required to be constructed on the side wall of the main structure of the station to realize the connection with the external station hall. The location of the opening is selected in the red box of Figure 2. The buried depth of the station is 10.2m, and the overlying soil layer from the top to bottom is composed of mixed fill, silty clay, strongly weathered conglomerate, medium weathered argillaceous siltstone, and breezy argillaceous siltstone. The main body of the station is located at the medium-weathered argillaceous siltstone. The calculation parameters about the surrounding rock are displayed in Table 2. ***Note:*** both of the parameters in Table 1 and Table 2 are taken from the engineering design data of Tianhe East Station of Guangzhou Metro Line 11.

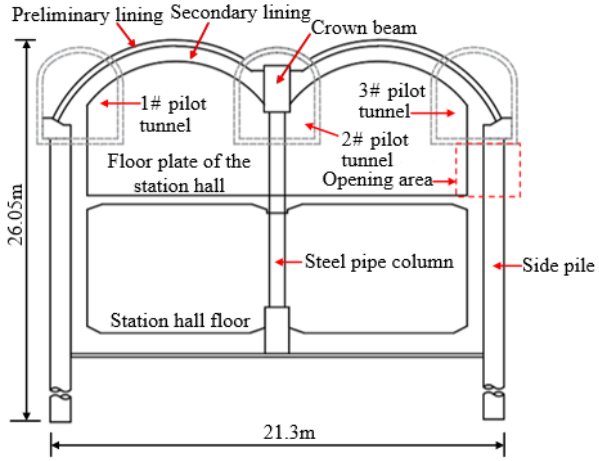

Fig. – 2 Cross section of the Tianhe East Station

Tab. 2 - Calculation parameters of the surrounding rock

Name	Thickness /m	Elastic modulus *E* /MPa	Density *ρ* /(kg/m^3)	Poisson's ratio *μ*	Cohesion *c* /kPa	Internal friction angle *φ* /°
Miscellaneous fill	6.0	10	1800	0.3	8	20
Silty clay	12.0	75.5	1900	0.38	5	30
Strongly weathered conglomerate	2.0	120	1950	0.33	2	25
Medium-weathered argillaceous siltstone	16.0	300	2200	0.25	180	33
Breezy argillaceous siltstone	42.0	500	2200	0.25	200	35

NUMERICAL CALCULATION INSTRUCTION

The finite element software FLAC3D is adopted to build the three-dimensional finite element model of the station, and the calculation model is shown in Figure 3. To reduce the impact about the boundary effect, the model size is set as 100m×100m×90m (length × width × height). The whole model contains 1330107 nodes and 1327313 units. Normal constraints are applied to the lateral side of the model, fixed constraints are adopted at the bottom, and the upper surface is set to free. Only gravity is considered to carry out the initial ground stress balance. The surrounding rock and lining structure are simulated by solid element, in which the surrounding rock obeys the Mohr-Coulomb strength criterion and the lining structure obeys the elastic criterion. The calculation parameters about the surrounding rock and lining structure are the same as in Tables 1~2.

The construction process of PBA method is realized by numerical simulation. The main construction procedures are: excavate the pilot tunnels → install the side piles → install the middle column and crown beam → install the middle longitudinal beam and buckle arch of both sides of pilot tunnel and concrete backfill → install the buckle arch of preliminary lining at the arch→ install the buckle arch of secondary lining at arch → excavate the soil of station and install the lining structure.

Since the focus of this paper is the influence of the opening of the side wall on the arch structure, the displacement of the station structure is cleared after the completion of the main structure of the station, then the sidewall opening is carried out.

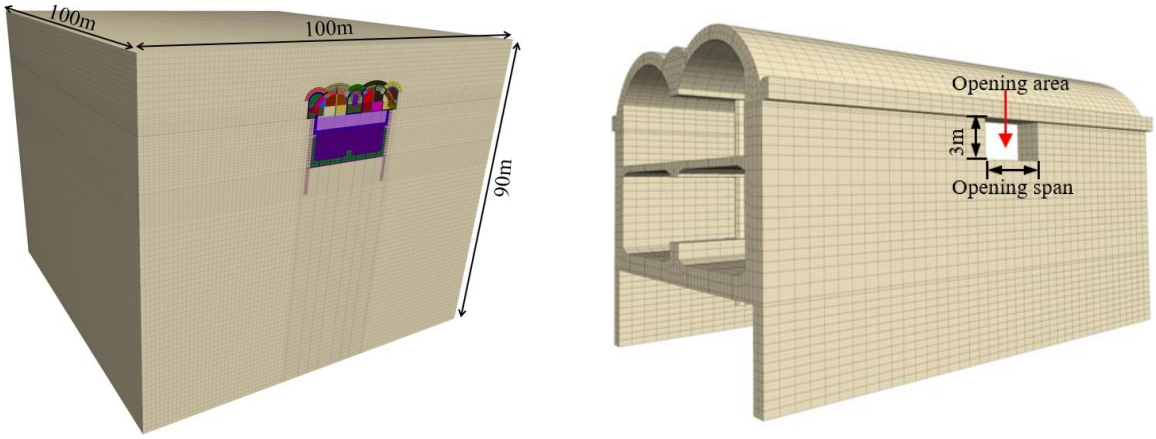

(a) Overall model *(b) Metro station model*

Fig. – 3 Calculation model

The finite element model of the opening area of the side wall is shown in Figure 3b by the actual on-site construction situation. To consider the mechanical response difference of the structure under different opening spans, the calculation conditions of opening spans of 4m, 6m, and 8m are set respectively, and the opening height is set to 3m.

ANALYSIS OF THE CALCULATION RESULTS

Influence of side wall opening on the deformation law of the side wall

The vertical displacement nephograms of side walls of different opening schemes are extracted after construction, as shown in Figure 4. In Figure 4, the settlement contour lines are symmetrically distributed and centered on the mid-span section. The settlement of the side wall is mainly concentrated above the opening area and spreads from the middle span to the perimeter of the opening. With the increase of opening spans, the settlement influencing area gradually wraps around the opening and expands to the opening periphery.

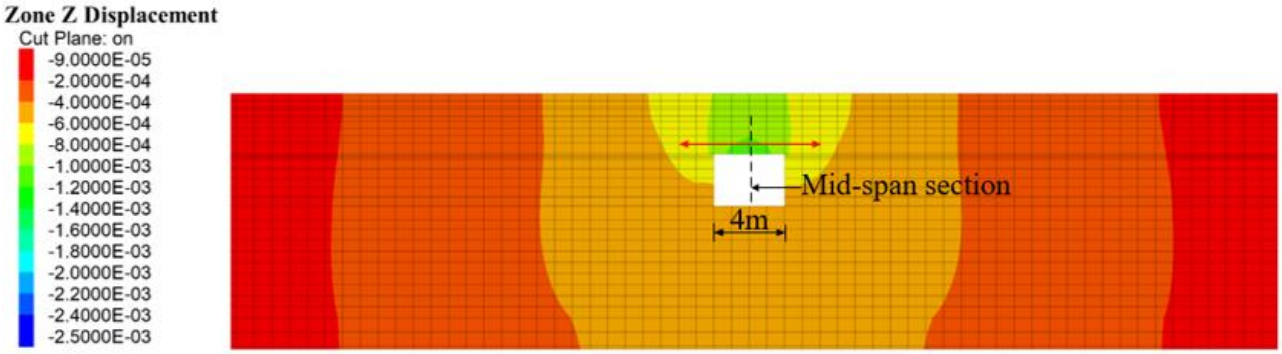

(a) The opening span is 4m

Fig. – 4 Settlement nephogram of the side wall under different opening spans of the side wall /m

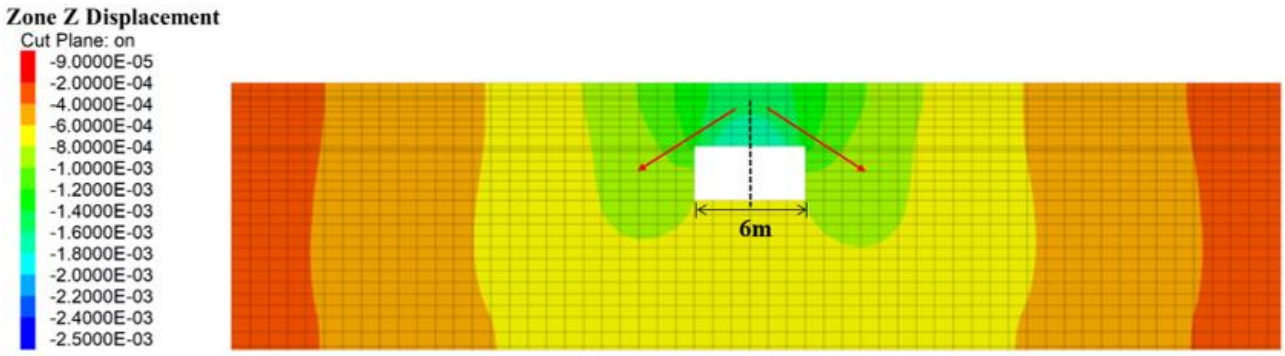

(b) The opening span is 6m

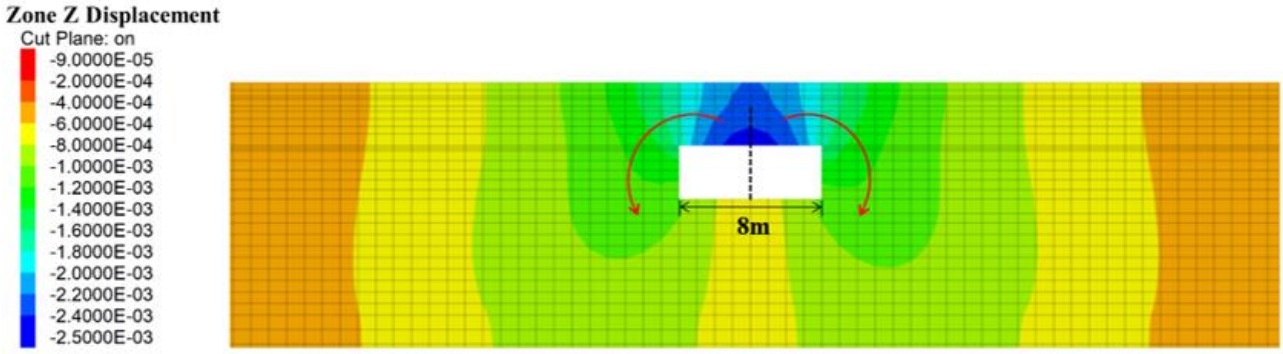

(c) The opening span is 8m

Fig. – 4 Settlement nephogram of the side wall under different opening spans of the side wall /m

To analyze the structural deformation law under different opening spans, the settlement curve above the opening circumference of the opening area is extracted by taking the mid-span section as the origin of coordinates, as displayed in Figure 5.

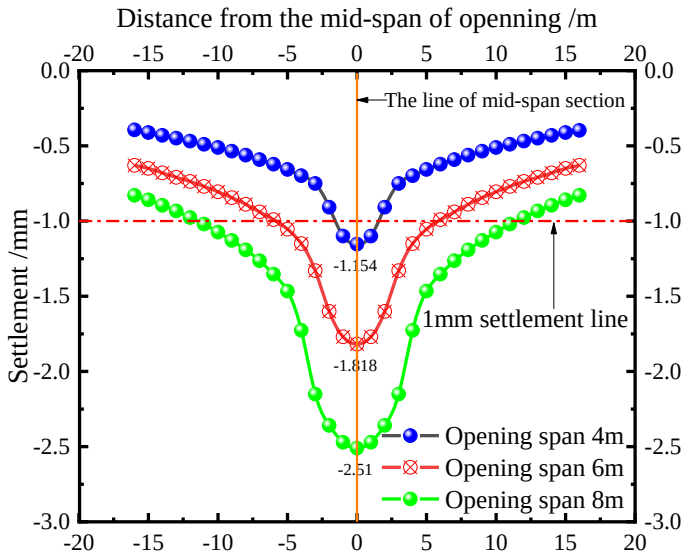

Fig. – 5 Settlement variation laws of the entrance and surrounding locations under different opening spans

In Figure 5, the settlement of the side wall increases with the opening span, and the maximum settlement occurs in the mid-span position. When the opening span is 4m, 6m, and 8m, the maximum settlement is 1.15mm, 1.81mm, and 2.51mm, respectively. The ratio of settlement increment to span

variation under adjacent opening conditions is taken as the gradient, and the two settlement growth gradients are 0.33 and 0.35, respectively, and the gradient increases slightly with the increase of opening span, namely, the growth rate of the maximum settlement value increases slightly with the opening span. Taking 1mm as the reference line of settlement (as shown in the red line in Fig. 6), when the opening span is 4m, the settlement is only slightly larger than 1mm within the opening span. When the opening span is 6m and 8m, the settlement within 6m and 11m from the middle span is greater than 1mm. From the shape of the settling trough, when the distance from the middle span is 1D (D is the opening span), the changing trend of settlement becomes slow. Based on this index, it can be considered that the influence range of the opening span is nearly 1D.

Influence of side wall opening on the deformation law of the whole metro structure

It can be seen from the above analysis that the mid-span part of the opening area is the most unfavorable section about the structure. The vertical displacement diagram of the overall structure of the station under different opening spans of this section is taken, as shown in Figure 6. The settlement curve of the right arch with different opening spans is extracted, as shown in Figure 7.

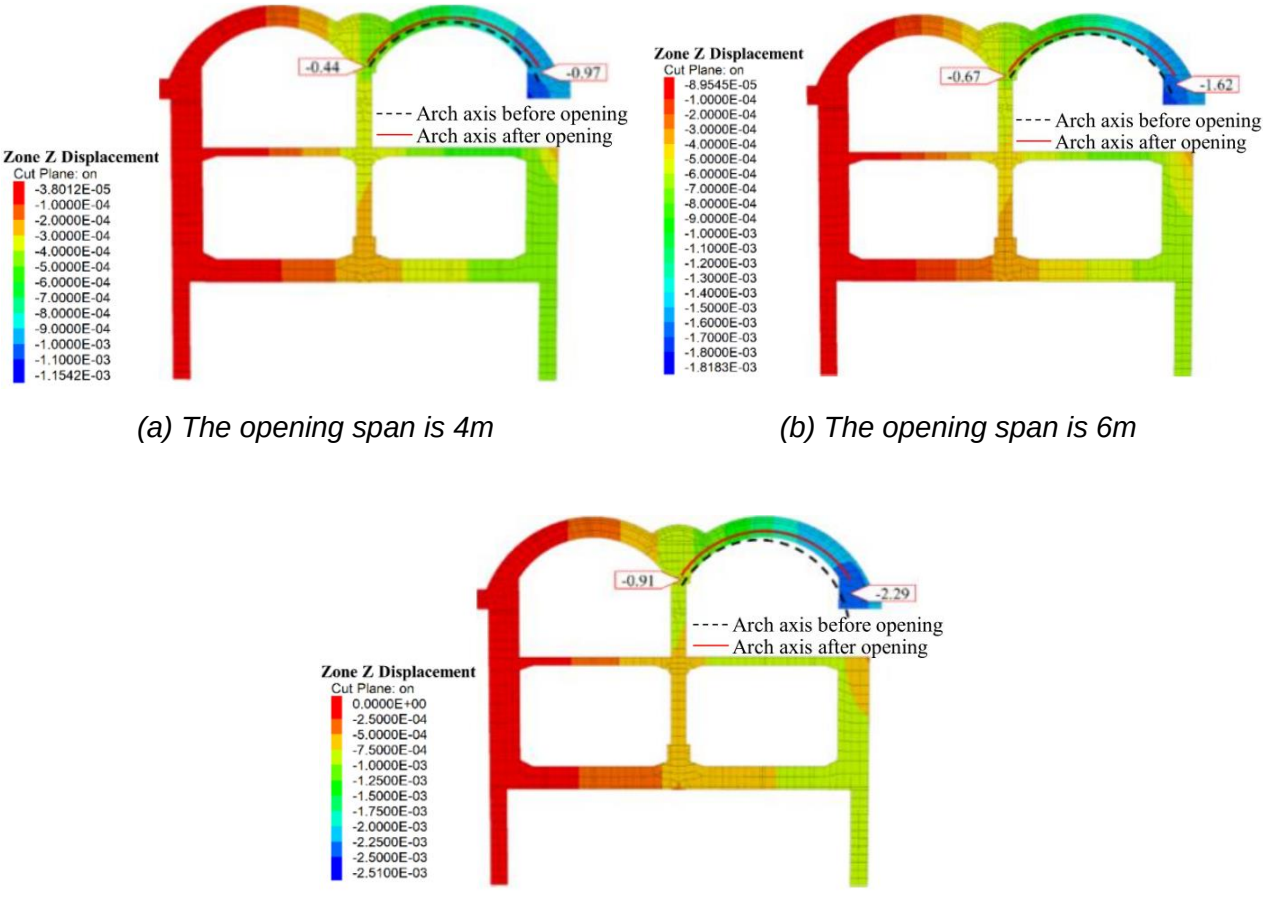

(a) The opening span is 4m

(b) The opening span is 6m

(c) The opening span is 8m

Fig. – 6 *Settlement nephogram of the whole metro structure under different opening spans of the side wall /m*

In Figure 6, due to the opening of the right side wall, the lining structure above the opening loses original support and then redistribution of the internal force occurs, resulting in significant downward settlement of the structure until the structure reaches equilibrium state, with a maximum value of 2.29mm (for opening span = 8m). The left side wall has not been opened, so its settlement is very small, i.e., forming the asymmetric phenomenon of displacement distribution of the left and right side walls. With the increase of the opening span of the side wall, the overall settlement of the station structure gradually

increases, but the settlement distribution law remains unchanged. From the distribution law of structure settlement, the structure settlement value decreases gradually as it leaves the opening area, and the right arch structure is in the most unfavorable state, and this law is basically consistent with the literature [22].

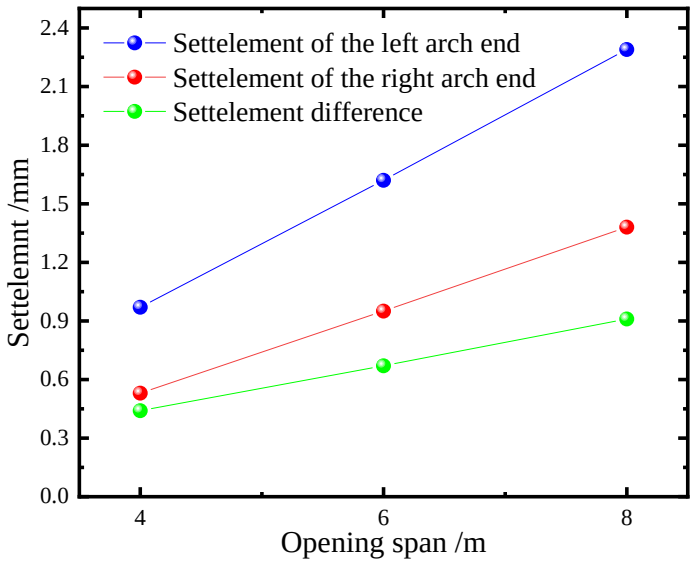

Fig. – 7 Change law of the settlement of the arch end under different opening spans of the side wall

In Figure 7, when the opening span is 4m, 6m, and 8m, the maximum settlement of the left end of the right arch reaches 0.44mm, 0.67mm, and 0.91mm respectively. The ratio of settlement increment to span variation is taken as a gradient, and the two sedimentation gradients are 0.115 and 0.12, respectively, and the gradient increases slightly with the increase of span. The maximum settlement value of the right end of the right arch under different opening spans is 0.97mm, 1.62mm, and 2.29mm, respectively, and the gradient is 0.325 and 0.335, respectively. Obviously, the gradient increases slightly with the increase of the opening span, and the settlement gradient at the right end is greater than that at the left end. With the increase of the opening span, the increased rate of settlement at the right end of the right arch is greater than that at the left end of the right arch. When the opening span is 4m, 6m, and 8m, the differential settlement at both ends of the right arch even reaches 0.53mm, 0.95mm, and 1.38mm, respectively, and the variation gradient is 0.21 and 0.215 respectively. Namely, the gradient of differential settlement increases slightly with the opening spans.

Influence of side wall opening on the mechanics of the arch

It can be seen from the above analysis that the right arch deformation is the largest after the opening of the side wall, which is the most unfavorable structural part. This is because the opening of the side wall will cause the missing part of the lining structure on the right side of the arch, resulting in a large differential settlement on the left and right side of the right arch, thus affecting the safety of the structure. Therefore, this part mainly analyzes the mechanical evolution laws about the right side of the arch under different side wall openings. The secondary lining structure on the right side of the arch is taken as the research object, as shown in Figure 8. The bending moment as well as axial force values about the secondary lining structures of the arch before and after the opening of the side wall are extracted to study the influence of the opening span of the side wall on the mechanical properties of the arch. The internal forces distribution about the secondary lining of the right arch is shown in Figure 9.

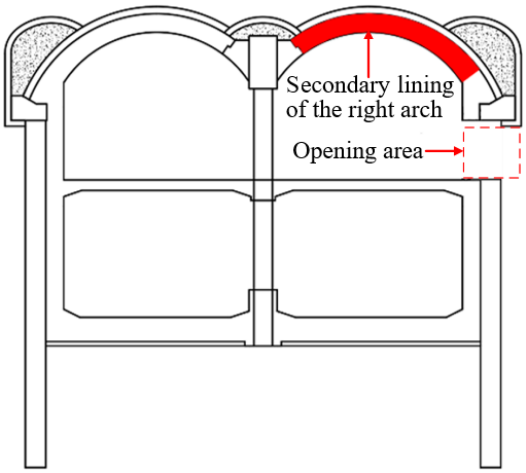

Fig. – 8 Secondary lining diagram of the arch

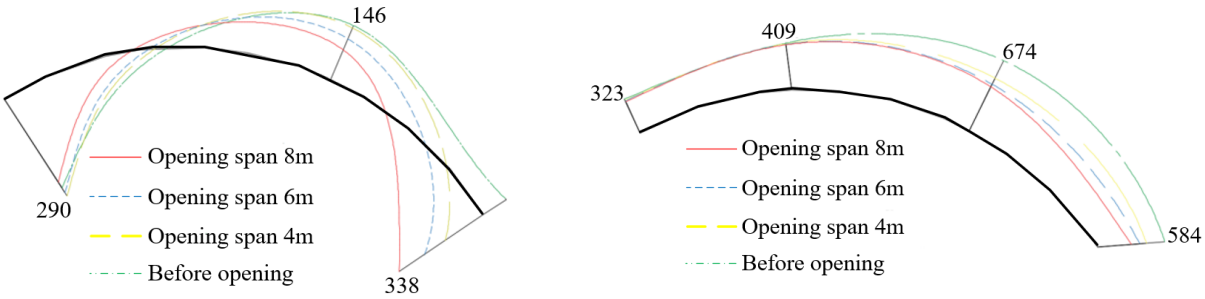

(a) Bending moments /(kN·m) (b) Axial forces /kN

Fig. – 9 Internal force distribution of the right arch under different opening spans of the side wall

According to Figures 8~9, before the opening of the side wall, the distribution of bending moment is manifested as tension on the left side of the arch and compression on the outside. The right side of the arch is strained externally and compressed inwards. After the opening of the side wall, the position of the arch foot on the right side of the arch is changed from the outside tension to the inside tension. The tensile and compressive state of the arch has no obvious difference before and after the opening of the side wall, and the axial force value decreases from the arch to the foot of both sides.

In terms of bending moment, the bending moment value of the right arch foot before the opening of the side wall is 68.0kN·m, which is manifested as inner compression and outer tension. The bending moment of this position corresponding to the opening span of 4m, 6m, and 8m is 115.0kN·m, 216.0kN·m, and 338kN·m, respectively, increasing by 69.11%, 217.65%, and 397.06% compared with that before the side wall opening respectively. The stress state is all manifested as inner tension and outer compression, so the tension state of the left side of the arch changed little before and after the opening. For the axial force, the influence caused by the opening is also mainly concentrated on the right side of the arch, that is, near the opening area. Before the opening of the side wall, the axial force value is 584kN, while the axial force value corresponding to the opening span of 4m, 6m, and 8m is 425kN, 364kN, and 294kN respectively, which decreases by 27.23%, 37.64%, and 49.66% compared with that of before the side wall opening. That is, the increasement of axial forces is less than that of the bending moment. Therefore, the opening construction greatly influences the bending moment at the arch foot of the arch structure above the opening area.

The influence of side wall opening on the arch safety

From the above analysis, it can be concluded that the side wall opening greatly influences the force as well as the deformation of the right arch foot. The bending moments as well as axial forces about the secondary lining structure are obtained to check the safety factor, and the safety of the secondary lining of right arch before and after the opening is analyzed. The distribution law of safety factor of the arch body is shown in Figures 10.

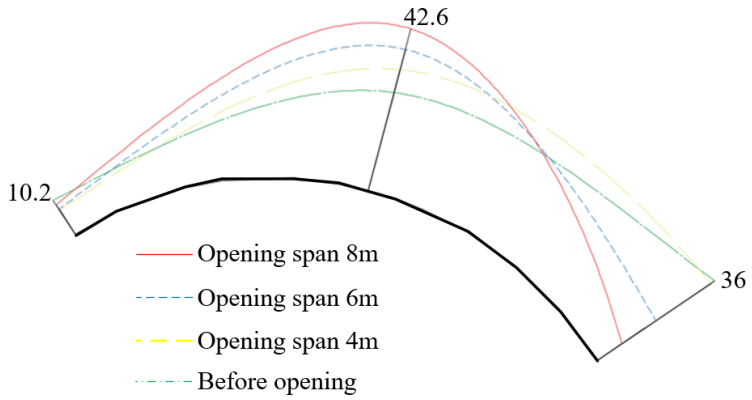

Fig. – 10 Distribution law of the arch safety factor under different opening spans of the side wall

In Figure 10, the influence of side wall opening construction on arch safety factors mainly focuses on the arch body and right arch foot. With the increasement about the excavation span, the safety factor about the arch continues to increase, but that of the right arch foot continues to decrease. Before the opening of the side wall, the safety factor of the right arch foot is 36.0. When the opening span of the side wall is 4m, 6m and 8m, the safety factor of this position is 34.9, 14.6 and 7.5, which is 3.06%, 59.44% and 79.17% lower than that before the opening of the side wall, respectively. When the excavation span increases from 4m to 6m, the safety factor of the position drops sharply. The safety factor of the left side of the arch changes little with the increase of the opening span. From the overall safety factor distribution, when the opening span is less than 6m, the most dangerous position is located at the left arch foot. When the opening span is 8m, the most dangerous position shifts to the right arch foot.

CONCLUSION

Based on the Tianhe East Station Project of Guangzhou Metro Line 11, this paper studies the change law deformation and mechanics of the arch structure of the metro caused by the opening of the side wall with the PBA method. The important findings are listed below.

(1) The settlement caused by the opening of the side wall is mainly concentrated in the upper part of the opening area and gradually expands around the opening area with the increase of the opening span. The affected area is mainly concentrated in the range of 1 time the opening span. The maximum settlement occurs in the middle and upper span, and the growth rate increases with the opening spans.

(2) The arch near the opening area is greatly affected by the opening of the side wall. With the increase of the opening span, the settlement growth trend of the right side of the arch is significantly larger than that of the left side of the arch, and the difference in settlement on both sides is up to 1.38mm.

(3) The construction of the side wall opening causes the arch foot of the opening position to be strained from the outside to the inside. When the excavation span is 4m, 6m, and 8m, the bending moment increases by 69.11%, 217.65%, and 397.06%, and the maximum axial force decreases by 27.23%, 37.64%, and 49.66%, respectively, compared with that before the construction of the side wall.

(4) The influence of side wall opening construction on arch safety factors mainly focuses on the arch body and right arch foot. With the increasement in the excavation span, the safety factor about the arch body continues to increase, while that of the right arch foot continues to decrease, and the safety factor of the left arch foot change little. When the excavation span increases from 4m to 6m, the safety factor at the right arch foot drops by 59.44%.
(5) From the overall safety factor distribution, when the opening span is less than 6m, the most dangerous position is located at the left arch foot. However, when the opening span is 8m, the most dangerous position shifts to the right arch foot.

It should also be noted that the influence of the conditions about symmetrical/asymmetrical opening of left and right side walls as well as the opening shapes on the arch structure of station with PBA method is not considered yet in this paper, more future work can be conducted on it.

COMPETING INTERESTS

The authors have no relevant financial or non-financial interests to disclose.

DATA AVAILABILITY

All data, models, and code generated or used during the study appear in the submitted article.

REFERENCES

[1] Yang, X., Liu, Y., 2017. Monitoring and controlling on surface settlement in sand and gravel strata caused by subway station construction applying pipe-roof pre-construction method (PPM). Stavební Obzor - Civil Engineering Journal, Vol. 26, 179-188. https://doi.org/10.14311/CEJ.2017.02
.0016
[2] Guo, Y., Zhu, Y.F., Pan, W.Q., et al, 2023. Research and application of u-bit construction method in subway station engineering located in saturated soft soil area. Stavební obzor-Civil Engineering Journal, Vol. 32, 108-121. https://doi.org/10.14311/CEJ.2023.01.0009
[3] Huang, P., Wei, L.W., Zhang, X.F., 2021. Study on reinforcement of large arch foot of mined and overlapped metro transfer stations. Modern Tunnelling Technology, Vol. 58, 137-147. https://doi.org/10.13807/j.cnki.mtt.2021.06.016
[4] Lin, D., Broere, W., Cui, J.Q., 2022. Underground space utilisation and new town development: Experiences, lessons and implications. Tunnelling and Underground Space Technology, Vol. 119, 104204. https://doi.org/10.1016/j.tust.2021.104204
[5] Guo, X.Y., Wang, Z.Z., Geng, P., et al, 2021. Ground surface settlement response to subway station construction activities using pile-beam-arch method. Tunnelling and Underground Space Technology, Vol. 108, 103729. https://doi.org/10.1016/j.tust.2020.103729
[6] Guo, X.P., Jiang, A.N., Wang, S.Y., 2021. Study on the applicability of an improved pile-beam-arch method of subway station construction in the upper-soft and lower-hard stratum. Advances in Civil Engineering, Vol. 2021, 6615016. https://doi.org/10.1155/2021/6615016
[7] Yang, Z.X., Yao, A.J., Zhang, D., et al, 2020. Study on settlement control of tunnel closely passing through existing metro station. Chinese Journal of Underground Space and Engineering, Vol. 16, 442-449.
[8] Zhao, J.T., Niu, X.K., Su, J., et al, 2018. Optimization of the construction scheme for a PBA metro station adjacent to an existing metro tunnel. Modern Tunnelling Technology, Vol. 55, 176-185. https://doi.org/ 10.13807/j.cnki.mtt.2018.03.024
[9] Liu, Q.W., Wang, M.S., Hu, S.M., 2013. Control measures for surrounding rock displacement induced by metro station construction with PBA method. China Railway Science, Vol. 34, 61-65. https://doi.org/10. 3969/j.issn.1001-4632.2013.06.10
[10] Huang, S.G., Fu, Z., Liu, J., 2018. Study of soil deformation caused by construction with PBA method. Journal of Railway Engineering Society, Vol. 35, 11-16. https://doi.org/10.3969/j.issn.1006-2106.201
[11] Zhang, J. L., Liu, X., Ren, T. Y., Yuan, Y., Mang, H. A., 2019. Structural behavior of reinforced concrete segments of tunnel linings strengthened by a steel-concrete composite. Composites Part B: Engineering, Vol. 178, 107444. https://doi.org/10.1016/j.compositesb.2019.107444

[12] Zhang, J. L., Liu, X., Ren, T. Y., Shi, Y. M., Yuan, Y., 2022. Numerical analysis of tunnel segments strengthened by steel–concrete composites. Underground Space, Vol. 7, 1115-1124. https://doi.org/10.1016/j.undsp.2022.02.004
[13] Liu, X., Jiang, Z.J, Mang, H. A., 2023. Experimental investigation of the influence of the timing of strengthening on the structural behavior of segmental tunnel linings. Engineering Structures, Vol. 274, 115070. https://doi.org/10.1016/j.engstruct.2022.115070
[14] Liu, X., Gao, Y.M., Zhang, J.L., Zhu, Y.H., 2020. Structural response of main tunnel linings during construction of connecting aisle by means of mechanized drilling. Chinese Journal of Geotechnical Engineering, Vol. 42, 951-960. https://doi.org/10.11779/CJGE202005018
[15] Zhang, C.T., 2014. Mechanical analysis of existing structure removal for transfer station construction. Municipal Engineering Technology, Vol. 32, 90-92.
[16] Du, Z.T., Guo, H.B., 2020. Analysis of side wall reconstruction at existing subway station. Construction Technology, Vol. 49, 109-113. https://doi.org/10. 7672/sgjs2020130109
[17] Xu, B., 2015. On flank punch of existing subway stations. Chinese and Overseas Architecture, Vol. 166, 121-123. https://doi.org/10.19940/j.cnki.1008-0422.2015.02.037
[18] Yuan, C.Y., 2019. Safety analysis of side wall opening at existing subway station. Municipal Engineering Technology, Vol. 37, 106-109.
[19] Wang, B., 2023. Side wall opening reconstruction design of existing metro station. Urban Mass Transit, Vol. 26, 78-81. https://doi.org/10.16037/j.1007-869x.2023.01.015
[20] Hu, Z.N., Mao, H.T., Zhang, L.X., et al, 2023. Experimental tests and theoretical analysis for mechanical behaviors of side wall opening construction in mined excavation subway station. Frontiers in Earth Science, Vol. 11, 1127078. https://doi.org/10.3389/feart.2023.1127078
[21] An, D.H., Shao, W., 2020. Analysis on the effect of the expansion and reconstruction of the metro station on the stress of original structures. Railway Standard Design, Vol. 64, 129-135. https://doi.org/10.13238/j.issn.1004-2954.201911060004
[22] Li, C.J., Wang, L.X., Hu, R.Q., et al, 2019. Study on mechanical behavior of transfer and reconstruction of metro stations in loess area. Railway Standard Design, Vol. 63, 101-109. https://doi.org/10.13238/ j.issn.1004-2954.201811110004
[23] Wang, Q.S., 2021. Transfer reconstruction technology of existing subway station during operation. Railway Construction Technology, Vol. 340, 116-120. https://doi.org/10.3969/j.issn.1009-4539.2021. 07.025
[24] An, D.H., Shao, W., 2020. Analysis on the effect of the expansion and reconstruction of the metro station on the stress of original structures. Railway Standard Design, Vol. 64, 129-135. https://doi.org/10.13238/j.issn.1004-2954.201911060004
[25] Guo, R., Zheng, B., Li C., 2019. Settlement law and its influence range of tunnel crossing underneath loose high filling embankment. Tunnel Construction, Vol. 39, 601-608. https://doi.org/10.3973/j.issn.2 096-4498.2019.04.010

CIVIL ENGINEERING JOURNAL

Article no. 31

THE CIVIL ENGINEERING JOURNAL 3-2023

INVESTIGATION ON THE ROCK-FRAGMENTATION PROCESS OF CONICAL-SHAPED TBM CUTTERHEAD IN EXTREMELY HARD ROCK GROUND

Shijun Chen[1], Xinyu Jin[2], Rucheng Hu[1], Fei Liu[1] and Zhongsheng Hu[1]*

1. *The Electricity Engineering CO., LTD under CREC NO.5 Group, Changsha, Hunan District, 410205, China; 764193226@qq.com, 876111908@qq.com, 2279227407@qq.com, 2575641835@qq.com*
2. *School of Construction Machinery, Chang'an University, Xi'an 710064, China; 2474535362@qq.com*

ABSTRACT

The main objective is to clarify the rock-fragmentation mechanism of a conical-shaped Tunnel Boring Machine (TBM) cutterhead that has rarely been investigated before. The main method is a numerical simulation which is verified by laboratory rock-fragmentation tests. The research process is as follows: Firstly, the numerical model is designed based on cutting mode analysis; Then, the rock sample is synthesized using a Grain-based Discrete Element Method (GDEM) that is verified via scaled rock-fragmentation tests; Finally, a series of numerical simulations are conducted to study the influence of cutterhead cone angle, cutter spacing, and cutter installation angle on the rock-fragmentation performance. The main findings are as follows: First, the rock fragmentation mechanism of conical-shaped TBM cutterhead is free-face-assisted rock breaking; Second, the rock-fragmentation efficiency can be improved by appropriately increasing the conical angle, reducing the cutter spacing, and increasing the cutter installation angle; Third, for the studied granite, the optimal conical angle is 25°, the tilt cutter spacing is suggested to be no more than 70 mm, and the cutter tilt angle is suggested to be no more than 3°. This study reveals the rock fragmentation mechanism of conical-shaped TBM cutterhead and provides suggestions for cutterhead design.

KEYWORDS

Full-face tunnel boring machine, Conical-shaped cutterhead, Disc cutter, PFC, rock-fragmentation mechanism

ABBREVIATIONS

TBM	Tunnel boring machine
GDEM	Grain-based discrete element method
D&B	Drilling and blasting
UCS	Uniaxial compressive strength
BTS	Brazilian Tensile Strength
LCM	Linear cutting machine
CCS	Constant cross-section
PSE	Penetration specific energy
FJM	Flat-jointed method

* Corresponding author

LIST OF SYMBOLS

H	The height of each stage in mm
D	The distance from the cutter penetration point to the stage edge in mm
S	Cutter spacing in mm
α	The cutterhead conical angle
β	The cutter tilted angle
F_{NP}	The peak penetration force;

INTRODUCTION

Full-face Rock Tunnel Boring Machine (TBM) cutterheads can have a cone, dome, or flat shape [1]. The flat-profile cutterhead has been widely used owing to its advantages in geological adaptability, manufacturing, and thrust utilization. Although the other cutterheads are less applied in engineering projects, they have their advantages such as higher structural strength and rigidity [2], higher rock-breaking efficiency [3-4], and lower cutter side slipping level [5]. Zhang et al. [6-7] found that the thrust of a conical-shaped cutterhead can be reduced by properly designing the conical angle. Liu et al. [8] analyzed the adaptability of conical-shaped cutterhead under different ground conditions, and found that the conical-shaped cutterhead is suitable for hard grounds due to its stability during tunneling. Zhang et al. [9] analyzed the vibration characteristics of the conical-shaped cutterhead applied in Dahuofang hydraulic tunnel in China and deduced that the abnormal vibration is caused by the radial alternate rock-breaking load. According to the above review, the study on the structural characteristics and tunneling performance of the conical-shaped cutterhead is very insufficient. Moreover, the relative research mostly stays at the level of theoretical analysis. Furthermore, almost no studies have been conducted and reported for the rock-fragmentation mechanism of conical-shaped cutterhead, resulting in a very limited basis for the cutterhead structure and cutter layout design.

We think that the critical rock-fragmentation mechanism of conical-shaped TBM cutterhead is free-face-assisted rock breaking. This is because the tunnel face is excavated as a multi-step cone by the tilt-installed disc cutters, as shown in Figure 1a. The front steps provide free faces to assist the rock fragmentation of cutters in the back. Thus, the rock fragmentation efficiency may be significantly improved especially in extremely hard rock ground. There are many rock-fragmentation studies based on the free-face-assisted rock-breaking theory, which can provide references for this study. Innaurato et al. [10] conducted indentation tests on hard limestone and extremely hard granite and found that the rock-breaking efficiency can be significantly improved under side-free-face conditions. Ramezanzadeh et al. [11] reported a multi-arm type and a reaming type undercutting roadheader that disc cutters break rock under free-face conditions. Based on these machines, Jiang et al. [12] simulated the rock-breaking process of a disc cutter under side free face and pre-slotting conditions. The results proved that the free-face-assisted methods provide a potential approach for efficiently breaking hard and extremely hard rock. Geng et al. [13-14] proposed the structural scheme of a multi-stage TBM cutterhead and systematically discussed the dynamic evolution mechanism of the side free faces. On this basis, Xia et al. [15] and Zhang et al. [16] carried out full-scale linear cutting tests and simulations on hard granite to study the influence of free-face spacing on the rock-breaking performance. Xu et al. [17] carried out full-scale rotary cutting tests on hard granite to study the critical threshold of free-face spacing. Wang et al. [18] simulated the rock indentation process induced by TBM cutters under different free-face conditions using a grain-based DEM approach, and discovered that there exist two critical thresholds for the free-face height and spacing respectively. Shang et al. [19] simulated the rock fragmentation process caused by TBM disc cutters under free-face-assisted conditions using a peridynamics model. The results can guide the cutter layout design. Bilgin et al. [20] thought that waterjet-assisted cutting may be the most promising method when used in combination with mechanical cutting tools. The essence of a high-pressure hydraulic coupling rock breaking is to use high-pressure abrasive water jet to prepare kerfs in the surrounding rock to form free faces, to improve the rock-breaking efficiency of cutters. Based on this, Zhang et al. [21] carried

out full-scale linear cutting tests induced by a disc cutter on hard rock that narrow kerfs had been prepared by waterjet. Results show that the cutter's normal force was decreased by 40% and the rock-breaking efficiency was significantly improved. Geng et al. [22] built rock indentation numerical models of disc cutters under different kerf conditions using a Grain-based Discrete Element Method (GDEM). The influence of the precut-kerf structure on the rock-fragmentation mechanism was investigated and some suggestions for high-efficiency rock breaking were given. Cheng et al. [23] carried out an experimental and numerical study on the indentation behavior of TBM disc cutter on hard-rock precutting kerfs by high-pressure abrasive waterjet. The results show that the average peak force decreases significantly with the increase of the kerf depth. Li et al. [24-25] conducted full-face linear cutting tests and numerical simulations on pre-grooved rock to study the influence of cutting modes, pre-groove depth, and pre-groove spacing on assisted rock breaking performance. The results can inspire the design of waterjet-coupling TBMs. Zhou et al. [26] conducted static penetration tests on a rock with pre-cutting grooves to study the influence of groove depth on the rock-breaking mechanism.

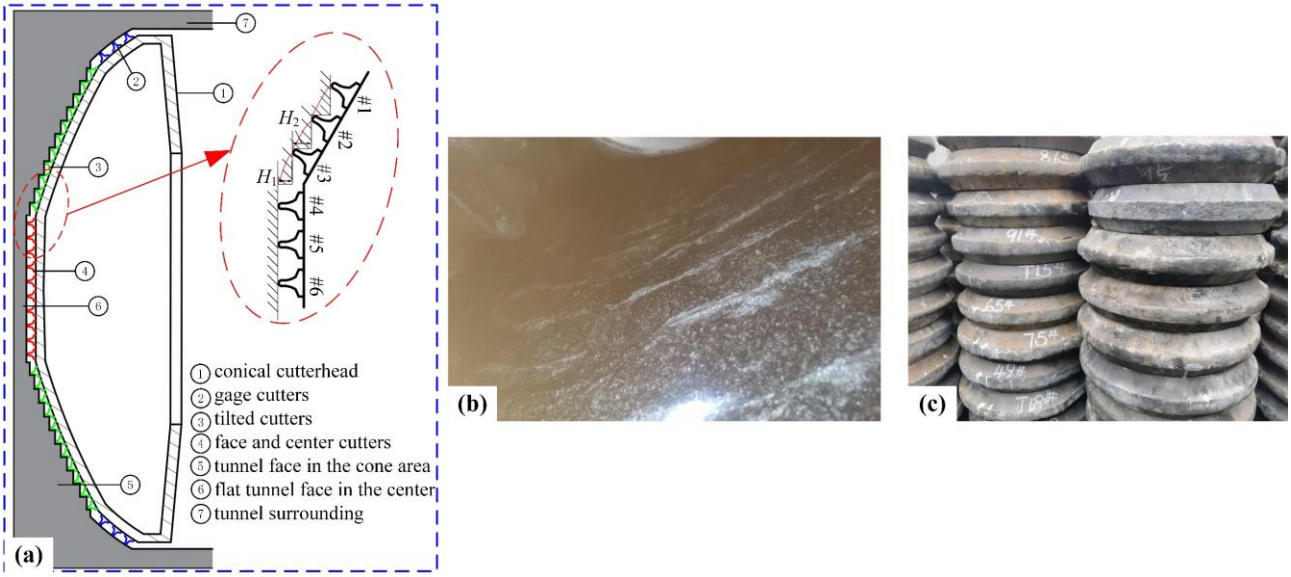

Fig. – 1 (a)Schematic diagram of rock excavation by a conical TBM cutterhead; (b) tunnel face in the extremely hard rock; (c) severe cutter wear.

The above study shows that the free face is an effective method to improve the rock-breaking efficiency of disc cutters. Exploration and research have been carried out based on various TBM equipment and cutterhead. However, there are few reports on the mechanism of free-face-assisted rock breaking of conical-shaped cutterhead, although it is much easier for practical implementation than the other designs such as the undercutting TBM, multi-stage cutterhead, and waterjet-assisted TBM. As a result, aiming at the problem encountered in the Zijing tunnel that the rock-breaking efficiency is low and cutter consumption is high, a conical-shaped cutterhead is assumed to be applied in the extremely hard rock ground and the rock-fragmentation mechanism is investigated. Firstly, a GDEM numerical model for the rock-fragmentation process of a conical-shaped cutterhead was built. Then, factors of cutterhead cone angle, cutter spacing, and cutter installation angle were studied in detail to explore their influence on the rock-fragmentation performance. This study can fill in gaps in the rock-fragmentation mechanism of the conical-shaped TBM cutterhead and can provide some suggestions for the cutterhead design.

PROJECT OVERVIEW

As shown in Figure 2, the Zijing Tunnel is between Yingxiu Town and Gengda Town in Sichuan Province, China. The tunnel has an entrance mileage of DK35+667 and an exit mileage of DK46+084, with a total length of 10413 m. The drilling and blasting (D&B) method is applied for 414 m excavation, a TBM is applied for 5199 m excavation, and the drilling and splitting (D&S) method is applied for 4800 m excavation. It is a single tunnel with double tracks and a maximum buried depth of about 709m. An open-type TBM was developed for the 5199 m-length tunnel excavation. The total length of the TBM is 222 m, the length of the main machine is 25 m, the total weight of the TBM is about 2500 t, the total installed power is 7613.2 kW, and the maximum thrust is 27586 kN. The cutterhead is a flat-face type and is 10.23 m in diameter. A total of 4 double-ring center cutters (432 mm in diameter) and 58 single-ring face and gage cutters (483 mm in diameter) are installed on the cutterhead. As shown in Fig. 1(b), when the TBM excavates in the mileage from DK 37+000 to DK 37+419, extremely hard diorite with uniaxial compressive strength (UCS) of approximately 250 MPa and Brazilian Tensile Strength (BTS) of approximately 20 MPa was frequently encountered; when the TBM excavates in the mileage from DK 37+509 to DK 39+150, hard granite whose UCS was approximately 180 MPa was frequently encountered. When the TBM excavates in these grounds, the rock is mainly ground into powder or small chips, resulting in a very low advancing rate and severe cutter wear, as shown in Fig. 1(c). For example, the advance distance per day and the TBM thrust is given in Fig. 3 when the TBM excavates in the mileage from DK 37+000 to DK 37+400 in hard diorite-dominated ground. The TBM was stopped due to the maintenance of the main belt from December 28, 2022, to February 17, 2023. Thus, there are no data for this period. The average thrust is approximately 24870 kN, which is 90% of the maximum thrust. However, the average advance distance per day is 8.2 m per day, which is quite low. There are some days that the advance distance is lower than 4 m, indicating that the advance rate and rock-breaking efficiency are very low.

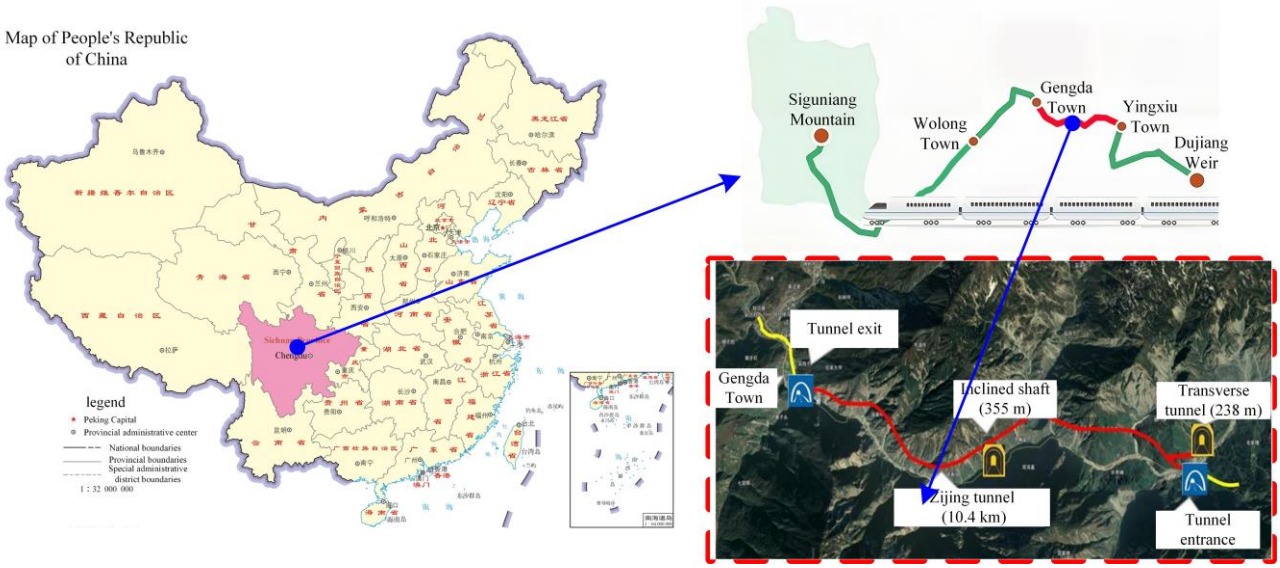

Fig. 2 - General view of the location of the studied Zijing Tunnel Project

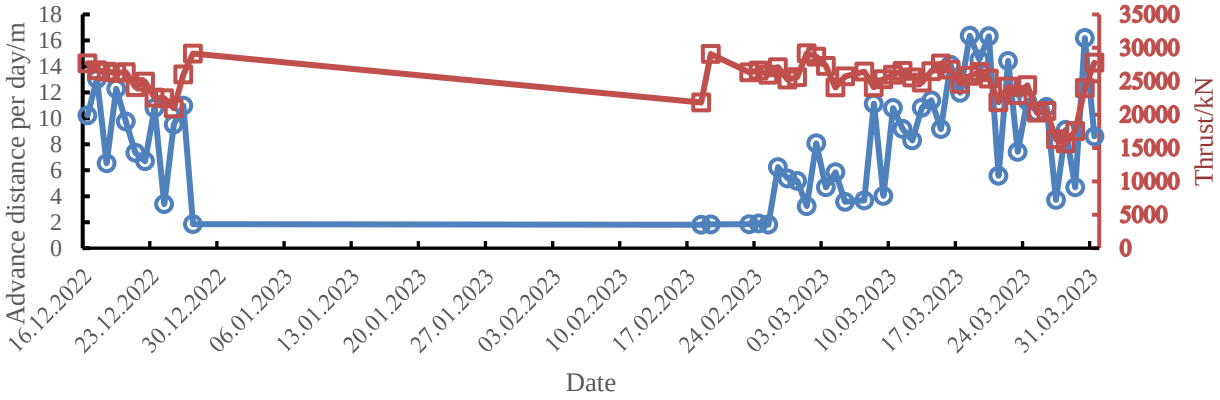

Fig. 3 - The advance distance per day and the TBM thrust in the mileage from DK 37+000 to DK 37+400

CALCULATION INSTRUCTIONS OF THE NUMERICAL SIMULATION

Calculation model

PFC2D software is used in this paper. According to the schematic diagram of rock excavation by a conical TBM cutterhead shown in Fig. 1(a), the typical calculation model is built as illustrated in Figure 4. Three normal cutters numbered #4 to #6 and three tilted cutters numbered #1 to #3 are considered. As several studies (e.g. [10, 27, 28]) have verified the appropriateness of the two-dimensional equivalent model, disc cutter indentation is considered a plane problem. Six cutters are included in the numerical model considering the simulation cost. The rock-breaking of the six cutters can represent the general performances of the normal and tilted cutters.

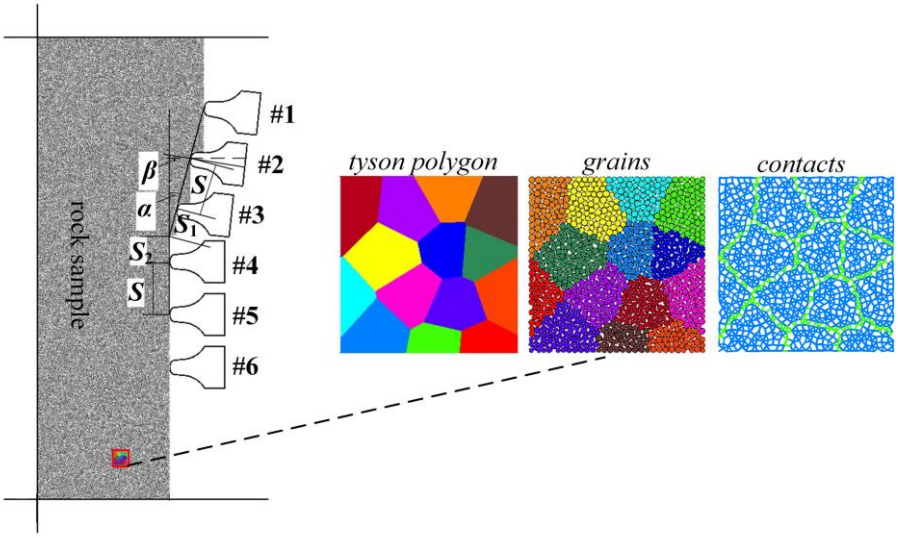

Fig. 4 - Numerical calculation model

Because the essence of the rock-fragmentation of conical-shaped cutterhead is free-face-assisted rock breaking, the height (H) of each stage and the distance (D) from the cutter penetration point to the stage edge are the critical structural factors affecting the rock fragmentation performance. Thus, three factors that determine the H and D are considered in the calculation model, which is the cutter spacing (S), the cutterhead conical angle (α), and the cutter tilted angle (β). It is assumed that the spacing of the normal cutters and the spacing of the tilted cutters are equal, both are S, and the spacings in the transition area are $S_1 = S_2 = S/2$. The cutterhead conical angle (α)

represents the angle between the enveloped surface of the ring tips of the tilted cutters and the flat surface in the front. The cutter tilted angle (β) represents the angle between the center surface of the cutter ring and the vertical line of the cone surface. The disc cutters are modeled by rigid wall elements in the PFC2D software. The maximum penetration displacement of the cutters is 3 mm. Referring to existing research [22], the penetration speed is set as 0.02 m/s, and the time step is 5.5×10^{-8} s to ensure the quasi-static penetration state.

Rock can be regarded as a granular discrete medium. Thus, the rock sample was synthesized using a GDEM approach. This approach is an optimization of the regular Parallel-Bonding (PB) method to solve its shortage of large errors for the UCS/BTS ratio [29]. The interlocking friction along irregular rock grain boundaries can be simulated by using the GDEM approach, and the fractures that follow the grain boundaries and traverse the grain body can be both simulated. This approach is becoming popular and has been applied by several researchers, proving its reasonability and effectiveness [17, 28, 30-31]. The GDEM modeling process is shown in Fig. 4. Firstly, the Tyson polygon algorithm is used to divide the rock into different polygons. Secondly, the rock area is filled with spherical particles, and the particles are grouped according to the polygons to characterize different rock grains. The color of rock grains in the same group is the same. Thirdly, the contact bonds with different meso mechanical parameters are added between the particles and the walls. The contacts between the particles are divided into intragranular contact (blue short line) and intergranular contact (green short line). The intragranular contact and intergranular contact parameters are calibrated and assigned. The contacts between the particles and the walls are not illustrated.

Proper selection of the particle packing and contact parameters are a critical problem that determines the accuracy of the DEM model. However, for a particle aggregating system, the relationships between the particles' mesoscopic parameters and the sample's macroscopic physical properties are very complex and cannot correspond one-to-one. As a result, scholars usually use a trial-and-error method to obtain the mesoscopic parameters of particles based on UCS and BTS tests and simulations, which is also called parameter calibration. UCS and BTS tests were carried out to obtain the macroscopic physical parameters of rock samples. UCS tests are performed on trimmed core samples, which have a diameter of 50 mm and a length-to-diameter ratio of 2. BTS tests are conducted on core samples having diameter of 50 mm and a length-to-diameter ratio of 1. Groups of UCS and BTS tests were simulated for the rock synthesized using the GDEM approach described in the preceding paragraph. To reduce the number of independent parameters during calibration, several assumptions were made according to previous publications [28-29, 32-33]: (i) the density of the particles was determined by the realistic density of the rock material, (ii) the particle radius was smaller than 0.9 mm and the porosity was approximately 0.1 for two-dimensional models, (iii) Young's modulus was determined by the effective modulus 'emod' and the Poisson's ratio was determined by the stiffness ratio 'kratio' and 'pb_kratio', (iv) the 'emod' of the particles and bonds was set the same and so was the stiffness ratio. During the UCS and BTS simulations, the loading speed was set to 0.02 m/s with a time step of 5.5×10^{-8} s to ensure that the simulation is quasi-static penetration. The obtained meso mechanical parameters of granite are shown in Table 1, and the obtained macro mechanical parameters of rock are shown in Table 2. The micromechanical parameters of Set 1 are used for model calculation, and the micromechanical parameters of Set 2 are used for model verification. The errors between the elastic modulus, Poisson's ratio, UCS, and BTS of the rock model and the actual rock are within 5%, which indicates that the numerical model is reliable. To further prove the GDEM accuracy and discuss the sensitivities of particle parameters on the results, another UCS and BTS simulations were conducted using the PB method. The obtained parameters and properties are listed in Set 1-1. Compared with Set 1, the only difference in the mesoscopic parameter setting is ignoring the grain representation. Results listed in Tab. 2 show that the E and υ of Set 1 and Set 1-1 are almost the same since they are determined by the 'emod', 'kratio' and 'pb_kratio' as assumed before. The UCS and BTS of Set 1-1 are obviously increased and decreased respectively compared with those of Set 1, confirming the effectiveness of GDEM in improving the model accuracy. Comparing Set 2 with Set 1, the particle packing

parameters including the ball radius, porosity, and grain size are different. Thus, the contact parameters are also varied to obtain the target values of E, υ, UCS, and BTS. The above analyses indicate that the simulation results are sensitive to the particle packing and contact parameters. That's why great efforts have been spared by scholars to develop modeling and calibration approaches. Following the above assumptions during calibration, a unique set of contacting parameters can be obtained for a set of given packing parameters. This can ensure the stability of the simulation results.

Tab. 1 - The mesoscopic parameters of the rock sample (note: Set 1 and Set 2 use GDEM and Set 1-1 uses PB method)

Parameters	Set 1	Set 1-1	Set 2
Ball density (kg/m3)	2610	2610	2610
Porosity	0.1	0.1	0.075
Ball radius (mm)	0.5±0.1	0.5±0.1	0.025±0.05
emod /GPa	20	20	19
kratio	1.2	1.2	1.4
Intragranular friction coefficient	0.52	0.52	0.52
Intergranular friction coefficient	0.44		0.44
pb_emod (GPa)	20	20	19
pb_kratio	1.2	1.2	1.2
Intragranular pb_ten (MPa)	90±9	90±9	200±20
Intergranular pb_ten (MPa)	70±7		50±5
Intragranular pb_coh (MPa)	90±9	90±9	200±20
Intergranular pb_coh (MPa)	90±9		50±5
Average grain size /mm2	3.2	/	1.6

Tab. 2 - The mechanical properties of the actual rock and the rock sample (note: Set 1 and Set 2 use

Properties	Test	Set 1		Set 1-1		Set 2	
		Sample	Error/%	Sample	Error/%	Sample	Error/%
Modulus, E/GPa	38.6	40.1	3.9	40.1	3.9	39.6	2.5
Poisson's ratio,υ	0.170	0.1697	0.2	0.1642	0.3	0.168	1.1
UCS/MPa	177.9	176.8	0.6	191.6	7.7	185.3	3.9
BTS/MPa	12.6	12.0	2.4	11.8	6.3	12.64	0.3

GDEM and Set 1-1 uses PB method)

Introduction to the test platform

As shown in Figure 5, a small-scale linear cutting machine (LCM) was used in this study to verify the numerical model. The rationality of using small-scale LCM to investigate the rock-breaking mechanism of disc cutters should be stated first. According to several similar studies [34-36], the rock-breaking theory of small disc cutters is almost identical to that of full-scale disc cutters, considering the critical problems of dense core and side crack evolution. In addition, the stiffness of the small-scale LCM can be ensured by using a thick steel frame, high-strength bearing, and strong cutter ring. As a result, small-scale tests are becoming more and more popular in investigating the rock-breaking process of TBM disc cutters. The applied small-scale LCM can perform linear rock-breaking tests under different confining pressure conditions. The working principle of this platform is similar to that of a full-scale LCM [15, 25, 37-39]. It has the advantages of a similar rock-breaking mechanism to the actual TBM cutter, a high utilization rate of rock samples, convenient confining pressure loading, and convenient rock-breaking load acquisition. A disc cutter and a three-directional force sensor are installed on the vertical lifting plate. The cutter is adjusted to the set cutting position via a screw and is then fixed. The rock is placed into the inner layer of the double-layer specimen box. The confining pressure sensor and lateral hydraulic cylinder are installed between the inner and outer layers of the specimen box for rock clamping and confining pressure loading (maximum to 40 MPa). The specimen box is integrally installed on two horizontal slide rails and moves along the horizontal direction through the drive system composed of a stepping motor, reducer, and lead screw. Based on this, the relative linear rolling cutting motion between the cutter and the rock can be realized, which is consistent with a full-scale LCM. The test platform can accommodate the largest cuboid rock sample of 500 × 200 × 100 mm. Using the three-directional force sensor, the cutter's normal force, rolling force, and side force can be collected and recorded. The data sampling frequency is 5 Hz and the sampling accuracy is 1 N. For rock-breaking by full-scale disc cutters, the linear cutting speed is approximately 1.5 m/s and the data sampling frequency is higher than 20 Hz [40]. It means that the rock-breaking forces are sampled at the maximum cutting distance interval of 75 mm. For the small-scale tests, although the data sampling frequency is only 5 Hz, the linear cutting speed can be very low (1.2 mm/s in this study), resulting in a sampling interval of 0.24 mm, which can ensure the integrity of the sampled data. The normal force in the small-scale test is usually several kilonewtons, meaning that the relative sampling accuracy is higher than 0.1%.

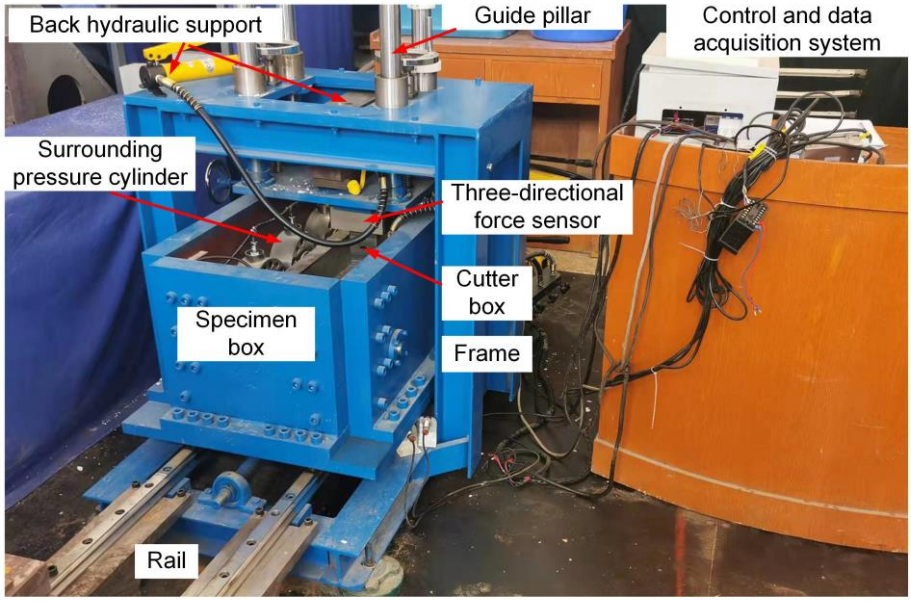

Fig. 5 - Small-scale linear cutting machine (LCM)

Verification of the numerical model

The numerical model is tested and verified to prove the reliability of the numerical model. As discussed above, the essence of the rock fragmentation of conical cutterhead is free-face-assisted rock breaking. As a result, a small-scale linear cutting test under a side-free-face condition and a small-scale cutter penetration simulation under a side-free-face condition were performed and compared.

The rock-breaking test result is shown in Figure 6(a). The rock sample in the test is 320×100×100 mm. The sample surface was first trimmed and polished, and then placed into the specimen box and fixed. Two steel blocks with a thickness of 30 mm were placed on the bottom side of the rock so that a side-free face with a height of 40 mm was prepared. The spacing between the cutting line and the side-free face was 15 mm. The applied cutter was a small-scale constant cross-section (CCS) cutter with a diameter of 43.2 mm and a ring tip width of 1.2 mm. During the test, the cutter remained stationary, and the specimen box was moved linearly along the rails at a speed of 1.2 mm/s driven by the stepping motor. The peak normal force of the test was recorded as 6.7 kN, and several triangular rock debris was formed on the right free face.

The rock-breaking simulation result is shown in Figure 6(b). The rock sample is 100×60 mm and the height of the side free face is 40 mm. The spacing between the cutter penetration point and the side free face is 15 mm. The sizes of the cutter are identical to those of the cutter applied in the test. The rock sample was synthesized using the Set 2 microscopic parameters given in Table 1 and the mechanical properties of the rock sample are shown in Table 2. The cutter penetrated the rock with a speed of 0.02 m/s until the rock in the free-face side was split into a triangular chip. Using the equation proposed by Xu et al. [17], the two-dimensional penetration force obtained from the simulation was converted into an equivalent value of a three-dimensional situation as 7.3 kN, with an error of 11% compared with the test. The shape of the rock debris was like a triangle, which was very similar to the test result. Parameters in Set 2 rather than Set 1 were used to build the scaled indentation model considering the coordination of particle size and cutter tip width. The similarity of the rock-breaking results for the scaled test and simulation can verify the reliability of the GDEM numerical model. Thus, full-scale simulations considering large particles of Set 1 are justified.

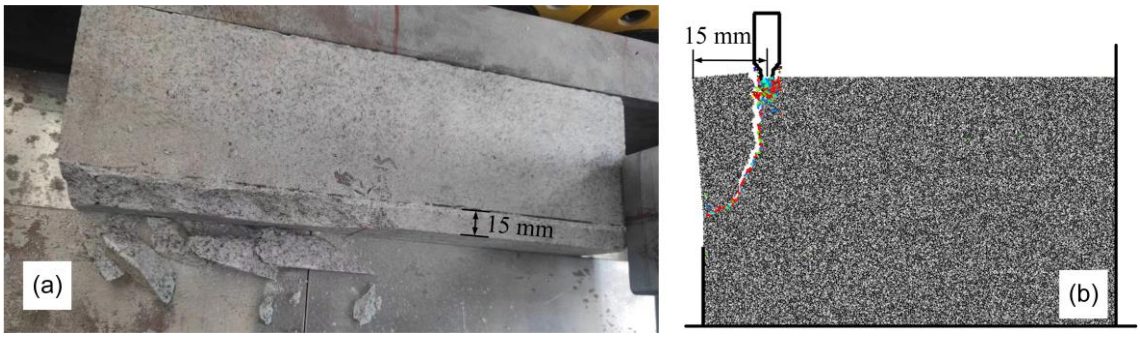

Fig. 6 - Comparison of the rock-breaking test and simulation

SIMULATION RESULTS AND DISCUSSION

Influence of cutterhead conical angle on rock breaking

To explore the influence of cutterhead conical angle α on rock breaking, 10 groups of simulations were performed. The independent variable α was set as 5°, 8°, 10°, 13°, 15°, 18°, 20°, 23°, 25° and 28°, respectively. The dependent variables were the penetration force of each cutter and the rock debris area. The constant variables through the simulations were cutter spacing (S, 80 mm) and cutter tilted angle (β, 0°).

The rock-breaking performance under different α is shown in Figure 7. With the increase of α, the rock-crushing performance induced by face cutters #4 to #6 does not change obviously. The

main damage pattern is shear-type crushing beneath the cutter tip. Some radial cracks initiate and propagate along the penetration direction, while few lateral cracks develop. This results in only a little small rock debris between neighbouring cutters but much powder beneath the cutters. This is possible because the *S* of 80 mm is too large for the studied hard rock to achieve high-efficiency rock-breaking by the normal cutters.

With the increase of *α*, the rock-crushing performance induced by tilt cutters #1 to #3 changed significantly. When *α* is smaller than 15°, even if some macro cracks are generated beneath the tilt cutters, there is little large rock debris. When *α* is greater than 18°, the macro cracks beneath the tilt cutters extend toward the side free faces, generating triangular rock debris. When *α* is greater than 25°, large rock debris forms between the three tilt cutters. This is because the height of the free face ($H=S\cdot\sin\alpha$) increases and the distance ($D=S\cdot\cos\alpha$) between the penetration point and the side free face decreases, both improving the promoting effect of side free face on crack propagation and thus improving the rock-breaking efficiency of the tilt cutters. This is because the rock-breaking difficulty is in positive and negative correlation with *D* and *H*, respectively, according to Geng et al. [14]. The rock-breaking of conical-shaped cutterhead also follows this law.

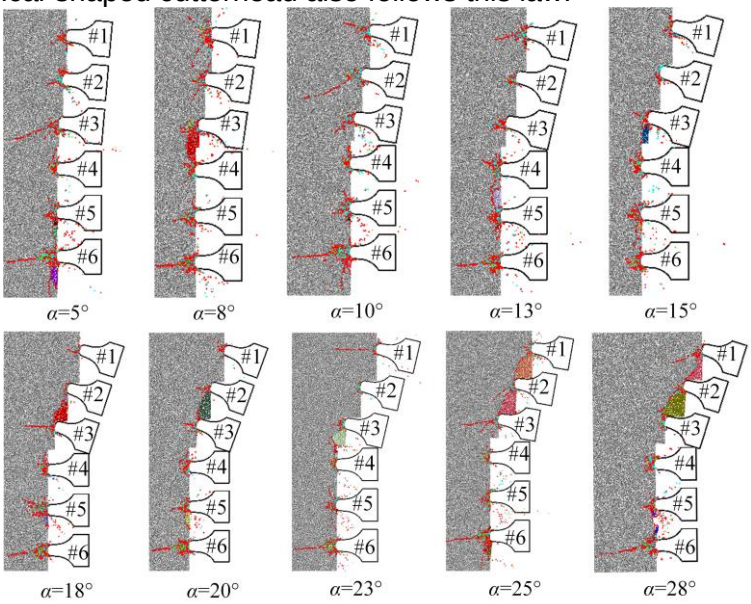

Fig. 7 - Rock-breaking performance under different cutterhead conical angles, α

As shown in Figure 8, the average values of the peak penetration force (F_{NP}) of the tilt cutters #1 to #3 are lower than those of the normal cutters #4 to #6. This is because the side-free face can effectively reduce the cutter penetration force which has been proved by some previous studies [10, 13, 14]. Furthermore, the average F_{NP} of normal cutters does not change with the increase of *α*, while the average F_{NP} of tilt cutters is obviously affected by *α*. These results indicate that conical angle *α* can help reduce the cutter penetration force and hence improve the rock-breaking efficiency. When *α* increases from 10° to 15°, there is a significant drop in F_{NP}; after that, the F_{NP} is generally stable as *α* increases. This means that for the studied models there exists a critical angle of 15° that the promoting effect for reducing the cutter penetration force by the free faces induced by the conical angel *α* is fully exploited. The peak penetration force of the tilt cutters is estimated to be reduced by approximately 50% compared with that of the normal cutters when *α* is larger than 15°.

The overall penetration specific energy (PSE) of the six cutters #1 to #6 is calculated as the energy required to produce unit volume (area for two-dimensional situation) of rock debris, which is used to evaluate the rock-breaking efficiency. For three-dimensional conditions, the rock-breaking specific energy is mainly affected by cutter rolling force and rock chip area [38]. However, in two-dimensional conditions, the cutter rolling force is ignored and thus the cutter penetration force is used to calculate PSE. This indicator is reasonable and has been widely applied in two-dimensional simulations and tests [17, 22]. As shown in Figure 8, as *α* increases from 5° to 10°, the *PSE* increases

to a peak value; as *α* increases from 10° to 25°, the *PSE* decreases to the lowest value. This is because the *PSE* is determined by both the penetration force and the rock debris area. Even though the F_{NP} will not decrease significantly after the *α* is larger than 15°, more debris will be produced after the *α* is larger than 25°. Based on the above analysis, it is suggested that the critical value of the cutterhead conical angle *α* is 25°, to achieve low cutter penetration force and high rock-breaking efficiency.

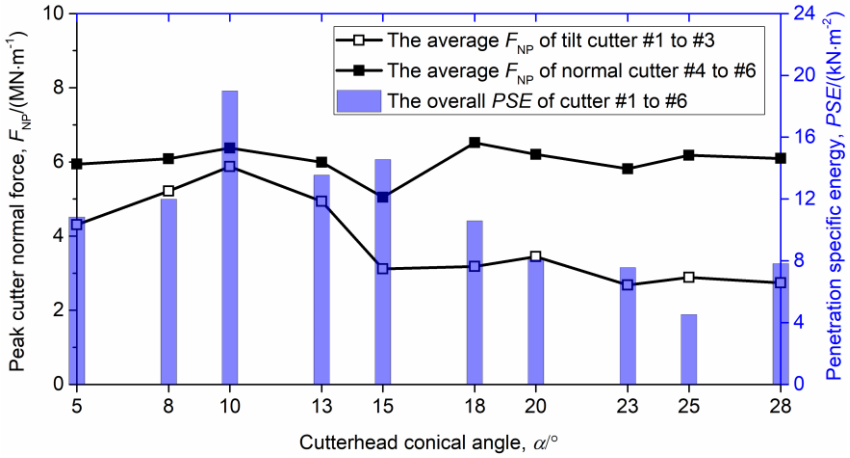

Fig. 8 - Rock-breaking normal force and specific energy under different cutterhead conical angles, α

Influence of cutter spacing on rock breaking

To explore the influence of cutter spacing *S* on rock breaking, 8 groups of simulations were performed. The independent variable *S* was set as 60, 65, 70, 75, 80, 85, 90, and 95, respectively. This parameter setting is based on the common rule that the TBM cutter spacing for hard rock conditions is usually in the range of 60-90 mm [24-25]. The dependent variables were the penetration force of each cutter and the rock debris area. The constant variables through the simulations were cutterhead conical angle cutter spacing (*α*, 15°) and cutter tilt angle (*β*, 0°).

The rock-breaking performance at different *S* is shown in Figure 9. The macro cracks beneath the face cutters #4 to #6 are difficult to connect, and thus there is no large rock debris produced between the neighbouring face cutter. This is because the rock is too hard and the confining stress that may promote rock breaking is not considered in this study [39]. When *S* is smaller than 70 mm, the macro cracks beneath the tilt cutters #1 to #3 can connect, and thus large triangular rock debris can be produced. When *S* is larger than 70 mm, it is difficult to produce large rock debris between neighbouring tilt cutters. The reasons are as follows: firstly, it has been proved that the increase of the free-face height (H=S·sin*α*) and the decrease of the distance (D=S·cos*α*) between the penetration point and the side free face can promote the rock-breaking performance, and vice versa [15]; Secondly, although *H* increases with the increase of *S* and the auxiliary rock-breaking of the free face can be promoted, *D* also increases with the increase of *S* and the promotion effect of free face on rock breaking is weakened and further suppresses the positive effect of *H*. Therefore, the rock-breaking performance of the tilt cutter in the conical area decreases with the increase of the cutter spacing.

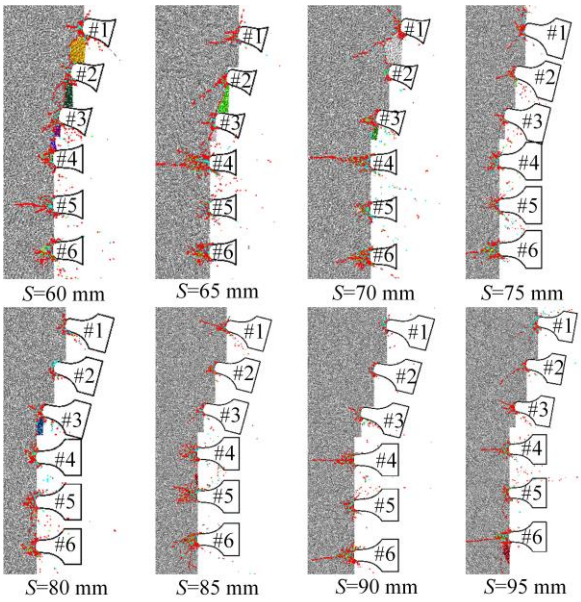

Fig. 9 - Rock-breaking performance under different cutter spacing, S

As shown in Fig. 10, the average values of the peak penetration force (F_{NP}) of the tilt cutters #1 to #3 are lower than those of the normal cutters #4 to #6. Furthermore, the average F_{NP} of normal and tilt cutters does not change obviously with the increase *S*. This is because the rock is too hard and it is difficult for the cracks initiating from neighbouring cutters to propagate and intersect with each other. There exists a critical value of 70 mm for *S* considering the *PSE*. When *S* is lower than 70 mm, the *PSE* is lower than those of the models when *S* is larger than 80 mm. This is because when *S* is lower than 70 mm, large rock debris can be formed between neighbouring tilt cutters. It is acknowledged that too small cutter spacing will increase the number of cutters and increase the difficulty of cutter installation. Thus, based on the studied models, it is suggested that the optimal cutter spacing for the tilt cutters is smaller than 70 mm, and the cutter spacing for the normal cutters should be smaller than that of tilt cutters.

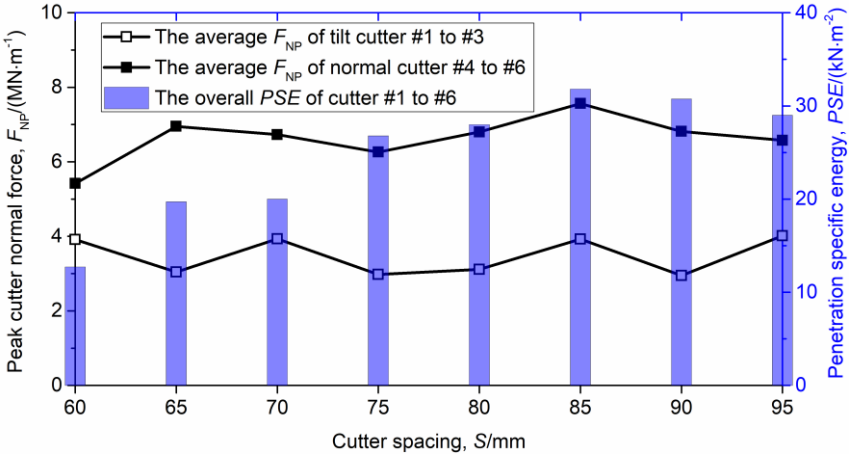

Fig. 10 - Rock-breaking normal force and specific energy under different cutter spacing, S

Influence of cutter tilt angle on rock breaking

To explore the influence of cutter tilt angle *β* on rock breaking, 9 groups of simulations were performed. The independent variable *β* was set as 0°, 1°, 3°, 5°, 7°, 9°, 11°, 13° and 15°, respectively. The dependent variables were the penetration force of each cutter and the rock debris area. The

constant variables through the simulations were cutterhead conical angle cutter spacing (α, 15°) and cutter spacing (S, 80 mm).

The rock-breaking performance at different β is shown in Figure 11. The rock-breaking performance in the rock area of the normal cutter has no obvious change trend. The crack beneath the # 6 normal cutter is the deepest, because it is located at the bottom, and it is less affected by the rock breaking of neighbouring cutters. When β is larger than 9°, there is only small rock debris generated beside the #3 tilt cutter in the conical area. When β is lower than 7°, side cracks initiate from the bottom of the tilt cutters and begin to extend to the side-free face, and thus large rock debris begins to be produced beneath the tilt cutters. The weight of rock debris decreases with the increase of β.

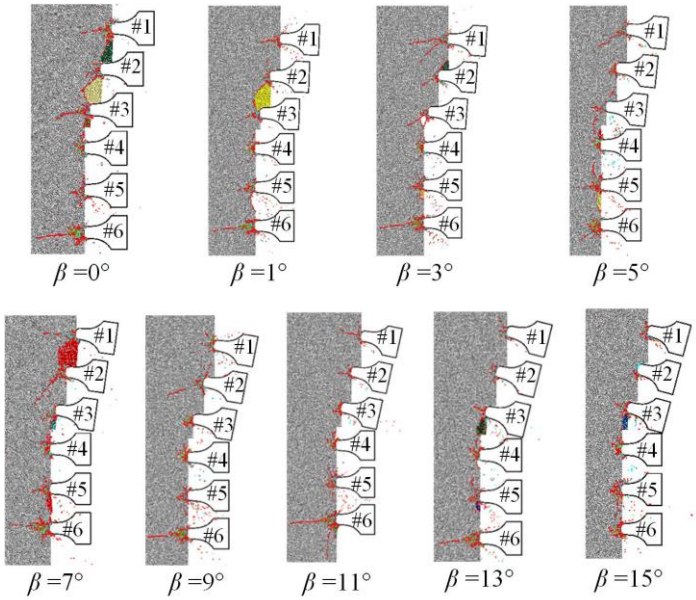

Fig. 11 - Rock-breaking performance under different cutter tilt angles, β

As shown in Figure 12, the average values of the peak penetration force (F_{NP}) of the tilt cutters #1 to #3 are lower than those of the normal cutters #4 to #6. The F_{NP} of the normal cutters #4 to #6 does not change with β because the arrangement of the normal cutters is not affected by β. When β is lower than 5°, the F_{NP} of the tilt cutters increases with the increase of the β. When β is between 7° to 13°, the F_{NP} of the tilt cutters decreases with the increase of the β. It means that there exists a critical value of 5° for β at which the rock-breaking performance is the worst, and this is in accordance with the results shown in Figure 10. If the model that β equals 7° is not considered, the *PSE* increases to the peak value when β is 9° and then decreases. The *PSE* of the model that β equals 7° is abruptly low because the rock-breaking process is somehow randomized and a large rock debris is produced between tilt cutter #1 and #2. The *PSE* of the models that β is larger than 13° is relatively low because the cutter is tilted and the ring tip penetrates the rock like a wedge, resulting in low penetration force. Even so, it is suggested that β should be close to 0° or no more than 3° considering both the rock-breaking performance and the penetration force.

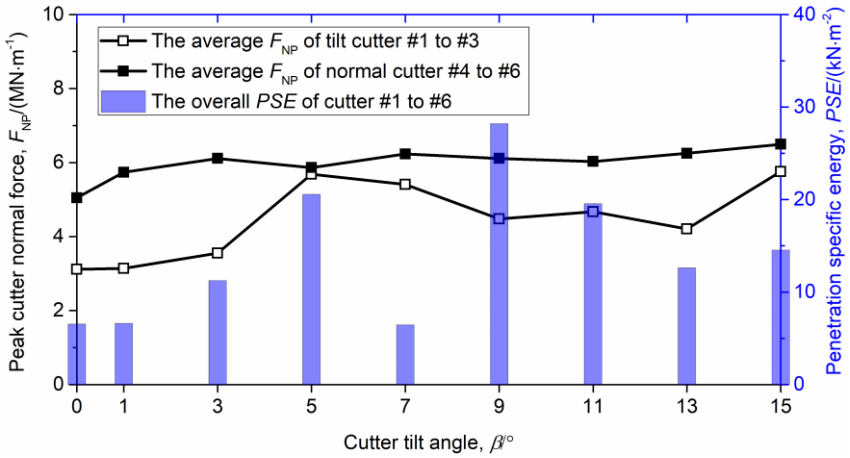

Fig.12 - Rock-breaking normal force and specific energy under different cutter tilt angles, β

Discussions considering previous studies

We reviewed previous studies on the rock-breaking mechanism of conical-shaped cutterhead but found no valuable information. However, many rock-breaking studies under different side-free-face conditions can provide inspiration. Some representative studies are shown in Figure 13. The UCS of the studied rocks varies from 64 MPa to 234 MPa, covering medium strength, hard, and extremely hard rock. The laboratory test methods include static penetration based on simplified indenters and rotary or linear cutting based on full-scale disc cutters. As discussed before, the working principle of the applied small-scale LCM in this study is identical to that of a full-scale LCM. The numerical simulation methods in previous studies include finite element method (FEM) (Figure 13e), GDEM (Figure 13f), PB (Figure 13g), and flat-jointed method (FJM) (Figure 13h). The successful application of these methods confirms the rationality of the numerical simulation in this study.

According to previous studies, the typical rock-fragmentation mode under side-free-face conditions is 'oblique splitting'. The phenomenon is that a macro crack initiates from the cutter penetration point and then propagates to the bottom of the side free face, generating a triangular cross-section chip. This phenomenon is also observed in this study for rock fragmentation by conical-shaped cutterhead. As shown in Figure 7, 9, and 11, the rock beneath several tilt cutters is broken in the 'oblique splitting' mode, exploiting the side-free face to improve the rock-breaking performance. The critical parameters considered in previous studies are *D* and *H*. Previous studies find that there is usually a critical threshold for the ratio of (*D*/*H*). When *D*/*H* is smaller than the critical threshold, the side-free face can help improve the rock-breaking efficiency. The critical thresholds of *D*/*H* for the studies by Innaurato et al.[10], Xu et al.[17], Xia et al.[15], Geng et al.[14], and Jiang et al.[12] are 2.5, 1.0, 0.5, 1.2, and 0.5, respectively. This value is affected by the rock type and cutter geometry. In this study, the influences of *α*, *S*, and *β* on cutter penetration force and specific energy are analyzed considering their relationship with *D* and *H*. It is deduced that *D*/*H* denotes *ctg*(*α*) and the critical threshold is approximately 2.1 when *α* is 25°. Besides, the parameter *S* and *β* also affects the rock-breaking performance.

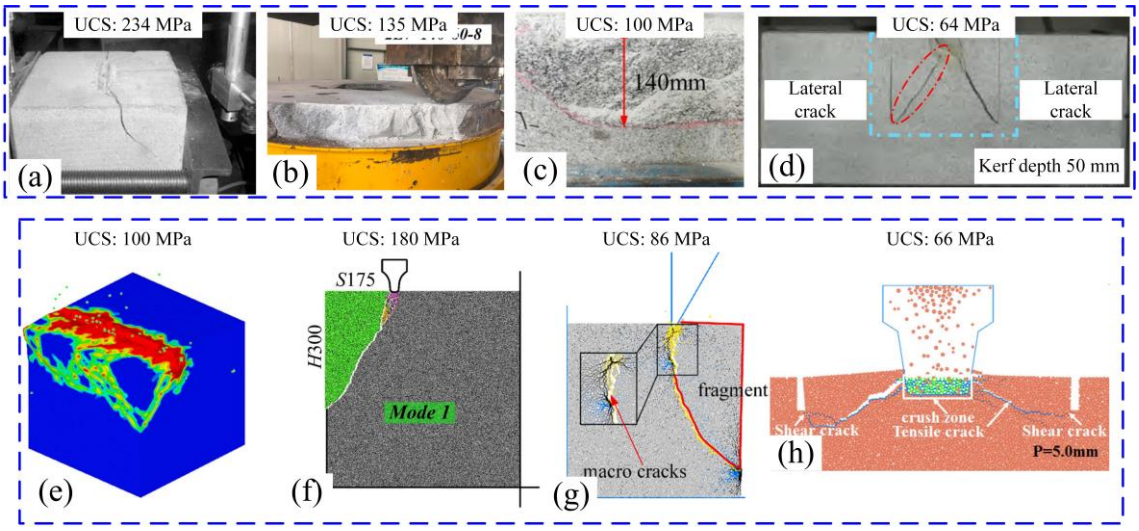

Fig. 13 - Representative studies of rock-breaking under different side-free-face conditions

***(a)** static penetration test on a diorite, D =75 mm, H =30 mm[10];**(b)** rotary cutting test on a granite, D =40~180 mm, H =140 mm[17];**(c)** linear cutting test on a granite, D =20~120 mm, H =200 mm[15]; **(d)** static penetration test on a sandstone, D =60 mm, H =0~50 mm[26]; **(e)** linear cutting simulation on a granite, D =20~120 mm, H =300 mm[15]; **(f)** static penetration simulation on a granite, D =75~200 mm, H =100~350 mm[14]; **(g)** static penetration simulation on a rock sample, D =5~30 mm, H =50 mm[12]; **(h)** static penetration simulation on a sandstone, D =30~45 mm, H =10 mm[23].*

CONCLUSION

In this study, to investigate the rock-breaking mechanism and then optimize the structure of the transition zone of the conical cutterhead, a rock-penetration numerical model is built using a grain-based discrete element method (GDEM) to synthesize rock. After the numerical model is verified, a group of simulations are conducted considering the influence of cutterhead conical angle, cutter spacing, and cutter tilt angle on the rock-breaking performance. The mainly analyzed indicators are the rock chipping, cutter penetration force, and penetration-specific energy. The rock-breaking mechanism of the cutters in the conical area of the conical-shaped cutterhead is free-face-assisted rock breaking. The rock-breaking force and efficiency of the tilt cutters are lower and higher than those of the normal cutters, respectively. Two key factors considering free face structure that affect rock-breaking performance are the free face height and the distance between the penetration point and the side free face. The two factors are then affected by cutter spacing and cutterhead conical angle. The rock-breaking efficiency increases with the increase of cutterhead conical angle but decreases with the increasing of cutter spacing and cutter tilt angle. For hard rock with a UCS of approximately 180 MPa, from the perspective of efficient rock breaking, it is preliminarily suggested that the tilt-cutters' spacing of the conical cutterhead should be less than 70 mm, cutterhead conical angle should be approximately 25°, and the cutter tilt angle should be no more than 3°. The conclusions drawn can provide a theoretical basis for the design of the conical TBM cutterhead.

CONFLICTS OF INTEREST

The authors declare no conflicts of interest.

DATA AVAILABILITY

All data, models, and code generated or used during the study appear in the submitted article.

ACKNOWLEDGMENTS

This work was supported by the Research Program of The Electricity Engineering CO.,LTD under CREC NO.5 Group (Grant number: 2022-DSZQ-007).

REFERENCES

[1] Rostami J., Chang S., 2017. A Closer Look at the Design of Cutterheads for Hard Rock Tunnel-Boring Machines. Engineering, Vol. 3, 892-904.
[2] Zhao Z.W., Zheng K.T., Li N., et al., 2016. Analysis on Static Mechanical Performances of TBM Cutterhead with Different Geometries. Tunnel Construction, Vol. 36, 102-107.
[3] Zhang Z.H., Li Z., Song C.N., 2018. Development and Challenge on Structural Design of Cutterhead of Full-face Rock TBM. Mining Machinery, Vol. 46, 1-7.
[4] Zhang Z.H., Chai C.Q., Zhao H., 2020. Research on Cutterhead Structural Design of TBM. Heavy Machinery, Vol. 13, 69-76.
[5] Zhang Z.H., 2003. Side Slip Analysis of Disc Cutter on Different Cutter Face of Roadheader. Modern Electric Power, Vol. 20, 16-18.
[6] Zhang Z.H., Sun F., 2016. Thrust Analysis of Full Face TBM with Conical Cutter Head during Operation. Construction Machinery, Vol. 47, 33-37.
[7] Zhang Z.H., Ji W., Weng Z.C., 2021. Determination Theory of Main Parameters and Simulation Analysis of the Conical Cutterhead Shield. Journal of Mechanical Engineering, Vol. 57, 243-255.
[8] Liu Y.Y., 2003. Determination of Type and Main Parameters of Full Face Rock Roadheader. Construction Machinery, Vol. 1, 11-15.
[9] Zhang H.X., Zhang N.C., 2007. Brief Discussion on Cutter Head Vibration of Type 803E TBM. Tunnel Construction, Vol. 12, 76-78.
[10] Innaurato N., Oggeri C., Oreste P.P., et al., 2007. Experimental and Numerical Studies on Rock Breaking with TBM Tools under High Stress Confinement. Rock Mechanics and Rock Engineering, Vol. 40, 429-451.
[11] Ramezanzadeh A., Hood M., 2010. A state-of-the-art review of mechanical rock exvacation technologies. International Journal of Medical Engineering and Informatics, Vol. 1, 29-39.
[12] Jiang H.X., Zhang X.D., Liu S.Y., et al., 2022. Research on the mechanism and performance of free-surface rock breakage by a disc cutter. Engineering Fracture Mechanics, Vol. 264, 108336.
[13] Geng Q., Wei Z.Y., Meng H., et al., 2016. Free-face-Assisted Rock Breaking Method Based on the Multi-stage Tunnel Boring Machine (TBM) Cutterhead. Rock Mechanics and Rock Engineering, Vol. 49, 4459-4472.
[14] Geng Q., Ye M., Lu Z.Y., et al., 2021. Numerical Study on Free Face-Assisted Rock Fragmentation Induced by a TBM Disk Cutter. 11th Conference of Asian Rock Mechanics Society.
[15] Xia Y. M., Guo B., Cong G. Q., et al., 2017. Numerical simulation of rock fragmentation induced by a single TBM disc cutter close to a side free surface. International Journal of Rock Mechanics and Mining Sciences, Vol. 91, 40-48.
[16] Zhang X.H., Xia Y.M., Zeng G., et al., 2018. Numerical and Experimental Investigation of Rock Breaking Method under Free Surface by TBM Disc Cutter. Journal of Central South University, Vol. 25, 2107-2118.
[17] Xu H.G., Geng Q., Sun Z.C., et al., 2021. Full-scale granite cutting experiments using tunnel boring machine disc cutters at different free-face conditions. Tunnelling and Underground Space Technology, Vol. 108, 103719.
[18] Wang K., 2020. Numerical Simulation Research on the Rock Fracturing by a TBM Disc Cutter Assisted by Free Faces. Journal of Railway Engineering Society. Vol. 37, 96-102.
[19] Shang X.N., Zhou J., Liu, F.S., et al., 2023. A peridynamics study for the free-surface-assisted rock fragmentation caused by TBM disc cutters. Computers and Geotechnics, Vol. 158, 105380.
[20] Bilgin, N., Copur, H., Balci, C., 2013. Mechanical excavation in mining and civil industries. CRC Press.
[21] Zhang J.L., Li Y., Zhang Y., et al., 2020. Using a high-pressure water jet-assisted tunnel boring machine to break rock. Advances in Mechanical Engineering, Vol. 12, 1-16.
[22] Geng Q., Lu Z.Y., Zhang Z.Y., et al., 2021. Numerical Simulation on the Rock Fragmentation Process Induced by Tunnel Boring Machine Disc Cutters Assisted by Pre-Cut Grooves. Journal of Xi'an Jiaotong University, Vol. 55, 9-19.

[23] Cheng J.L., Yang S.Q., Han W.F., et al., 2022. Experimental and numerical study on the indentation behavior of TBM disc cutter on hard-rock precutting kerfs by high-pressure abrasive water jet. Archives of Civil and Mechanical Engineering, Vol. 22, 1-23.
[24] Li B., Hu M.M., Zhang B., et al., 2022. Numerical simulation and experimental studies of rock-breaking methods for pre-grooving-assisted disc cutter. Bulletin of Engineering Geology and the Environment, Vol. 81, 90.
[25] Li B., Zhang B., Hu M.M., et al., 2022. Full-scale linear cutting tests to study the influence of pre-groove depth on rock-cutting performance by TBM disc cutter. Tunnelling and Underground Space Technology, Vol. 122, 104366.
[26] Zhou H., Xu F.T., Lu J.J., et al., 2022. Influence of pre-cutting groove on rock breaking mechanism of tunnel boring machine disc cutter. Rock and Soil Mechanics, Vol. 43, 625-634.
[27] Gong Q.M., Zhao J., Jiao Y.Y., 2005. Numerical modeling of the effects of joint orientation on rock fragmentation by TBM cutters. Tunnelling and Underground Space Technology, Vol. 20, 183-191.
[28] Li X.F., Li H.B., Liu Y.Q., et al., 2016. Numerical simulation of rock fragmentation mechanisms subject to wedge penetration for TBMs. Tunnelling and Underground Space Technology, Vol. 53, 96-108.
[29] Potyondy D.O., Cundall P.A., 2004. A bonded-particle model for rock. International Journal of Rock Mechanics and Mining Sciences, Vol. 41, 1329-1364.
[30] Ghazvinian E., Diederichs M.S., Quey, R., 2014. 3D random Voronoi grain-based models for simulation of brittle rock damage and fabric-guided micro-fracturing. Journal of Rock Mechanics and Geotechnical Engineering, Vol. 6, 506-521.
[31] Li X.F., Zhang Q.B., Li H.B., et al., 2018. Grain-Based Discrete Element Method (GB-DEM) Modelling of Multi-scale Fracturing in Rocks Under Dynamic Loading. Rock Mechanics and Rock Engineering, Vol. 51, 3785-3817.
[32] Li X.F., Li H.B., Zhao, J., 2017. 3D polycrystalline discrete element method (3PDEM) for simulation of crack initiation and propagation in granular rock. Computers and Geotechnics, Vol. 90, 96-112.
[33] Cho N., Martin C.D., Sego D.C., 2007. A clumped particle model for rock. International Journal of Rock Mechanics and Mining Sciences, Vol. 44, 997-1010.
[34] Balci C., Bilgin N., 2007. Correlative study of linear small and full-scale rock cutting tests to select mechanized excavation machines. International Journal of Rock Mechanics and Mining Sciences, Vol. 44, 468-476.
[35] Entacher M., Lorenz S., Galler R., 2014. Tunnel boring machine performance prediction with scaled rock cutting tests. International Journal of Rock Mechanics and Mining Sciences, Vol. 70, 450-459.
[36] Comakli R., Balci C., Copur H., et al., 2021. Experimental studies using a new portable linear rock cutting machine and verification for disc cutters. Tunnelling and Underground Space Technology, Vol. 108, 103702.
[37] Gong Q.M., Du X., Li, Z., et al., 2016. Development of a mechanical rock breakage experimental platform. Tunnelling and Underground Space Technology, Vol. 57, 129-136.
[38] Cho J.W., Jeon S., 2010. Optimum spacing of TBM disc cutters: A numerical simulation using the three-dimensional dynamic fracturing method. Tunnelling and Underground Space Technology, Vol. 25, 230-244.
[39] Pan Y.C., Liu, Q.S., Liu, J., et al., 2018. Full-scale linear cutting tests in Chongqing Sandstone to study the influence of confining stress on rock cutting efficiency by TBM disc cutter. Tunnelling and Underground Space Technology, Vol. 80, 197-210.
[40] Entacher M., Winter G., Bumberger T., et al., 2012. Cutter force measurement on tunnel boring machines-System design. Tunnelling and Underground Space Technology, Vol. 31, 97-106.

CIVIL ENGINEERING JOURNAL

Article no. 32

THE CIVIL ENGINEERING JOURNAL 3-2023

MONITORING AND ANALYSIS OF CANTILEVER JACKING OF HIGH SLOPE PRESTRESSED CONCRETE CONTINUOUS BOX GIRDER

Zhe Zhang, Quansheng Sun, Chao Zhang and Xiaoqian Li

School of Civil Engineering and Transportation, Northeast Forestry University, Harbin 150040, China; sunquansheng@nefu.edu.cn

ABSTRACT

Due to the rapid development of the transportation industry and economy, an increasing number of bridges have been unable to meet the demands of traffic. Demolishing and rebuilding bridges can lengthen the construction period, waste a lot of resources, and increase construction costs. Based on the lifting renovation project of the old Harbin Dongsan Ring Expressway viaduct, this paper combines finite element analysis and on-site testing to analyze the construction process. The bridge alignment, elevation, and deviations were monitored during the construction process, and a correction system was developed to address such issues. Structural analysis was conducted to evaluate the internal forces when uneven jacking occurred. The construction process described in this paper can effectively solve the jacking problems of urban continuous bridges with large tonnage, high slopes, and heights. The successful implementation of the jacking retrofitting project has verified the reliability of the measures taken.

KEYWORDS

Bridges, Structural analysis, Finite element methods

INTRODUCTION

The construction of bridges around the world has a history spanning thousands of years. In the past century, the construction technology of concrete bridges has undergone multiple transformations and advancements. With the rapid development of China's economy and construction industry, urban transportation is transitioning from traditional ground transportation to three-dimensional transportation. Creating more transportation resources within limited space has become an important goal of urban planning today; therefore, urban expressway bridges have been widely constructed and applied as a type of spatial architecture. However, this transformation of urban transportation structures has also brought some challenges. The issue of rebuilding existing bridges is becoming increasingly prominent, leading to a serious waste of social and economic resources. To avoid unnecessary construction, lifting and renovating existing bridges has become an effective solution. This method can maximize the utilization of existing bridge structures and save socio-economic resources. Lifting renovation technology improves the deck of existing bridges to adapt to new traffic needs without the need for complete demolition and reconstruction. This method has significant advantages, one of which is that it reduces engineering costs. Compared to comprehensive reconstruction, lifting renovation can significantly reduce investment and save construction time. Secondly, the lifting renovation can maximize the preservation of the original bridge structure and historical value while reducing the impact on the environment. This method has been widely applied in the renovation of urban expressway bridges, providing sustainable solutions for urban development. The top lifting renovation technology for bridges was first used domestically in the 1950s and was mainly used for the construction, displacement, and setting of railway bridges. With the development of hydraulic technology, in September 2003, computer-controlled hydraulic synchronous jacking

technology was first applied to the integral jacking of bridges[1]. As a newly developed bridge renovation technology, jacking has the characteristics of high economic efficiency, efficiency, and environmental friendliness, and has been widely applied in the renovation projects of urban expressway bridges, with good application prospects [2]~[6]. The common jacking methods used now include: sleeper-filled support method, bridge deck steel rail method, end integral jacking method, saddle bracket method, steel girder method, steel butterfly beam method, steel casing method, and hydraulic jacking method. The abbreviation of programmable logic controller is PLC, which is a kind of digital operation electronic system specially designed for application in industrial environment. It uses a programmable memory to store instructions for performing logical operations, sequential control, timing, counting, and arithmetic operations within it, and controls various types of mechanical equipment or production processes through digital or analogue input and output. This project adopts a PLC multi-point synchronous displacement jacking system, integrates digital monitoring transmission, hydraulic transmission control, and computer digital signal processing technology. It combines mechanical equipment systems with traditional bridge structure analysis technology, and uses multiple sets of jacks to achieve balanced, safe, and efficient bridge jacking [7]. The lifting system used is shown in Figure 1.

Fig. 1 - PLC multi-pump group multi-point displacement synchronization system

Figure 1 shows a PLC-controlled multi-point synchronous displacement control system for pump groups, which utilizes a closed-loop control system with variable frequency speed regulation. The flow rate of the oil pump is continuously adjusted by changing the frequency of the power supply to alter the speed of the hydraulic motor. With advanced electronic control equipment and displacement and pressure detection systems, precise control of the jack during synchronous lifting is achieved.

Bridge jacking, as a key technology in bridge renovation and maintenance, has achieved some successful practices in the displacement and jacking of building structures both domestically and internationally. Wu proposed the overall process principles of "divided lifting, synchronous control, and partial rotation angle displacement lifting", and elaborated on the key technologies such as synchronous lifting parameters, partial rotation angle displacement lifting, and construction monitoring[8]. The Golden Gate Bridge in the United States underwent repair and strengthening work using jacking technology in 2002, greatly improving its seismic resistance and load-bearing capacity [9]. A range of techniques based on jacking precast units have been developed in the UK since 1967. Thomson introduced the development and application of the tunnel jacking method, which can avoid traffic interruption. "Zhao, Y analyzed the contact behavior and stress distribution characteristics between the main beam and the supporting beam, and monitored and analyzed the induced stresses of the upper structure and support structure[10]. This article investigates the mechanical characteristics of a high-slope continuous beam during cantilever jacking through a combination of jacking tests and finite element analysis using the extended finite element method. Construction monitoring of bridge alignment, elevation, and lateral displacement is performed, and a correction system for lateral displacement is developed. The article also analyzes the internal forces of the structure in cases of uneven jacking caused by mechanical or human factors.

CANTILEVER JACKING PROJECT TEST

Project profile

The Harbin Dong San Huan Expressway lifting renovation project adopted the jack-up renovation construction of the old bridge on Huagong Road. The upper structure adopts a simple supporting continuous small box beam, and the bridge pier adopts a cap beam column pier. The bridge deck is arranged in two spans, with both the left and right spans arranged in the following span configuration: 4×30m+3×40m+3×30m+3×30m. The starting pile number of the bridge is K40+392.5, and the ending pile number is K40+812.5. The total length of the bridge is 420m. The section between K40+512.5 and K40+632.5 spans the railway, with a length of 120m. The load level of the bridge is urban A level, and seismic measures are designed according to a seismic fortification intensity of 7 degrees. It was completed in 2012. This paper takes the left span 3×30m continuous small box girder as the research object, and the bridge layout is shown in Figure 2. The main beam of the upper structure is 1.6m high, and the width of a single span bridge deck is 23m. The specific geographical location of this project is shown in Figure 3.

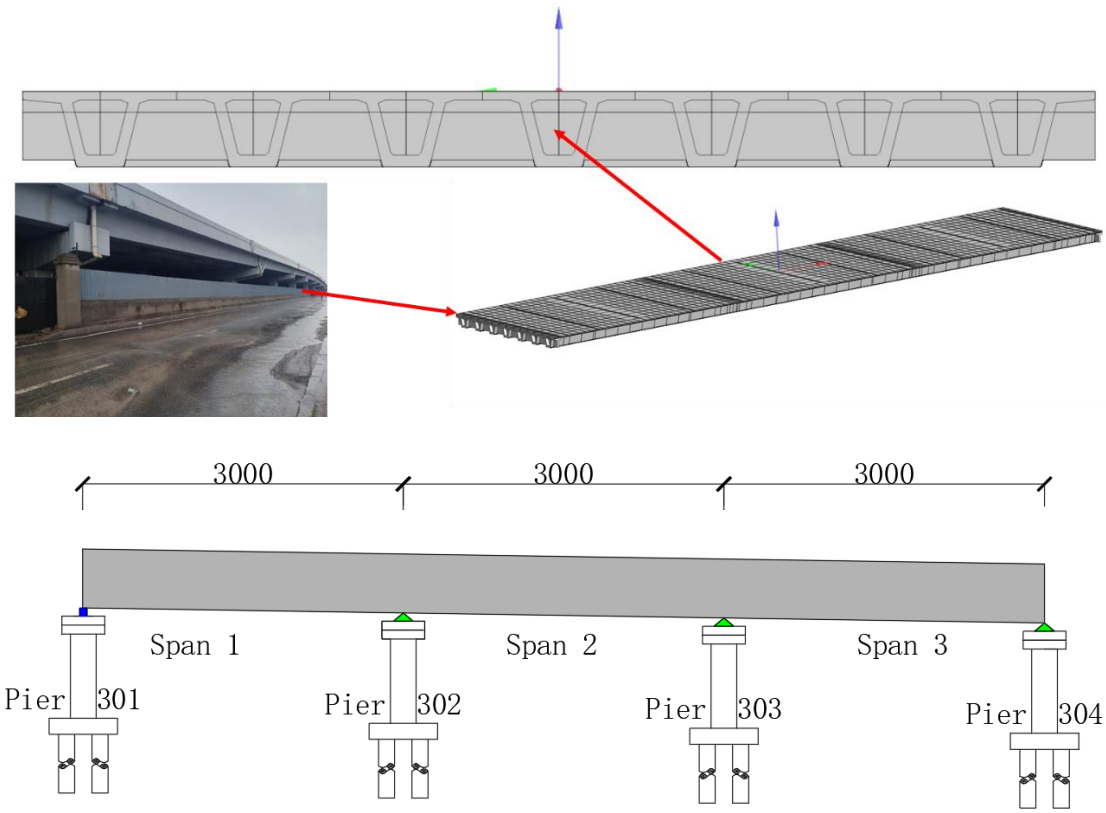

Fig. 2 - Bridge layout (Units: cm)

Fig. 3 - Geographical Location Map of the Project

Due to the construction needs of Harbin East Third Ring Expressway, the bridge needs to complete the transformation from the approach bridge to the viaduct through the leveling and jacking stage, upgrade to the new design elevation, and connect with the new viaduct. According to the design requirements and the actual situation of the bridge, the project has the following characteristics: Large lifting weight, with a single span lifting weight of 4400 tons, requiring a large number of lifting equipment, limiting devices, and monitoring equipment; Large lifting area, requiring high precision control of multi-point synchronous lifting equipment within a single area of 2000m^2; Large lifting height, with a maximum lifting height of 6.897m, requiring multiple temporary shims placement and lifting cycles; Design involves rotational lifting, and the bridge undergoes length changes in the projection direction, which results in secondary internal forces. According to the analysis of the overall drawing of the East Third Ring Road, the heights of each support point of the bridge need to be adjusted as shown in Table 1.

Tab. 1 - North approach bridge lifting height (Units: m)

Pier fulcrum	lifting height	Pier fulcrum	lifting height
301#	4.197	302#	5.097
303#	5.997	304#	6.897

Finite element model

According to the design drawings of the original bridge, a finite element three-dimensional spatial calculation model of the original bridge was established using the finite element analysis software Midas Civil to conduct structural simulation analysis. The 3x30m prestressed concrete continuous box girder was divided into 598 nodes and 921 elements for the entire bridge, and the model is shown in Figure 4.

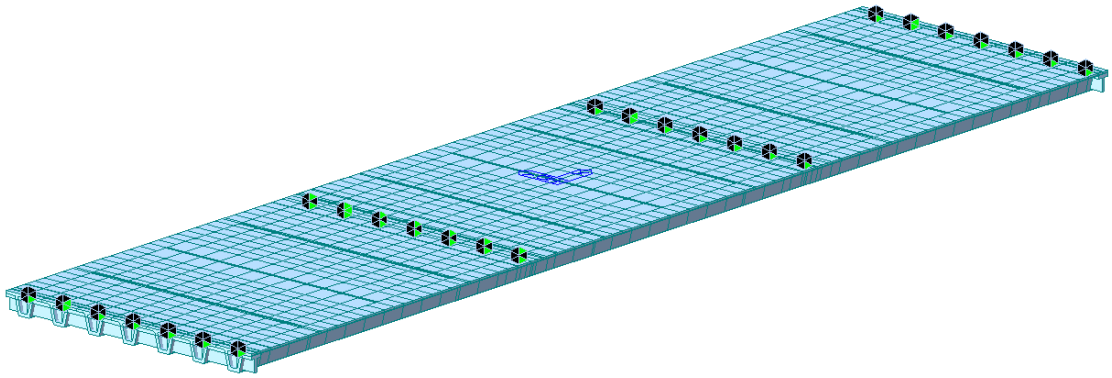

Fig..4 - Diagram of finite element model

The material and structural parameters used in the finite element software simulation of the original bridge state are all based on the data provided when the bridge was completed. At the same time, the impact of the overall weight of the structure, permanent load in the second phase, shrinkage and creep, non-uniform settlement, and temperature load on the theoretical model were considered. The node forced displacement was used to simulate the on-site jacking construction process, and the jacking simulation of the model structure was completed during the construction phase. The material parameters are shown in Table 2.

Tab. 2 - Main material parameter table

materials	volumetric weight（kN/m3）	elastic modulus（MPa）	poisson ratio
C50	26.0	3.5×104	0.2

Cantilever lifting test

For the sake of economic and construction difficulty considerations, the column-breaking jacking method was used for jacking construction, while retaining the upper structure, cover beams, and some pier columns of the original bridge. The bridge was first rotated at the same angle and then jacked up to the target height at the same displacement. At the higher part of the pier, cast-in-place corbel beams were used for jacking, while cover beams were used for jacking at the lower part of the pier. Steel distribution beams were used for cantilever jacking at the original bridge abutment. The jacking arrangement is shown in Figure 5, and the jacking process is shown in Figure 6.

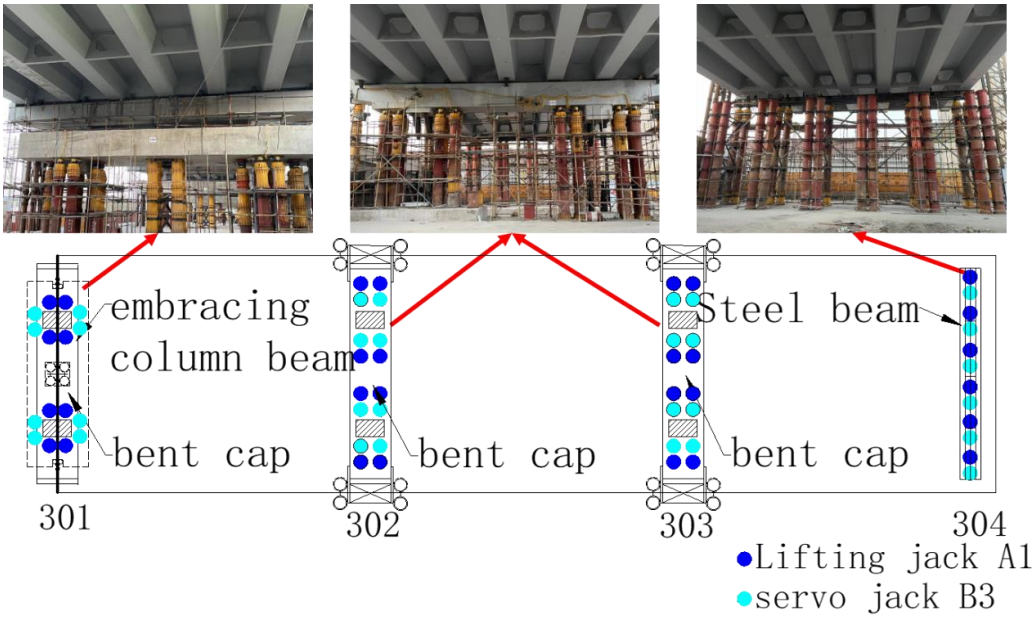

Fig. 5 - Lifting device layout (Units : cm)

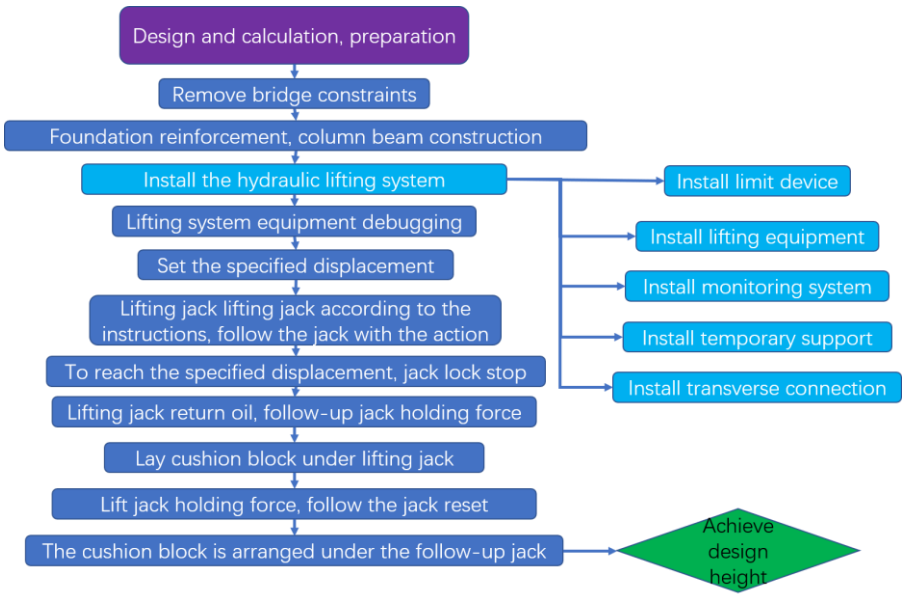

Fig. 6 - Lifting construction flow chart

From Figures 5 to 6, it can be seen that the jacking process adopts the combination of jacking jacks and follower jacks, using small displacements and multiple cycles as the jacking method. By increasing the number of steel support pipes, the purpose of lifting the bridge is achieved.

The bridge lifting process adopts a PLC multi-pump group multi-point displacement synchronous system, which integrates technologies such as displacement sensors, digital transmission, hydraulic control, and computer signal processing[11]. It can realize dual-loop control of force and displacement to ensure the safety of the structure. During the cantilever rotation and lifting of the bridge, the concentrated force on the lifting point exceeds 1500kN, and internal force analysis of the lifting bridge is required[12]. In order to prevent the deviation of the lifting system caused by vibrations during the lifting construction process due to construction equipment, passing trains, and natural factors, multiple limiting systems are used in this project. When the height of the original pier is low, a lateral limiting bracket is used in combination with a skew bridge for limiting; when the height

of the original pier is high, a column-beam and limiting bracket are used for limiting, as shown in Figure 7.

a) cantilevered end

b) bent cap

c) embracing column beam

Fig. 7 - Lifting and limiting device installation diagram

As shown in Figure 7, the jacking process utilizes a combination of transverse Beray beam, anti-torsion limiting frame, cover beam limiting frame, and concrete column-beam limiting system. Beray beam and various types of limiting frames are connected by circular steel column flanges. The stability, safety, and reliability of the limiting system are ensured by presetting the connection between the foundation and the structural foundation.

This study considers the three stages of cantilever rotation and lifting, namely, condition 1, where the boundary system of the original bridge is transformed from the 304 bridge abutment to the steel distribution beam; condition 2, where the bridge is rotated and lifted at the same angle; and condition 3, where the bridge is lifted vertically with the same displacement. The experimental conditions are shown in Table 3.

Tab. 3 - condition (Units: m)

Pier / condition	301	302	303	Steel beam
1	0	0	0	0
2	0	0.0357	0.0714	0.1
3	0.1	0.1	0.1	0.1

The internal force diagrams for each condition were obtained by analyzing each stage of the bridge lifting construction using the Midas Civil finite element analysis software, as shown in Figure 8.

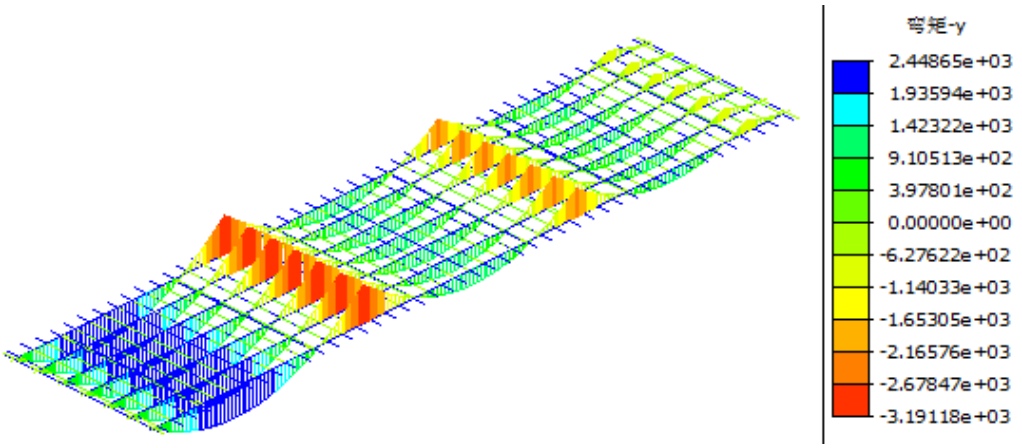

a) Condition 1, the internal force diagram of the original bridge system

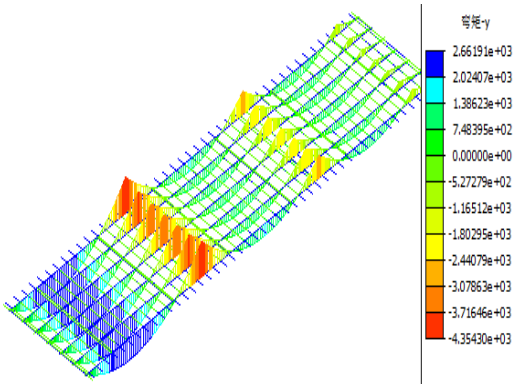

b) Condition 2, synchronous rotating jacking internal force diagram

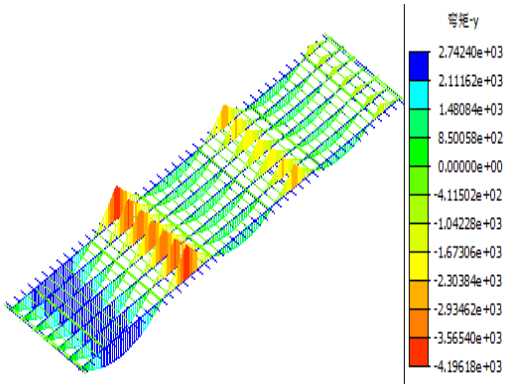

c) Condition 3, synchronous displacement jacking internal force diagram

Fig. 8 - Main girder jacking internal force diagram of each stage

From Figure 8, it can be seen that during the jacking phase of the bridge, due to the transformation of the structural system, the main beam at the steel distribution beam produces a maximum negative bending moment of -1305kN·m. The main beam is under tension and exhibits tension on the upper surface of the structure. Since the tensile strength of concrete is much lower than its compressive strength, to prevent cracking of the upper part of the main beam under tension, carbon fiber plates are used to reinforce the cantilever jacking position of the main beam to bear some of the surface tensile stress. The reinforcement design of the main beam is shown in Figure 9 [13]~[15].

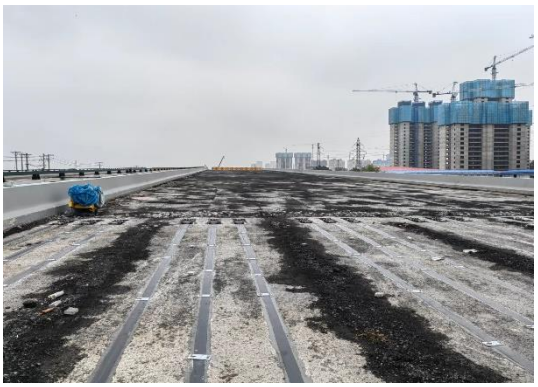

Fig. 9 - Carbon fiberboard active reinforcement diagram

The maximum internal forces and their locations of the main beam under different working conditions were recorded based on Figure 8, as shown in Table 4.

Tab. 4 - Internal force of main beam

internal force / condition	maximum positive moment		maximum negative moment	
	position (m)	bending moment (kN/m)	position (m)	bending moment (kN/m)
1	No.1 spans 12m	2448.65	302 pier top	-3191.18
2	No.1 spans 12m	2661.91	302 pier top	-4354.30
3	No.1 spans 12m	2742.40	302 pier top	-4196.18

According to Table 4, the maximum negative bending moment and positive bending moment during the synchronous rotation lifting and synchronous displacement lifting processes occur at span 1, 12m and pier 302, respectively. Furthermore, the lifting process has a relatively small impact on the positive bending moment of the structure, but a significant impact on the negative bending moment of the pier top. In order to study and evaluate the mechanical behavior of the bridge structure during the lifting process, the top section of pier 302 was selected as the testing section, and HY-65B digital strain gauges were used to measure the stress of the bridge structure. The layout of the strain measurement points is shown in Figure 10.

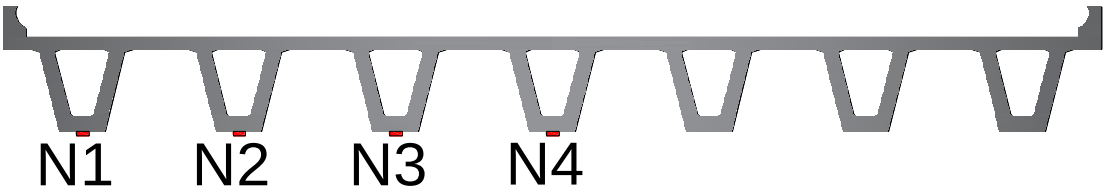

Fig. 10 - Measurement point layout

Test result analysis

Stress and strain are key data that reflect the structural loading conditions. Monitoring the lifted bridge, the stress conditions of the structure during the lifting process can be reflected by the theoretical values and measured strain values at each measurement point. According to the superposition principle, the stress data of the main beam caused by the lifting can be obtained from the difference of stress values at each stage of the theoretical model, as well as the measured strain data, as shown in Figure 11.

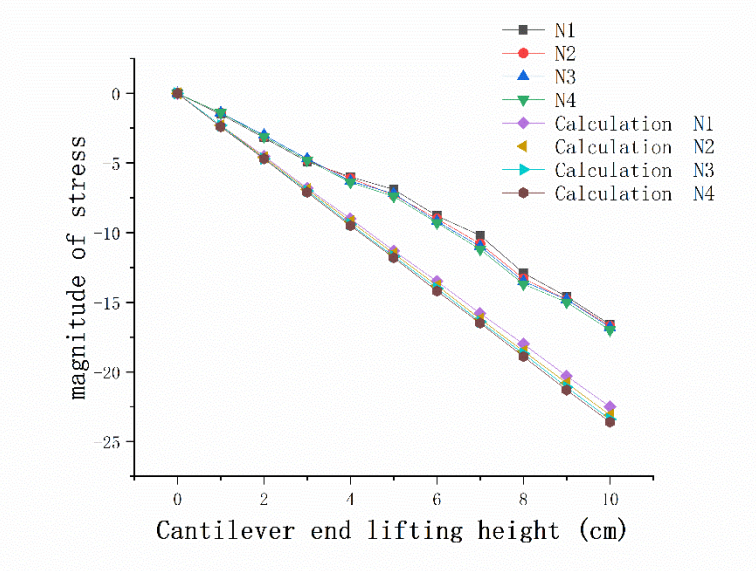

Synchronous rotation lifting

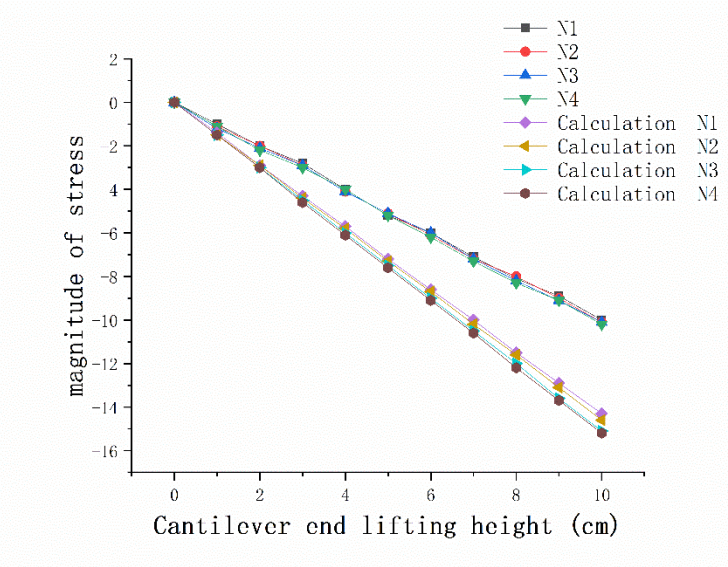

synchronous lifting displacement

Fig. 11- Measured and theoretical strain value

Based on Figure 11, it can be seen that the stress of the cross section at the top of pier 302 is proportional to the lifting stroke during the two lifting stages, and the data at each measuring point is balanced, indicating that the structural integrity is relatively good. The experimental verification coefficient ranges from 0.58 to 0.80, and the sectional stress shows linear changes. The measured values of each section are smaller than the theoretical calculated values, and the maximum verification coefficient is 0.80, indicating that the structure is in a reasonable control state during the lifting process. The maximum stress change of the cross section at the top of pier 302 during the synchronous rotation lifting process is -17; the maximum stress change during the synchronous displacement lifting process is -10.2, indicating that the synchronous rotation lifting process has a greater effect on the internal force of the main beam than the synchronous displacement lifting stage. The linear relationship between the theoretical calculation values and the measured values is good, indicating that the finite element model can well reflect the stress status of the structure during the lifting process.

JACKING CONSTRUCTION MONITORING AND ANALYSIS

The lifting process was monitored by using a total station for point layout. In order to address the issue of top lifting deviation caused by construction factors, mechanical vibration, external loads, etc., this study analyzed the influence of top lifting deviation on the structure during the construction process using a finite element model.

Lifting construction monitoring

To accurately understand the stress situation of the jacking beam and ensure the smooth progress of the jacking project, in the cantilevered rotating jacking process, the linearity and deviation of the beam are monitored. Measurement points are set up at the top of the pier, on the side of the beam, and at the cantilever jacking end, and monitoring measurements are carried out using a total station based on the second-class engineering level standard.

(1) Linear monitoring

Based on the characteristics of continuous beam structures, a linear monitoring plan was developed, and total station points were arranged as shown in Figure 12.

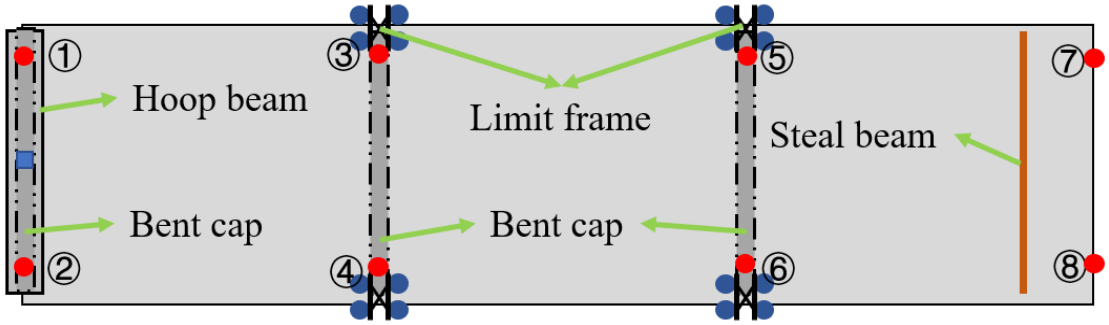

Fig. 12 - Bridge deck elevation measuring point layout

By establishing stations, transferring stations, and setting up intermediate stations using a permanent benchmark and total station, the observation points in Figure 12 were monitored regularly to capture the bridge posture during the jacking construction process. The elevation data of the bridge control points collected during the construction process are shown in Table 5.

Tab 5 - Elevation measurement data (unit: m)

Date / point	9.29	10.04	10.05	10.07	10.08	10.09	10.10	10.19	10.21
1	126.819	128.064	128.153	128.504	128.709	129.093	129.429	130.639	126.819
2	127.115	128.359	128.449	128.796	129	129.385	129.694	130.888	127.115
3	126.737	127.996	128.088	128.398	128.603	128.913	129.271	130.435	126.737
4	127.011	128.269	128.36	128.719	128.911	129.283	129.527	130.737	127.011
5	126.541	127.792	127.883	128.139	128.436	128.813	129.043	130.216	126.541
6	126.863	128.117	128.204	128.424	128.756	129.135	129.344	130.533	126.863
7	126.491	127.721	127.81	128.074	128.385	128.78	128.954	130.21	126.491
8	126.813	128.056	128.138	128.394	128.695	129.089	129.269	130.498	126.813

Due to the existence of transverse slope in the bridge, the average of the symmetric monitoring points is used to represent the elevation of the bridge section center. The elevation profile of the bridge during the jacking process is shown in Figure 13.

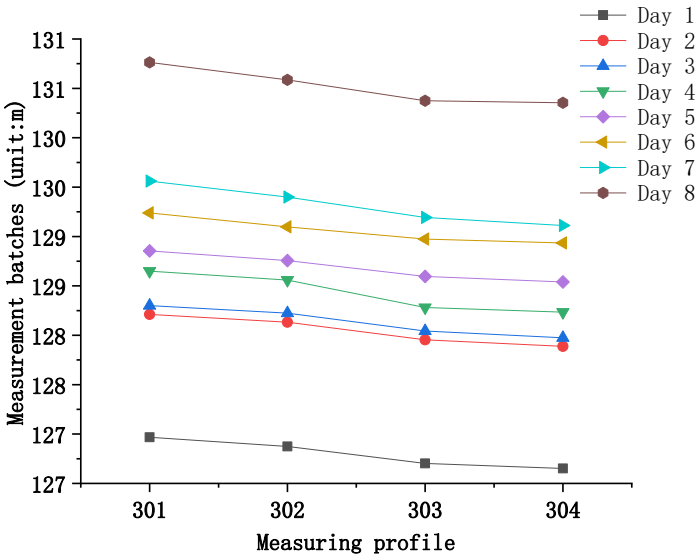

Fig. 13 - Bridge lifting elevation line chart

As shown in Figure 13, all control sections were uniformly and synchronously lifted during the jacking process, and no jacking differences occurred. The ramp adjustment and jacking were completed according to the predetermined height, achieving the control elevation. After that, the elevation was fine-tuned through bridge deck paving and other methods to achieve the target alignment.

(2) Bias monitoring

Continuous beam cantilever rotating lifting, the length in the bridge projection direction increases, and there is frictional force between the beam and the cover beam, which causes the support system such as the cover beam to shift, further causing the beam to shift. Due to factors such as construction errors, frictional forces, and construction machinery vibrations, there may be displacement errors during the bridge lifting process. Through laser measurement, total station point measurement, and bridge static measurement equipment, the bridge lifting posture is determined, and the bridge lifting system has cover beam rotation deviation and main beam longitudinal deviation as shown in Figure 14.

(a) Cover beam overturning offset

(b) Main girder deflection

Fig. 14 - Deflection diagram of jacking system

Based on the characteristics of the project, a correction method was developed. The structural system used column dismantling jacking, and the main components for correction were the cover

beam and main beam, with the main deviations being the overturning and offset of the cover beam and the lateral displacement of the main beam as shown in Figure 14. Different correction methods were adopted for different deviations, including pier foundation reaction correction, limit frame reaction correction, and main beam reaction correction as shown in Figure 15.

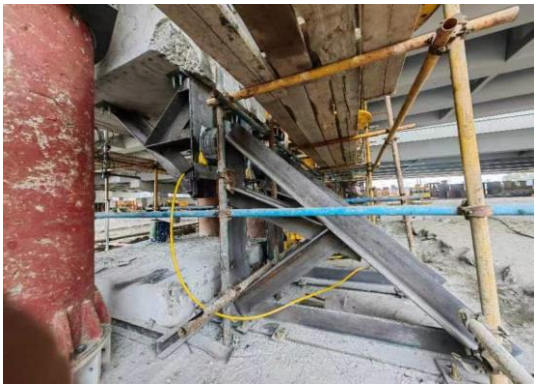

(a) Pier foundation reaction correction

(b) Counterforce correction of limit frame

(c) Main beam reaction correction

Fig. 15 - Lifting correction system

During the top-down lifting process of the structure, the lifting system, monitoring system, and correction system work together to achieve structural system transformation, cyclic lifting, and system correction, and thus achieve the lifting goal. The lifted bridge is shown in Figure 16.

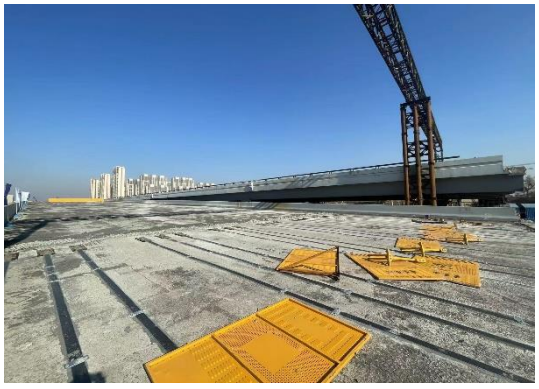

Fig. 16 - Comparison diagram of left and right bridge jacking construction

Analysis of jacking deviation

During the synchronous lifting of the multi-span continuous beam, longitudinal deviations may occur due to the unsynchronized hydraulic devices of the bridge pier, distribution beam, and brace beam, as well as the uneven temporary support structure. Midas Civil was used to analyze the

possible longitudinal deviations during the lifting process, including scenario 1: lifting of pier No. 301 alone; scenario 2: lifting of pier No. 302 alone; scenario 3: lifting of pier No. 303 alone; and scenario 4: lifting of the cantilever end of pier No. 304 alone. The internal force diagrams of the main beam under various longitudinal deviation scenarios are shown in Figure 17.

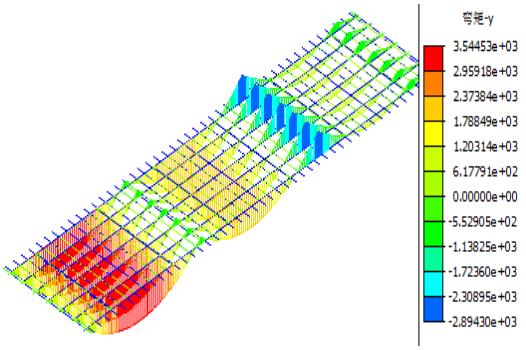

a) condition 1 internal force diagram

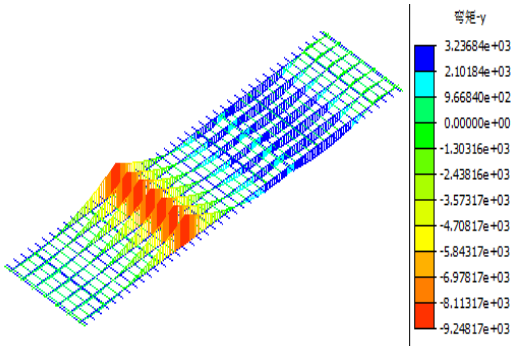

b) condition 2 internal force diagram

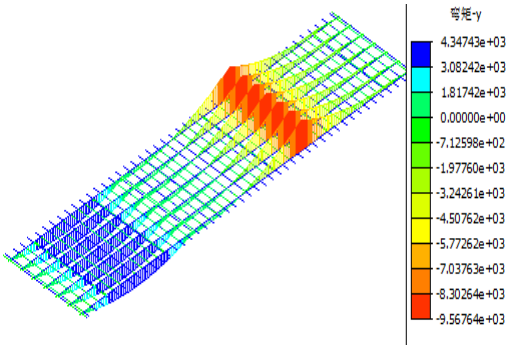

c) condition 3 internal force diagram

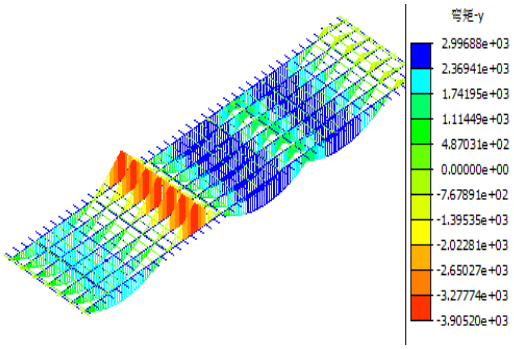

d) condition 4 internal force diagram

Fig. 17 - Internal force diagram of each deviation condition

Based on the comparative analysis of Figures 8 and 17, it can be concluded that when uneven lifting occurs at the edge support, the positive bending moment of the adjacent span increases, and the negative bending moment of the non-edge support on the symmetrical side increases. When uneven lifting occurs at the non-edge support, the negative bending moment at the top of the pier at that support point increases, and the positive bending moment of the adjacent span on the symmetrical side increases. Stress analyses were conducted on the maximum changing cross-sections of each working condition, and the stress changes for each working condition are shown in Figure 18.

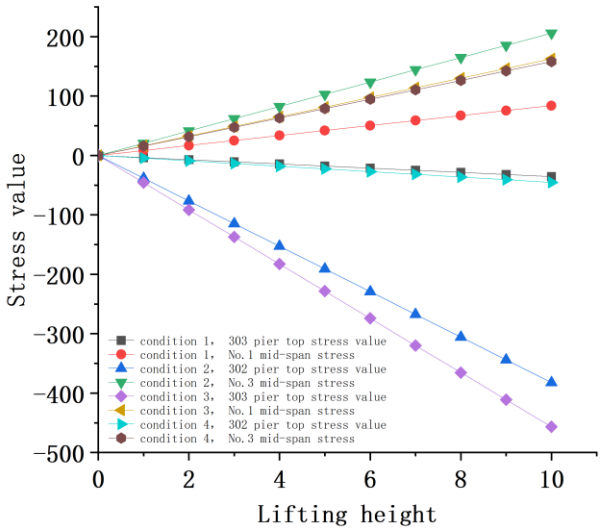

Fig. 18 - Longitudinal deviation stress variation diagram (unit : cm)

Comparing Figure 6 and Figure 15, it can be seen that when there is uneven lifting at the edge support, the positive bending moment of the adjacent span increases, and the negative bending moment of the non-edge support side increases; when there is uneven lifting at the non-edge support, the negative bending moment of the pier top at this support increases, and the positive bending moment of the edge span on the symmetrical side increases. Stress analysis was carried out for the sections with the greatest changes in each working condition, and the stress changes for each working condition are shown in Figure 16.

From Figure 16, it can be seen that when there is uneven lifting at the edge support, the stresses at the section of the pier support and adjacent span on the symmetrical side increase, but the changes are small; when there is uneven lifting at the non-edge support, the stresses at the pier top section and the section of the edge span on the symmetrical side increase significantly, and the stress changes caused by uneven lifting increase linearly with the lifting height. The changes in the internal forces of the main beam caused by uneven lifting at non-edge supports have a greater impact than those caused by uneven lifting at edge supports. Therefore, in the lifting construction process, it is necessary to strictly control the synchronization and uniformity of lifting at each pier to prevent the occurrence of uneven lifting, which may lead to excessively large negative bending moment at the main beam support and positive bending moment at the midspan.

RESULTS

This article takes the lifting project of the East Third Ring Expressway in Harbin as the research object, using cantilever rotation lifting and synchronous displacement lifting to lift the old bridge to the design elevation and connect it to the newly built elevated bridge. The construction monitoring of cantilever rotation lifting is carried out, and the structural internal force during the lifting process is analyzed through lifting tests and Midas Civil finite element analysis software, and the possible deviations are studied and analyzed. The following conclusions are drawn:

(1) The main beam internal force changes significantly more during the synchronous rotation lifting process than during the synchronous displacement lifting stage. The synchronous rotation lifting and synchronous displacement lifting processes have a relatively small impact on the structure's positive bending moment, but a significant impact on the negative bending moment at the top of the pier. Carbon fiber reinforced plates can be used to strengthen the main beam to prevent cracking due to negative bending moment at the steel distribution beam.

(2) The bridge alignment and deviation during the lifting construction are monitored to verify the correctness of the lifting method. Correction methods for deviations such as foundation reaction

correction, limit frame reaction correction, and main beam reaction correction after replacement of the bearing are proposed.

(3) Using the finite element extension method, this study investigates the distribution of internal forces in the main beam of a bridge during vertical lifting when longitudinal uneven lifting deviation occurs. When there is uneven lifting at the edge support points, the stress in the section of the symmetrical abutment support points and adjacent spans increases but changes only slightly. However, when there is uneven lifting at non-edge support points, the stress at the top section of the pier and the symmetrical adjacent spans increases significantly, and the sectional stress caused by uneven lifting increases linearly with the lifting height. The effect of uneven lifting at non-edge support points on the change of internal forces in the main beam is greater than that of uneven lifting at edge support points. Therefore, during the lifting construction process, it is necessary to strictly control the synchronized and uniform lifting of each pier to prevent the occurrence of uneven lifting conditions, which can lead to excessive negative bending moments at the main beam support points and excessive positive bending moments at the midspan.

(4) The lifting method used in this project is well-suited for urban bridge renovation to meet the needs of modern transportation development. This method has a high lifting speed, high safety, and high accuracy, and the proposed correction method has been proven to be efficient and accurate through simulation and construction verification.

ACKNOWLEDGEMENTS

The authors gratefully appreciate the support from the Key R & D Plan Guidance Projects of Heilongjiang Province (GZ20220133).

REFERENCES

[1] Qian Jihong & Chen Cheng. (2022). Application of bridge jacking technology in urban viaduct reconstruction. Engineering quality (06), 48-51 + 60.

[2] Jiang Yanfeng & Lan Wuyi. (2007) Research on key technology of integral lifting of bridge. Editorial Department of Building Structures. (eds.) The First National Symposium on Reinforcement Design and Construction Technology of Existing Structures (pp.577-579).

[3] Ge Yaojun & Xiang Haifan (2010). The concept and mission of sustainable development of bridge engineering. China Civil Engineering Society Bridge and Structural Engineering Branch. (eds.) The 19 th National Bridge Academic Conference Proceedings (Volume I) (pp.23-39). People 's Transportation Publishing House.

[4] LIU Gao,GAO Yuan,WU HongBo,MA JunHai,ZHANG XiGang & FU BaiYong.(2016).Status and prospect of technical development for bridges in China. Chinese Science Bulletin (4-5). doi:10.1360/n972015-00912.

[5] Min Liu & Dan M. Frangopol.(2004).Optimal bridge maintenance planning based on probabilistic performance prediction. Engineering Structures (7). doi: 10.1016/j.engstruct.2004.03.003.

[6] Itunumi Savage,John C. Eddy & Gregory I. Orsolini.(1999).Seismic analysis and base isolation retrofit design of a steel truss vertical lift bridge. Computers and Structures (1). doi:10.1016/S0045-7949(99)00027-9.

[7] Yuan Zhen, Zhu Wenxia & Xiao Han. (2013). Application of PLC synchronous lifting system in highway bridge reconstruction. Chinese and foreign highway (05), 170-173. doi : 10.14048 / j.issn.1671-2579.2013.05.076.

[8] Wu Yibin & Xu Lihua. (2017). Construction and control technology of large-tonnage synchronous jacking of urban interchange overpass. Construction Technology (20), 31-33 + 60.

[9] James C Thomson (2018).Jacked installation of underbridges. Proceedings of the Institution of Civil Engineers - Bridge Engineering (2). doi:10.1680/jbren.16.00032.

[10] ZHAO Y, WANG J F, PANG M. (2012). Integral lifting project of the Qifeng bridge. Journal of Performance of Constructed Facilities, 26(3):353-361 https://doi.org/10.1061/（ASCE）CF.1943-5509.0000211

[11] Song Chuanwang, Xie Shuaihu, Wang Jing, Sun Fanqing, Xia Xin, Ouyang Ganlin & Wu Zeju. (2018). Design of shift synchronous control system based on PLC.Instrument technology and sensors (08), 47-51.

[12] WANG Yan & CHEN Huai. (2008). Local stress analysis of No.0 beam section of long-span cantilever assembled continuous beam bridge. JOURNAL OF RAILWAY SCIENCE AND ENGINEERING (03), 23-27. DOI : 10.19713 / j.cnki.43-1423 / u.2008.03.005.

[13] Ning Baokuan, Hu Haitao, Xu Yongze & Yang Siting. (2020). Experiment on mechanical properties of reinforced concrete beams strengthened with prestressed carbon fiber sheet. Building Structure (06), 90-94. doi : 10.19701 / j.jzjg.2020.06.017.
[14] Roberto di Giulio,Zivko Bozinovski,Leo G.W. Verhoef... & Dionys Van Gemert.(2007).Externally Bonded Steel or Carbon Fiber Reinforcement. Research in Architectural Engineering Series.
[15] Beth Khan. (2015). Test analysis of continuous box girder bridge loading. Road and Automobile Transport (03), 196-201.